SCUOLA DI DOTTORATO

UNIVERSITÀ DEGLI STUDI DI MILANO-BICOCCA

Department of Physics "Giuseppe Occhialini"

PhD in Physics ed Astronomy, Cicle XXXVI
Physics of the Matter Curriculum

Development and Characterization of Silicon Carbide Neutron Detectors for Fusion Reactors

Matteo Hakeem **Kushoro**
ID Number: 748218

Tutor: Dr. Marco **Tardocchi**

Supervisor: Dr. Marica **Rebai**

Coordinator: Prof. Stefano **Ragazzi**

ANNO ACCADEMICO / ACADEMIC YEAR 2022/2023

To those who wished not to be told about my work
But to whom I told it anyway.

Abstract

This thesis is a monography on the use of Silicon Carbide (SiC) Solid State Detector (SSD) as a fast neutron counter and spectrometer for fusion plasma applications. It details the research activities conducted on a series of SiC prototypes to characterize them, contributing to their development and assessment of their potential.

Neutron detection is possibly the main way of obtaining information from a fusion plasma in a Tokamak. Through it is possible to determine the fusion power, determine the plasma location and density and estimate the production of tritium in the breeder elements. By measuring the neutron energy spectrum it is also possible to infer other plasma properties, like the fuel ion ratio or the ion temperature. Tokamak environments, though, put unprecedented challenges on the diagnostics: large neutron fluxes, the presence of intense magnetic fields, high temperatures, and intense radiation. SSDs feature very promising characteristics for handling the aforementioned challenges. Since the SiC is a relatively unexplored SSD active material, the research activities of this PhD project aimed to characterize a series of SiC prototypes, developed in conjunction with IMM-CNR, finding their strengths compared to the state of art of SSDs, the diamond detector.

The activity has been dedicated to characterization of eight prototypes through neutron and charged particles irradiation, developing methods for data analysis, electronics management, hardware manufacturing and more. Detection characteristics (efficiency, energy resolution, stability and more) were studied in different configurations, finding methods to improve them and using the results as a basis for the manufacturing of new, improved prototypes. Stress tests were also conducted under harsh conditions, highlighting the functionality of the detector in harsh environments. Unprecedented methods of operations, like the partial depletion detection, were also experimented, finding new beneficial uses for the detector.

Results point out that the SiC is a valid alternative for neutron counting and spectroscopy in Tokamaks, possibly being a better than diamond in some context (e.g.: high temperature detection or high dynamic range flux measurements) but not all context (e.g.: high resolution spectroscopy). The research may serve as a comprehensive basis for future SiC developments and manufacturing, as well as experiments and the use of the detector on future Tokamak experiments for a variety of purposes.

Chapter 1
Introduction

1.1 Decarbonization and the Increasing Demand for Energy

Since the earliest stages of the industrial revolution, there has been a strong correlation between the economic output of societies and their energy consumption. The transition from hand assemblies and animal-powered tools to steam-powered devices, which happened during the latter half of the 19th century in many regions of the world, opened the way for levels of economic output never reached before in recorded history, both in the resource extraction and manufacturing sector. Such output required practical and abundant energy sources, which were mostly found in the chemical reactions involving hydrocarbons. The combustion of hydrocarbons has been the source of heat for thermal machines, converting a fraction of such heat in work to be used for both industrial and day-to-day processes: the long and complex structure of hydrocarbon molecules found in nature are in a comparatively high energy state and, by breaking down such molecules in combustion processes, it is possible to extract orders of energy of $\simeq eV$ per molecule, corresponding to $\simeq 10^8$ Joule per mole of fuel (in a pure state) and to roughly $\simeq 10^7 - 10^8$ Joule per kilogram of fuel. Innovations in the choice of fuels (wood, coal, oil, natural gas, etc.), in the thermal machines (diesel engines, electrical engines, etc.) and in the power transmission and storage (electrical grid, batteries, etc.) significantly improved the efficiency and the amount of energy extracted but did not change the fundamental chemical processes underlying the energy extraction.

To this day, hydrocarbons are still the main source of energy for most human activity on the planet, accounting for 84% of the 176000 TWh (or $6.35 \cdot 10^{20}$ Joule) primary energy consumption in 2021 [1]. Most of the source of hydrocarbons are fossil fuels (namely coal, oil, natural gas and few others), accumulated in the Earth's crust in the course of millions of years of biological processes. The reliance on these fossil fuels is so widespread that the byproducts of their combustion, like carbon dioxide and methane, altered the composition of the atmosphere to the extent of altering global climate and the balance of the ecosystem in the entire planet. The awareness of the seriousness of global warming gradually made into the political agendas of the governments since the latter third of the 20th century, as well as the hearts and minds of people. This brought forward the challenge of transitioning away from the fossil fuel sources while not compromising the global economic output on which the prosperity of billions of people relies on. Such economic output, in fact, is ever hungrier of power despite the attempts in optimizing and reducing the energy consumption (as can be seen in figure 1.1).

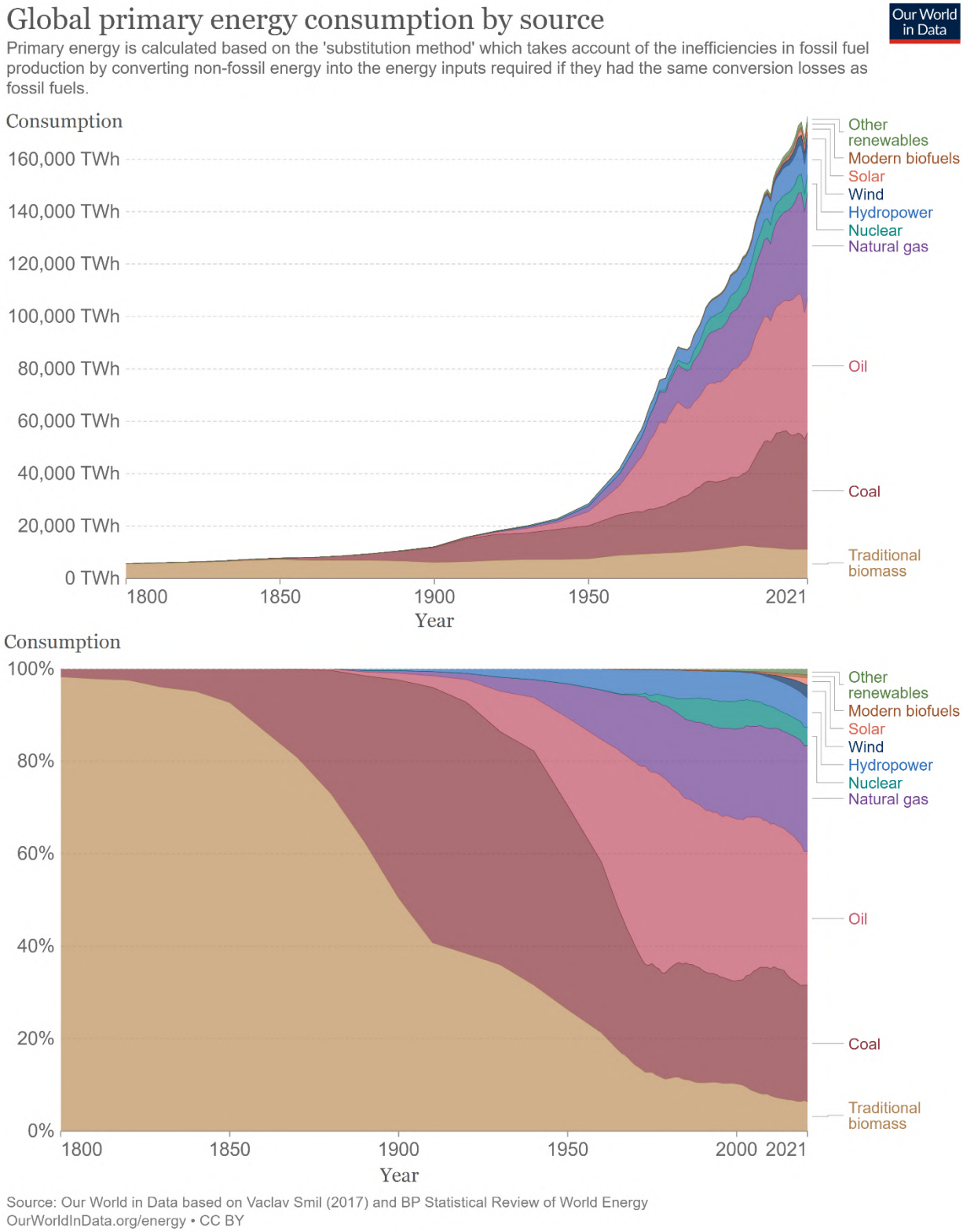

Figure 1.1: Global energy consumption divided by the share of different sources. While the use of fossil fuels (coal, oil and natural gas) in the last seventy years is decreasing in relative terms (bottom picture), it has increased sharply in absolute terms driven by the sharp increase of the overall global consumption (top picture). Image taken from [1]. Data from [2].

The transition away from fossil fuels requires the expansion of production of energy of a variety of energy sources. Among them, a strong focus is put on renewables, mainly hydroelectric, solar and wind, currently constituting almost the 12% of the global energy production. Hydroelectric is a long-known and well-developed energy source, and solar and wind are expanding rapidly. Renewable sources have their main advantage in not needing any fuel and not producing polluting byproducts, thus having a negligible impact on the climate.

On the other hand, the power production through solar and wind is usually unpredictable (since it depends on uncontrollable factors like the weather) meaning that their expansion needs to be complemented by some source providing for the baseload production of energy, while hydroelectric is limited to suitable reservoirs and has an environmental impact in terms of disruption of ecologies [3]. Such baseload is nowadays produced almost exclusively by hydrocarbons, constituting almost the 84% of the mix. The only large scale, not hydrocarbon-based and fully controllable energy source available is nuclear energy, which came in the scenes in the 1950s' and currently accounting for about 4% of the energy mix. The history, functionality and perspectives of such energy sources will be detailed in the next sections.

1.2 Nuclear Energy as a Power Source

The astounding advancements in the nuclear physics in the first three decades of the 20th century revealed the nature of atomic nuclei, their composition and their arrangements. It was only a matter of time before, analogously to the combustion of hydrocarbons, some process causing some nuclei transitioning from a higher energy state to a lower one was harnessed to extract energy. These discoveries opened the way for nuclear power, an energy source differing from the hydrocarbon on a fundamental level: through these processes it is possible to extract $\simeq 10^6 eV$ from every atom, leading to $\simeq 10^{12} - 10^{13}$ Joule per kilogram of fuel, which is five to six orders of magnitude more than chemical-based reactions. This abundance in the availability of energy shows the potential of nuclear for powering the ever-growing need for energy of the world civilization while reducing the reliance on fossil fuels as much as possible. In the last seventy years this potential has been exploited through nuclear fission, coming with a series of contraindications which limited a more widespread reliance. Such contraindications are solved through the future adoption of nuclear fusion, which is still under research phase. A more thorough discussion on the two energy sources will be presented in the next two sections.

1.2.1 Nuclear Fission

The first widespread and commercially available source of nuclear energy was ^{235}U (uranium-235). ^{235}U nuclei are in a high potential nuclear energy configuration which is also stable, allowing for the element to be found in nature in reasonable concentrations (2.8 parts per million in the Earth's crust, which are about the same as tin) [4]. One notable property of such nucleus is the high fission cross section to thermal neutrons, meaning that there is a high probability for the interaction of a slow neutron with the nucleus resulting in a split of the nucleus in two fragments, plus two-three neutrons. Since the new smaller nuclei have a configuration which is more energetically favorable than the one of ^{235}U, the fission reaction is exothermic; this results in an increase in the total kinetic energy of the species. The relative ease with which ^{235}U nuclei split meant that uranium-powered fission reactions were the most easy and convenient ways to produce nuclear energy, and therefore the first to be engineered to be

reliable energy sources. Another favorable condition is due to the production of multiple neutrons as a consequence of the fission, allowing those to trigger new fission reaction (if moderated to appropriate energies) and thus enabling a self-sustaining (or even expanding) chain reaction.

The fission of ^{235}U comes with its own flaws:

- Uranium is not a common material on the Earth's crust: its mining is usually costly, almost exclusive to some region of the world and its availability limited. In fact, economically viable (< 40 USD/kg) world reserves of Uranium, either confirmed or inferred, were 2,16 million tons in 2019 at the front of a worldwide yearly consumption of 59,2 thousand tons of uranium in the same year [5]. This prospect an availability of cheap uranium for less than 40 years at current consumption rates, which meets less than 4% of the worldwide need for energy [1] (and about 10% of electrical energy). While it is reasonable to expect new reserves being found each year and that technological advancements might reduce the cost of confirmed reserves which are not economically viable to present date, this is unlikely to be able to replace hydrocarbons as the workhorse of energy production in the decades to come.
- The product of the ^{235}U fission are usually unstable nuclei with long decay chains. This means that spent fuel is radioactive, requiring either to be stored in safe facilities behind biological shields or to undergo treatments that are currently outside of the technical for large quantities of spent fuel.
- The chain reaction involves one neutron triggering a fission which produces between two or three neutrons. If, on average, more than one of such neutrons triggers another fission, the reaction will reach the condition of supercriticality, in which it will grow exponentially. While nuclear reactors are specifically manufactured never to reach supercritical stage, some of the technologies used to build a nuclear reactor can be re-engineered to build supercritical devices, namely a nuclear bomb. This generates political issues on the basis of nuclear proliferation. Serious incidents may also emerge from the lack of control due to natural disasters (like the incident of the central of Fukushima), poor design choices or serious mismanagement (like the one leading to the disaster in Černobyl).

1.2.2 Nuclear Fusion

The principle of nuclear fusion is diametrically opposed to the one of nuclear fission: instead of splitting a heavy nucleus, the energy is gained from the fusion of two light nuclei. Such process was correctly theorized in the early '20s of the 20th century as the source of power for the Sun (and stars in general) even before the understanding of the process of fission (which was reached in the late '30s). The first man-made fusion reaction was achieved with the development of thermonuclear hydrogen bombs in the early '50s, both in the USA and the USSR.

A successful fusion reaction on a large scale requires the interaction of particles in a very high temperature environment. Such environment is reached through the means of gravity on stars and through the explosion of a fission bomb in a hydrogen bomb. To achieve the same environment on earth in a controlled manner, though, has been proven a daunting task. A

controlled fusion device is under research since the mid '50s by research centers all over the world (mainly USSR - and more recently Russia -, USA, UE, UK, Japan and China).

All the difficulties on the fusion research are more than motivated by the perspectives offered by such a technology employed in the energy production. Among those:

- Fusion reactions are not chain reactions; as such, they can't physically reach a state of supercriticality in any conditions. This is a huge safety factor, since any loss of control of the reaction will inevitably result in its powering down.
- The prospected fusion reaction to be used for the energy production involves two hydrogen isotopes, deuterium and tritium. The first is widely available, being a fraction of all natural hydrogen present on Earth, while the second can be produced from Lithium in fusion power plants [6]. This allows for a supply of reactants of tens of thousands of years of current consumption rates even if the entire electrical energy should be produced through fusion.
- Spent fuel is constituted by light nuclei with stable isotopes (^{4}He in the case of deuterium-tritium fusion), which have few chemical and radioactive concerns. This means that, contrary to fission, fusion does have any problem with spent radioactive fuel to be treated or stored. A concern regarding radioactive source is the tritium to be supplied to the reactor, which is a dangerous radioactive element if dispersed in the environment: although no more than few hundred grams of tritium will be present in any power plant at any time, reducing the impact of any tritium-related accident to be almost unharmful. Another concern is the damaging and activation of the materials containing the fusion reaction due to the radiation emitted by the fusion reactions (mostly, fast neutrons), which is a difficulty that will be mostly contained in the reactor site.

The next section will expand the description on fusion by giving a general description of the theory behind it. Section 1.4 will expand on the Tokamak, which is the most advanced design for a nuclear fusion device to date. Section 1.5 will than give a brief overview of a selection of relevant present and future tokamaks.

1.3 Fusion Theory

With nuclear fusion it is referred to a nuclear reaction by which two nuclei (or subatomic particles) are combined to form one different atomic nucleus, usually producing other subatomic particles as a result. From Figure 1.2 it can be seen that, among stable nuclei, the most energetically favorable nuclear configurations are those with intermediate Zs (iron-56 being the most favorable). This makes it so that reactions resulting in nuclei closer to the intermediate Zs results in reduction of the binding energy of the nuclear species and, therefore, in a positive energy output (Q-value), making the reaction exothermic. Among these reactions are both fissions of high-Z nuclei (e.g., ^{235}U) and nuclear fusion reactions between light nuclei.

Being exothermic does not mean that fusion reaction between lighter nuclei happen spontaneously. Before the forces due to strong nuclear interaction can take place and rearrange the nuclear structure, the two nuclei must overcome their mutual Coulombian barrier U_{Coul} due to the repulsion of the positively charged nuclei ($Z_1 e$ and $Z_2 e$):

$$U_{Coul} = \frac{Z_1 Z_2 e^2}{4\pi\epsilon_0} \cdot \frac{1}{r}$$

ϵ_0 being the vacuum permittivity constant. Since the typical distances r at which the strong interaction take place are on the order of few femtometers, the coulombian barrier are between few hundreds of keV and few MeVs – which is an energy comparable to the energy gained by the nuclear reaction itself.

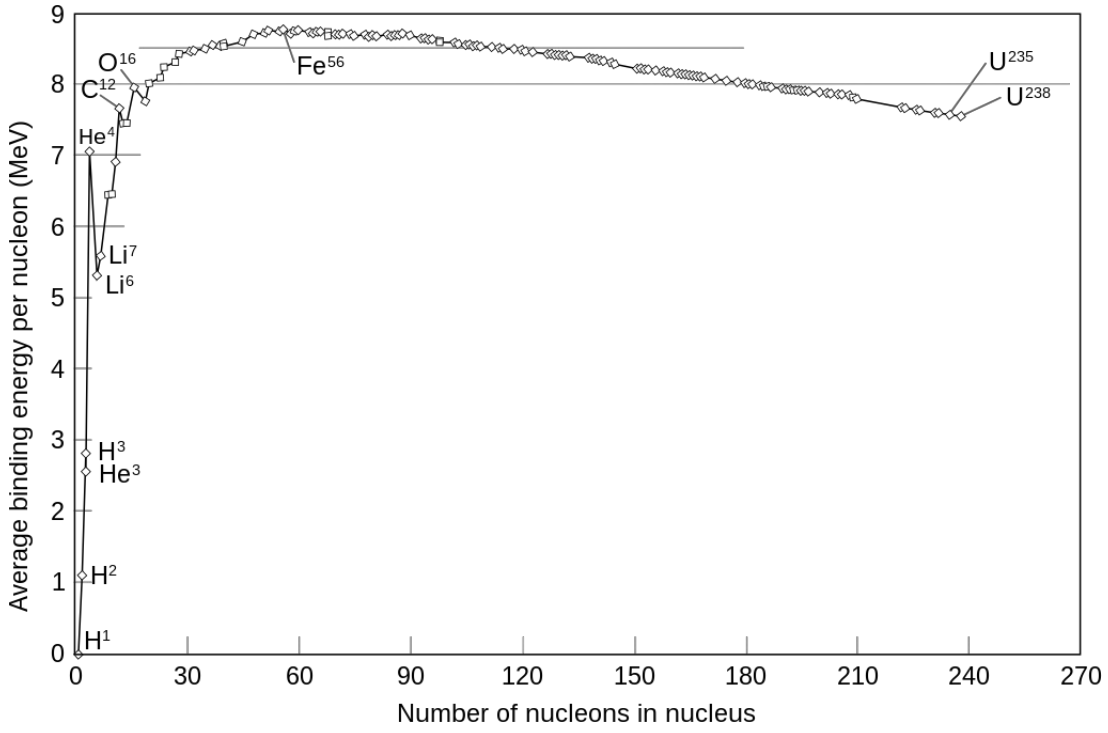

Figure 1.2: Dependence of the binding energy between nucleons divided by the number of nucleons as a function of the atomic mass number. Only stable nuclei of the periodic table are considered. Both light and heavy nuclei tend to be loosely bonded together, with elements around mass number 56 being the most bonded. Processes involving either light nuclei or heavy nuclei moving towards the mid atomic numbers will result in exothermic reactions.

1.3.1 Fusion Reaction Candidates

The ideal candidate for a nuclear fusion reaction to be employed for energy production should:

- Have a high, positive Q-value.
- Have a Coulombian barrier as low as possible, in order to allow the reaction even for smaller reactant energies.
- Have a fusion cross-section as high as possible, in order to reduce the number of interactions between nuclei not resulting in fusion.
- Be a 2-bodies reaction, in order to avoid the need of three-body interactions, which are more improbable and difficult to achieve.
- Produce no gamma radiation as a result, since gamma radiation energy is more difficult to harness than the one from heavy particles.

Since the Coulombian barrier is proportional to the Zs of the nuclei involved in the interaction, the reaction of interest for the realization of a reactor are going to be the ones with the lowest Zs. Combining this with the other needs, a small number of reactions are left as candidates:

1.	D + T	→	^{4}He (3.52 MeV) + n (14.06 MeV)	
2.	D + D	→	T (1.01 MeV) + p (3.02 MeV)	[50%]
		→	^{3}He (0.82 MeV) + n (2.45 MeV)	[50%]
3.	D + ^{3}He	→	^{4}He (3.6 MeV) + p (14.7 MeV)	
4.	T + T	→	^{4}He + n + n (+11.3 MeV)	
5.	^{3}He + ^{3}He	→	^{4}He + p + p (+12.9 MeV)	
6.	^{3}He + T	→	^{4}He + n + p (+12.1 MeV)	[57%]
		→	^{4}He (4.8 MeV) + D (9.5 MeV)	[43%]
7.	^{2}D + ^{6}Li	→	^{4}He + ^{4}He (+22.4 MeV)	
		→	^{3}He + ^{4}He + n (+2.56 MeV)	
		→	^{7}Li + p (+5.0 MeV)	
		→	^{7}Be + n (+3.4 MeV)	
8.	P + ^{6}Li	→	^{4}He (1.7 MeV) + ^{3}He (2.3 MeV)	
9.	^{3}He + ^{6}Li	→	^{4}He + ^{4}He + p (+16.9 MeV)	
10.	p + ^{11}B	→	^{4}He + ^{4}He + ^{4}He (+8.7 MeV)	

Some of the listed reaction can result in a final state: those are listed as double (or more) lines with the probability of each output reported in square brackets.

In choosing between the listed reaction numerous factors must be taken into account: reactivity, availability of fuel, species of the products, cross-section of the reaction and other. By taking into account all of these factors the reaction ^{2}D + ^{3}T comes on top of the list of candidates, having the highest cross section ($\simeq$ 50 Barn) at relative low energies ($\simeq$ 60 keV), as shown in Figure 1.3. On the downsides, ^{2}D + ^{3}T requires deuterium and tritium as fuels: while the first has a natural abundance of 0.016% and is therefore widely available [6], tritium has a relatively short half-life of 12.32 years and is, therefore, practically absent on Earth. For this reason, tritium should be produced in an energetically convenient manner and promptly supplied to the reaction; ideally the production should happen in the same facility achieving the fusion reactions. To this end, a few interactions of neutrons with Lithium and Boron can produce tritium:

n + ^{6}Li	→	^{4}He (2.05 MeV) + T (2.75 MeV)
n + ^{7}Li	→	^{4}He + T + n (-2.466 MeV)
n + ^{10}B	→	^{4}He + ^{4}He + T

These reactions are of particular interest since they require a neutron which could be the same produced by the DT reaction. The reaction involving ^{6}Li is particularly interesting for its positive balance of energy. A combination of the first two reaction can be used to produce the tritium needed to provide fuel to the fusion reaction.

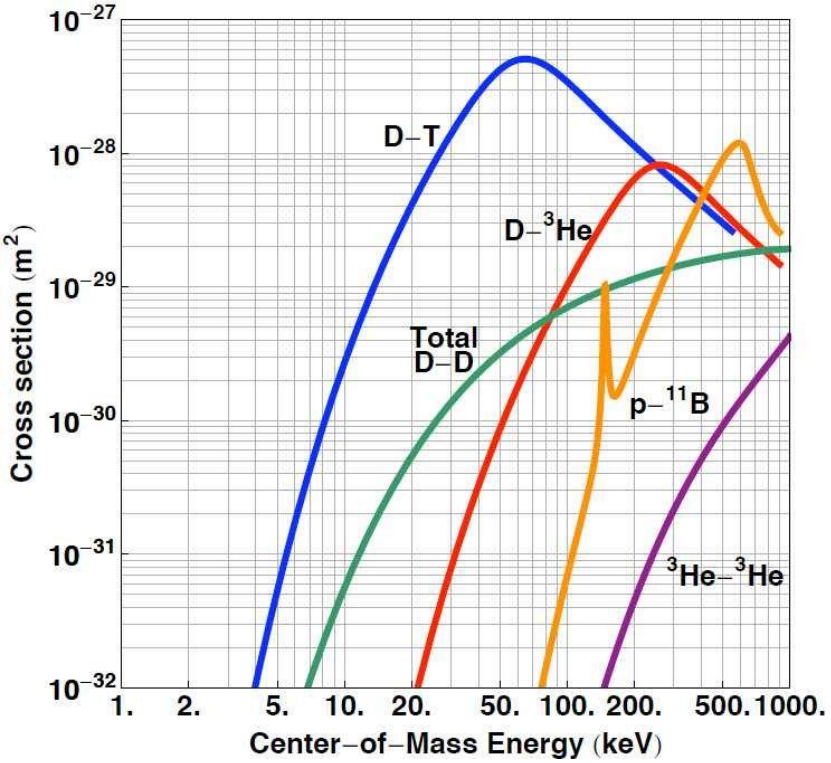

Figure 1.3: Dependence of the cross-section of several fusion reactions for energies between 1 keV and 1 MeV. The DT reaction around 60 keV has the highest cross-section of any of the reaction listed among the fusion reaction candidates, allowing for an easier time in triggering it.

1.3.2 Magnetic Confinement

In order to have the highest probability of DT interaction the deuterium and tritium need to collide with a kinetic energy of about 60 keV with respect with the centre of mass. These energies can be achieved with linear particle accelerators, impinging deuterium projectiles onto tritium targets. Such a process, although, would have an extremely low efficiency since only a very small fraction of the accelerated fuel would undergo fusion, the rest being wasted, making the perspective of gaining net energy almost impossible. Conversely, if the fuel could be kept in a keV-hot plasma state the random motion of particles would repeatedly see the interaction of deuterium and tritium nuclei. The advantages are:

- The number of reactions, and therefore the power produced, would depend on the size of the plasma, which could be (at least in principle) arbitrarily large.
- If the plasma is able to keep the kinetic energy of the deuterium and tritium nuclei confined in the plasma for enough time, the interaction between deuterium and tritium failing in resulting in a DT fusion would not waste the kinetic energy of the reactants, allowing the two species to retain their fusion-allowing energy.
- If the products of the fusion reaction cede a large fraction of their energy to the plasma before escaping it, the fusion reaction will contribute to keep the plasma "hot". In other words, the plasma would "burn" since DT reaction would contribute to sustain the plasma temperature.

In the case of a thermalized plasma (whose particles distribution of energy follows a Maxwellian law) it's sufficient for the plasma to have a mean particle kinetic energy of few keVs

(8-15 keV) in order for the fusion reaction being triggered by fraction of nuclei with the highest energy. Such a highly energetic plasma needs to avoid contact with solid surfaces in order not to disperse the heat almost immediately and not to damage the solid surface itself. This can be achieved through magnetic confinement: since all the particles in a fully ionized plasma are charged, their motion incurs in the Lorentz force $\overrightarrow{F_L} = q \cdot \vec{v}x\vec{B}$ while in presence of a magnetic field $\vec{B}$. The force perpendicular to both the particle motion and the magnetic field causes charge particles to describe an orbital movement around the magnetic field line, resulting in particles being confined along the two directions perpendicular to the magnetic field $\vec{B}$. To achieve a confinement along the third dimension (the one parallel to $\vec{B}$) it's much harder: it is possible to increase the field strength at the two ends of the plasma to create a magnetic mirror (figure 1.4), but such effect wouldn't affect the particles whose motion is roughly aligned with the magnetic field, regardless of the magnitude of the gradient. The combined effect of particles with velocity almost parallel to $\vec{B}$ and collisions shuffling the distribution of velocities in the plasma would cause the rapid emptying of the plasma confined in a linear machine. In other words, random collisions between confined particles would cause a fraction of plasma particles to align their motion to the magnetic field, and those particles would promptly escape the magnetic confinement, resulting in a quick depletion of the plasma.

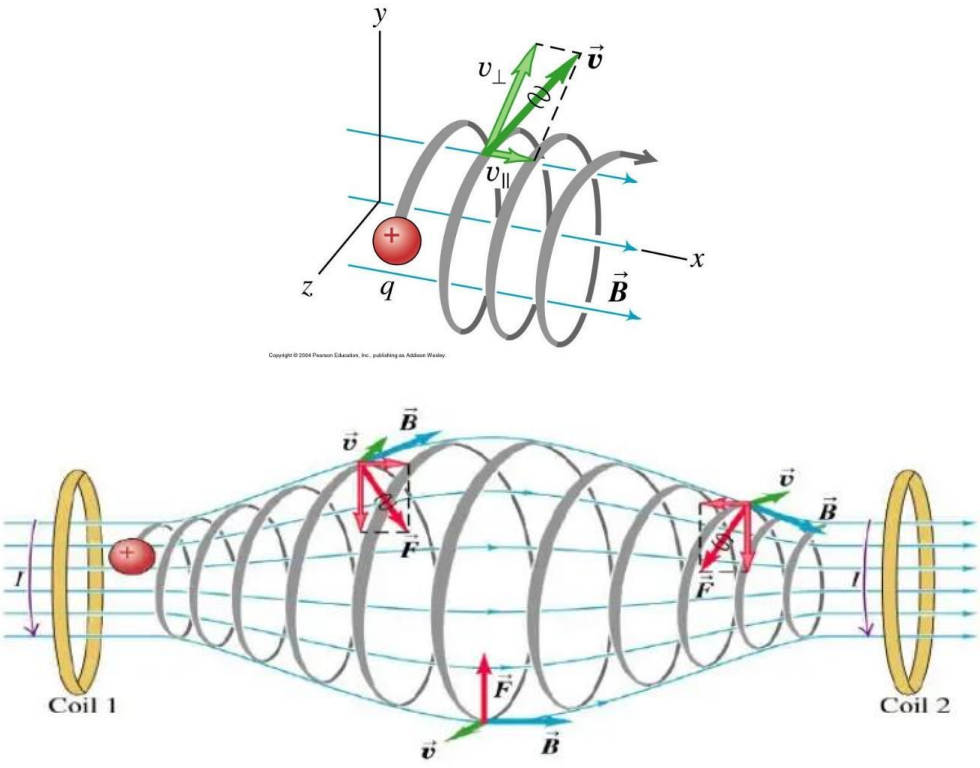

Figure 1.4: ***Top*** *- Helicoidal motion of a charge particle moving in a straight magnetic field. The perpendicular component of the velocity is twisted around the field lines, while parallel component of the velocity ($v_{//}$) is unaffected by the field.*
Bottom *– Effect of an increasing magnetic field on the motion of a charged particle (magnetic mirror). The bending of the field lines induces a force opposing to the parallel motion of the particle.*

To avoid losses along the direction parallel to the magnetic field an effective solution is to join the two ends of the cylinder by bending its lines, turning the cylindrical shape into a torus. One downside is that the bending causes the magnetic field to have a gradient: higher field inside the curve, lower field on the outer part of the curve. This causes the orbits of the plasma components to have a smaller radius while moving through the region of higher field and a bigger radius while moving through the lower field, resulting in spiralling orbits drifting in the direction perpendicular to $\vec{B}$ and $\overrightarrow{\nabla B}$ (the vertical axis, if the torus is on a horizontal plane). Such drifts, depicted in figure 1.5, have opposing directions for ions and electrons: this does not cause a displacement of the plasma since the separation of the charges induces an electric field $\vec{E}$ that opposes to the drift. This $\vec{E}$, although, causes a second drift velocity $\overrightarrow{v_E} = \frac{\vec{E}x\vec{B}}{B^2}$ for both species, pointed toward the external part of the torus, that displaces the plasma making it collide with the external walls.

In order to prevent this, magnetic confinement designs add a poloidal component to the magnetic field in order to twist the magnetic field into helicoidal spirals (like the one in figure 1.6). Such a shape changes the direction of $\overrightarrow{v_E}$ along the toroidal coordinate, twisting the trajectories of the particles keeping them inside the torus.

This design is common for all magnetically confined fusion plasma devices. The means by which the poloidal magnetic field is produced differentiate between the two most popular and successful designs, the Tokamak and the Stellarator, which will be illustrated in the next section.

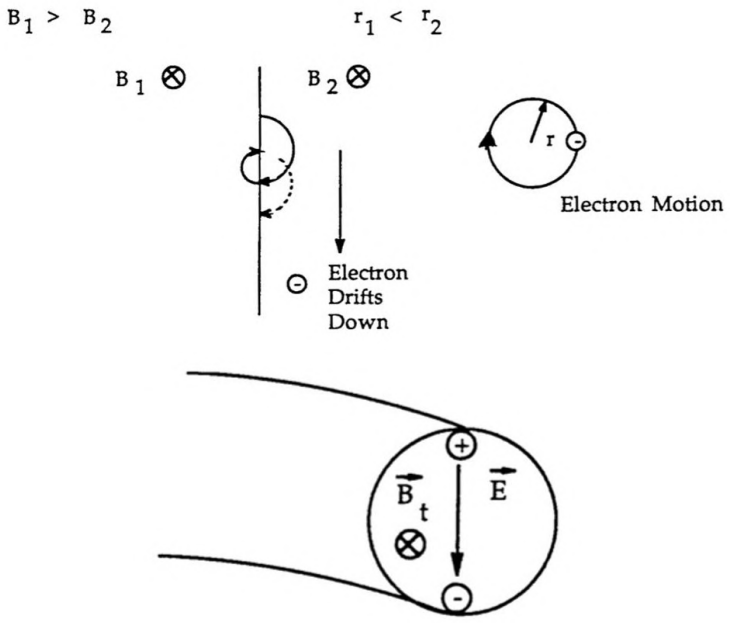

Figure 1.5: Forces and gradients affecting particle motion in a toroidal magnetic field.

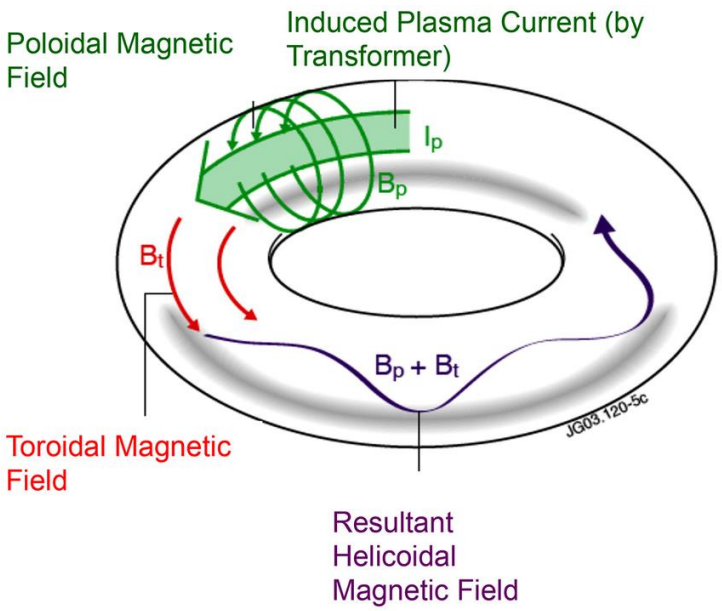

Figure 1.6: Schematic representation of the toroidal and poloidal magnetic field component resulting in an helicoidal magnetic field, allowing for the motion of a charged particle to be confined inside the torus. The helicoidal magnetic field is the basis for both the Tokamak and Stellarator designs.

1.3.3 Tokamak and Stellarator

A magnetic confinement fusion plasma device needs to produce a strong helicoidal magnetic field (sum of a toroidal and a poloidal component, as described in section 1.3.2) inside a vacuum chamber. The toroidal component of the magnetic field can be obtained through a series of coils arranged like toroidal solenoid, like the one in figure 1.6. The poloidal component can be obtained in two different methods, which define the two most successful designs for a fusion plasma device:

- The Tokamak design (figure 1.7, on the left) obtains the poloidal component by inducing a toroidal current in the plasma. This is induced by altering a current in a solenoid passing through the surface enclosed by the torus. The changing current generates a varying magnetic field which intersects the enclosed torus surface, generating an electromotive force in the plasma by induction (as predicted by Faraday-Neumann-Lenz Law). Since the plasma has low resistivity, this results in a plasma current.
- The Stellarator design (figure 1.7, on the right) obtains the poloidal component from the bent shape of the toroidal coils.

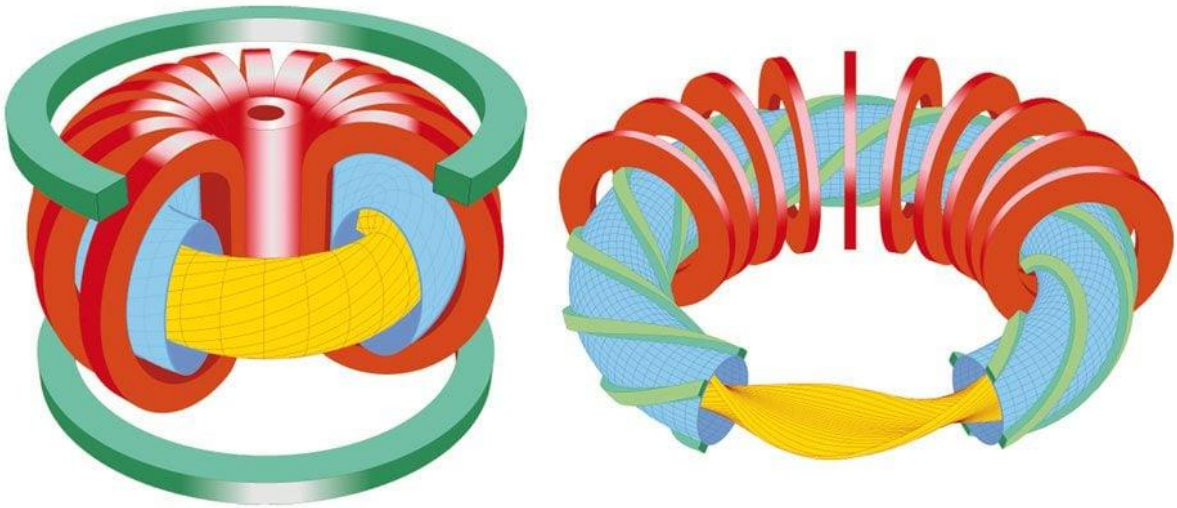

Figure 1.7: Exemplificative representation of a tokamak design (on the left) and a stellarator design (on the right). Both designs feature a curved solenoid (in red) generating the toroidal component of the magnetic field. The tokamak design features coils (in green) inducing a current in the plasma (yellow), which is responsible for the poloidal field. The stellarator, on the other hand, features a series of spiral coils (in light green) which produce the poloidal field directly.

Tokamaks have an intrinsic disadvantage compared to Stellarators: since the current in the central solenoid can only be increased to a certain limit, they can only operate in pulsed mode, reaching a point in which it's necessary to break the plasma. Stellarators, on the other hand, can in principle operate in a steady-state mode. Nevertheless, it's the Tokamak design which achieved the best results since the '60s.

Research on fusion proceeds on both types of machines, with Tokamaks having a lead in the research, with the majority of the most advanced experiments being Tokamaks [6]. For this reason, this thesis will focus almost exclusively on Tokamaks and their diagnostics; it must be pointed out, although, that most of the conclusions and results obtained can also be used for all type of fusion plasma devices.

1.4 Tokamak Theory

1.4.1 Ignition, Q-factor and the Triple Product

One of the major challenges in sustaining a fusion plasma is keeping the plasma hot and confined. Two sources of loss of plasma energy are radiation and the energy lost by particles leaving the plasma (carrying away their kinetic energy). Among the latter there is the energy loss due to neutrons produced by fusion reactions. Being neutral, neutrons are not confined by the magnetic field and escape the plasma, carrying a big fraction of the reaction energy (in the case of $^{2}D + ^{3}T$, the resulting neutron carries around 80% of the 17.6 MeV energy). Other sources of loss are plasma particles that diffuse away from the center of the plasma due to collisions.

If the power losses equal the power generated through the fusion reactions the fusion plasma reaches a self-sustaining state called ignition (the name deriving from the analogy with the self-sustaining chemical combustion). If power losses are greater than fusion power than the plasma cools down, eventually reaching temperatures at which fusion reaction cease completely. It's not necessary to reach ignition to sustain a fusion reaction, since additional power can be supplied from the outside to compensate for the net losses of energy. The ratio between the energy produced by fusion and the energy supplied is the Fusion Gain Energy Factor, usually called Q. Ignition corresponds to Q = ∞, while Q = 1, referred to as "scientific breakeven", corresponds to the situation in which the power produced by fusion reactions is equal to the power supplied. It is not enough to reach Q > 1 to achieve a power plant, since various additional factors need to be considered:

- The initial heating to bring the plasma to a fusion-enabling temperature (which is not included in the Q).
- The efficiency in the conversion from power extracted by the plasma and electrical power (between 35% to 40% [7]).
- The efficiency of the plasma heating systems (between 60% and 70% [7]).
- The economic investment of building the reactor and relative infrastructure, to be compensated by the selling of electrical power at market price.

It is prospected that a commercially viable fusion power plant should have a Q of at least 25 – 30 [8]. In order to achieve this, it is paramount to either increase the self-heating of the plasma as much as possible (by triggering nuclear reaction more often) or to reduce the power irradiated by the plasma as long as possible. Such conditions are summed up in the triple product:

$$n \cdot T \cdot \tau_E \geq 1.2 \cdot 10^{21} m^{-3} keV \cdot s$$

Where n and T are the plasma density (in units of ions per cubic meter) and the temperature (in units of keV). τ_E is the confinement time, measuring the rate at which the system loses energy to the environment. Such product must be at least $1.2 \cdot 10^{21} m^{-3} keV \cdot s$ in order to achieve a successful fusion.

For Tokamaks, the triple product usually translates to a lower limit for τ_E. This is because the optimal T is defined by the need of obtaining the maximum reaction rate between deuterium and tritium (see section 1.3.1), while a maximum n is due to the Greenwald limit, linking the maximum plasma average density to the plasma current I_p and the minor toroidal radius a [9]:

$$n \leq \frac{I_p}{\pi a^2}$$

Exceeding the Greenwald limit typically leads to a disruption, possibly due to edge gradient limits or the formation of magnetic islands [10]. This leads to a commonly adopted target density on the order of $n \simeq 10^{20} m^{-3}$. Increasing such density would require increasing I_p, which would also increase the poloidal component of the magnetic field. This, in turn, would require rebalancing the toroidal component, which is limited by the technical feasibility of the superconducting coils.

The challenge for Tokamaks, therefore, is to increase the confinement time τ_E. By replacing $n = 10^{20} m^{-3}$ and $T = 12keV$, the requisite for the confinement time for achieving fusion becomes $\tau_E \geq 1s$.

1.4.2 Plasma Heating

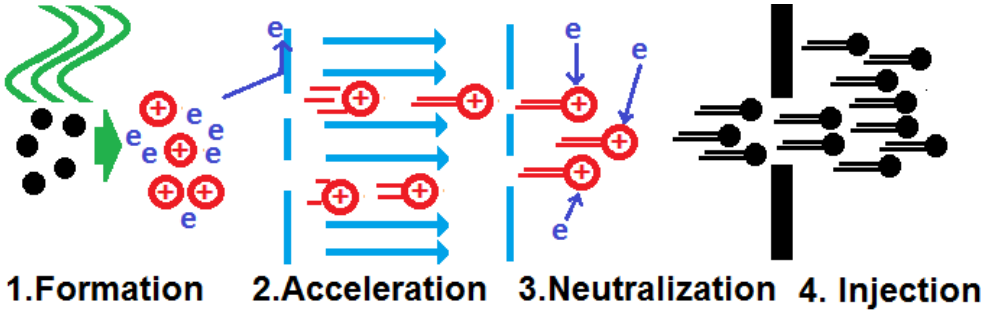

Figure 1.8: Four phases for the neutral beam injection.

The heating of the plasma is one of the most important components for a fusion plasma device. Not only the heating is necessary to reach the temperatures needed for fusion reaction to happen, but, since both existing machines and upcoming designs do not reach ignition, some form of heating will be essential even to sustain the reaction.

One of the prominent methods to heat up the plasma is **Neutral-Beam Injection** (**NBI**). The method consists in the acceleration of a beam neutral particles to high energies (hundreds of keV and more) to be injected into the plasma. Particles in the beam need to be neutral in order not to be deflected by the magnetic field confining the plasma due to Lorentz force. When the particles enter the plasma, they are quickly ionized by collisions with plasma particles, becoming charged particles part of the plasma confined by the magnetic field. This high energy particles then proceed to cede their energy to the rest of the plasma through collisions, introducing thermal energy. If the NBI is injected in the toroidal plasma tangentially the beam particle will also provide momentum to the plasma particles, contributing to drive the plasma current.

Since it is not possible to accelerate neutrals through electromagnetic processes, to achieve a neutral beam it is necessary to accelerate ions and neutralize them before injection. This is generally performed in four stages, schematically illustrated in figure 1.8:

1. A plasma is produced by microwaving a low-pressure gas.
2. A strong electric field is used to accelerate the ions up to the desired energy of the beam.
3. The beam ions are neutralized capturing electrons.
4. The beam is collimated and injected inside the plasma.

While the schematics above apply to positively charged ions, negative ion sources are also used in an analogue way: ions are accelerated by the electric field and subsequently stripped of the excess electron. The atomic species to be accelerated are usually deuterium or tritium (or a mix of the two) which become part of the burning plasma after the injection. Before being slowed down by collisions, the ensemble of particles injected by the neutral beam has kinetic energies higher than the typical energies of the particles in the plasma. The interaction between a nucleus of the beam and a nucleus of the plasma (or between two nuclei of the beam) might result in a fusion reaction which is not governed by the Maxwellian statistic, introducing differences in

respect to a fully thermalized situation (among which a component of neutrons with energies higher than 14.06 MeV, due to the high energy of the impinging beam nucleus).

Other ways to heat the plasma involves the acceleration of plasma components by microwaves. The microwaves are produced at exact frequencies of the rotation around the magnetic field lines of either electron or ions in the plasma. This accentuates their motion, making it so that the energy of the microwave is transferred to the plasma species. Heating devices relying on this phenomenon are called **electron cyclotron resonance heating** (**ECRH**), when the frequency is chosen to resonate with the electrons, or **ion cyclotron resonance heating** (**ICRH**), when the frequency is chosen to resonate with the ions. It is also possible to exploit the **lower hybrid oscillation** (**LH**), which involves a hybrid resonance with both ions and electrons.

1.4.3 Breeding Blanket

In section 1.2.2 it was illustrated that a fusion device should provide for its own supply of tritium. This task should be carried out in the breeding blanket, a set of modules covering the inner part of the reactor vessel. The vicinity of the blanket to the vessel is needed to intercept the maximum number of neutrons produced by the plasma, which are needed to produce the tritium through the reactions detailed in section 1.3.1. This means that the breeding blanket should support a very high heat load and a very intense neutron flux. The breeding blanket will also be used as the main conversion stage between neutron power and thermal power: the blanket coolant, in fact, should be used as a mean of transmission of the heat to the turbines.

Currently, no breeding blanket has ever been tested on a Tokamak. The upcoming fusion experiment ITER should test tritium breeding module concepts that would lead in a future reactor to tritium self-sufficiency and to the extraction of high-grade heat and electricity production [11]. For this reason, a series of Test Blanket Modules, based on different technologies, will be tested in the different operation phases of ITER [12]. Concepts for the breeder blanket include helium-cooled lithium lead (HCLL), helium-cooled pebble bed (HCPB), and water-cooled lithium lead (WCLL) methods [13].

1.5 Tokamaks in the World

Since the first facilities were assembled between the 1955 and 1965 in the Soviet Union [14], many Tokamaks were built all around the world for research purposes. With the passing of the years various Tokamaks were build, increasing the triple product value (see section 1.4.1) and approaching to the conditions of scientific breakthrough.

This section will provide a brief description of some of the most important Tokamaks in operation and in the construction or design phase. The list is not comprehensive and focuses on the most relevant tokamaks for this thesis.

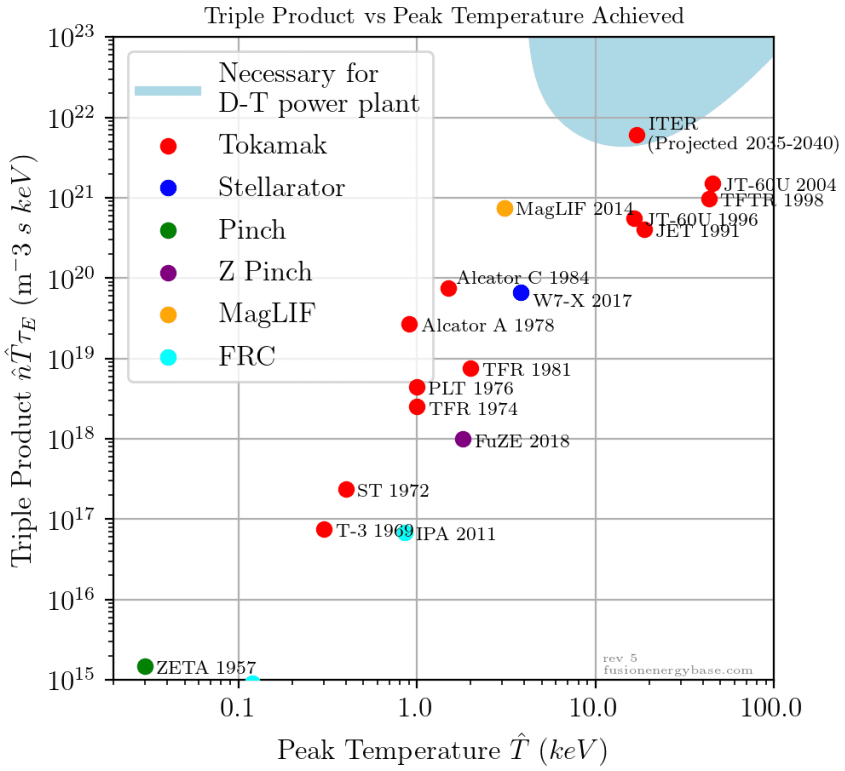

Figure 1.9: Graph showing a series of past and present fusion machines, plotted as a function of the maximum plasma ion temperature and the maximum value of triple product achieved. With the progress of time machines trended toward higher temperatures and triple products. On the top-right a region of parameters useful for a power plant is highlighted, with ITER occupying its point with the most optimal temperature.

1.5.1 Joint European Torus (JET)

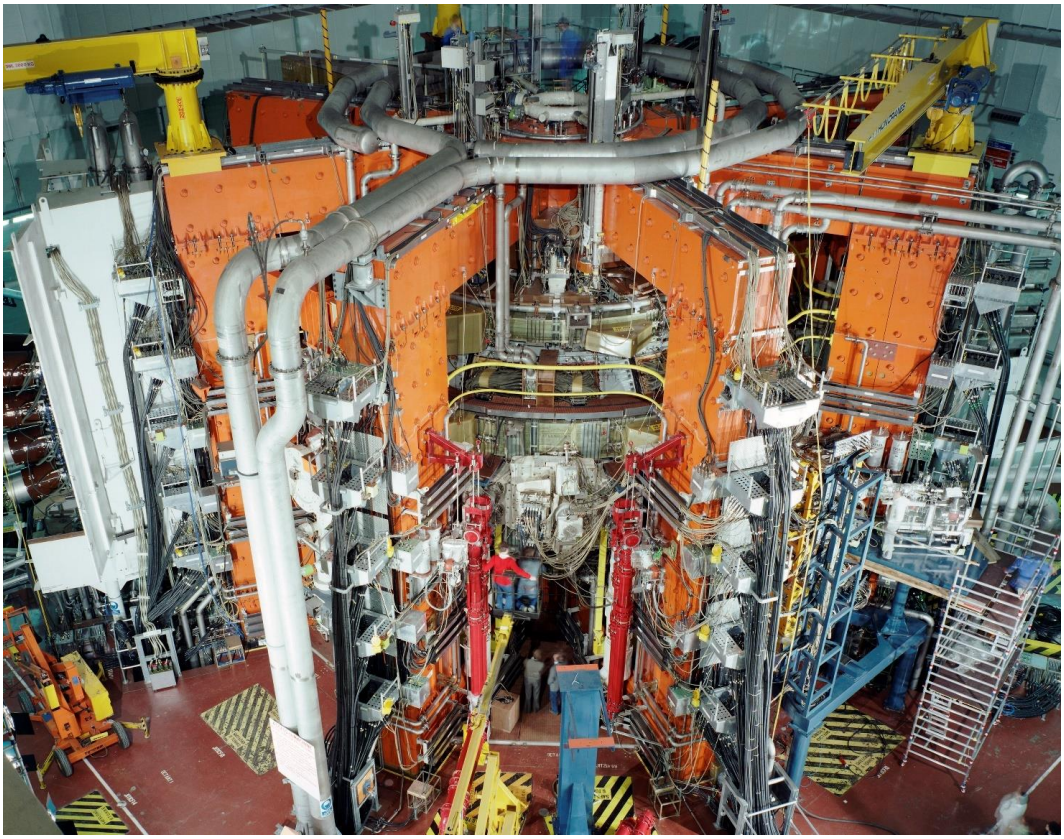

Figure 1.10: Picture of the Joint European Torus (JET).

The Joint European Torus is a Tokamak located at the Culham Centre for Fusion Energy in Oxfordshire, UK. While its operation started in 1984, JET is still the largest operating Tokamak in the world and probably the most important fusion machine for this thesis. With a major radius of 2.96 meters and a minor radius of 1.25 meters, it features a plasma volume of about $100m^2$[15]. The plasma is heated by a 34 MW neutral beam injector, a 10 MW ICRH and a 7 MW lower hybrid [15]. The initial objective of JET was the achievement of the scientific breakeven, which was nearly achieved during the DT campaign in 1997, when a Q=0.67 was reached [16].

Between 2009 and 2011, JET underwent updates to adopt concepts being used in the development of the ITER project; since then, JET has been used as a preliminary experiment for the construction and testing of the specifics of ITER, which will be detailed below.

1.5.2 ITER

ITER is the upcoming fusion Tokamak experiment, which will replace JET as the biggest fusion plasma device. It's currently in the construction phase in Cadarache, in Provence (France), and is expected to feature the first plasma around 2028.

The goal of ITER is to demonstrate a Q-factor high enough for fusion power to be exploitable. In order to reach it, the machine will feature a major radius of 6.2 meters and an unprecedentedly high plasma volume of 840 m^3, which is almost ten times the plasma volume of JET. The large volume will be an important factor in increasing the confinement time τ_E,

allowing for Q-factor which are prospected to reach Q = 10 and above. The plasma will be heated by a combination of heating systems: a 33 MW neutral beam injector (producing neutrals from negative ions), a 20 MW ECRH system and a 20MW ICRH system. ITER will also test a number of supporting technologies, like the tritium production: a series of test blanket modules (TBM) will be installed in different sections of the machine to test different method of tritium production. Divertor, diagnostic, heat exhaust and first wall interactions will also be tested, in order to finalize the DEMO Tokamak design.

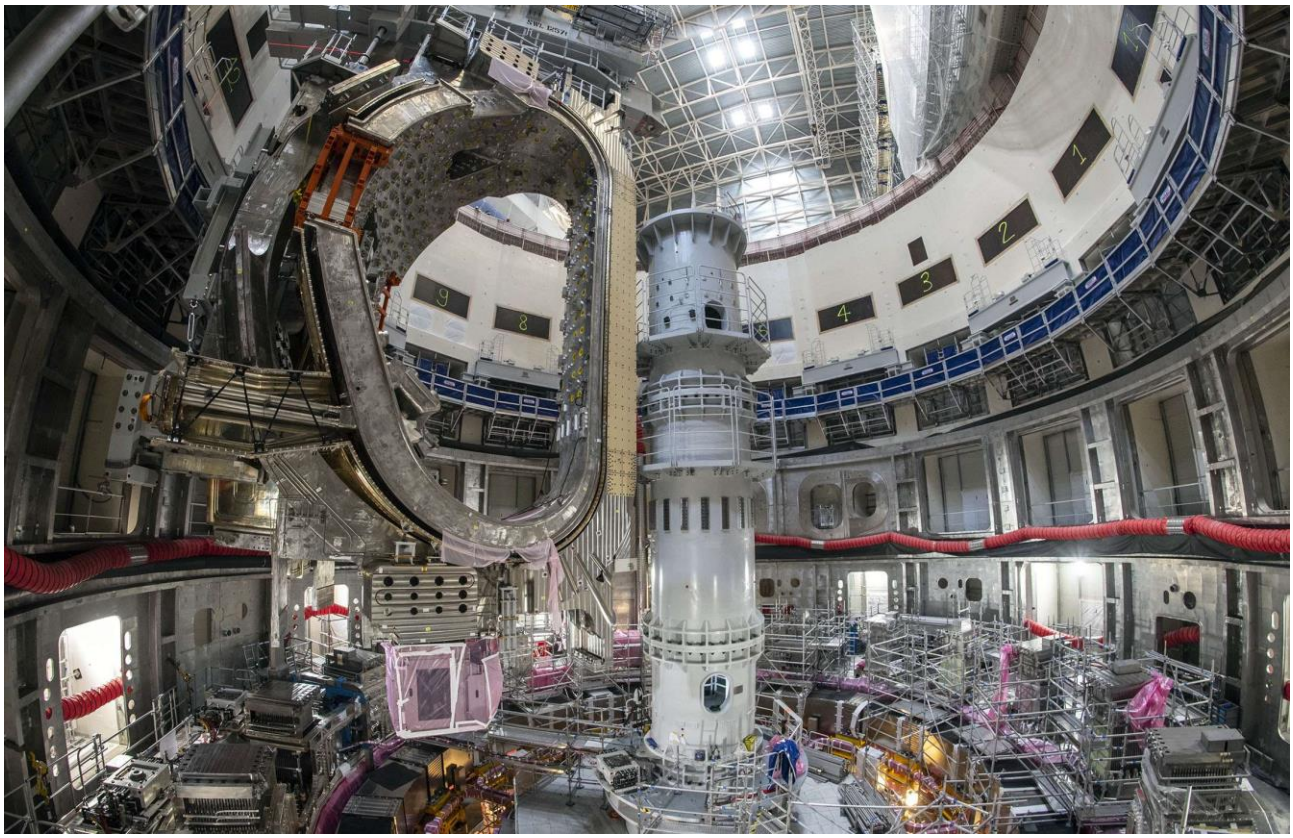

Figure 1.11: Picture of the chamber in which ITER is installed, taken in 2022. On the left one section of the torus is being put in place.

1.5.3 DEMO

ITER's successor, DEMO (short for "Demonstration Power Plant"), will be the transition between a fusion research facility to an industrial and technological driven machine. The goal is to demonstrate the necessary technologies not only for controlling a more powerful plasma than has previously existed, but for safely generating electricity consistently, and for regular, rapid, and reliable maintenance of the plant [17]. As such, it will feature a close tritium breeding and fuel cycle, the most promising designs of divertor, first wall, and heating systems and a turbine cycle for electrical generation.

The device is currently under planning phase, using the experience and data gained from JET and ITER to serve as a basis for the design. Since the scope of the machine regards industrial application (as opposed to fusion research), the number of diagnostic and control systems will probably be kept as low as possible, in order to optimize cost and reduce complexity. This paves

the way for the research and demonstration of simple diagnostics that provides the necessary plasma information to achieve plasma control.

1.5.4 SPARC

Figure 1.12: Manufacturing of SPARC tokamak components. Note the relatively small dimensions when compared to ITER's components.

SPARC is a tokamak under development by Commonwealth Fusion Systems (CFS) in collaboration with the Massachusetts Institute of Technology (MIT) Plasma Science and Fusion Center (PSFC) [18]. In a similar way as ITER, its goal is to verify the technology and physics required to build a power plant based on the ARC fusion power plant concept, which follows a different approach than ITER to increase the triple product: while ITER aims to increase τ_E by the means of increasing the plasma size, the ARC design aim to increase the magnetic confinement, allowing for a smaller machine that is able of achieving up to 140 MW of fusion power [18]. The higher magnetic field (12.2 T, comparing with the 5.3 T of ITER and the 3.45 T of JET) will be achieved by high-temperature superconducting magnets based on yttrium barium copper oxide (YBCO).

Even if the SPARC project started much later than ITER's, it has an extremely ambitious goal of achieving a first plasma by 2025, which is even before the first plasma of ITER.

1.5.5 Comparison between Tokamaks specifications

	Major Radius	Minor Radius	Plasma Volume	Magnetic Field	Heating Power	Plasma Current	Pulse Lenght	Start of Operations
JET	2,96 m	1,25 m	100 m^3	3,45 T	38 MW	4,8 MA	5 s	1984
ITER (goal)	6,2 m	2,8 m	840 m^3	5,3 T	50 MW	15 MA	400 s	2028
DEMO (goal)	7,5 m		1650 m^3	6,0 T	80 MW	20 MA	7200 s	2060 (?)
SPARC (goal)	1,85 m	0,57 m	20 m^3	12,2 T	25 MW	8,7 MA	10 s	2025

Chapter 2
Neutron Detection

Monitoring and understanding plasma conditions is crucial for achieving fusion. This is especially true during the research phase, where the focus is characterizing the plasma behaviour and optimize the tokamak operation. This drives the interest toward many types of plasma diagnostics; among those, neutron diagnostics play a crucial role, since neutrons constitute the main emission from the plasma. From the neutron emission several crucial parameters can be measured, like fusion power, ion temperature, plasma shape and more.

In this chapter the basic principles of neutron detection for fusion plasma applications will be analysed. Neutron diagnostics will be contextualized in the fusion research in section 2.2, highlighting the information that can be extracted from the plasma through neutron detection and spectroscopy, as well as reporting the challenges that neutron diagnostics have to face in Tokamaks environment. A brief overview of the diagnostic which are used in current tokamaks (and especially JET) will be given in section 2.3. The last section (2.4) will describe solid state detectors.

2.1 Neutron Detection Principles

Neutrons are neutral particles: for them to be detected a conversion stage is needed, by which the neutron interacts with the detector charged particles which, in turn, can be detected by electromagnetic means. As an example, nuclear interactions allowing neutron detection are [19]:

- **Nuclear elastic scattering**: the neutron interacts with a nucleus making it recoil. In the interaction the neutron transfers a fraction of its kinetic energy to the nucleus depending on the scattering angle α and the mass of the recoiling nucleus A. The amount of energy transferred to the nucleus is $E_d = \frac{2A}{(1+A)^2}\cos(\alpha)$. The total kinetic energy is conserved in the process.
- **Nuclear inelastic scattering**: similarly to the elastic scattering process, the neutron transfers a fraction of its kinetic energy to the nucleus, but part of this energy is used to promote the nucleus to an excited state. The nucleus then decays into its ground state, emitting gamma radiation.
- **Nuclear reactions**, by which the interaction results in one, two or more charged reaction products. The kinetic energy is not conserved in the process: each reaction has a specific Q-value representing the energy employed (if positive) or given (if negative) to make the reaction happen.
- **Nuclear fission**, subcategory of the nuclear reaction involving at least two heavy charged fission fragments.

After the interaction, the detection can happen by detecting the charged products of the reaction (e.g., the recoiling nucleus in the case of nuclear elastic scattering). The sensitive area can be either be separated from the conversion stage in which the neutron interacted or be the same volume. If a detector translates the charged products into a signal in real time it will be referred to as an **active detector**, while a **passive detector** will not produce a real time response. A detector having the ability to detect the number of neutrons interacting with it is called **neutron counter**, while a detector also having the ability to measure the energy of the interacting neutron will be called **neutron spectrometer**.

2.2 The Roles of Neutron Diagnostics in Fusion

2.2.1 Absolute Neutron Counting

One of the most important types of information that can be extracted from the neutrons escaping the plasma is the power produced through fusion reactions, or **fusion power**. The main reactions producing power in a fusion plasma are the deuterium-tritium (DT) fusion reactions, each of which produces one 14.06 MeV neutron. By counting the neutron flux coming from the plasma it is possible to count the number of DT reactions and, therefore, assess the power produced by them.

To this end neutron counters are used. Their purpose is to measure either the neutron fluence (the number of neutrons flowing through the detector in an extended period of time, measured

in n/cm^2) or the neutron flux (the number of neutrons flowing through the detector volume per unit time, measured in $n/(s \cdot cm^2)$). Besides measuring it with sufficient precision, neutron counters must address some challenges:

- Being able to have a very large **dynamic range**. In fact, upcoming tokamaks will operate in very different plasma conditions, producing neutron fluxes spanning over four orders of magnitude [20] or more [21][22][23] depending on plasma composition, plasma regime, heating power and more. A neutron counter should be able to count with good precision the neutron fluxes both at high fluxes and low fluxes.
- **Neutron/gamma discrimination**: fusion environments will be rich of MeV-ranged gamma rays which may be counted by neutron detectors. A neutron counter should be able to distinguish between a neutron-induced event and a gamma-induced event, or at least it should be much less efficient to gamma than neutrons [24].
- **Radiation hardness**: detectors in the vicinity of the plasma may experience very high neutron fluxes ($10^9\ n/(cm^2 \cdot s)$ and more) which will induce damage and loss of performances overtime. Since replacing the detector's hardware might be a complex operation to be performed only during shutdowns, detectors should be as resistant to the high levels of radiation as possible [25].
- **Direct/scattered discrimination**: to correctly assess the number of neutrons coming from the plasma a detector should be able to discriminate the neutrons directly coming from the plasma by the neutrons scattered on the solid volumes around the tokamak [19]. If not possible, simulations should be performed and validated in order to correlate the total number of neutrons with the fraction of direct neutrons, in order to derive the latter information from the former.

Activation foils (described in more detail in section 2.3.6) are used to perform neutron counting [26]. They feature an excellent dynamic range and, being passive detectors, have few problems in terms of radiation hardness [21]. On the other hand, they're passive detectors, allowing only for the measurement of the neutron fluence over one or multiple discharge, and not the measurement of neutron flux. Other active neutron detectors are the **fission chambers** (described in more detail in section 2.3.5), which allow for the measurement of neutron flux with reasonable time resolution. Both activation foils and fission chambers are not able to measure neutron energy, and thus obtaining the direct flux component require extensive Monte Carlo simulation and validation.

2.2.2 Neutron Spectroscopy

To measure the energy of the neutrons can yield a great amount of information about the plasma. Among those:

- **Plasma Ion Temperature**, which can be obtained from the broadening of the 14.06 MeV spectral line. All unscattered DT neutron should, in fact, have 14.06 MeV of energy modified by the cinematic of the reacting deuterium and tritium (if the center of mass of the reactant was moving withing respect of the detector the neutron energy can be higher or lower due to the Doppler effect). By measuring the broadening of the spectral line it is possible to estimate how fast plasma ions are moving and, thus, the ion temperature.

- **Fuel Ion Ratio**: by counting the number of 14 MeV neutrons and the number of 2.5 MeV neutrons it is possible to discover the number of DT and DD reaction happening inside the plasma. By considering the fusion reaction rate r, which is different for DD and DT, it is possible to calculate the ratio between the deuterium density n_D and tritium density n_T in the plasma. The reaction rate can be calculated as

$$r = \frac{n_D n_T}{1 + \delta_{ij}} < \sigma v >$$

  where n is the density of the plasma species, δ is the Kronecker delta and $< \sigma v >$ the reactivity (average of the product between the species fusion cross section σ and their relative velocities v) [27]. An example of an ideal spectrum featuring DT, DD and TT components is depicted in figure 2.1.

- **Not-thermalized plasma components**: while a thermalized fusion plasma features an ion temperature which follows a Maxwellian function, the external heating from the NBI (see section 1.4.2) introduces in the plasma an ensemble of fast ions that alters the distribution of velocities in the plasma, like shown in figure 2.1. By performing spectroscopy, it is possible to measure it from the high energy tails on the DT component.
- **Direct/scattered neutron discrimination**: since scattered neutrons have a lower energy than the ones emitted by the plasma, by performing spectroscopy it is possible to measure the amount of unscattered neutrons, possibly validating the flux measurements described in the previous section.

The critical factor in performing spectroscopy is the energy resolution of the detectors (see section 2.4.4), which should be lower than 5%@14MeV to perform the measurements listed above [24]. On JET (section 1.5.1) these measurements are performed by MPR (section 2.3.2) and TOFOR (section 2.3.1), which allow very good energy resolutions but are also very big and costly machines: this limits their measurement to a single line of sight, not allowing any degree of spatial resolution. Their size and complexity also constitutes a problem for the very crowded environment near the plasma, and their cost means they're not well suited to a plasma monitor for a commercial fusion power plant in the future.

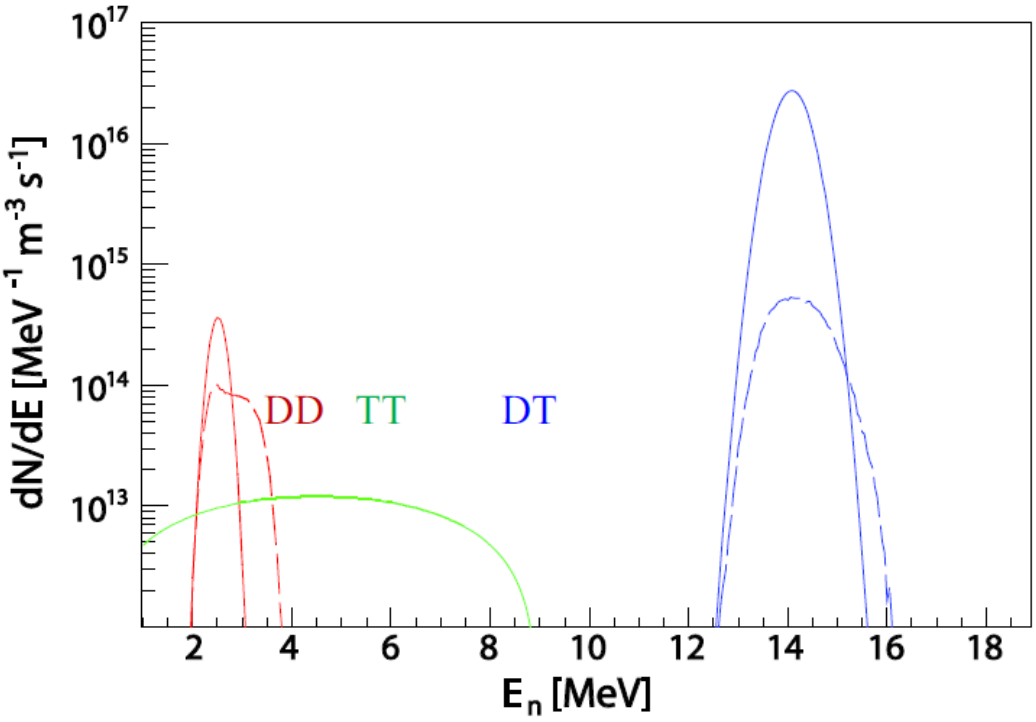

Figure 2.1: Exemplificative spectrum of the primary emission components in a 50:50 DT plasma. ITER conditions are taken as a reference. The full lines correspond to thermal reactions, while the broken line corresponds to reaction involving the non-thermalized component due to neutral beam injection. The spectrum is strongly dominated by the 14.1 MeV emission peak, which is at least two orders of magnitude more intense than the other components. Source: [19]

2.2.3 Plasma Profile

In order to perform measurements with a degree of spatial resolution (that is, inspecting the local properties of the plasma instead of the global ones) a solution relies on the installation of multiple detectors on different, collimated and intersecting lines of sight. By merging the data of the different detectors,it is possible to perform a tomography, obtaining information on the plasma in the region of the intersection of two lines of sight [28]. This is the case of **neutron cameras**, which are described in section 2.3.4.

By measuring the neutron flux on multiple line of sights it is possible to extract information on the plasma activity, density, size and position, which can be helpful in supplementing magnetic diagnostic performing the same task. If the detectors are also able to perform spectroscopy, though, it would also be possible to obtain all the information described in the previous section on a local scale instead of a global one. The challenges, though, are that a neutron camera require fast, small and relatively unexpensive detectors, since they'd need to be installed in big numbers on multiple lines of sight. Liquid scintillators are currently used at JET (see section 2.3.4), which doesn't allow for spectroscopy.

2.2.4 Neutron Interaction Rate

The future use of Breeding Blankets and Test Blanket Modules (see section 1.4.3) will call for methods to measure the amount of tritium generated. One way is to measure the neutron flux inside of the breeder region: by multiplying it by the known cross sections of lithium it will be possible to obtain the tritium production rate. To measure the neutron flux inside the breeding regions is challenging, since the breeding blanket will be located very close to the plasma: the detector will have to operate inside environments with temperatures of 300°C or more, neutron fluxes between 10^9 and 10^{14} $n/(cm^2 \cdot s)$ and very intense magnetic fields, while featuring very small sizes due to space constraints.

Since there is no big interest in performing the measurement with a degree of temporal resolution, activation foils can be good candidates for the task. However, since they lack completely the ability of determining the energy of the neutrons, they also lack the ability of estimating the difference in production rate due to fast and slowed down neutrons, as well as assessing the neutron multiplication rate. For these reasons a detector being capable of a degree of spectroscopy is warranted to validate the measurements of passive detectors.

2.3 Fusion Plasma Neutron Detectors

Detectors to monitor the neutron inclusive flux are installed on most fusion plasma devices [29]. The purpose of those detectors is to measure the uncollimated neutron flux, which can be related to the total neutron yield rate (i.e., the number of neutrons produced by the plasma) and, thus, the fusion power. In order to convert the neutron flux measurement at the point of installation of the detector to the measurement of the fusion power a calibration is needed [30]: in most cases this calibration assumes that only one neutron producing fusion reaction dominates, usually the DD reaction (for pure deuterium plasmas) or the DT reaction (for 50:50 deuterium and tritium plasmas).

One evolution of the neutron inclusive flux measurement is constituted by the neutron emission tomography, which is in use at JET [29]. The tomography is based on the neutron flux measurements of a series of neutron detector arranged in arrays, called neutron cameras. The line of sight on the plasma of the neutron cameras is collimated, thus intersecting only one linear region of the plasma. This allows for the measurement of the radial distribution of neutron emission, from which different types of plasma parameter information can be extracted [31]. It is preferred to have two perpendicular cameras each with good radial coverage.

Another advanced neutron diagnostic is the neutron emission spectrometry diagnostic, which measures the energy distribution of the collimated neutron flux along one or several sight lines [31][32]. The spectroscopy can be used to derive information on a number of plasma parameters, as illustrated in section 2.2. It can also be used as a calibration for both the uncollimated and collimated diagnostic without spectral information, as well as serving as a benchmark for simulations of the neutron flux field in a Tokamak. The latter is crucial issue in many areas, from the neutron damage to materials to the tritium production rate, from the radiation protection to the correct interpretation of neutron flux by excluding the scattered component.

In the next section a small selection of the most used and successful detectors installed on Tokamaks (and especially JET) are presented.

2.3.1 TOFOR

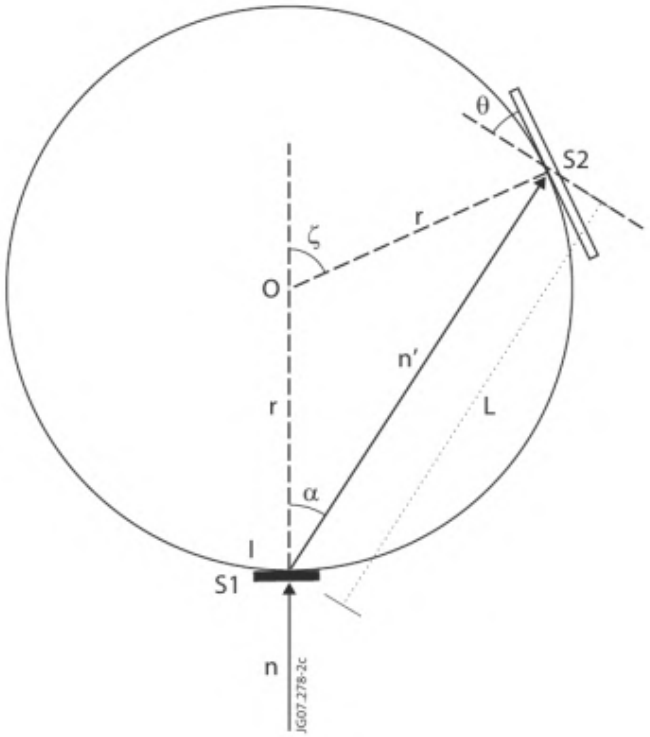

Figure 2.2: Schematics of the time-of-flight system behind the TOFOR. The neutron beam comes from the bottom, interacting with the first set of scintillators (S_1). Neutrons are then deflected with an angle a and detected by a second set of scintillators (S_2). Time of Flight considerations and the knowledge of the S_1-S_2 distance allow for the determination of the original neutron energy. Image taken from [33].

The Time-of-Flight spectrometer Optimized for high Rate (TOFOR) is a neutron spectrometer based on the measurement of the time for a scattered neutron to cover a certain distance. The device is made by two series of fast hydrogen-based plastic scintillators with a photomultiplier tube readout: one set of detectors (S2) is arranged on a hemispherical shape with an angle $\alpha \simeq 30°$ [34], while the other set of detectors (S1) being at the centre of the hemisphere. A collimated beam coming from the plasma is directed on the S1 set of detectors, as depicted in figure 2.2. The TOFOR measures the fraction of neutrons that scatter on the S1 set and are detected by the S2 set. The neutron time of flight is measured by the difference in the detection time of the S1 and S2 sets. Knowing the distance L between the two sets S1 and S2 as well as time of flight with a very good precision it is possible to obtain the velocity, and therefore kinetic energy E_n', of the neutron scattered on S1. Since the scattered neutron feature a univocal relation between its energy and the scattering angle α, being $E_n' = E_n cos^2(\alpha)$, it is possible to derive the incoming neutron energy E_n with good precision.

Two TOFOR spectrometers installed on JET and EAST Tokamaks, being optimized for DD neutrons (but ultimately being able to perform spectroscopy on most fast neutron energies) [33]. Its design allows, on JET, for a very high count rate capability of $\simeq$ 300 kHz for neutron fluxes of $2.5 \cdot 10^6 ncm^{-2}s^{-1}$, corresponding to $10^{17} ns^{-1}$ neutron yields [34]. Since background high-energy radiation is a big issue for the S2 set, TOFOR is installed away from the plasma, on the rooftop of JET behind a concrete shielding which also provide for the collimation of the beam

(see figure 2.3). This make it so that TOFOR is a massive detector, measuring more than a couple of meters in radius.

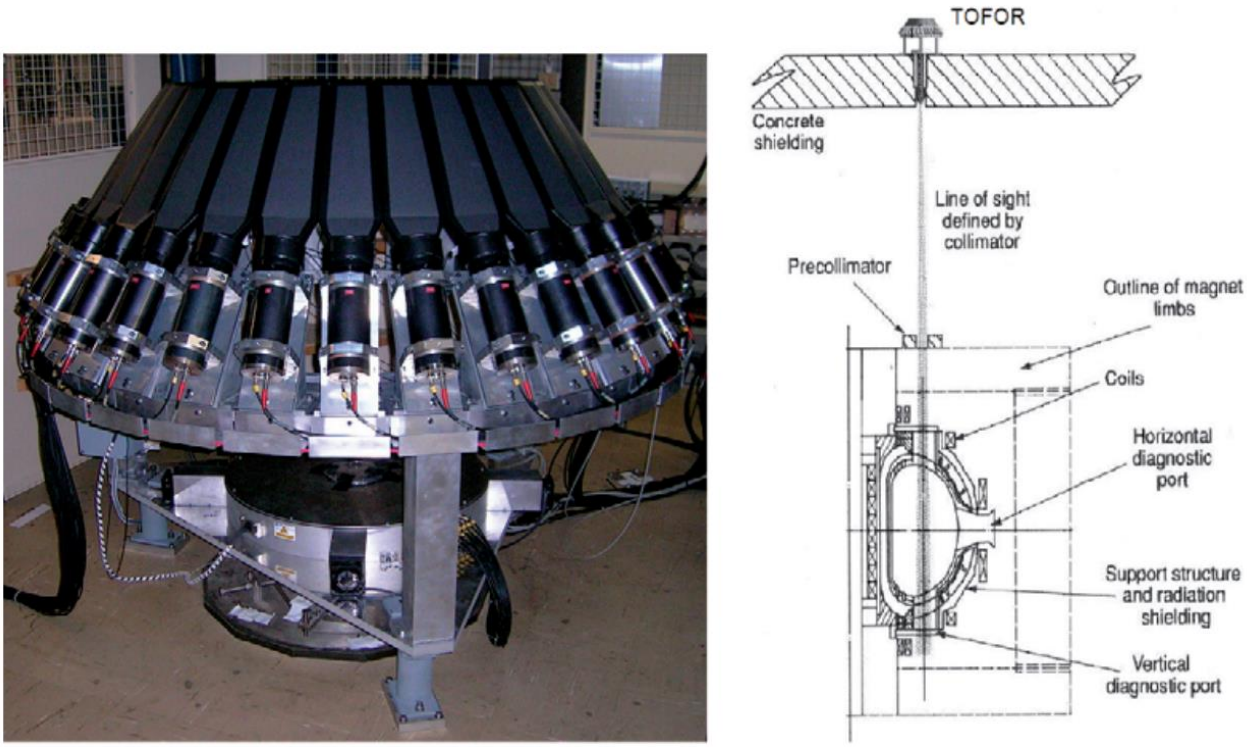

Figure 2.3: ***Left*** *– Picture of the TOFOR installed at JET.*
Right *– Location of the installation of the TOFOR, on the roof lab above the JET Tokamak. Images taken from [34].*

2.3.2 MPR

The MPR spectrometer is based on the Magnetic Proton Recoil technique. The incoming neutron flux from the plasma is collimated onto a thin CH_2 target foil. The foil acts as a convertor: a small fraction of neutrons scattering on hydrogen nuclei generate protons, which are collimated in order to select only the protons along the same direction of the neutron beam (which are the protons produced by a head-on interaction). After collimation, the head-on protons are deflected from the neutron beam by a magnetic field onto an array of monolithic plastic scintillation counters (hodoscopes), which records the position of the protons. Since the magnitude of the deflection depends on the energy of the proton, the position of the interacting proton reveals its energy, which is tightly linked to the interacting neutron (since it underwent a head-on collision, ceding the maximum amount of energy to the proton).

The MPR efficiency and resolution can be adjusted by choice of target thickness and proton collimator aperture. While installed on JET [35], MPR demonstrated a very good energy resolution of 2.5% to DT neutrons [36]. As such, it was taken as a reference for the DT data for the entire JET. The structure of MPR also allows it to separate the neutron component from the gamma background. On the downsides, MPR suffers from problems similar to TOFOR: since the scintillators need to be shielded from radiation coming from the plasma and the activated material. Therefore, the apparatus is encased in a $3m^3$, 20-tons shielding which also isolates the

detector's magnetic field. While this allows for a good signal-to-noise ratio (10^4 for DT plasmas [34]) it also makes the detector extremely heavy and bulky.

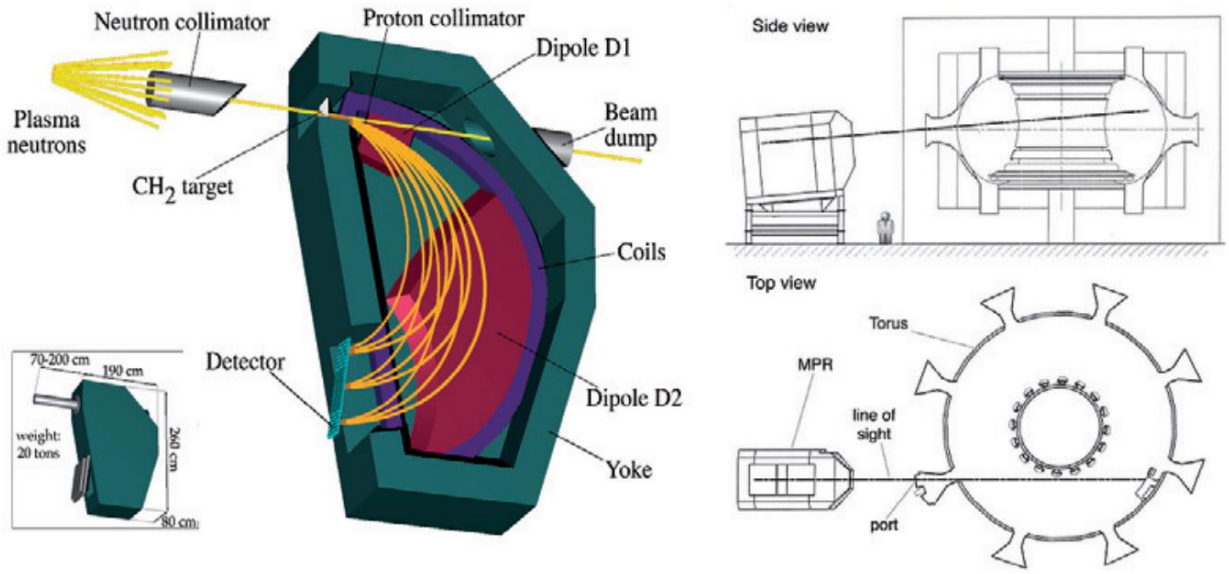

Figure 2.4: Schematics, sizes, location and line of sight of the MPR installed at the JET Tokamak. Image taken from [34]

2.3.3 Liquid Scintillators

In the cavity before the beam dump of MPR an organic liquid scintillator was installed, measuring the neutrons having gone through the thin conversion foil. For this reason, the installation was given the name of "Afterburner" [37]. The interaction of a fast neutron with hydrogen or carbon nuclei (via elastic scattering or, in the case of DT neutrons, via nuclear reactions like $^{12}C(n,\alpha)^{9}Be$) produce energetic protons or ions that are slowed down by Coulombian interactions in the material, resulting in the excitation of molecular levels in the scintillator. The subsequent de-excitation produces light in the visible range, with a total intensity which depends on the energy deposited by the recoil nucleus. The light produced is then converted into a current signal by a photomultiplier tube (PMT) which is proportional to the energy deposited by the detector in the liquid medium, allowing for the use of the detector as a spectrometer.

Since the active volume has a direct line of sight on the plasma, the scintillators are also exposed to gamma radiation. Since gamma radiation can interact with the electrons of the active volume (mostly via Compton Scattering), it constitutes an important source of background for the scintillator. To manage this, it is possible to take advantage to the different de-excitation processes depending on the incident particle, which produce different light pulses. By performing an analysis on the pulse shape obtained after the PMT it is possible to distinguish the signals generated by gammas and neutrons [37].

Liquid Scintillators are very small in size, consisting in few cm^3 active volume coupled to the hundreds of cm^3 of the PMT. On the other hand, their performance in terms of neutron energy measurements is usually worse than that of the non-compact spectrometers [37].

2.3.4 Neutron Camera

The JET neutron camera is a neutron profile monitor system composed of 19 lines of sight (10 horizontal, 9 vertical), each equipped with an NE213 liquid scintillator (used for measurements during DD plasma discharges), and a BC418 (used for measurements in DT plasmas) [37]. For a reference scheme refer to figure 2.5. Two concrete shielding protect the detectors from background radiation from x-rays and scattered neutrons, while the direct gamma background is separated from the neutron data via pulse shape discrimination [39]. A collimator reduces the aperture on the plasma, restricting the line of sights of the detectors.

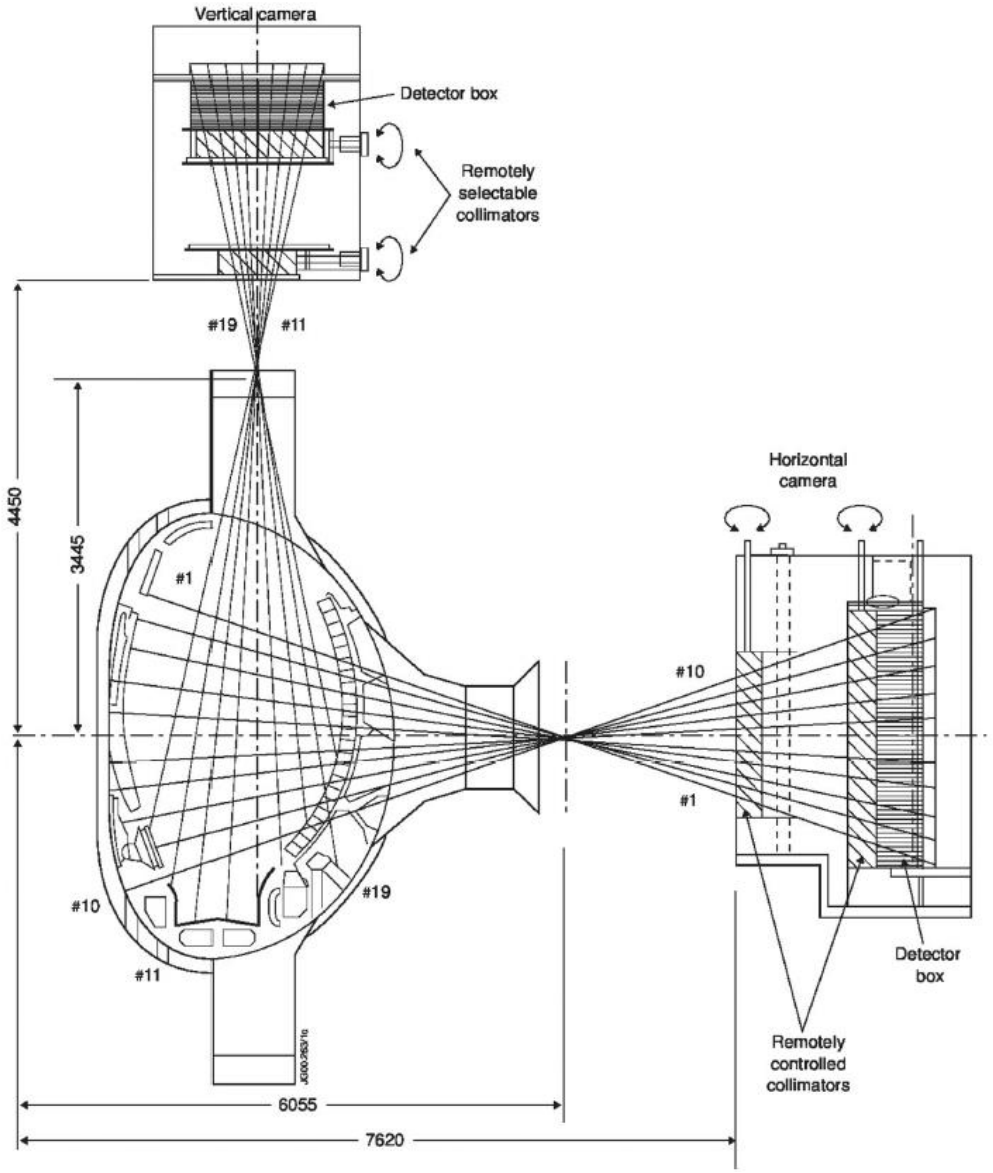

Figure 2.5: Poloidal cross section of JET with the horizontal and vertical neutron cameras. Lines of sight are also represented. Figure taken from [38]

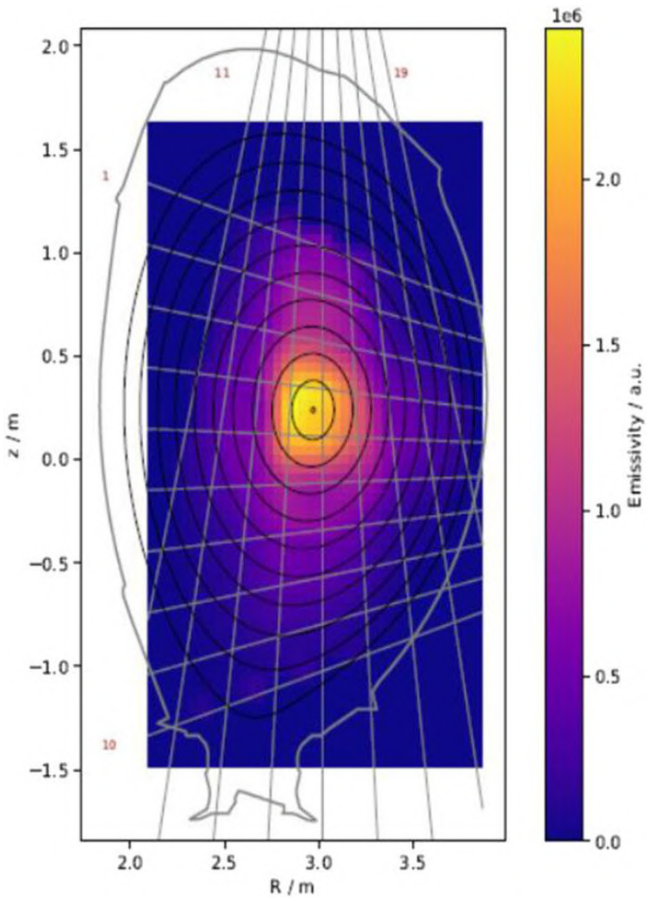

Figure 2.6: Exemplificative neutron tomographic reconstruction for a JET discharge (#99608). Figure taken from [39]

The neutron camera is used to provide information on the spatial distribution of the neutron emission from the plasma. An example of tomographic reconstruction is shown in figure 2.6 for a DT discharge. In general, very limited or no information about the neutron energy spectrum is available from the camera due to the characteristic flat response of the scintillator to incoming neutrons and some instrumental effects [39].

2.3.5 Fission Chambers

Fission Chambers have been used to measure neutrons at JET since 1983 [40]. The working principles of fission chamber relies on a uranium converter stage (either ^{235}U or ^{238}U) inducing a fission of the uranium isotopes. The charges fission fragments are then detected in a gas ionization chamber. 3 pairs of moderated ion chambers are mounted on JET in moderator packages, capable of operating in both pulse counting and current mode, allowing a very wide dynamic range covering neutron emissions between 10^{10} and $10^{18}\, n/s$, achieving accuracies between 8% and 10% on the neutron fluency. Fission chambers do not offer spectral information and are therefore limited to the measurement of neutron flux only.

2.3.6 Activation Foils

Activation foils are a passive neutron detector whose means of detection rely on the activation of a known material to neutron irradiation. The sample material is exposed to a flux of neutron for a period of time and then removed; by measuring the radiation emitted by the sample due to activation (either gammas or charged particles) information on the neutron fluence and the neutron energy can be obtained [41].

Activations foils used at JET demonstrated an accurate monitoring of neutron fluence at positions far from the tokamak and along shielding penetrations [26]. On the other hand, they lack both on the temporal resolution (being able to measure only the fluence between two sampling with no information on the time evolution of the flux) and can provide only limited information on the spectroscopy. They are also ill-suited for operation close to the plasma, due to the need of measuring the activity which should be conducted in an environment with as little as radioactive background as possible.

2.4 Solid State Detectors

Solid State Detectors (SSDs) are a class of radiation detectors whose active volume is a solid semiconductor lattice. The interaction of a particle in the lattice produces electron-hole pairs that alter abruptly the lattice resistivity, allowing a current signal to be detected if an electric field is applied on the two ends of the lattice. In such a way the lattice fulfils both the role of conversion stage and active volume.

Semiconductor properties and SSDs behaviour will be thoroughly analysed in the subsequent sections, along with an introduction to the specifics of the Silicon Carbide detector, a comparison with other SSDs and the manufacturing process of the prototypes characterized in this thesis.

2.4.1 Semiconductor behaviour

Insulators and semiconductors are materials whose valence band and conduction band are separated by an energy gap, called band gap. The difference between semiconductors and insulators lies in the magnitude of the band gap. Insulators have large band gaps, preventing low-energy processes (like room temperature) to randomly promote valence band electrons to the conduction band on a scale that produces macroscopic effects. Conversely, semiconductors have comparatively small band gaps, allowing for an easier promotion of a valence band electron to the conduction band (see figure 2.7). The threshold between insulators and semiconductors is, in principle, arbitrary: since one of the main macroscopic characteristics of semiconductors is to reduce resistivity with the increasing temperature, most literature puts the threshold in an energy range which allows for a significant number of electrons to promote due to thermal interaction at the most common temperatures for the electronics. The probability per unit time that an electron-hole pair is thermally generated as a function of the absolute temperature T is given by [41]:

$$p(T) = CT^{3/2} exp\left(\frac{-E_G}{2k_B T}\right)$$

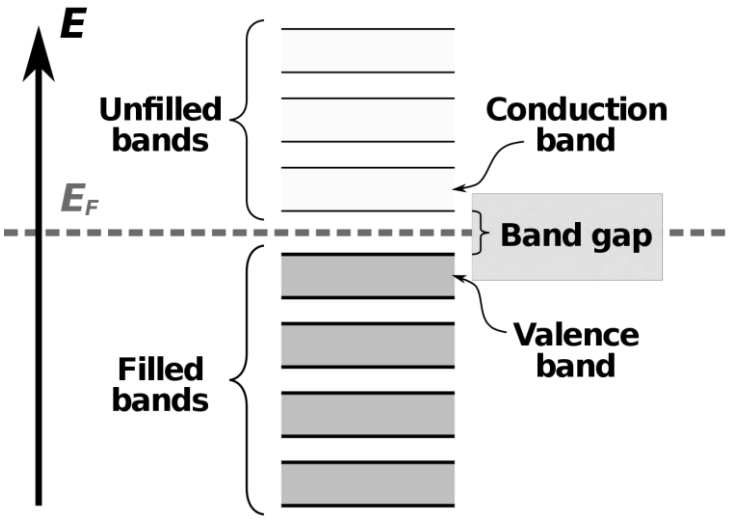

Figure 2.7: Schematics showing a simplified band structure for a semiconductor. All the bands below and including the valence band are occupied by electrons, while all the bands above and including the conduction band are unfilled, as it is the case when no processes promote electrons to an excited state (zero temperature). The Fermi energy E_f serves as a delimiter between the two regions. The distance between the conduction and valence band is the band gap.

where C is a proportionality constant that depends on the material, E_G is the band-gap energy and k_B is the Boltzmann constant. Materials with 0.5 eV to 5 eV band gaps are usually referred to as semiconductors, while higher band gaps are usually referred to as insulators.

One important factor in altering the behaviour of a semiconductor are impurities. By replacing one atom in a lattice structure with an atom with very similar properties having one more electron in the valence shell (for example, by introducing a phosphorus atom in a silicon lattice) the resulting structure will be electrically neutral but will have an electron not involved in either the covalent bonds between the atoms or the lattice orbital. This will create a loosely bond electron with a high mobility, which will be able to partake into the current flow if an external electric field is applied. The same happens if the replacing atom has one less electron in the valence shell: in that case the orbital structure lacks an electron, which can be filled by adjacent valence electrons leaving another hole in its wake. Impurities generate donor and acceptor levels, respectively, that lies at an energy level inside the band gap, facilitating the transition between valence and conduction bands.

2.4.2 p-n junctions and Schottky

A **p-n junction** is realized when a semiconductor volume with a high doping causing it to have an excess of electrons (n-doped) is put in direct electrical contact with a semiconductor volume highly doped with an excess of holes (p-doped). The contact between the two volumes causes the formation of a depletion region, as depicted in figure 2.8: this is due to the random thermal motion of the excess electrons in the n-region, which can migrate by diffusion mechanism in the p-doped region (if they are close enough to it) causing them to cancel out with the excess holes. Such region generates a charge unbalance, producing an electric field opposing to this motion. By applying an external bias, we see two very different behaviours depending on the direction of the bias application:

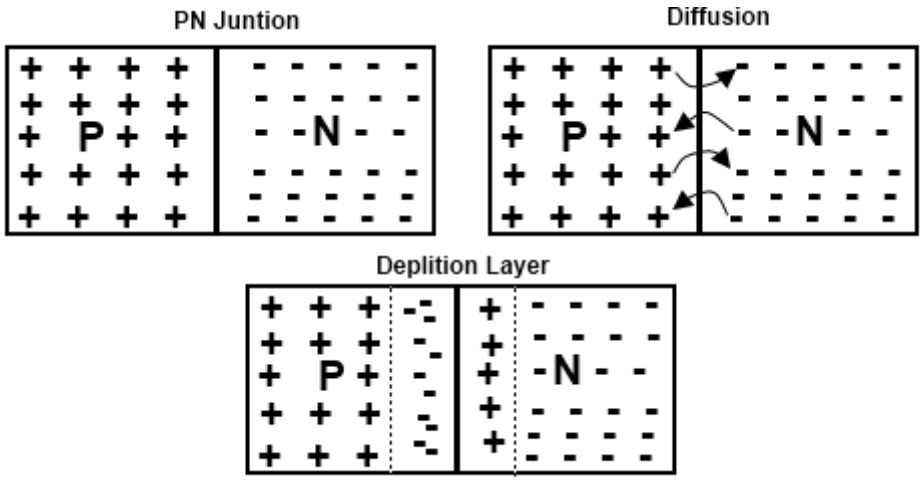

Figure 2.8: Formation of the depletion layer in a p-n junction.

- **Forward bias**: if the positive terminal of the bias is applied to the p-region and the negative terminal to the n-region, the bias causes a force on the electrons that pushes them from the n-region to the p-region. This causes a shrinking of the size of the depletion region and the electric field, to the point in which electrons can cross the junction and inject into the p-region. Holes also move in the same way, crossing the depletion region in the opposite direction. Summing the currents due to electron and holes we find that the application of the potential results in a current flowing through the junction unimpeded as in a conductor.
- **Reverse bias**: if the positive terminal of the bias is connected to the n-region and the negative terminal to the p-region, the excess holes in the p-region are pulled away from the junction, exacerbating the deficit of holes and widening the depletion region. This is the same for the n-region for the electrons. The widening of the depletion region increases the internal electric field opposing to the flow of current, allowing only for a minimal electric current to flow through the junction. From a macroscopic perspective the junction behaves like an insulator, up to a breakdown voltage when an avalanche breakdown process allows for a current to flow again.

So, a p-n junction is an electric device behaving like a conductor while polarized with a forward bias and like an insulator while polarized with a reverse bias. Such behaviour is used for diodes, but it will also be useful for extrinsic SSDs.

A **Schottky barrier** is formed through the contact between a doped semiconductor and a conducting metal. The functionality is similar to the p-n junction, with the semiconductor being usually n-doped and serving as the cathode, while the metal contact serving as the anode. Since the application of a reverse bias causes the formation of a depletion region, the two types of junctions will be treated similarly in the context of this thesis.

2.4.3 Radiation Detection with Semiconductors

When a charged particle passes through a semiconductor material it can ionize it through Coulombian interactions with the valence electrons. Neutrons, being neutral, can only interact with a lattice nucleus: this produces charged particles (either alphas, betas, protons and/or a displaced nucleus) which, in turn, ionize the semiconductor. The kinetic energy of the neutron,

which will be indicated with E_n, is partially transferred to the products of the interaction: the energy transferred will be called "deposited energy" and indicated with E_d. E_d will spread out to the lattice atoms, ultimately causing a number of ionizations n equal to

$$n = E_d/\epsilon$$

Where ϵ is the ionization energy of the material – thus, the energy necessary for the creation of an electron-hole couple.

The promotion of a number of electrons to the conduction band changes the resistivity of the junction, which is a macroscopic parameter and, thus, can be easily detected and registered. In particular, the easiest way is to have a reverse bias applied on the two ends of the active volume: only a negligible current will flow through the active volume in static condition, whereas the abrupt change in resistivity following a ionizing particle interaction will cause a sudden current signal which will be detectable by an electronic chain. Another feature of this process is that the integral in time of the current signal (thus, the charge collected) will be proportional to the number of electron-hole pairs and, thus, to energy deposited by the neutron. This allows solid state detectors to operate as spectroscope, since the integral of the current signal will be proportional to E_d.

2.4.4 Energy Resolution

Energy resolution is defined the ability of the detector to accurately determine the energy of the incident radiation E_n [41]. It is more often expressed in relative terms, meaning that the detector of the example before features a $EnRes = \frac{140\ keV}{14000\ keV} = 0.01 = 1\%$ energy resolution while measuring 14 MeV particles. This is often expressed as $EnRes = 1\%\ @14MeV$.

Energy resolution has the effect of causing the broadening of the component of the E_d spectrum, that would otherwise be sharp lines. The main method to determine the energy resolution of the detector is, therefore, measuring the Full Width Half Maximum ($FWHM$), which is width of the broadened signal taken at the point of abscissa equal to half its maximum height. Energy resolution in then often expressed as a ratio between the FWHM and the neutron energy E_n:

$$EnRes = \frac{FWHM}{E_{n\ reference}}$$

If the broadened signal can be fitted by a gaussian function, the $FWHM$ also relates to the σ of the gaussian through:

$$FWHM = 2\sqrt{2\ln(2)} \cdot \sigma$$

A poor energy resolution is undesirable in a detector, and the interest is in detectors being able to offer the lowest energy resolution possible. Solid state detectors feature excellent energy resolutions, with the diamond detector having a resolution to neutrons of less than 1% @14MeV [42][43][44]. For most fusion applications an energy resolution of 5% (or better) is required [24], giving good perspectives for SSDs.

2.4.5 Semiconductor detectors materials

Many semiconductor materials can be used as active volume for a solid state detector. Some of the most popular materials are Germanium, Silicon, Gallium Arsenide, Carbon and Silicon Carbide, whose main properties are summarized in table 2.1.

		Ge	Si	GaAs	Diamond	SiC (4H)
Atomic number	$\boldsymbol{Z}$	32	14	31/33	6	14/6
Bandgap	$\boldsymbol{E_g}$ **[eV]**	0.66	1.12	1.42	5.5	3.3
e-h pair form. energy	$\boldsymbol{E_{e-h}}$ **[eV]**	2.9	3.6	4.3	13	7.6-8.4
Density	$\boldsymbol{d\ [g/cm^3]}$	5.32	2.33	5.32	3.515	3.22
Electron mobility	$\boldsymbol{\mu_e}$	3900	1450	8500	1800	800
Hole mobility	$\boldsymbol{\mu_h}$	1900	450	400	1200	115

Table 2.1: Properties of semiconductors used for the manufacturing of solid state detectors active volumes. Source: [45]

Germanium detectors are the first semiconductor to be used as a solid state detectors. The relatively low pair formation energy allows to produce a larger number of e-h pairs per unit of deposited energy by the particle when compared with other materials, thus producing stronger and better resolved signals. The technology in the fabrication of larger crystals is also improved in the last ten to fifteen years, allowing to construct large active volumes with a relatively low density of impurities. On the other hand, the bandgap of Germanium is low to the point in which thermal excitation can promote electrons to the valence band quite often even at room temperature. This make it necessary for the detector to be cooled with liquid nitrogen in order to avoid strong dark currents submerging the signal. This adds complexity in their installation, increasing their size and cost.

Germanium has a high atomic number Z, making it most sensitive to gamma ray and x-ray (since photon cross section roughly scales as a function of Z^4, while neutron cross sections roughly scale as a function of Z [41]). For this reason, germanium detectors are much more well suited for gamma and even hard X-ray detection and spectroscopy than to neutron spectroscopy. The same applies for **Gallium Arsenide detectors**.

Silicon detectors benefit from the great technological advances in electronics achieved since the '90s, allowing to manufacture active volumes in a great range of geometries and an outstanding level of purity. The technology to manufacture high-purity silicon strips arranged in a p-n junction is also mature, allowing for a relatively low cost of production. The low atomic number also ensures that their sensitivity to gamma is relatively low compared to the one to neutrons, allowing them to be used as neutron detectors in gamma-rich environments (as it is the case of the vast majority, if not totality, of neutron sources). It is also reported for them to have an excellent energy resolution [46][47]. The drawback of Si detectors is that they suffer from degradation over time from radiation, and especially neutron irradiation. This prospects them to have a small operating lifetime, which is not well suited for very high neutron flux environments like fusion experiments. They also feature a medium band-gap: this means that they can operate at room temperature while arranged in an inversely polarized p-n junction, but problems arise when exposed to higher temperatures.

Diamond detectors are the newest addition to the scene of solid state detectors. They feature a very high bandgap and e-h pair energy which, while reducing considerably the signal width (making it necessary to develop a fine-tuned and high-quality amplification stage), allow them to be almost completely insensitive to thermal noise. The very low Z of carbon, combined with the small volume and the moderately high cross section to fast neutron interaction, makes them good neutron spectrometers relatively insensitive to gamma rays. Diamond, being one of the most robust materials in nature, also features a very high mechanical resistance and very high radiation hardness, allowing for very resilient detectors. The downside of diamond detector is the manufacturing difficulties: it is very difficult to grow volumes of the material with the required high purity and there are limitations in the size of plates, allowing for single-crystal up to the range of few mm x few mm. This allows only a limited selection of geometries and a very high cost with respect of silicon detectors.

Chapter 3
Silicon Carbide Neutron Detector

The Silicon Carbide Detector ("SiC") is a solid state detector whose active volume is made by a Silicon Carbide semiconductor lattice. Silicon Carbide is a material which is known in literature for its resilience, wide band-gap width, thermal resistance, and high energy threshold for defect formation [48]. These properties made it an interesting material for high-power electronic applications. The interest in SSD based on SiC grew with the development of manufacturing processes, allowing the growth of crystals with high purity and low density of defects. A collaboration between CNR-ISTP and CNR-IMM, sponsored by Eni s.p.a., was established to produce and characterize a series of SiC SSD prototypes, in order to determine its features, as well as assessing their functionality, study their perspectives as a neutron counter and spectrometer and optimizing their parameters, like geometry, doping and more.

In this chapter a description of the various SiC detectors developed and characterized in the course of this thesis will be given. The characteristic of the material will be described, drawing a comparison with the materials presented in section 2.4. The manufacturing process of the prototypes will be also detailed, as well as a presentation of the various prototypes used during this thesis.

3.1 SiC Properties

3.1.1 Lattice Structure

The active volume of the SiC detector is made of a lattice constituted by Silicon Carbide, forming crystalline structures having a 50:50 molar ratio of Silicon and Carbon. Silicon Carbide can form more than 250 different crystalline structures (polytypes) [49]. The one used for the prototypes in this thesis (and more often in literature) is the 4H structure. 4H polytype is a near-thetraedric structure [50] that is comparable to the diamond structure.

The structure of the SiC 4H features a wide, indirect bandgap of 3.23 eV, one of the highest between SiC polytypes, and a e-h formation energy of 8.0 eV [52]. Such bandgap makes the SiC less sensitive to low-pulse amplitudes when compared to Silicon but allows for a reduction of the noise due to temperature and environmental radiation that overcompensates for the reduction in signal level for the concerns of signal-to-noise ratio. This also allow for the SiC to be entirely insensitive to visible light, as well to feature low noises without external cooling.

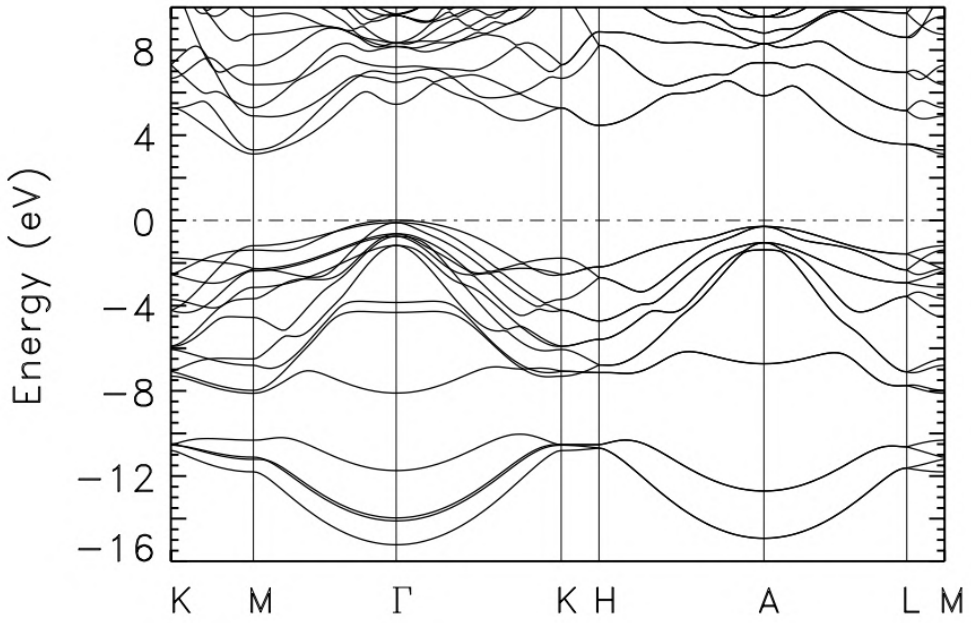

Figure 3.1: Electronic energy band structure of the 4H-SiC along high-symmetry directions. Image taken from [51]

3.1.2 Electrical Properties

SiC detectors are arranged as an inversely polarized diode like the one described in section 2.4.2. They feature an insulator-like resistivity (ideally, infinite) which abruptly drops after the interaction of a neutron in the active region. The difference from ideality is due to the resistivity being finite, and thus allowing some amount of current even without particle interaction. Such current is referred to as **dark current**. The presence of a strong dark current is undesirable, since the charges can add up to a signal due to particles and false the relation between charge collected and the energy deposited by the interacting particle E_d. In extreme cases the fluctuation in the current can be mistaken for particle signal, or it can be high enough for the

noise to totally submerge it. In this sense, the detectors need to work in conditions in which the dark current is very low and, possibly, constant in time. High temperatures or environments with EM noise can increase significantly the dark current by inducing lattice electron promotions to the conduction band.

Such conditions are reached only within an interval of voltages applied to the two ends of the active volume. By applying a small voltage difference on the two ends of the active volume a **depletion region** characterized by an electric field opposed to the external field (see section 2.4.2) will emerge starting on the junction between the p-doped region and the n-doped region (or the contact between the metal and the n-doped region in the case of a Schottky barrier). The depletion region is limited in volume and will grow in the active volume perpendicularly to the electrical field lines. The depth of the depletion region depends on the voltage applied (V), on the dielectric constant of the material (ϵ_{SiC}) and on the n-layer doping concentration (n_A) [41]:

$$d \simeq \sqrt{\frac{2\epsilon_{SiC}}{e \cdot n_A} \cdot V}$$

The equation therefore begets a minimum voltage to be applied to the detector to achieve full depletion. Since the minimum voltage depends on the specifics of the prototypes (especially their thickness) it's not possible to indicate a single appropriate voltage for all the prototypes used in the thesis. A thorough analysis of the behaviour of the detector while partially polarized will also be performed in section 3.3.3 and section 5.4.

The application of a very high voltage might also trigger either a **breakdown** of the diode or the ensuing of a **leakage current**, resulting in a strong current flowing through the active volume. Such current is usually very high, making the detection process impossible due to particle signal being submerged by the breakdown current. The breakdown can be caused by electrons being able to "skip" the depletion region when a sufficiently high field is reached, while leakage currents are due to defects in the edge structures of the field plates. While the breakdown is usually triggered at a specific breakdown voltage, depending on the specific detector, the amount of voltage needed to activate a leakage current can vary greatly, since very small variations in the geometry of the detector and the distribution of dopants can affect the field distribution.

I/V test determining the behaviour of the SiC as a function of the bias voltage will be described in section 4.9 and section 5.4.

3.1.3 Neutron Interaction Channels

The nuclei constituting the Silicon Carbide are mostly of two isotopes: ^{12}C (which constitutes the 98.89% of natural carbon) and ^{28}Si (which constitutes the 92.23% of natural silicon). Since the interactions through which a neutron deposits energy in the lattice depends on the species of the interacting nucleus, the presence of two species complicates the process of correlating the deposited energy E_d and the incoming neutron energy E_n. This is because, as stated in section 1.3.1, each nuclear specie has its own reaction channels, each of which features a different relation between E_d and E_n. The presence of two atomic species, carbon and silicon, makes the SiC feature the reaction channels of both elements, producing a more complicated response function than monoatomic detectors, like diamond and silicon. All the possible nuclear

interaction channels for neutron with 1 MeV< E_n < 15 MeV are reported in the table 3.1 below. Two reactions involving ^{29}Si, a stable silicon isotope with 4.7% natural abundance, are also reported by virtue of their low Q_{value}.

	Reaction	Q-value [keV]	Cross Section @14MeV [Barn]
Carbon	Elastic Scattering		0.95
	Inelastic Scattering		0.50
	^{12}C(n,γ)^{13}C	-4946.0	$< 10^{-3}$
	^{12}C(n, α)^{9}Be	5702.0	0.08
	^{12}C(n,n)3α	7274.7	0.18
	^{12}C(n,n+α)^{8}Be	7366.6	$< 10^{-3}$
	^{12}C(n,2α)^{5}He	8010.0	$< 10^{-3}$
	^{12}C(n,p)^{12}B	12587.1	$< 10^{-3}$
Silicon	Elastic Scattering		0.68
	Inelastic Scattering		1.08
	^{28}Si(n, γ)^{29}Si	-8473.6	$< 10^{-3}$
	^{28}Si(n, α)^{25}Mg	2653.6	0.18
	^{28}Si(n,p)^{28}Al	3859.7	0.30
	^{28}Si(n,D)^{27}Al	9360.3	0.02
	^{28}Si(n,n+α)^{24}Mg	9984.1	0.02
	^{28}Si(n,n+p)^{27}Al	11584.9	0.07
	^{28}Si(n,3He)^{26}Mg	12138.2	$< 10^{-3}$
	^{28}Si(n,2α)^{21}Ne	12539.5	$< 10^{-3}$
	^{28}Si(n,2p)^{27}Mg	13412.8	$< 10^{-3}$
Silicon-29	^{29}Si(n, α)^{26}Mg	34.1	0.17
	^{29}Si(n, p)^{29}Al	2905.0	0.14

Table 3.1: Reactions that fast neutrons (between 1 MeV and 15 MeV) undergo with nuclear species in the SiC. The Q-values of the elastic nuclear reactions (not leaving the nucleus on an excited state) are listed: a positive Q-value corresponds to an endothermic reaction ($E_d < E_n$). The cross sections to 14 MeV neutrons are also reported: the highest cross sections, corresponding to the most probable (and thus relevant) reactions are highlighted.

Reactions in the table are reported with their relative Q_{Value}, which is the energy involved in the reaction. E_d is linked to E_n by $E_d = E_n + Q_{Value}$ for all nuclear reactions, meaning that a neutron with a certain E_n will always produce particles having an exact total kinetic energy E_d. An exception to this rule is the scatterings, for which E_d varies as a function of the scattering angle. Scatterings, therefore, have a spectrum of E_d ranging from zero (in the case of a "grazing" collision) to a maximum $E_{d\,max}$ (in the case of a "head-on" collision) given by:

$$E_{d\,max} = \frac{4A}{(1+A)^2} \cdot E_n$$

A is the ratio between the mass of the target nucleus over the mass of the neutron. This leads to a $E_{d\,max} = 28.610\% \cdot E_n$ for the ^{12}C and a $E_{d\,max} = 13.435\% \cdot E_n$ for the ^{28}Si.

All the reactions reported in table 3.1 have a positive Q_{Value}, meaning all reactions are endothermic ($E_d < E_n$). This is a feature in the context of fast neutron detection, since it allows the detector to be insensitive to lower energy neutrons. Radiative capture interactions (featuring a (n, γ)) are an exception for this rule, but since the probability of a neutron interacting through radiative capture and the gamma generated undergoing interaction within the active volume as well is very small, such occurrences are deemed negligible.

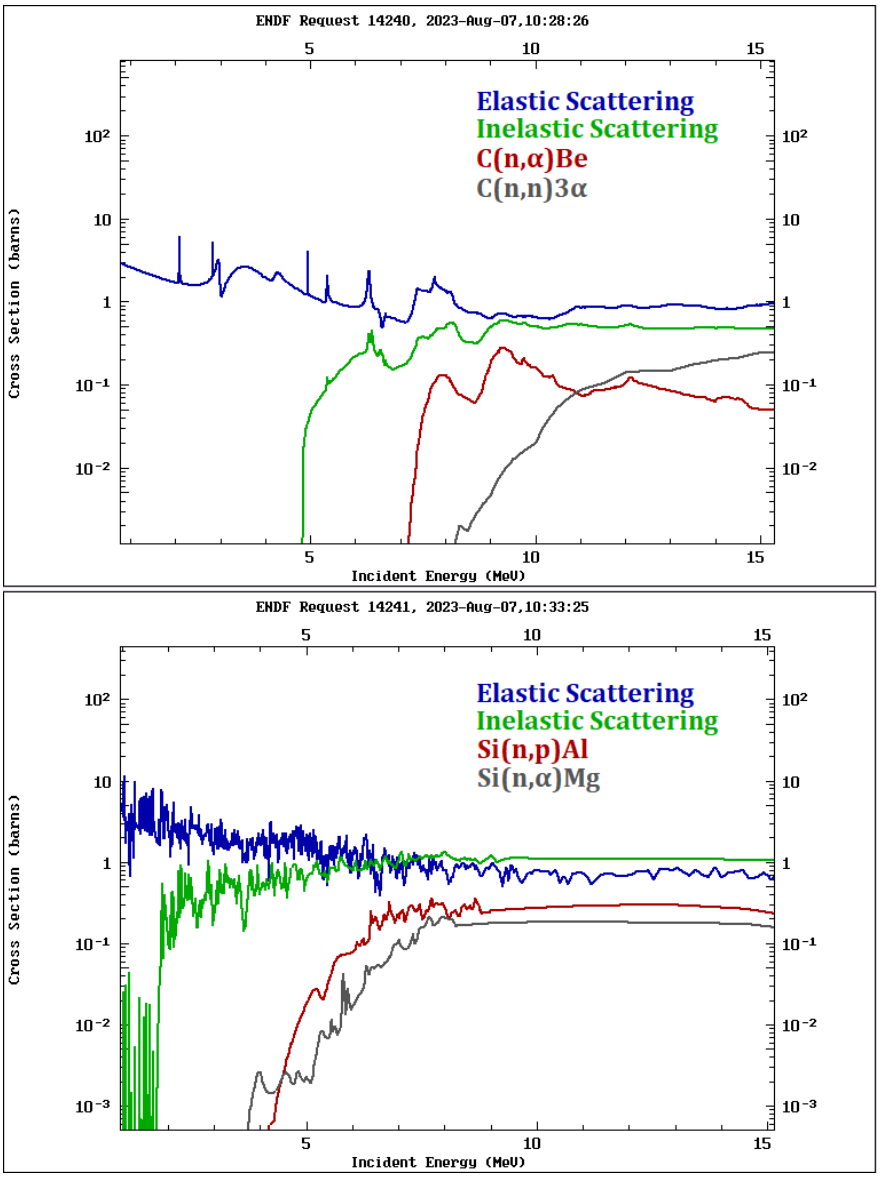

Figure 3.2: Cross section of eight different reaction between a fast neutron and a carbon (top) or silicon (bottom) nucleus. Neutron energy E_n (in MeV) is on the x-axis and the cross section (in Barn) on the y-axis. Red and grey lines, corresponding to four endothermic nuclear reactions, have zero cross section for energies lower than their Q_{value}.

3.1.4 Manufacturing

As described in section 2.4.2, SiC detectors are either p-n junction or Schottky barriers operating as an inversely polarized diode. The active volume is very small (few mm^2 in area and between tens or hundreds of μm in thickness) and is made by a doped 4H-SiC lattice. The crystal is manufactured through the Chemical Vapor Deposition technique, consisting in the deposition of a solid material from a vapor on a heated substrate surface [53].

The process consists in an epitaxial growth performed in a hot-wall reactor by using trichlorosilane and ethylene as silicon and carbon precursors, respectively, and hydrogen as gas carrier [48]. The doping is achieved by mixing Nitrogen impurities for the n-type doping and Aluminium for the p-type doping. The former is obtained by mixing gaseous nitrogen in the growth process and the latter by mixing Trimethylaluminium ($Al_2(CH_3)_6$) [54].

The detectors, structured as p-n junctions, are produced in wafers of large areas. The production process starts with a double layer epitaxy, a p+ layer 0.3 μm thick with a doping concentration of $10^{18} - 10^{19}\ cm^{-3}$ grown on a n-epilayer with a doping concentration of $5 \cdot 10^{13} cm^{-3}$. It is then followed by two photolithographies for the definition of the detector's area and the edge structures (the purpose of which is to reduce the electrical field at the device border, preventing discharges). Bonding is then realized with a thicker layer of Ti and Al deposited on the periphery of the detector, over which an ohmic contact is formed by Ti/Ni/Au deposition [48].

3.2 Data Analysis

3.2.1 Response Function

The interpretation of SiC's response function – and solid state detectors in general – to high energy neutrons is rather challenging. It is not possible to determine univocally the incident neutron energy E_n from the energy it has deposited in the detector E_d since there is no univocal way to determine which reaction channel (section 3.1.3) took place. However, by collecting the E_d of a sufficiently large number of neutrons and by building a pulse height spectrum it is possible to identify the spectral structures that each reaction channel features. In figure 3.3 are depicted two examples of the response of a SiC detector to neutrons with $E_n = 14$ MeV and $E_n = 2.5$ MeV, obtained through a Geant4 simulation. Thanks to the peculiar spectral shape it is possible to recognize the reaction channels that produced the specific features and from the knowledge of the associated Q_v (see section 3.1.3) it is possible to calibrate the detector's response to derive information on the incoming neutron energy.

Since the energy deposited through a two-body nuclear reaction is uniquely identified as $E_d = E_n - Q_v$, the theoretical spectral component due to it is made by a sharp line at the exact value E_d (if the incoming neutrons are all the same energy E_n). In a real-world scenario the uncertainty in the number of e-h pairs generated after an E_d deposition causes the broadening of the sharp line into a gaussian peak centered at E_d (the broadening of which is strictly linked to energy resolution – see section 2.4.4). On the other hand, in the scattering processes only a fraction of the neutron energy can be deposited depending on the cinematics of the collision.

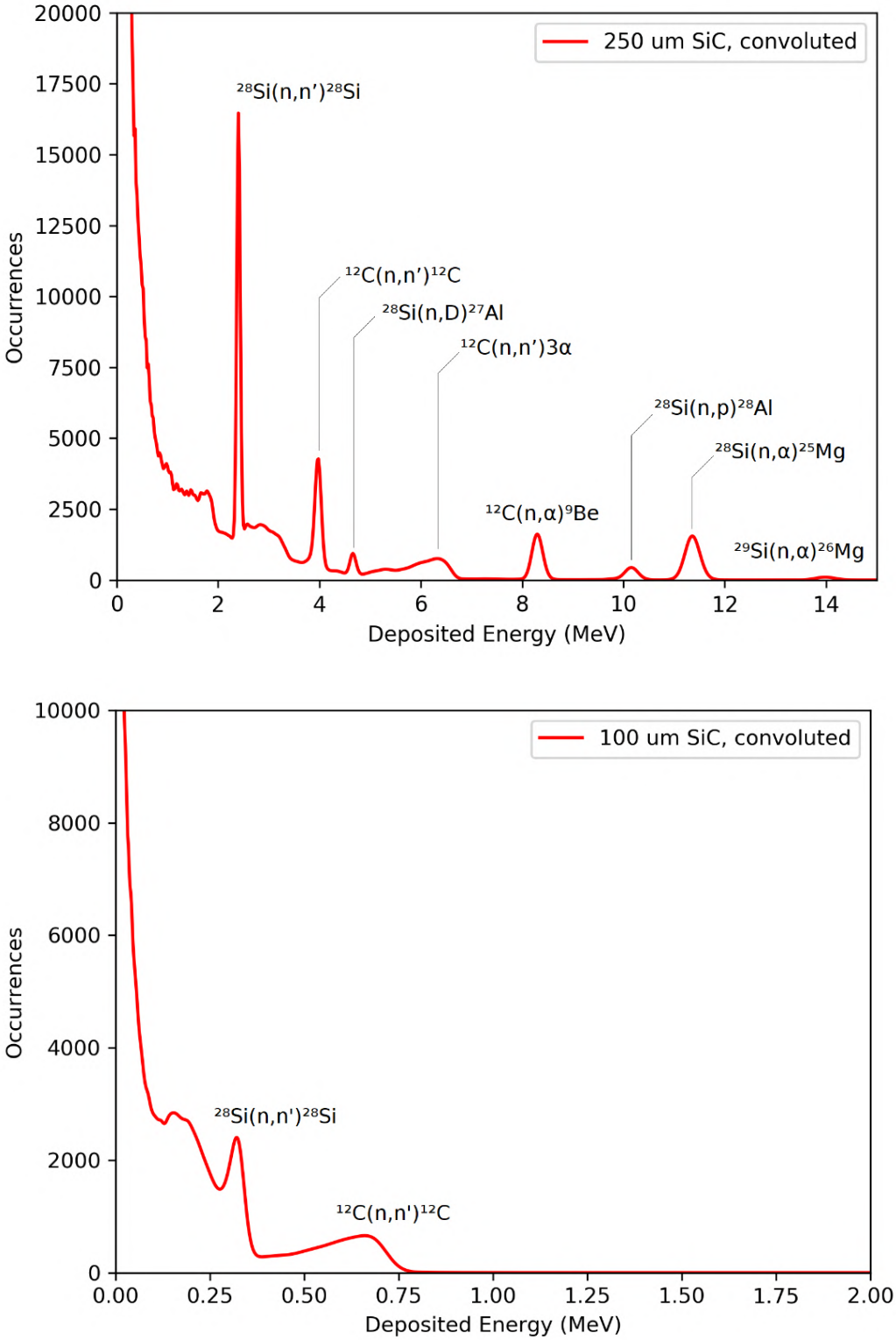

Figure 3.3: Spectra obtained through Geant4 simulation of $5.2 \cdot 10^8$ 14 MeV neutrons on a 250μm SiC (top) and $3.6 \cdot 10^8$ 2.5 MeV neutrons on a 100μm SiC (bottom). Spectra are broadened by a gaussian convolution with a 3% and 10% width, respectively, in order to simulate for the effect of the energy resolution. The figures are used to highlight the various spectral features due to different reaction channels. The reaction producing the features are written on the spectra.

This means that the resulting pulse height spectrum is almost uniform up to the maximum energy depositable defined by the formula in section 3.1.3. Such spectrum is then broadened in the same way as a nuclear reaction, obtaining an edge whose inflection point corresponds to $E_{d_{max}}$. The same is also valid for reactions involving non-charged particles among the products, like ^{12}C(n,n')3α: only the three alphas cause e-h pairs in the crystal, and the ratio between the amount of energy on the three alphas and the neutron depends on the cinematics of the reaction.

The most interesting peaks and edges for neutron spectroscopy are the ones with the highest E_d. The reason is due to the fact that many processes can cause an event to result in a signal smaller than its relative E_d, including (but not limited to) partial charge deposition (section 3.3.2), incomplete charge collection, neutron conversion or backscattering in solid volumes near the detector (section 4.3.1). This causes some events being moved from the high-E_d parts of the spectrum to lower E_d, generating a baseline of events that worsens the quality of the low-E_d structures. On the other hand, there are very few processes through which E_d can be overestimated, making the high-E_d region much cleaner. For this reason, high-E_d structures are the best candidates for the determination of E_n.

3.2.2 Spectral Analysis on JET Data

Since the determination of E_n requires the identification of peculiar structures at precise position on the x-axis, to perform the spectroscopy of an ensemble of neutrons with different E_n is extremely challenging. If incoming neutrons can have two possible E_n, two E_d spectra will add, generating a spectrum featuring a superimposition of the structures of both. Adding more energies in the E_n spectrum further complicates the extraction of meaningful spectral information, to the point of making it almost impossible if the E_n are a spectrum of continuous values. This is the case of most real-world applications.

Nevertheless, nuclear fusion experiments have some characteristics that allow the use of solid state detectors as spectrometers:

- Neutron spectra on tokamaks operating in DD feature almost exclusively a component centred around 2.5 MeV.
- Neutron spectra on tokamaks operating in DT feature almost exclusively a component centred around 14.1 MeV, along with a component centred at 2.5 MeV. The two components are sufficiently separated so they can be easily discriminated (see figure 3.4). Furthermore, since the reactivity of DT is two orders of magnitude higher than the DD reactivity, the number of 14.1 MeV neutrons exceeds greatly the number of 2.5 MeV neutrons, allowing to treat the DD component as a rounding error of the DT component for high regime concentrations (D:T around 50:50).
- E_n spectral components that are not due to either direct emission from DD or DT are mostly due to neutron scattering in solid materials and other processes reducing the E_n. This means that, while the low-E_d regions of the E_d spectra might experience an overlap between neutrons emitted directly interacting with the detector with a high-Q_v process and scattered neutrons interacting through a low-Q_v process, the highest-E_d regions can only feature direct emission neutrons.
- Most spectroscopic applications on fusion plasmas require to measure small E_n shifts or broadenings of a spectrum centered on a particular E_n. For example, both the measurement of the plasma ion temperature and plasma current requires a

spectroscopic capability focused on a small interval around 14.1 MeV (in the case of DT plasmas), which can be covered by monitoring the evolution of the broadening of the higher-E_d reaction channels. Another example is the measurement of tritium production rate (see section 2.2.4) that requires the measurement of the number of neutrons within a range of E_n as opposed to the exact determination of the E_n energy spectrum.

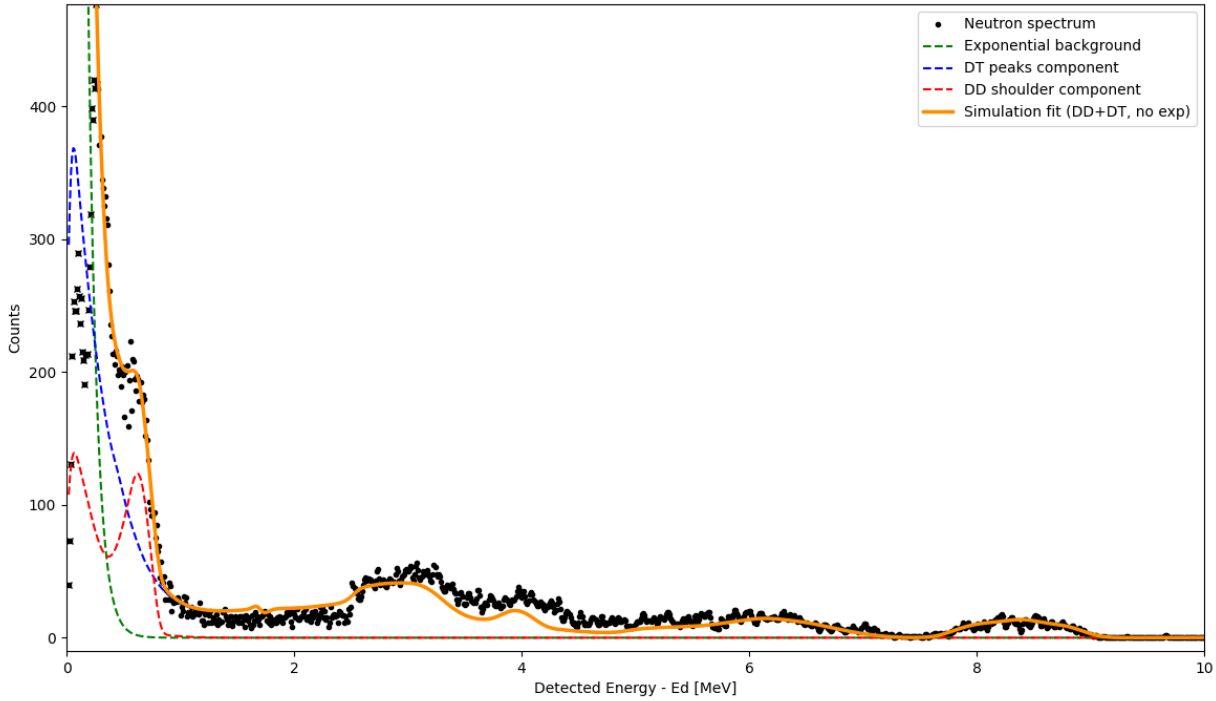

Figure 3.4: Spectral fit on JET data to determine the fuel ion ratio. Black points are spectral data obtained by a diamond detector on a DT discharge with low T. The points are fitted with a DT simulation, a DD simulation and an exponential to determine the magnitude of the three components.

A spectroscopic application of a solid state detector was tested using a series of diamond detectors installed at JET for determining the Ion Fuel Ratio (described in detail in 2.2.2). Scope of the experiment was to demonstrate that the spectroscopic capabilities of the detectors can be used to extract information from an experimental situation. Since it was not possible to test the SiC prototypes on a tokamak during the period of the thesis, the choice fell on the diamond detectors, which are the closest relative to the SiC detectors. The analyzed data were taken during a series of plasma discharges (numbering between 98044 and 98858) featuring a small tritium component in the plasma mix. The E_d of neutrons detected during the entire duration of the discharge ($\simeq$ 5s) were organized in a spectrum reported in figure 3.4. A calibration was performed in order to adjust the proper E_d values. The spectrum was then fitted with a function featuring three components:

- A DT component, obtained from a Geant4 simulation performed ad-hoc for the diamond under 14 MeV irradiation.
- A DD component, obtained from a Geant4 simulation performed ad-hoc for the diamond under 2.5 MeV irradiation.
- A decreasing exponential component, taking into account noise, backscattering events and other spurious components.

Each of the three components had amplitudes as a free parameter, while the exponential component also had a component parallel to the x-axis. The amplitude of the DT component was the first to be computed by fitting the data in the high-E_d region; after that the other components were fitted on the subtraction between the data and the projected DT component. The ratio between the amplitude of the DT and DD component was then used to calculate the ratio between the number of DT and DD reactions (after having applied a correction for the different reactivity). The estimates produced with this method are validated by independent references, showing good accordance. As an example, in the case of the discharge reported in figure 3.4 the method applied on the diamond data obtains a fuel ion ratio of $1.06\% \pm 0.1$, which compares to the accepted value of $0.87\% \pm 0.06$, meaning a correlation of 2σ. This confirms the good perspectives for solid state detectors to operate as neutron spectrometers for many of the fusion monitoring applications described in section 2.2.

3.3 Geometry Optimization

One crucial step of the development phase of SiC detectors concerns the choice of the geometry of the active volume, which must comply with the production standards and the detector requirements. There are a number of factors influencing the choice of geometry for the active volume:

- Efficiency, which scales linearly with the detector's volume.
- Partial charge deposition (which was described in section 3.3.2) calls for detectors with higher thicknesses.
- The production of a high-purity active volume is a challenge that scales up steeply with the size, and especially with the thickness of the detector.
- The polarization necessary to achieve a depletion region extending along all the thickness of the detector scales quadratically with the thickness of the detector (direct consequence of the formula in section 3.1.2). This means that thicker detectors require higher HV which can put the detector component under stress, causing discharges or leakage currents.
- Bigger active volumes have a higher probability of experiencing damage, lattice displacements and other wearing down phenomena due to neutron irradiation. Such phenomena can degrade the detector's characteristics, reducing the durability of the instrument.
- Diamond detectors are reported [55] to feature a decreasing resilience to temperature with increasing volumes. While this conclusion is unexplored for the SiC, it is worthy of consideration that the same processes could apply also for it.

The prototypes developed for this thesis have a combination of three different areas ($5x5\ mm^2$, $2.5x5\ mm^2$ and $2.5x2.5\ mm^2$) and three different thicknesses ($10\ \mu m$, $100\ \mu m$ and $250\ \mu m$). Prototypes will be collectively grouped up by their thickness, and referred to as SiC10, SiC100 and SiC250. For more information on the prototypes see section 4.2.

3.3.1 Efficiency

The main requirement for neutron detection is dictated by the detector's efficiency, which scales linearly with the size of the active volume. The efficiency is defined as the ratio of particles (in this case, neutrons) crossing the active volume resulting in a detected and registered signal. The optimal efficiency ϵ_{opt} depends strongly on the expected neutron flux Φ (measured in s^{-1}). It should be roughly:

$$\epsilon_{opt} \simeq \Phi \cdot \tau_p / 1000$$

where τ_p is the formation time of the preamplifier associated to the detector, i.e. the time required for a signal to be fully processed and the signal being restored to the steady state (see 4.4 for more details). The factor of 1000 is chosen to keep a small probability of pile-up. If the efficiency of the detector is significantly higher than ϵ_{opt} the probability of two events being piled-up increases, potentially becoming a big fraction of the total number of events. This might lead to a high number of discarded events and the complication in the determination of the E_d spectrum (see section 4.6.2 for more details). On the other hand, even if having an efficiency lower than ϵ_{opt} does not introduce problem in the detection, the detection will require a higher neutron fluence to reach the number of counts necessary to create a meaningful E_d spectrum, thus requiring a higher exposition time. This is an issue for those applications requiring a small time resolution, like the monitoring of ion temperature.

3.3.2 Partial Charge Deposition

As said in section 2.4.3, the interaction of a neutron generates charged products inside the active volume that, in turn, ionize the lattice atoms and generate electron-hole pairs. The number of pairs is linked to E_d only if the charged products deplete their kinetic energy through interactions before exiting the active volume: if one (or more) charged particle(s) exits the active volume, they'll carry a fraction of E_d with them. In such a case the detector incurs in a partial charge deposition (introduced in section 3.3.2).

Partial charge deposition plays a role in determining the optimal geometry of the detector. Charged particles with $\simeq$ MeV kinetic energies can travel short distances inside the solid structure of the active volume before ceding all their kinetic energies through collisions. Such paths are not necessarily straight, and their length is on the order of less than μm for heavy ions, few tens of μm for alpha particles and few mm for protons. Since typical sizes for solid state detectors are comparable with this range (especially the thickness, ranging between tens and hundreds of μm) the partial deposition effect plays an important role in determining detector's geometry.

Let's take into consideration three of the reaction channels for DT neutrons with the lowest Q_{value} from table 3.1: ^{28}Si(n,α)^{25}Mg, ^{28}Si(n,p)^{28}Al and ^{12}C(n,α)^{9}Be. These reaction are among the most important for DT neutron spectroscopy and are also among the most susceptible to partial deposition effect (since they possess the highest E_d among all reactions). The mean range of the lighter reaction product of the three reactions (either alpha particle or proton) is computed using the ASTAR and PSTAR catalogues [56][57] and it is reported in table 3.2.

Reaction	Ed [keV]	Max light particle Ed [keV]	Mean range in SiC [um]
$^{28}Si(n,\alpha)^{25}Mg$	11446	9867	43.6
$^{28}Si(n,p)^{28}Al$	10240	9887	455.1
$^{12}C(n,\alpha)^{9}Be$	8398	5814	19.1

Table 3.2: Energy and mean path for the products of the three most important nuclear reactions in SiC. Mean path is computed from ASTAR and PSTAR data [56][57].

The alpha particles range from the $^{12}C(n,\alpha)^{9}Be$ and the $^{28}Si(n,\alpha)^{25}Mg$ reactions is comparable with the SiC thicknesses, meaning that a relevant fraction of alphas will undergo partial deposition. In fact, taking the $^{12}C(n,\alpha)^{9}Be$ reaction channel as an example, if alpha particles are produced in the direction parallel to the SiCs thickness and are assumed moving in a straight line, a 19.1 µm mean path would mean that every neutron interaction within the bottom 19.1 µm of the active volume would result in partial deposition: this would amount for the 7.64% of the events in a SiC250, 19.1% in a SiC100 and the 100% of events of a SiC10. This, although, is not the case, since reaction products are produced isotropically, and thus may be produced parallel to the long side of the SiC and be fully stopped before leaving the active volume. This allows the full deposition of the proton of the $^{28}Si(n,p)^{28}Al$ reaction, with its 455 µm mean path.

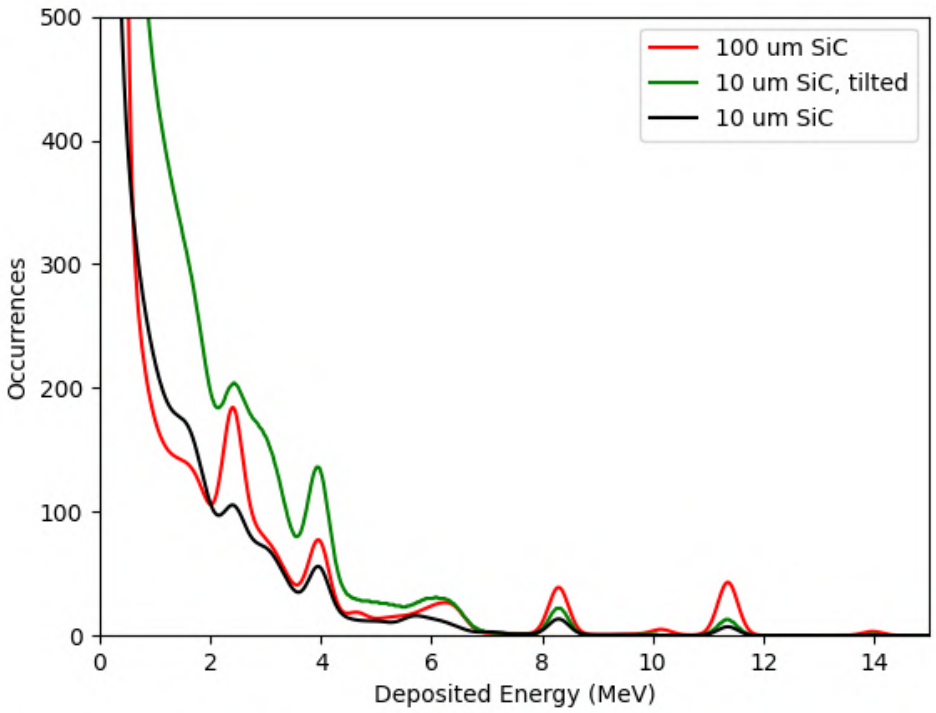

Figure 3.5: Comparison between three Geant4 simulations using 14 MeV neutrons. The red spectrum refers to a 100µm SiC, the black spectrum refers to a 10µm SiC and the green spectrum refers to a 10µm SiC which was tilted by 45° with respect of the beam. All simulations were normalized to the same number of interacting neutrons (thus, normalized for the detector's efficiencies) and broadened simulating an energy resolution of 3%.

Figure 3.5 compares a simulated spectrum produced for a SiC100 (analogous to the one in figure 3.3) with the same spectrum for a SiC10 and a SiC10 which was tilted by 45° degrees with respect of the neutron beam. The number of counts of the two SiC10 was rescaled up of a factor

ten, to compensate for the different efficiencies; despite of that, the number of counts for the two SiC10 spectra are lower than the one for the SiC100 spectra due to the partial deposition effect, moving high E_ds events to lower E_ds. It's also worth noting that the tilted measurement loses less counts to partial deposition effect due to the increase of the effective depth of the active volume from the beam direction point of view. All the structures are still present with the thinner SiCs: it should be taken into account, though, that relying on high-E_d counts will inevitably incur in an important loss of efficiency.

3.3.3 Partial Depletion

As discussed in section 3.1.2, the depth of the depletion region in SiCs grows as a function of the bias voltage inputted, making it so that there is a minimum voltage needed to achieve a depletion region encompassing the entirety of the active volume (condition which is referred to as "full depletion"). Full depletion, however, is not a prerequisite for neutron detection: SiC can detect neutrons even with a bias lower than the minimum needed to fully deplete them – thus, having a depletion region extending only for a fraction of the entire thickness (condition referred to as "partial depletion"). This was first proven with the first SiC250 prototypes, whose minimum bias for achieving full depletion was 4.6 kV. Both alpha particle and neutron detection were achieved with detection characteristic like fully depleted SiCs, demonstrating that a partially depleted SiC behaves like a fully depleted SiC with thickness equal to the depleted thickness, with few (if any) negative effects on the detection characteristics. This property makes it so that the efficiency of the detector (which has a linear dependence on the active volume depleted size) has a dependency on the HV bias, as illustrated in figure 3.6.

The detection under partial depletion and its benefit will be thoroughly analysed in section 5.3 and section 5.4.

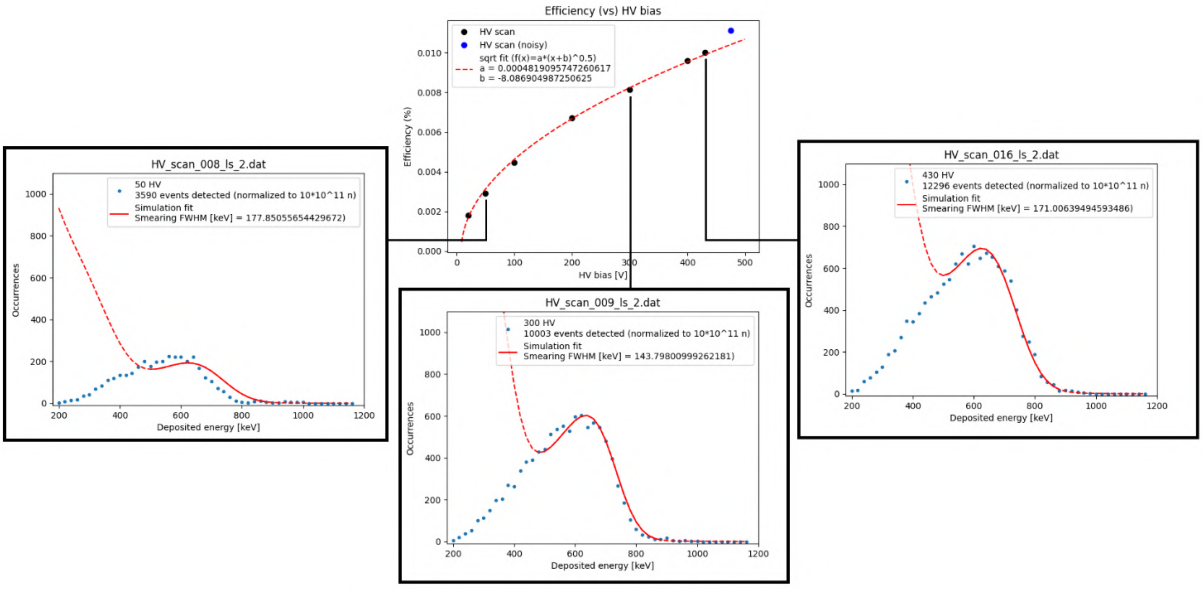

Figure 3.6: On top: number of counts obtained by the 250µm-thick SiC-B (section 4.2.1) as a function of the bias input while under irradiation of DD 2.5 MeV neutrons at FNG (section 4.7.4). The evolution of the number of counts follows a square root relation with the bias (represented with a dotted red line in the figure), as expected by the formula in section 3.1.2. On right, left and bottom, the E_d spectra of three bias values (50V, 300V and 450V) are presented and fitted with a Geant4 simulation through the method described in section 4.8.2. The spectra are normalized to the same neutron fluency. The 50V spectrum shows that the shoulder moves to lower E_d, highlighting a drift in the response function which will be furtherly analysed in the work presented in section 5.4.

Chapter 4
Experimental Techniques

This chapter feature a list of the instruments used in the research presented in this thesis, as well as the facilities in which the detectors were characterized. Each instrument and facility will be presented briefly to introduce its scope and general functionality. Technical information and external references will be also provided for completion. The chapter also feature a summary of various techniques (either numerical or practical) related to data analysis, optimization of the detector's performance and more.

The section is structured in a way to be consulted as needed more than be read top-to-bottom. To this end, many referenced in other chapters refer to section of this chapter.

4.1 Diagnostic Schematics

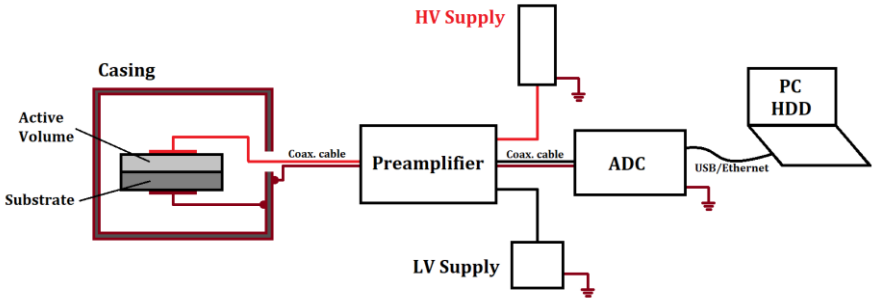

Figure 4.1: diagnostic schematics. The "hot" cable carrying the bias signal is represented in light red, while the connection to the ground is represented in dark red. The preamplifier and other components are represented as black boxes, since their electronical details are not core for this thesis.

Figure 4.1 presents a simple scheme of the whole diagnostic.

- The active volume is on the left side of the picture, encased in an aluminium casing that is used as a faraday cage (see section 4.3).
- Detector is connected to a preamplifier, whose purpose is to heighten and shape the voltage pulse received on the hot line (in red) of the coaxial cable connected to the active volume. For more information refer to section 4.4.
- The preamplifier is powered by an independent, low-voltage supply.
- The bias voltage at the edges of the active volume is provided by an HV supply (see section 4.5.1) and transmitted through the preamplifier.
- The preamplified signal is transmitted to an Analog-to-Digital Converter (ADC), which samples the signal and performs a series of fast process and operations described in section 4.6.
- The ADC communicates with a PC where the data are stored for off-line analysis.

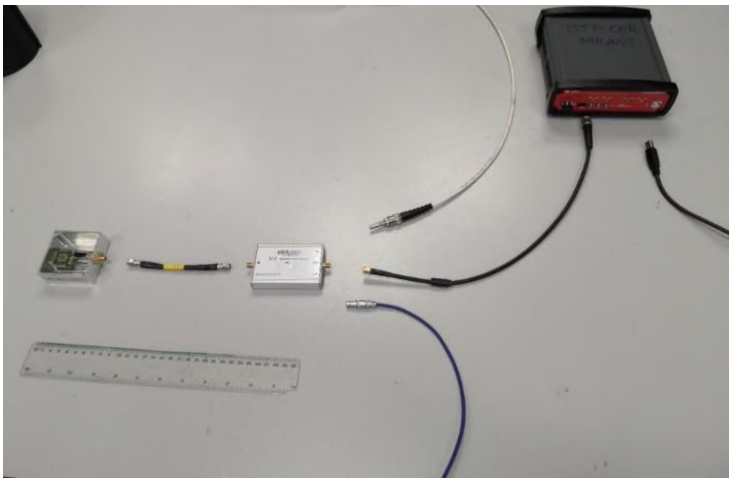

Figure 4.2: Exemplificative picture of the electronical apparatus, arranged in the same abstract geometry reported in figure 4.1. The white cable on top is supposed to be connected to the HV supply, while the blue cable on bottom to the LV supply. The ADC is on the top-right, while the computer is not shown in the picture. On bottom-left a ruler is used as a reference scale.

4.2 SiC Prototypes

This section will present a list and a brief description of the prototypes used in this thesis.

4.2.1 SiC-A and SiC-B (SiC250)

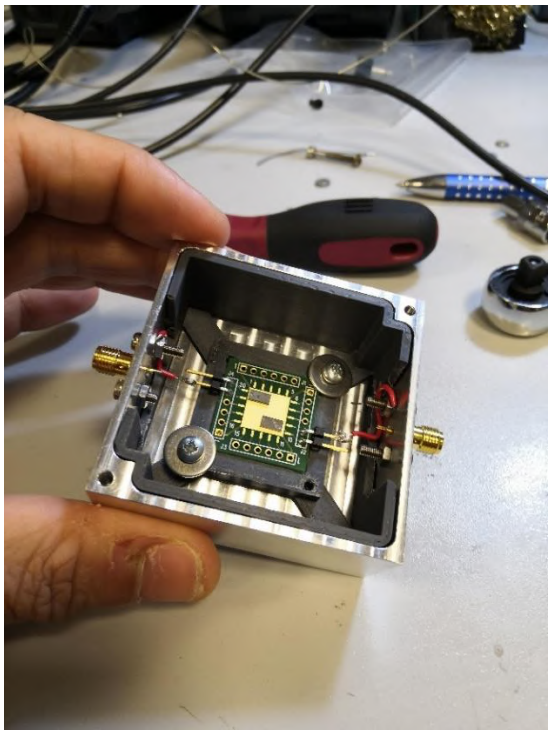

Figure 4.3: Picture of the twin SiC-A and SiC-B inside their casing.

The two prototypes are the first iterations of the 250μm-thick SiC. The two active volumes have 5mm x 2.5mm rectangular surfaces and, while independent, are installed on the same plate and Printed Circuit Board (PCB). The two detectors are shielded by a 3.0 mm thick aluminium box, which is covered with a 0.5 mm plaque. The black scaffold holding the PCB in place was manufactured with a 3D printer out of polylactide (PLA). The contacts between the PCB, the signal cable through a Sub-Miniature type A (SMA) port and the ground (also connected to the casing) are realized with small copper cables welded with tin.

The twin detectors exhibit an ohmic behaviour, described in section 4.9.2, which, while unwarranted, does not impair the detection capability of either detector for biases ranging from 0 V to 900 V.

The detector was used in the work reported in section 5.4.

4.2.2 SiC-C (SiC10)

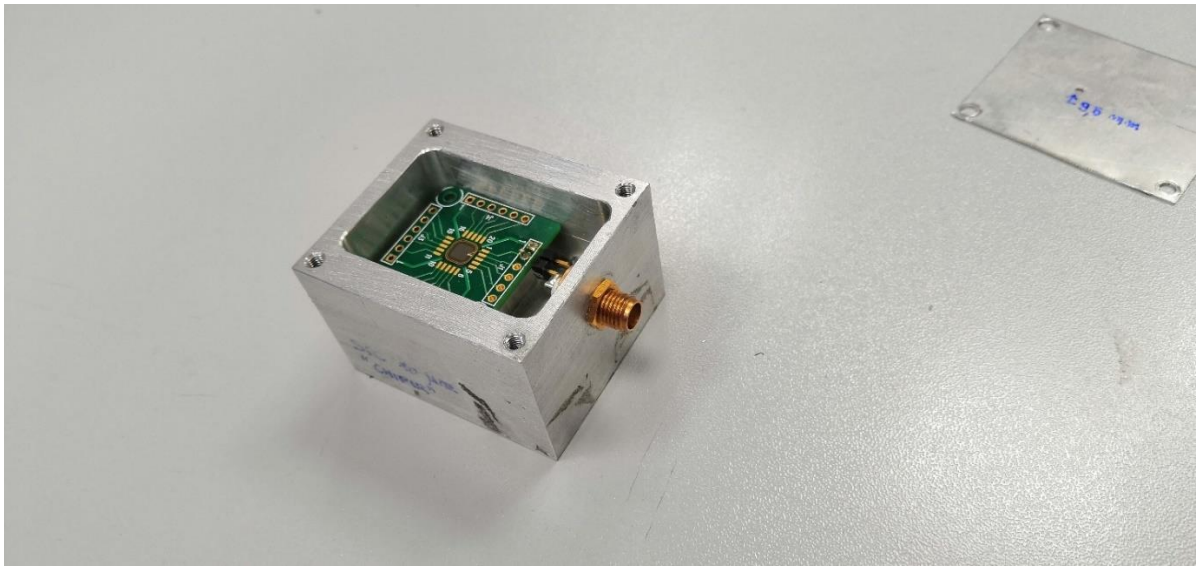

Figure 4.4: Picture of the SiC-C inside its casing.

The detector is the first 10μm-thick prototype tested, having an active volume measuring 5mm x 5mm in area. The detector is mounted on a PBC mounted on a cm-large aluminium support and is encased in an aluminium casing measuring between 3.0 mm and 8.0 mm in thickness. After proving how the thick casing influenced the detection (section 5.2, furtherly analysed in section 4.3.1) the cover was replaced with a 0.5 mm plaque with the aim of minimizing the number of neutrons converted to charged particles in the aluminium. The contacts between the PCB, the signal cable (though a SMA port) and the ground (also connected to the casing) are achieved through a conducting rigid structure welded in tin.

The prototype was used in the works reported in section 5.2 and 5.4.

4.2.3 SiC-D (SiC250)

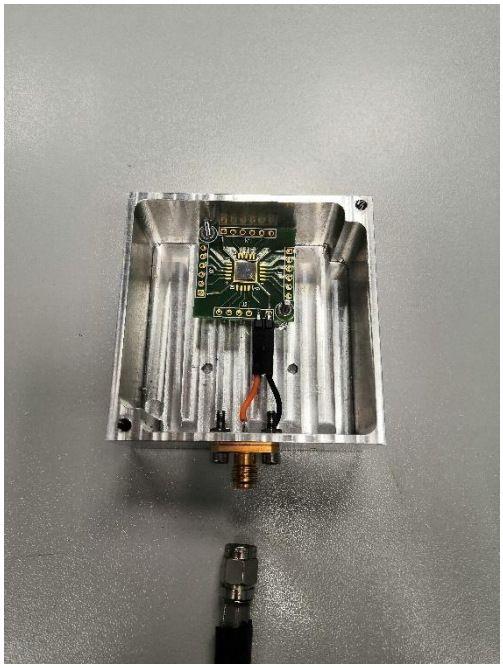

Figure 4.5: Picture of the SiC-D inside its casing.

The detector is a 250μm-thick prototype with an area of 5 mm x 5 mm. Since it was the second SiC250 to be manufactured (right after the twin SiC-A and SiC-B, which demonstrated an unwarranted ohmic behaviour) the prototype was taken as a staple for the SiC250. The casing has a thickness of 3.0 mm and is covered by a 0.5 mm thick plaque. Similarly to the SiC-E, the PCB was installed in the casing through two screws to have as less material close to the neutron detector as possible, in order to reduce the number of backscattered neutrons and converted radiation (see section 4.3.1). The contacts between the PCB, the signal cable (though a SMA port) and the ground (also connected to the casing) are achieved with copper cables terminating with Dupont connectors.

The prototype was used in the works reported in section 5.3 and section 5.4.

4.2.4 SiC-E (SiC250)

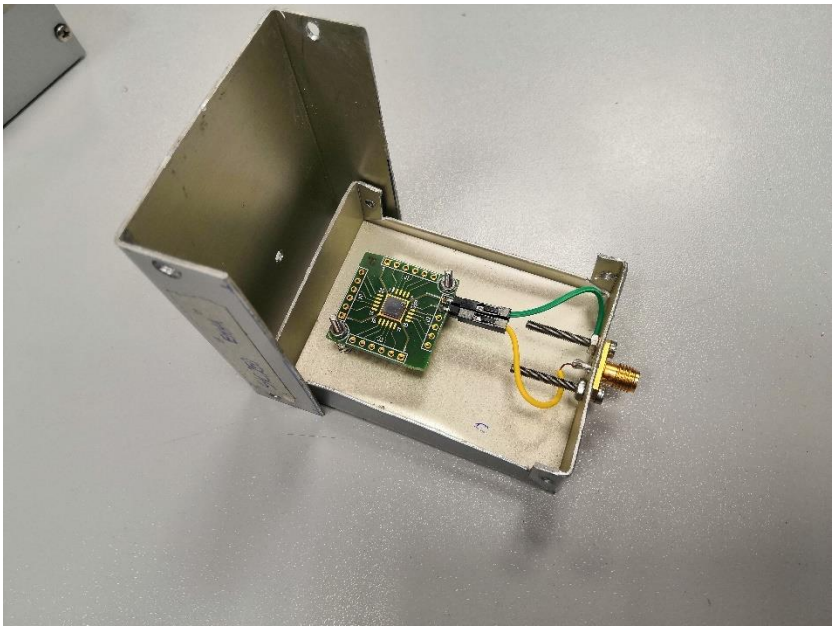

Figure 4.6: Picture of the SiC-E inside its casing.

The detector is a 250μm-thick prototype with an area of 5 mm x 5 mm. The active volume and PCB setup and size are the same as the SiC-D. The casing is smaller than SiC-D's, having a thickness of 2.5 mm. The contacts between the PCB, the signal cable (though a SMA port) and the ground (also connected to the casing) are achieved with copper cables terminating with Dupont connectors. Similarly to the SiC-D, the PCB was installed in the casing through two screws to have as less material close to the neutron detector as possible, in order to reduce the number of backscattered neutrons and converted radiation (see section 4.3.1).

The prototype was used in the works reported in section 5.3 and section 5.4.

4.2.5 SiC-L (SiC10)

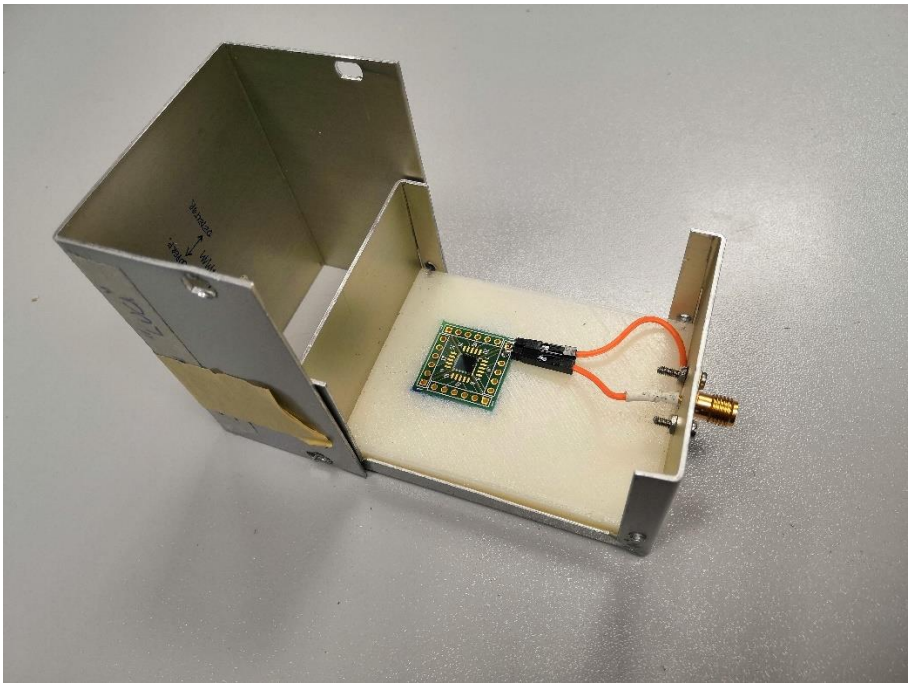

Figure 4.7: Picture of the SiC-L inside its casing.

The detector has a 10μm, 5 mm x 5 mm active volume installed on a small PCB. The PCB is installed in a 2.5-thick aluminium casing and is kept in place by a PLA sponge manufactured through a 3D printer. Connection between the cable, the casing and the ground is achieved through a copper cable welded to a SMA connector with tin and connected to the PCB with Dupont terminations.

The detector was used in the work reported in section 5.4.

4.2.6 SiC-m (SiC250)

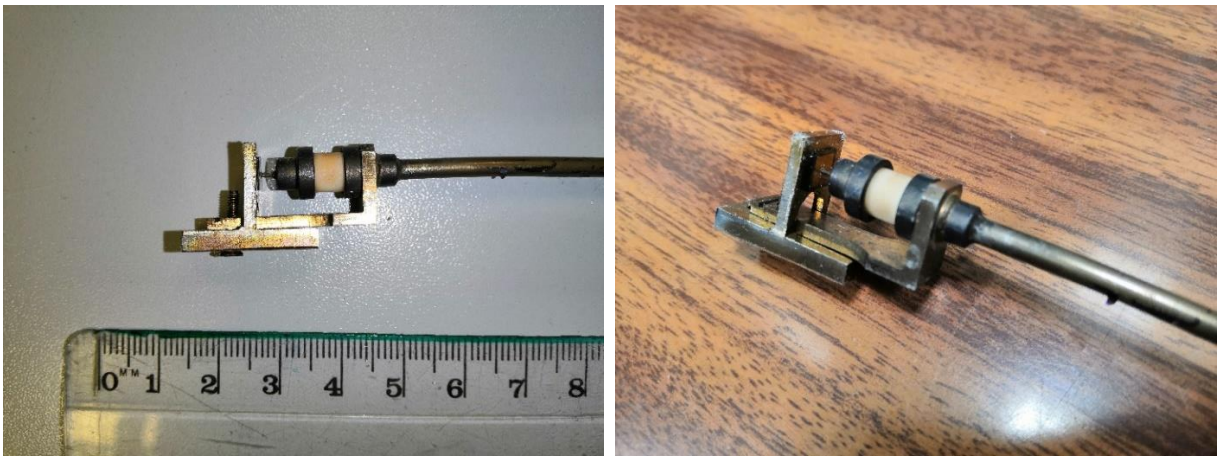

Figure 4.8: Pictures of the SiC-m mounted on its scaffold and mineral cable.

The SiC-m belongs to a second generation of SiC250, which were manufactured with a higher edge structure quality after the experiences detailed in section 5.3 and section 5.4. The active

volume is 5 mm x 5 mm x 250 µm in size. Differently from all other prototypes, the detector was not installed on a PBC nor welded; instead, a steel scaffold was manufactured to accommodate the detector and push it against a pin connected to a 1-meter-long mineral cable manufactured by Thermocoax [58]. The entire setup was put in place in order to be able to test the detector to high temperature and was realized imitating the setup used by Angelone in [55] testing the diamond detectors. To insulate the detector from EM radiation a faraday cage was realized with conducting tape wrapping the scaffold and detector and put into electrical contact with the outer part of the mineral cable.

The detector was used in the work reported in section 5.5.

4.2.6 SiC-O (SiC100)

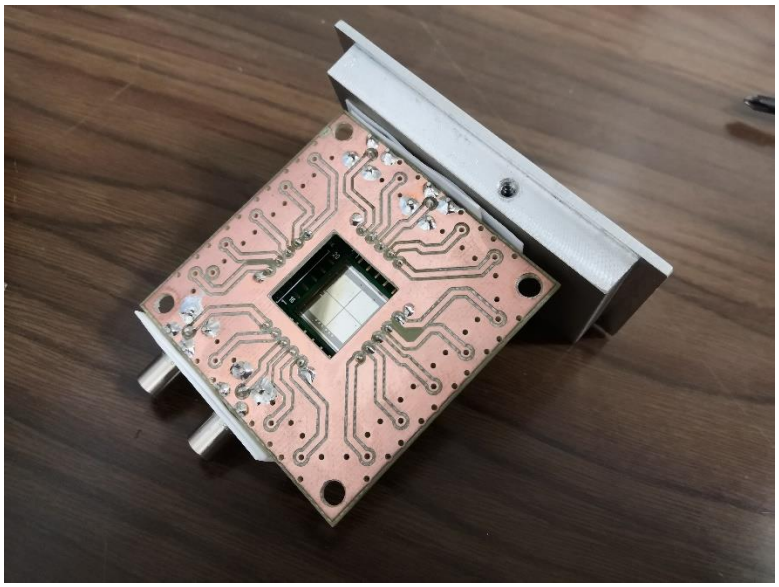

Figure 4.9: Picture of the SiC-O with a section of its casing.

The SiC-O is the first SiC prototype manufactured within the project. It was manufactured by CNR-IMM and INFN through a collaboration called SiCILIA [52]. It features four SiC active volumes of 5 mm x 5 mm of area each and 100 µm in thickness, all grown on the same substrate. Only one of the active volumes was used for neutron detection in this work. Contacts are printed directly on the PCB on which the detectors are installed and are connected to the signal cable though LEMO connectors. The detector in enveloped in a aluminium casing with thicknesses between 5 mm and 8 mm.

The prototype was used in the works reported in section 5.1 and section 5.2, as well as works predating the scope of this thesis, like [59].

4.3 Detector Housing

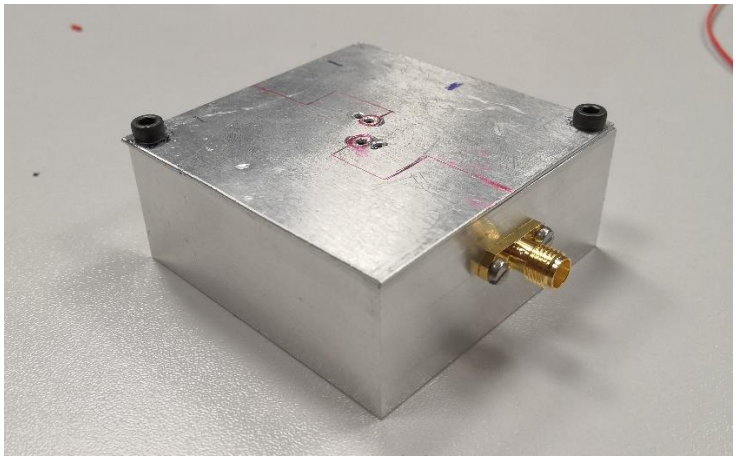

Figure 4.10: Picture of the SiC-A and SiC-B casing. On top the holes drilled for alpha irradiation can be seen, while on the right the SMA connector is used for the connection with the preamplifier.

The SiC active volume, substrate and relative PCB were encased in a series of aluminium conductive boxes, called "casings", whose purpose is to act as a Faraday cage, shielding the detector's active volume from light and other form of environmental radiation. The casings were also designed as a safety measure against accidental contacts between the hot line and other structure or the user, and as a physical structure that makes the detector handleable. Each detector's PCB was put in its own housing, each of which was manufactured inside ISTP-CNR laboratories (with the exception of SiC-O and SiC-C casings).

All casings are made of natural aluminium, having a thickness between 0.5 and 7.5 mm (depending on both the specific casing and the point on it). The casing were all connected electrically to the common ground of the coaxial signal cable and the detector's substrate. A small hole (between 2 and 3.5 mm in diameter) was drilled in the front panel of the housing directly above the active volume. This was done in order to allow the flux of alpha particles from alpha sources to reach the detector while preserving the Faraday cage. In other cases, the alpha source was installed inside the casing itself. The same holes were present during all neutron irradiations, but since its area is much smaller than the area of the active volume and the area of any of the neutron beam used, it can be assumed that most neutrons reaching the detector went through the upper part of the casing.

Since the interaction between neutrons and the aluminium casing can influence the detection process (as discussed in detail in the next section) later casing were manufactured to be as thin as possible, with caps having a uniform thickness of 0.5 mm.

4.3.1 Scattering and Conversion

Natural aluminium is composed almost exclusively by ^{27}Al. Fast neutrons can interact with ^{27}Al through nuclear scattering and nuclear reactions - the most common nuclear reaction being $^{27}Al(n,p)^{27}Mg$. This cause two phenomena that can alter the number of counts and the spectra detected by the detector while under fast neutron irradiation. First, neutrons **scattering** on the aluminium of the casing can be deflected toward the active volume and interacts with it. The

scattering interaction causes the neutron to deposit some energy on the aluminium nuclei, therefore shifting its E_n to lower energies. Secondly, neutrons undergoing nuclear interactions with the casing can produce charged particles that are detected if emitted in the direction of the active volume. The process will be referred to as neutron **conversion**.

The impact of conversion due to the aluminium cap was studied on the first design of the SiC-C housing, which featured the thickest cap of all the casings used (3.0 mm of thickness). The number of events due to converted protons was obtained via the calculation of the macroscopic cross section per unit area χ. This, in turn, was calculated multiplying the nuclear cross section σ (obtained from the ENDF catalogue [60], averaged on $5\ MeV < E_n < 20\ MeV$) by the number of atoms per unit area n_{at}/A, derived from the atomic density ρ and the thickness t. Such calculations were performed for both the cap and the 10 µm active volume, obtaining the macroscopic cross section per unit area for both the active volume (χ_{SiC}) and the cap (χ_{cap}):

$$\chi_{SiC} = 38.7 \cdot 10^{-6}$$

$$\chi_{cap} = 542.7 \cdot 10^{-6}$$

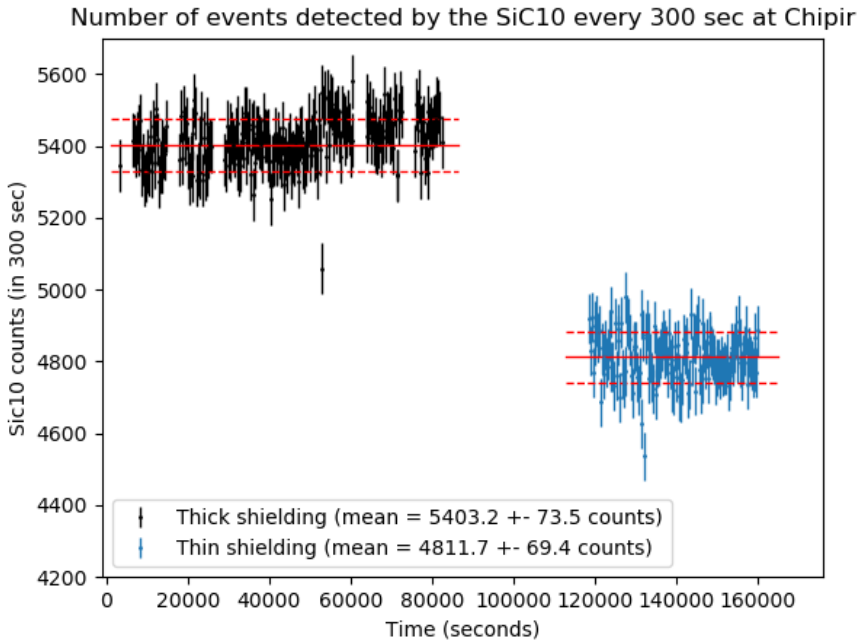

Figure 4.11: Number of events detected in a 300 second integration at ChipIr as a function of the irradiation time (spanning for more than 40h). All points (with their y error bars) are compared with a horizontal fit (solid red line), with the two dotted lines representing the standard deviation expected by random fluctuation in the number of events. Such fit shows a substantial stability in the number of counts. The two sets of data correspond to the irradiation with a thick aluminium shielding on the line of sight (in black) versus a thin shielding (in blue): the difference between the two suggests that the conversion on the shielding cap accounts for around 11% of the total counts of the detector when used.

The two results show that the probability of a neutron producing a charged particle in the cap is $\chi_{cap}/\chi_{SiC} \simeq 14$ times higher than the neutron interacting in the SiC. Assuming the charged particles are emitted isotropically, only a fraction $a = \frac{A_{SiC}}{4\pi \cdot d^2}$ of the produced protons interacts

with the active volume, $A_{SiC} = 25\ mm^2$ being the active volume area and $d = 15\ mm$ being the distance between the cap and the active volume. Assuming that the proton detection efficiency being nearly one (since it is a charged particle interacting in the SiC in a continuous way), it was estimated the protons constitute the 10.8% of all the detected events. This was confirmed experimentally at the neutron source ChipIr, where the SiC-C was irradiated with fast neutrons while using the aluminium cap and while using a 20 μm thin aluminium film. More detailed information can be found in section 5.2.

4.4 Preamplifiers

The role of the preamplifier is to take in input the signal from the detector, which is very small (on the order of few fC) and convert it to an mV—ranged, well detectable and shaped voltage signal lasting some tens of ns or more. The signals are, in the case of charge amplifier, always of the same shape, characterized by a typical rise time and decay time depending on the preamplifier specifications. The area underlying the shape (and, in case of charge preamplifier, also the height of the pulse) carries over the information on the number of charges collected by the detector after an interaction, allowing spectroscopy. The shaping time of the preamplifier has an unavoidable tradeoff: slower times allow to reduce charge collection uncertainties by increasing the number of charges in the signal, allowing to reduce statistical errors and, thus, increasing the energy resolution. On the other hand, faster shaping times allow to reduce the statistical relevance of pile-up effects, described in section 4.6.2, allowing the preamplifier to operate well under higher fluxes. Another crucial parameter is the gain of the preamplifier, measured in fC/mV (or dB, in the case of current amplifiers), which should match both the expected amount of charge extracted from the detector and the dynamic range of the readout (in this case, the ADC).

All the preamplifiers used in this thesis are manufactured by Cividec [61] and are either preamplifiers developed for diamond detectors or adapted from diamond detector preamplifiers. The amplifier used were:

- **Cividec C1** is a current amplifier featuring a small gain of 20 dB. Being a current amplifier, the amplified signals are much smaller and with more random oscillations than charge amplifiers. On the other hand, the amplifier is very fast, being able to shape signals with typical lengths of 10-15 ns. **Cividec C2** was also used, featuring the same characteristics but a higher gain (40 dB).
- **Cividec Cx-L** is charge amplifier originally developed for diamond detector and customized in order to operate on both polarities, it features a semi-gaussian pulse shape with a width of 180ns FWHM. Its gain is 12 mV/fC.
- **Cividec SiC Ampifier**, which was developed during the thesis work to match the specific characteristic of the SiC250s. It features a faster rise time with respect to the Cx-L (about 100 ns) and a very low dependence on the capacitance of the detector, allowing the optimal use on thin and thick detectors. Its gain is optimized such that $E_d = 20$ MeV corresponds to the maximum output for which the linearity of response in granted, 2 Volts.

4.5 Power Supplies

4.5.1 HV Power Supplies

The bias voltage is supplied to the preamplifier (which transmits it to the detector) by dedicated units of in-rack high-voltage supplies. The ones used in the experiments are:

- ORTEC Model 710 Quad 1-kV Bias Supply, which is capable to supply between 0 and 1kV (in either polarity) with a nominal precision of 0.1V (1V for voltages between 100V and 1kV). The supply is capable to administer up to 20 μA before incurring in an automatic shutdown. A current readout is also available. For more technical information see [62].
- ISEG type EBS 8005 HV generator, which is capable to supply a voltage up to 500V on either polarity with a maximum current of 15 mA (which is much higher than Ortec's). The noise and ripple for the supplier is also very low, being less than 10 mV. For more technical information see [63].
- CAEN NIM N1471 remote controllable Power Supply, which is capable to manage up to 8kV with a remote-controllable maximum output. The power supply is instrumental for those applications in which to have an active control of the bias is key. For more technical information see [64].

4.5.2 LV Power Supplies

All the preamplifier used required a 12V DC power supply in order to operate. The stable supply of it was assured through the use of either a single output Kert KAT 10VD or an Agilent E3612A power supply.

4.5.3 Picoamperometer

A Keithley 6487 Picoamperometer (detailed technical information in [65]) was used to perform the I/V characterizations, that is to read the flow of current in the detector as a function of the input bias. The Keithley 6487 has a huge dynamic current range spanning up to 20mA (DD or DC) with a resolution of 10 fA (DD or DC). Its HV source can supply up to 505 V with a nominal precision of ±0,1%. Since it is programmable, a Python-based software was developed and used to communicate with the picoamperometer and set the duration of acquisitions, the voltage ramps, the integration time of the current and the readout frequency. Thanks to the program developed it was possible to measure the evolution of the dark current as a function of time after a new voltage was set (see figure 4.25) and develop an automatic procedure for measuring the I response after a V was set. Results of the I/V characterization are reported in section 4.9.

4.6 Analog to Digital Converter (ADC)

The Analog-to-Digital converter is the instrument allowing the voltage signal coming out from the amplifier to be digitalized, i.e., to be turned into a series of data that can be stored into a PC for off-line and/or on-line analysis, data visualization and off-line storage. The basic principle of the ADC is to register the value of the voltage (within respect of the ground) at a frequency

given by its internal clock and send it to a PC in packages. The PC is then able to operate on the data either on-line (through some software paired with the ADC) or store it for off-line analysis.

The ADCs used during this thesis are all CAEN 5730 [66], which are desktop digitizers featuring:

- **8 channels**, allowing for the simultaneous input of 8 different signals.
- A **500 MHz clock**, meaning that the signal is sampled every 2 ns (simultaneously on each channel).
- A **full-scale maximum range of 2 Vpp**, allowing the readout of signals spanning up to ± 1V (assuming both the signal and the ADC share the same ground potential $V_0 = 0$ V).
- **14-bit resolution**, meaning that the voltage value is sampled and given it a value within 0 and 16383 ($= 2^{14} - 1$). If the maximum full-scale range of 2 V is used this corresponds to a maximum resolution on the potential value of 0.122 mV.

4.6.1 Software and Algorithms

The device is able to perform a series of algorithms for the online digital pulse processing. Among these, the most essential is the **triggering algorithm**, by which the signal received on a channel is not passed to the PC unless a certain condition happens, which is usually the signal crossing a certain threshold. By choosing an appropriate threshold it is possible to limit the transmission of data to the time windows in which a likely event took place in the detector. It is therefore necessary for the threshold to be close enough to the baseline (= the mean output value of the potential when no event is underway) for the signals of the events with the smallest E_d to cross it, but it is also useful for it to be far enough from the baseline so as to not intercept the random oscillation of the signal around the baseline. Since the targeted level of random noise for most setups is less than few mV (± 5 mV) and the signals reach peaks on the order of several 10s of mV or 100s of mV (heavily depending on the preamplifier and the electronics), this is usually easily achieved with a $\simeq 10$ mV threshold. The choice of the threshold, though, is not uniform and is heavily dependent on the detector, the preamplifier, the measuring environment, the particles to be measured and much more (noisier environments required higher thresholds, for example).

When a trigger happens, the ADC registers the input signals in a **time window**. Such window can (and usually does) start before the trigger, thanks to an internal buffering stage allowing to store the data of the past few microseconds. This allows to save the entire waveform related to the event, including its rise before the trigger happened. The length of the waveform can be chosen freely, but its not usually a big factor in detection: the only restriction adopted was for it to start at least 100 ns before the waveform starts and to end at least a few hundred ns after the end of the waveform, in order to be sure to not lose any feature of the waveform. Time window chosen generally varied between 800 ns and 6 µs. Longer time windows consisted in a higher stream of data from the ADC to the PC, with the risk of saturating the USB connection if the detection rate was very high; on the other hand, noisier environments benefit from a longer time window, since it was possible to compute the baseline on the mean value of a longer sample of points.

The signal captured in the time windows can then be passed to the PC and stored, saving the value of the potential every 2 ns. This operation is usually very heavy on the transmission load

and can be performed only for low event rates. One good way to lighten data transmission is to preprocess the data by computing the pseudo-integral of the waveform before the transmission. This is done by summing the values of the signal inside a time window called "**gate**", which it's defined manually by the user as a function of the trigger time. The gate is usually chosen to start few bins (= units of clock, i.e., units of 2 ns) before the trigger and end when the signal returns around the baseline value. The value of the baseline is subtracted from each of the 2-ns signal values, in order to find the "area" of the waveform, which represent the number of charges collected and, thus, is linked to E_d.

The **baseline** upon which the signal pseudo-integral is calculated is computed by the ADC algorithms as the mean signal of a number of points before the start of the two gates. This value can be set in a range between 16 samples (32 ns) and 1024 samples (2048 ns). A better method of calculating the baseline can be performed offline (if the waveforms are stored) by making a fit of all the points in the window outside the long gate. This was demonstrated to be the better method by irradiating a sample detector (SiCD – see section 4.2.3) with an electrodeposited ^{241}Am source (see section 4.7.1) in air at two different distances in order to have two monoenergetic alpha particles of 4.29 MeV and 2.95 MeV. The signal integrals obtained where put in a histogram (see figure 4.13): by assuming the particles to be monoenergetic, the broadening of the histogram on the X-axis is due to the energy resolution of the detector, which can be furtherly broadened by the uncertainty in the calculation of the baseline. Baseline uncertainty can be reduced (and, thus, energy resolution improved) by averaging on a longer time scale, as it is shown in figure 4.14.

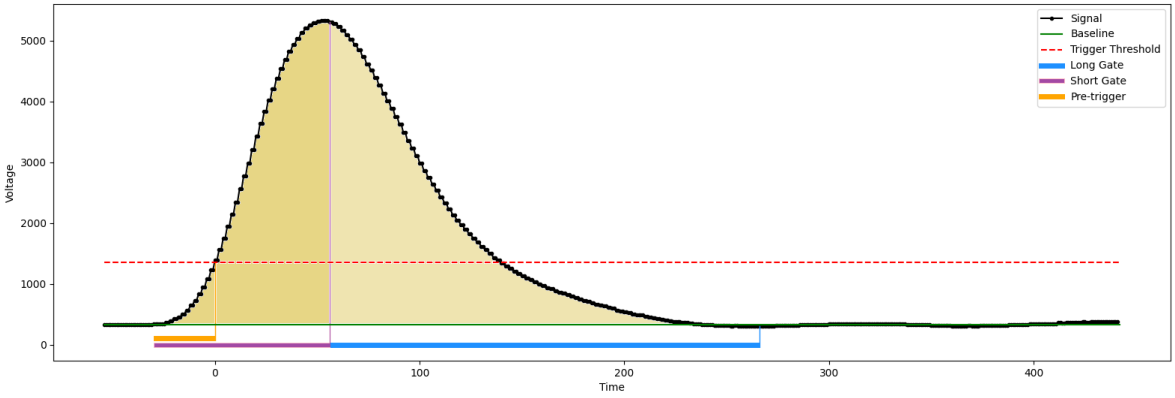

Figure 4.12: Visual representation of the quantities associated with a waveform (in black). The integral is the gold area underlying the waveform, to which the baseline (in green) is subtracted. The signal is triggered at t=0, when its value crosses the threshold (in red). Short gate and long gate (purple and purple + blue, respectively) are taken at a time t<0 before the threshold crossing (in orange). The integral is then calculated as area underlying the signal corresponding to the long gate, to which the baseline is subtracted.

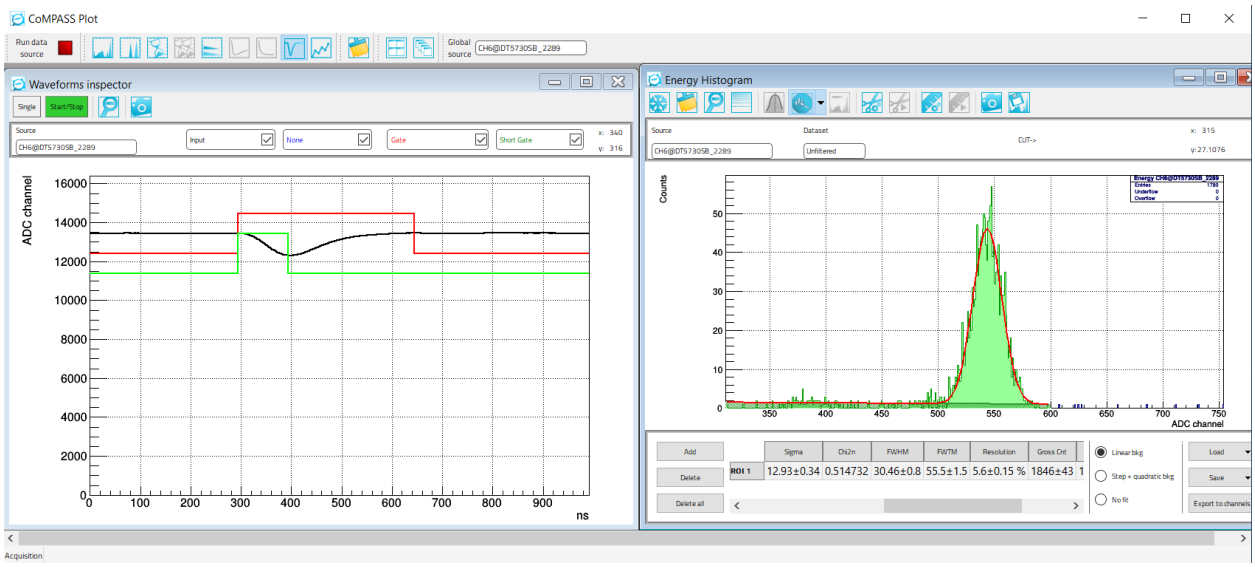

Figure 4.13: On the left side, real example of a wavefunction, with its relative long gate (in red) and short gate (in green). On the right side, a histogram collecting all the pulse heights is produced. The image is taken with the Compass software, one of the software used for controlling the flow of data through the ADC.

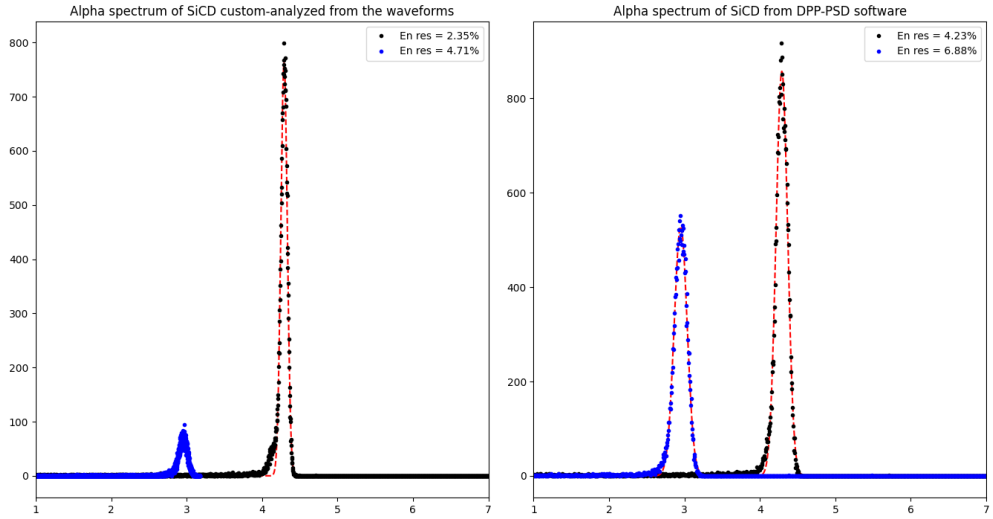

Figure 4.14: Difference between two E_d spectra obtained with SiC-D and the ^{241}Am source. On the right the spectra are obtained by computing the baseline on a 128 ns averaging, while on the right a custom-developed long averaging is used. The improvement in the baseline evaluation is enough to improve the energy resolution by 2%.

4.6.2 Pile-up Management

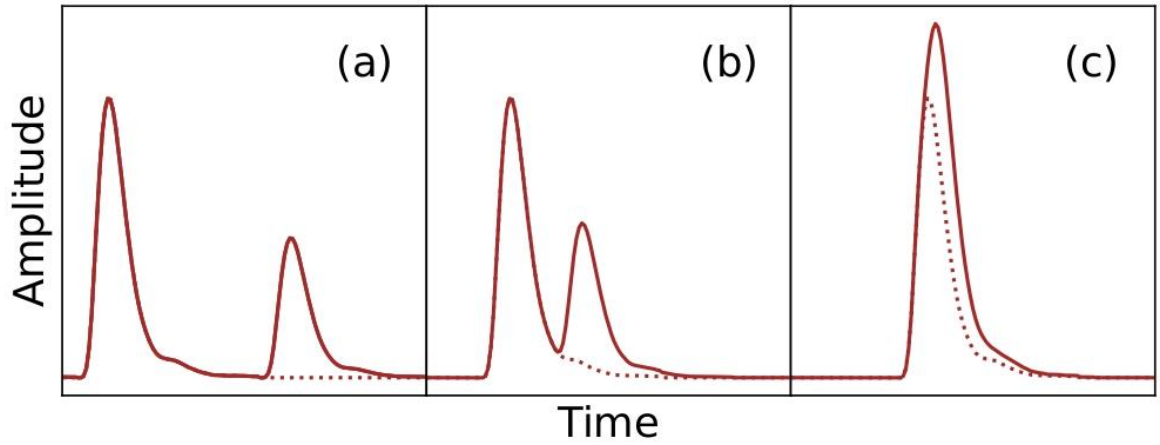

Figure 4.15: Illustrative example of a pile-up. The two events in (a) are distant in time enough for being recognized as two different events by the trigger, while the two events in (b) are overlapped and may cause the triggering algorithm to fail in acknowledging the being two separate events. Events in (c) are simultaneous and perfectly overlapped, making completely impossible to discern them from an event having a pulse height equal to the sum of their pulse heights.

Pile-up is the process by which two detection events happening within a time distance shorter that the preamplifiers processing time cause an overlap of the signals, like the examples reported in figure 4.15. This is an issue since two (or more) overlapping signals are integrated as one by the ADC, resulting in a single event with an E_d equal to the sum of the E_d of the overlapped events. This might not only lead to distortion in the spectroscopy, but also in the number of events counted (since two or more events are registered as one). The phenomenon, which can be safely ignored for low detection rates, becomes an issue when the detection rate r and the formation time of the preamplifier τ_f are such that $r \cdot \tau_f \gtrsim 0.01$; thus, when the time in which the preamplifier is busy processing a signal is about 1% of the total time. For similar and higher rates, the effect of the pile-up gains statistical relevance.

Besides the statistical corrections detailed in section 4.4, two operations were performed to manage pile-up in a direct way: Pulse Shape Discrimination and the Trapezoidal Transform.

Pulse Shape Discrimination

Pulse Shape Discrimination (PSD) allow for the active detection of signals suspected of pile-up and their removal from the data pool. It is implemented by performing a second gate integration using a second, shorter gate, called "short gate", along with the proper gate (which will also be referred to as "long gate" for avoiding misunderstanding). The short gate starts at the same time as the long gate and has a time duration set to be similar to the rise time of the preamplifier, in order for it to end roughly where the maximum of the waveform is. Since the signals shaped by the preamplifier are expected to have always the same shape (only changing in amplitude), it is expected for the ratio between the fixed short and long gate to be always equal. In case of pile-ups like the (b) of figure 4.15, the ratio between long gate integral and short gate integral will be much higher, since the long gate counts the underlying area of both events while the

short gate only measures the first event risetime underlying area. A difference in the ratio allow thus to perform a PSD and discard the event, removing it from the pool of data.

Trapezoidal Transform

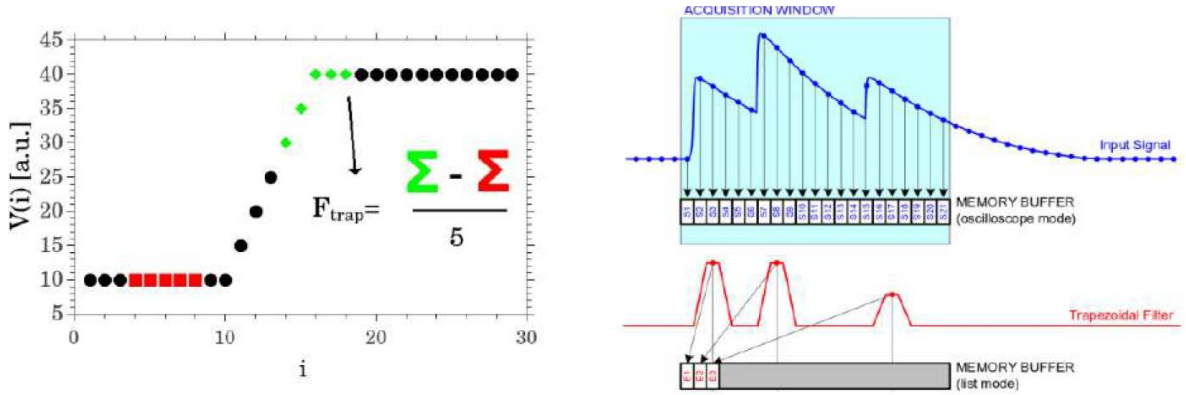

Figure 4.16: Graphical application of a trapezoidal transform. Image courtesy of Carlo Cazzaniga (taken from [67]).

One limit of the PSD is the fact that the signals that are identified as piled-up are discarded, losing data. This is a problem in the context of very high fluxes, like the short fast neutron pulses in pulsed spallation sources like n_ToF (section 4.7.2) or ISIS (section 4.7.3). A second method to process data without losing the piled-up events is the application of a trapezoidal transform, by which the voltage signal $V(t)$ is convolved with a shaping response function $H(t)$ which is characterized by a certain time length T:

$$F(t) = \int_{t-T}^{t} V(\tau) \cdot H(t-\tau)\, d\tau$$

The shaping function establishes an influence of the signal in the past $(t-\tau)$ on the signal at time t; in other words, the trapezoidal function replaces the signal output with a pseudo-derivative of the signal which considers the difference between the signal at time t and the signal in the past at time $t-\tau$. Since the signal is discrete (it is read by the ADC at a certain rate) the trapezoidal filter is implemented as:

$$F(i) = \frac{1}{m}\left[\sum_{j=i-m}^{i} V(j) - \sum_{j=i-m}^{i-L} V(k)\right]$$

The idea behind it is represented in Figure 4.16: the signal value $V(j)$ is replaced with the mean between it and the m-1 points which preceded it, and then the mean of the m points L bins before is subtracted to it. The subtraction makes the transform a differential one, while the mean between the m points is in place to reduce the influence of noise and fast oscillation. For this reason, for the optimal use of the transform L must be choose close to the typical rise time of the preamplifier used (in order to make the transform most sensitive to rises with that kind of timing) and m shorter than L but longer than the typical time of the random noise (in order to smoothen any random oscillation out of the transform).

A practical effect of the trapezoidal transform is reported in figure 4.17. Beyond discriminating piled-up signal without losing them the transform is also able to phase out fast noise and

undershoot effects (failures in reestablishing the baseline value of the signal output after an event). On the other side of the coin, trapezoidal transform is complex, requiring offline operation and, thus, the offline storing of the entirety of the signal windows, which is a very costly endeavour in terms of storing capacity and volume of data processing. As such, this transform was applied only in cases of very high fluxes; nominally, the tests on spallation sources (section 5.1 and section 5.2).

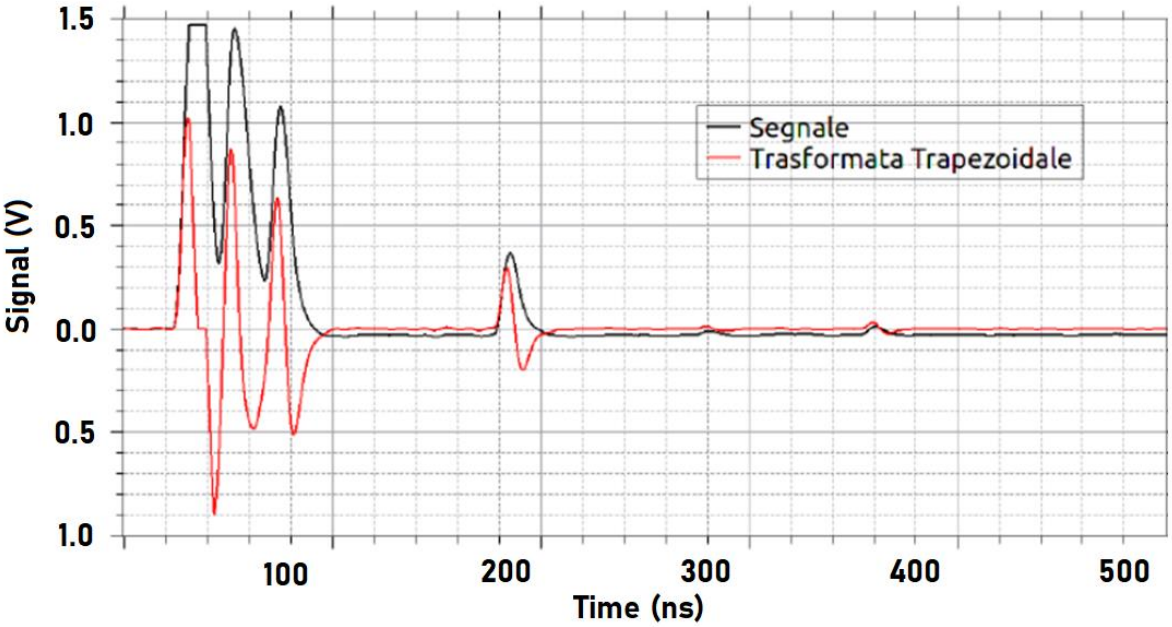

Figure 4.17: comparison between a signal of the SiC-O (in black) and the same signal after a trapezoidal transform with proper parameters is applied (in red). Note how the transformed signal can much more clearly identify and discriminate the three piled-up signal on the left, which would be otherwise be considered a single event if no filter was applied.

4.7 Neutron and Radiation Sources

4.7.1 Americium Source

Figure 4.18: The coin-shaped, ^{241}Am electrodeposited alpha source used in the thesis. The americium is deposited on the lower side, not depicted in the picture.

The most used calibration source in this thesis is a ^{241}Am electrodeposited radioactive source, depicted in figure 4.18. Americium is a synthetic unstable element undergoing alpha decay with a long half-time of 432.2 years, allowing it to be considered an alpha source emitting at a constant rate for typical lab timescales. The alpha particles produced have 5.486 MeV of energy: since the americium is deposited only on the surface of the solid volume, the energy deposited in the solid volume of the source causes a broadening of less than 20 keV [68], so it can be safely approximated the alpha particles to be produced at the same energy.

One factor complicating the irradiation is that alpha particles lose a very significant amount of energy even while travelling through air. In fact, ^{241}Am alpha particles lose between 85 and 230 keV per mm travelled in air and are stopped after 42.4 mm [56]. To know the alpha energy E_α requires an exact determination of the distance between the alpha source and the active volume of the crystal; on the other hand, altering the distance between the alpha source and the active volume allows to modify E_α. These characteristics make the ^{241}Am source the chosen method for the energy calibration of the detector: since E_α is known, $E_d = E_\alpha$ and the signal pulse height is proportional to E_d, it is possible to associate the measured level of pulse height to a certain E_d.

The assumption that alphas deposit the entirety of their energy in the active volume shows limitations when using SiC10s. In fact, 5.486 MeV alphas have a penetration of 26.1 μm in SiC, which is larger than the 10 μm thickness of the active volume: as such, partial deposition effect (see section 3.3.2) can happen even with alpha particles. This was verified during an irradiation with the SiC-C, finding the E_d spectrum featuring two structures: a gaussian peak at lower E_d and a shoulder at higher E_d. The two structures are caused by alpha particles that are emitted from the source perpendicularly and diagonally from the source, respectively: while the former

manage to cross the SiC parallelly to its width and leave the active volume with some leftover energy, the latter incise on the active volume with an angle that increases their path inside the SiC, up to an angle which allow for the total stopping of the particles. This was confirmed by studying the response of the SiC to different alpha energies (obtained through distancing the alpha source), obtaining a translation of the diagonal high-E_d shoulder but not a translation of the perpendicular low-E_d peak, down to the distance in which the two structures unite at the expected E_n for 10 µm penetration.

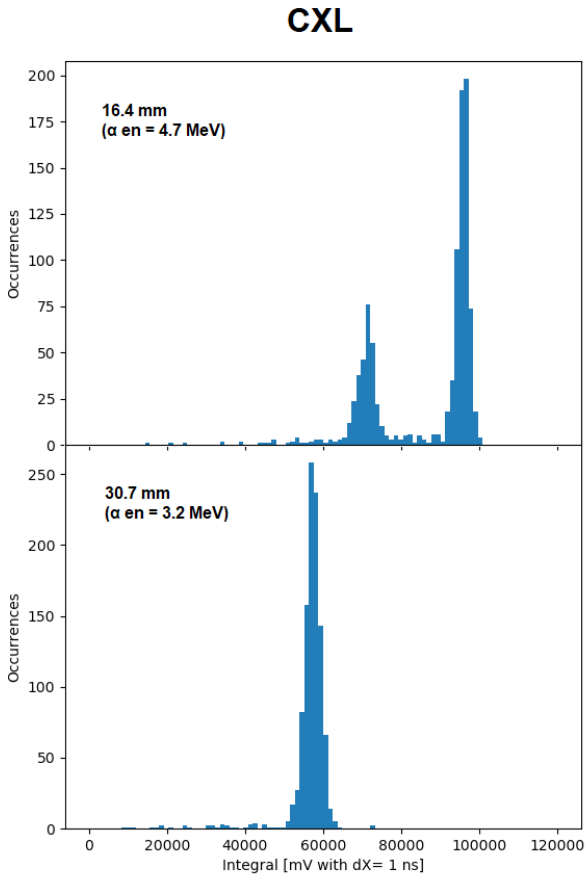

Figure 4.19: E_d spectrum of the SiC-C (section 4.2.2) under irradiation of ^{241}Am alpha particles. In the top figure the alpha particle is at 16.4 mm of distance in air from the active volume, resulting in 4.00 MeV alpha particles whose mean travel path is longer than the thickness of the detector: this generates two structures due to alpha impinging diagonally on the detector (on the right) and alpha impinging perpendicularly to the surface experiencing partial charge deposition (on the left). On the bottom figure the distance is increased to 30.7 mm, causing the alpha to be at 2.30 MeV: since the energy is no longer enough for the alphas to penetrate for more than 10 µm the structure collapse in a single, full-deposition peak.

4.7.2 n_ToF

Figure 4.20: The end of the n_ToF beamline, just before the beam dump (white block on the bottom left) where the detectors were installed during the experiments detailed in section 5.1.

n_ToF is a pulsed neutron source with a ≃200 meters flight path located at CERN, in Geneve (CH). Neutrons are generated through spallation from a 800 MeV proton synchrotron (PS) beam impinging on a target and are then moderated to obtain an ample spectrum of neutrons. Since the proton pulse impinging on the target is very short (≃7 ns [69]), the neutrons are produced almost simultaneously. During the flight path they are separated as a function of their (kinetic) energy and, therefore, reach the target station with a delay that depends on their energy. The facility allows then a unique opportunity to determine the neutron energy E_n from the delay between the PS and the time of arrival, knows as time of flight (ToF):

$$E_n = m_n \cdot \left(\frac{1}{\sqrt{1 - \frac{l^2/ToF^2}{c}}} - 1\right)$$

Where m_n is the neutron mass (expressed in eV), l the flight path (equal to 197.5 meters at the detector's location) and ToF is expressed in nanoseconds. For example, neutrons with E_n = 14

MeV are separated by the neutrons with E_n = 13 MeV by 142.5 nanoseconds, which are well inside the time resolution of the ADC (section 4.6). More information are available on [69].

SiC-O was irradiated at the n_ToF facility, along with two diamonds; the results are detailed in the article reported in section 5.1.

4.7.3 Rotax and ChipIr

Rotax and ChipIr are two beamlines originating from ISIS neutron and muon source located at the STFC Rutherford Appleton Laboratory in Didcot (UK). The source of the neutron is a proton synchrotron beam impinging on a target, producing neutrons and muons on a wide angle that are used by many beamlines. Rotax and Chipir have 15.5 m and 10.5 m flight paths, respectively, that are much shorter than the flight path of n_ToF (see previous section). As such, the separation by ToF is not enough with fast neutron to be able to assess fast neutron E_n from ToF with reasonable precision. The neutron flux for neutron with $E_n > 10$ MeV is $5 \cdot 10^6 \frac{n}{cm \cdot s}$ or more at the Chipir facility [70].

4.7.4 Frascati Neutron Generator (FNG)

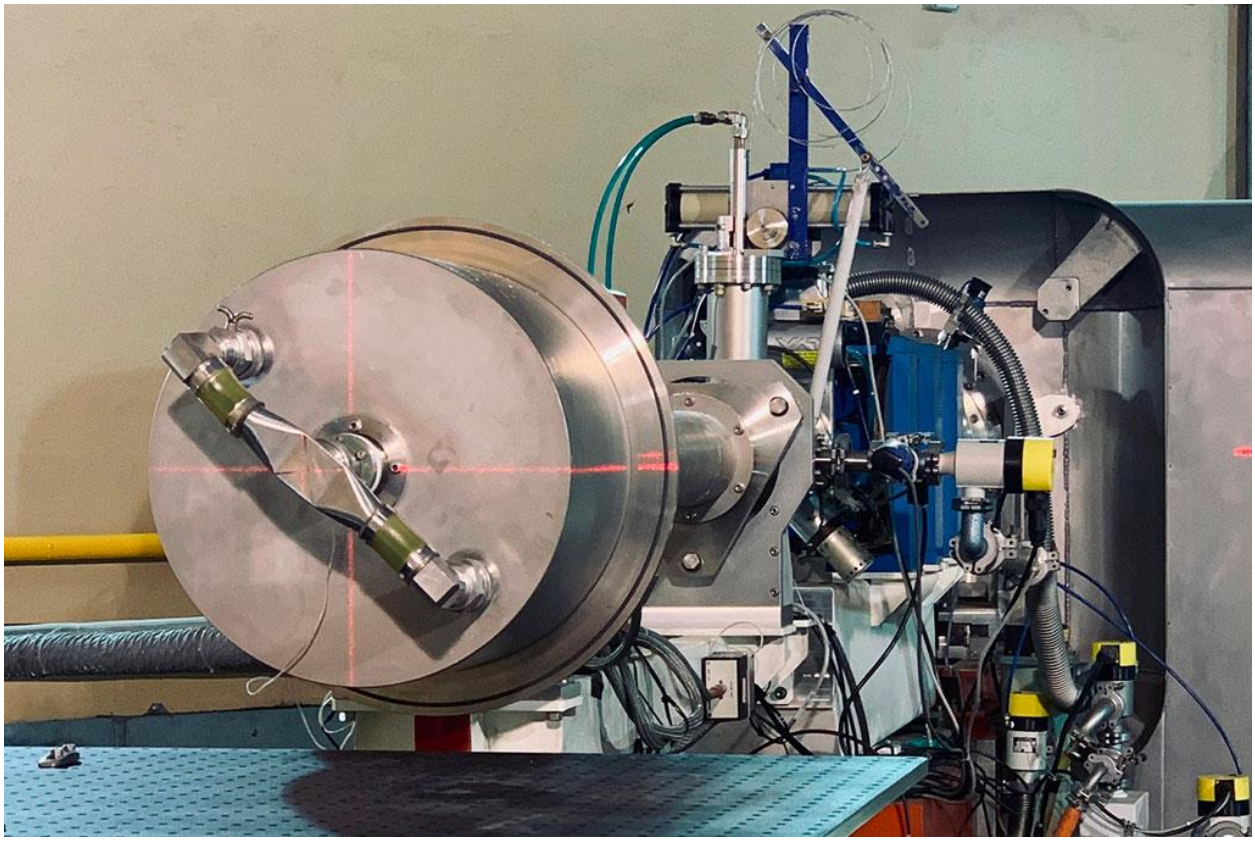

Figure 4.21: FNG deuterium accelerator and target. Image taken from [71]

The Frascati Neutron Generator (FNG) is a neutron source located at the Enea research centre of Frascati, Italy. It consists of a deuterium beam of up to 260 keV impinging on a target of either deuterium or tritium, producing DD or DT neutrons. Due to cinematic reasons the neutrons are produced with energies that depend on the angle, with neutrons moving perpendicularly to the

deuterium beam having exactly 2.45 MeV (DD) and 14.06 MeV (DT), as shown in figure 4.22. More information can be found in [71].

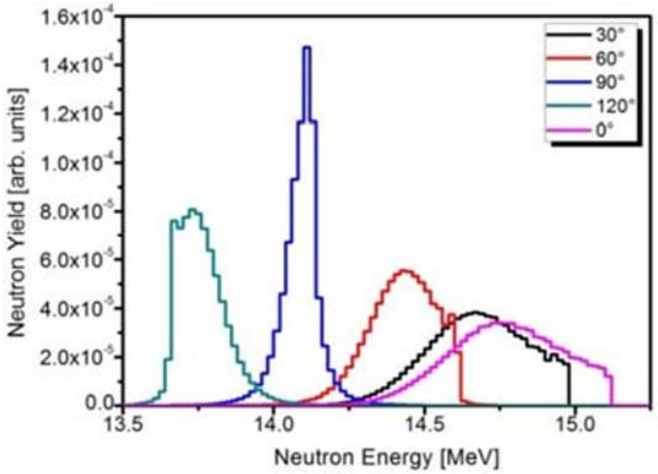

Figure 4.22: FNG neutron spectrum when the tritium target is installed as a function of the angle with the beamline. Image taken from [71].

4.8 Fitting Algorithms

Most data analysis is performed through programs written in the Python programming language (version 3). The library used for fitting is scipy.optimize, with the most used function being curve_fit, which fits a function (defined by the user) to data using a non-linear least squares method [72].

4.8.1 Peaks

As discussed in section 3.3.2, partial charge deposition can cause E_d spectral peaks having tails at lower energy regions, causing their shape to become elongated and asymmetric. This can happen both with neutrons and alpha particles. In order to properly fit those peaks with a gaussian function, a procedure was developed to fit the data prioritizing the data on the higher-energy side of the gaussian:

- The function scipy.optimize.curve_fit is used to fit a gaussian function to the data. The gaussian function is defined as

$$A \cdot \exp\left(-\frac{(x-x_0)^2}{2\sigma^2}\right) + N$$

  Where the amplitude A, the central value x_0 and the standard deviation σ are the three fitting values, optimized by the Python function. N is a fourth parameter used as a baseline, which is usually used only for low-E_d nuclear reaction peaks, while being set equal to zero for alpha irradiations and high-E_d nuclear reaction peaks.

- A subset of data having deposited energy between $x_0 - \frac{\sigma}{2} < E_d < x_0 + 2\sigma$ is selected.

- A new scipy.optimize.curve_fit is performed on the subset of data. The amplitude, central value and standard deviation are fed to the function as first guesses for fitting parameters.

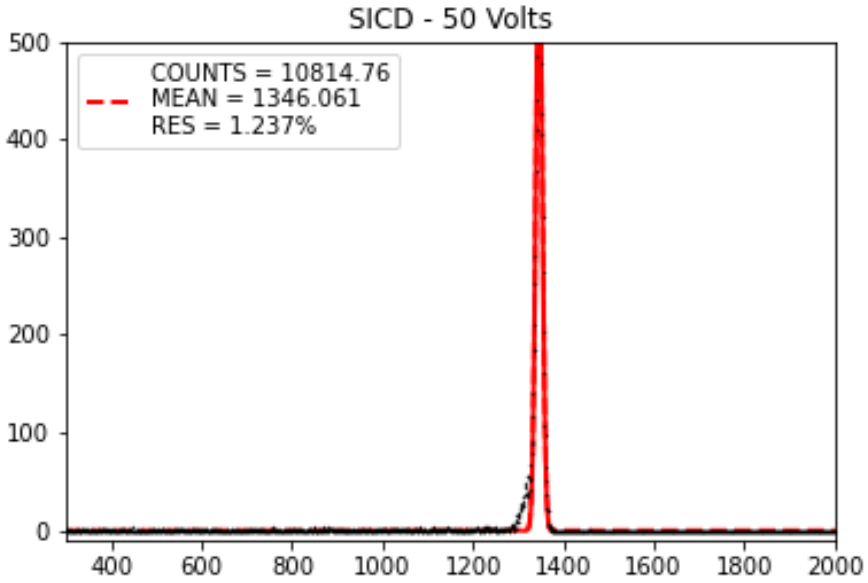

Figure 4.23: Example of an alpha irradiation E_d spectrum fitted asymmetricaly with a gaussian. The asymmetric fit favours the data on the high-E_d end side of the gaussian, giving less weight on the tail at lower E_ds.

4.8.2 Edges

Neutron scatterings and three-body reactions give rise to edge shape on the E_d spectra as opposed to peaks. These shapes can be approximated by a step function convoluted with a gaussian. In order to fit such spectral features a custom function was developed, adding together a step function (with inflection point x_0) smoothened by an error function (with the same standard deviation σ), a gaussian (centred in x_0 as well, with a standard deviation σ) and a baseline value N. The complete function is reported below.

$$\frac{B}{2}\cdot\left(1-\operatorname{erf}\left(\frac{x-x_0}{\sqrt{2}\sigma}\right)\right)+A\cdot\exp\left(-\frac{(x-x_0)^2}{2\sigma^2}\right)+N$$

4.8.3 Fit with Simulated Spectra

During this thesis various many spectra were produced to predict the behaviour of the SiC prototypes. In order to take into account the uncertainties due to the energy resolution (see 2.4.4) an algorithm was developed to simulate the detector broadening. First, the algorithm breaks down the spectra by isolating the value of the x-axis bin, one at a time. The broke down spectrum will be thus a histogram with a single column in x_0 (with height equal to the value $y(x_0)$ of the original spectrum), with the rest of the columns having $y = 0$. Then, each of the single-column histogram will be replaced with a broadened histogram whose columns will be

populated following a gaussian function with $y(x_0)$ amplitude and σ inputted as a factor. By replacing all the histograms for all the x-values with the broadened ones and summing them all together, the broadened spectrum will be obtained.

Since the algorithm took σ as an input factor, it was possible to use the algorithm to fit the spectral data with σ (and, thus, the energy resolution) as a fitting parameter. This was useful to confirm the energy resolution for spectra like the DD spectrum reported in figure 4.24. Figure 3.4, on the other hand, shows a complex application of the simulation fitting, albeit applied to the data from a diamond detector. In both cases amplitude and resolution are obtained by the fit.

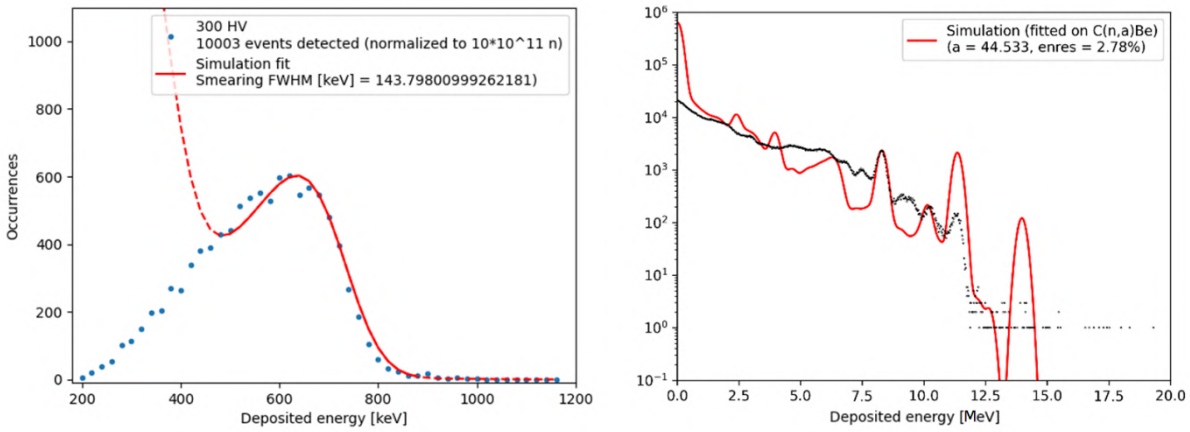

Figure 4.24: Examples of simulations fitting experimental data. On the left the fit is on a DD irradiation, while on the right the fit is on a DT irradiation. Note how the DT simulation overestimates the number of counts at high E_d, possibly due to a underestimation of the nuclear reactions leaving the nuclei in an excited state.

4.9 I-V Characterization

In section 2.4.2 it was explained how SiC detectors should behave like inversely polarized diodes, allowing only a negligible current to flow through the active region of the detector. In section 3.1.2 it was explored how a dark current can hamper the detection, as well as the limits imposed by the leakage currents.

The I/V characterization is a way to explore the diode-like behaviour of the detectors. It is conducted by measuring the current flowing through the detector as a function of the bias induced on its ends while the detector is not under irradiation. The current readout is a Keithly Picoamperometer (see 4.5.3), which serves also as a voltage source. Detectors are connected directly to the picoamperometer without any amplification stage in order to measure the properties of the active volume and its immediate surroundings (substrate, PCB and contacts). Results of the I-V characterization for all the detectors (with the exception of SiC-m) are reported in figure 4.25.

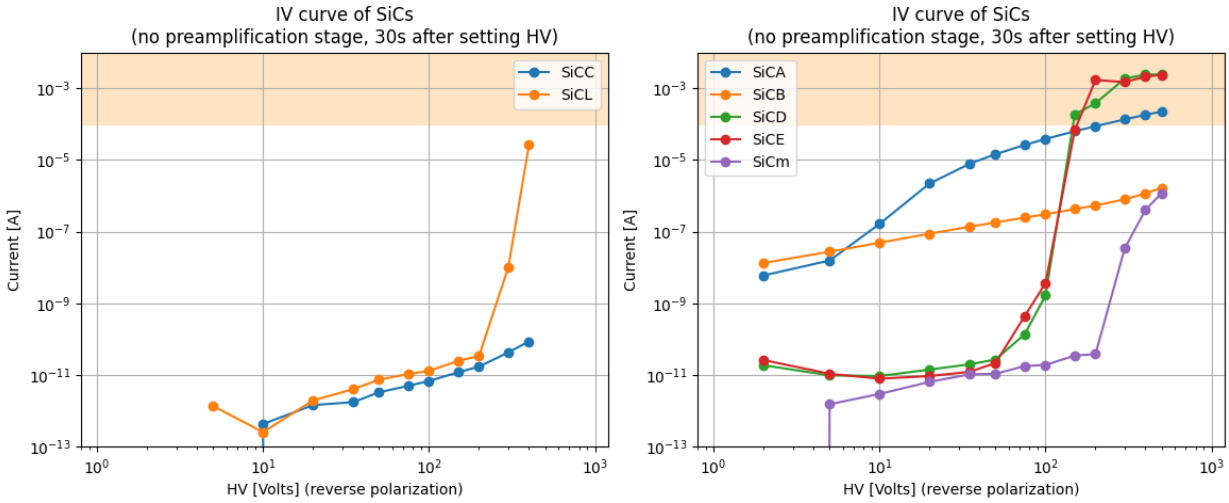

Figure 4.25: I/V curves for almost all the detectors studied in this thesis. The left figure collects the SiC10s, while the right figure the SiC250s. Note how all detectors feature a negligible current up until a threshold voltage, where it increases abruptly due to the ensuing of the leakage current. The twin detectors SiC-A and SiC-B, instead, exhibit a linear increase in the dark current with the bias, demonstrating an ohmic behaviour.

Detectors feature an array of different behaviours, with some notable points in common. All detectors increase their current slowly with the rising voltage input until a voltage threshold is reached. After the threshold the current increases very rapidly, often reaching level in which detection is entirely impossible (highlighted in orange in figure 4.25). This is common to all detectors but the SiC-C, whose high-quality field structure prevent the ensuing of a leakage current for all polarization up to 500V, and the twin detectors SiC-A and SiC-B, which will be discussed below.

4.9.1 Leakage Current

The sudden rise in the current signals the ensuing of a leakage current through the junction, which was reported to happen on the edges of the active volume due to the simple field plate structure (see section 5.4). The voltage threshold differs between different detectors: as an example, SiC-E experiencing the earliest current at 75V, while SiC-m experiencing the latest at 300V. It is common to all detector featuring the field plate technology: this is noteworthy since these detectors differ both in thickness (SiC-L being 10 µm thick while SiC-D, SiC-E and SiC-m being 250 µm thick) and in the type of contacting (SiC-m being a pressure-based SiC, while the others being a welded, PCB-mounted SiCs). It is reasonable to assume that SiC-C not experiencing a leakage current up to 500V being due to its different manufacturing, which proves itself to be more solid in preventing it.

The behaviour of the leakage currents was studied by analysing the current as a function of time, with $t = 0$ being the time at which the voltage was set. Results for the SiC-D under two different bias voltages are depicted in figure 4.26. It is evident that the current tends to decrease exponentially on the minutes time scale; but, especially at higher bias voltages, some processes cause sudden surges in the current which prolongs the current flow in the detector. Such processes prevent the use of these prototypes at HV levels higher than the threshold level.

It must also be noted that the electrical behaviour of the leakage is not fully reproducible: this is apparent if the levels of current for the SiC-D in figure 4.25 for 200V and 300V, which are both higher than 100 µA, are compared to the levels of current at $t = 30$ seconds in figure 4.26, which are around 0.2 µA and 1.1 µA for 200V and 300V respectively. The fact that the two datasets were produced with the same type of apparatus (the Keithley Picoamperometer) in two different experimental conditions suggest that environment has a huge effect in the physics of the leakage. Since the data of figure 4.25 was taken chronologically after the data of figure 4.26, it's also possible that the use of the prototype degraded its ability to prevent the leakage over time, use and irradiation.

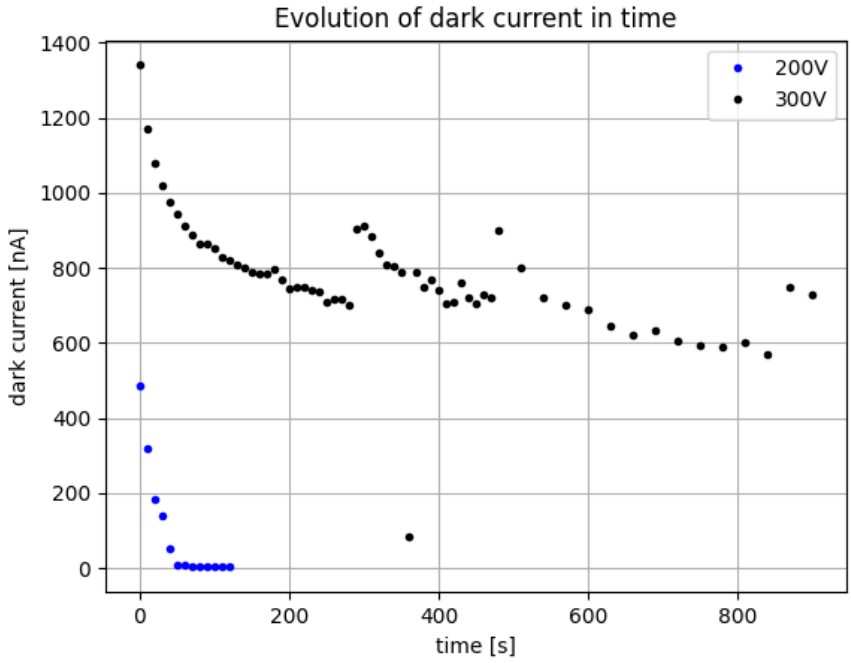

Figure 4.26: Study of the dark current as a function of time after a bias voltage of either 200V or 300V was inserted. The study was performed with a Keithley picoamperometer (see section 4.5.3) and the SiC-D (see 4.2.3) without a reamplifying stage. It is apparent how the current tends to decrease to zero overtime, but some excitations randomly re-ignite it.

4.9.2 Ohmic Behaviour

The twin prototypes SiC-A and SiC-B show a very different I-V behaviour with respect to the other field detector plates. In fact, they feature an ohmic behaviour by which the current rises almost linearly with the increasing voltage (like a resistor). This is proven in both figures 4.24 and 4.27, the latter also shows the SiC-D behaviour as a comparison.

Such ohmic behaviour is unwarranted for three reasons:

- The ohmic behaviour is a symptom of the junction not performing properly and cannot ensure that all the charges produced are collected.
- The ohmic behaviour produces higher levels of currents, which constitutes a baseline source of noise for the detection.

- The behaviour of the active volume as a resistor can form a resistive divider with the impedance of the preamplifier, altering substantially the value of the supplied voltage. This is particularly the case of the SiC-A, whose extrapolated impedance of 2.25 MΩ is even lower than the impedance for the transmission line of the preamplifier (being 5 MΩ).

Nevertheless, SiC-A and SiC-B can perform detection with good properties, as it will be shown in subsequent sections.

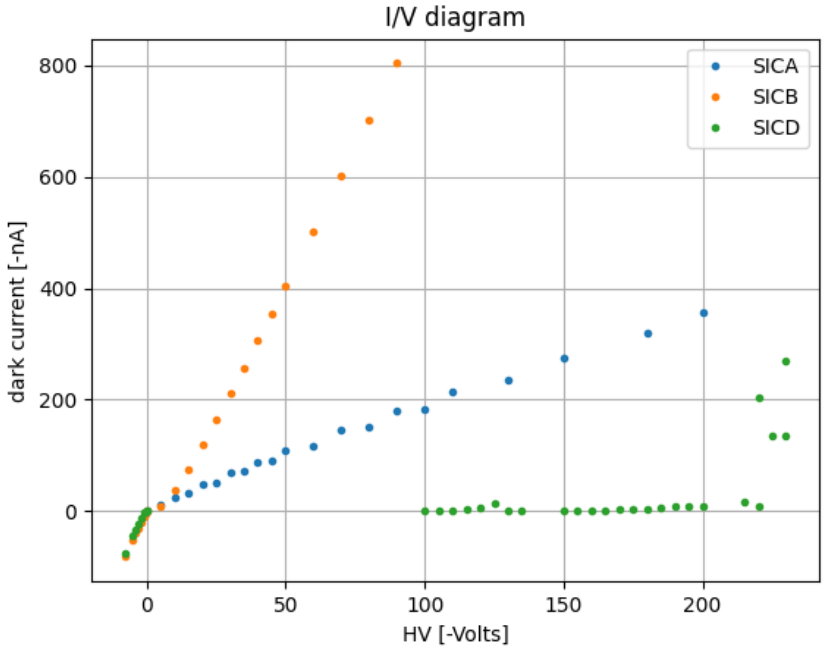

Figure 4.27: I/V curves for the SiC-A and SiC-B, highlighting their ohmic behavior. SiC-D, taken as a reference, features negligible current up to its threshold point instead.

Chapter 5
Results

This chapter shows the results of the research activity through the papers published during the PhD thesis period, sorted in a chronological order. Papers are introduced by a short synopsis that highlights the relevant results of the different characterizations on the SiC detectors.

5.1 Paper 1

Silicon Carbide characterization at the n_TOF spallation source with quasi-monoenergetic fast neutrons

M.H. Kushoro, M. Rebai, M. Dicorato, D. Rigamonti, C. Altana, C. Cazzaniga, G. Croci, G. Gorini, G. Lanzalone, F. La Via, A. Muoio, A. Muraro, F. Murtas, E. Perelli Cippo, M. Tardocchi, M. Barbagallo, F. Mingrone, S. Tudisco for the SICILIA collaboration

Nuclear Instruments and Methods in Physics Research: A
A 983 (2020) 164578

Summary:

The paper describes the irradiation activities performed at n_ToF with the SiC-O. The detector response to neutrons in the energy range between 3 and 20 MeV are presented. Although SiC response to neutrons is more complex than the one obtained with diamonds, the measured energy resolution (FWHM/Ed <4%) makes SiC an interesting alternative to diamond and silicon detectors for fast neutrons.
By selecting the neutron energy by means of the time of flight, the detector response to quasi-mono-energetic neutrons was measured. The main neutron-induced nuclear reactions were identified in the measured pulse height spectrum. Detection efficiency as a function of neutron energy was measured and interpreted based on available neutron cross section and by making use of Monte Carlo simulations.

Nuclear Inst. and Methods in Physics Research, A 983 (2020) 164578

Contents lists available at ScienceDirect

Nuclear Inst. and Methods in Physics Research, A

journal homepage: www.elsevier.com/locate/nima

Silicon Carbide characterization at the n_TOF spallation source with quasi-monoenergetic fast neutrons

M.H. Kushoro [a,b,*], M. Rebai [b,c], M. Dicorato [a,b], D. Rigamonti [b], C. Altana [d], C. Cazzaniga [e], G. Croci [a,c], G. Gorini [a,c], G. Lanzalone [d,f], F. La Via [d,g], A. Muoio [d,g], A. Muraro [b], F. Murtas [h], E. Perelli Cippo [b], M. Tardocchi [b,a], M. Barbagallo [i], F. Mingrone [i], S. Tudisco [d], for the SICILIA collaboration

[a] *Dipartimento di Fisica, "G. Occhialini", Università di Milano-Bicocca, Milano, Italy*
[b] *Istituto per la Scienza e Tecnologia dei Plasmi, CNR, via Cozzi 53, 20125 Milano, Italy*
[c] *INFN sezione di Milano-Bicocca, Milano, Italy*
[d] *Istituto Nazionale di Fisica Nucleare (INFN), Laboratori Nazionali del Sud (LNS), Via S. Sofia 62, 95123 Catania, Italy*
[e] *ISIS Facility, UKRI-STFC, Rutherford Appleton Laboratory, Didcot, OX110 QX, UK*
[f] *Università degli Studi di Enna "Kore", Enna, Italy*
[g] *Institute for Microelectronics and Microsystems, Consiglio Nazionale delle Ricerche VIII Strada, 5, 95121 Catania, Italy*
[h] *Istituto Nazionale di Fisica Nucleare, Laboratori Nazionali di Frascati, Frascati 0044, Italy*
[i] *European Organization for Nuclear Research (CERN), Switzerland*

ABSTRACT

Silicon Carbide (SiC) is a relatively new entry in the world of solid-state detectors. Although SiC response to neutrons is more complex than the one obtained with diamonds, the measured energy resolution (FWHM/E_d<4%) makes SiC an interesting alternative to diamond and silicon detectors for fast neutrons. The results obtained from the measurements of the response of a 100 μm thick SiC detector to neutrons in the energy range between 3 and 20 MeV at the n_TOF spallation source at CERN are presented in this paper.

By selecting the neutron energy by means of the time of flight, the detector response to quasi-mono-energetic neutrons was measured. The main neutron-induced nuclear reactions were identified in the measured pulse height spectrum. Detection efficiency as a function of neutron energy was measured and interpreted based on available neutron cross section and by making use of Monte Carlo simulations.

1. Introduction

There is currently a growing interest in wide band-gap Solid State Detectors (SSDs) for high neutron flux applications, such as thermonuclear fusion machines or spallation sources [1,2] but also for fundamental nuclear astrophysics studies [3–5]. SSDs combine a fast response-time with spectroscopic capabilities, making them an interesting solution for measuring and monitoring the high neutron fluxes of those environments. SSDs have small dimensions (in the range of few millimetres), which is ideal for spallation sources beamlines, allowing for local neutron flux measurements in the proximity of the sample position [6]. It is also ideal for fusion environments, as the small size simplifies their integration in neutron cameras for the spatial reconstruction of the plasma profile [7].

The working principle of the fast neutron detection with SSDs involves neutron interacting on a nucleus of the active volume, which is a semiconductor lattice on which a reverse bias is applied [8]. The neutron can interact either via elastic or inelastic scattering on a nucleus (which is displaced by the recoil, becoming a moving charged particle) or by triggering a nuclear reaction (which generates one or more charged products). The charged products, or the recoiling atoms, deposit energy in the lattice and then promote electrons to the conduction band.

If no one of these charged products leaves the active volume (*i.e.* there is no wall-effect [9]), the number of electrons promoted is proportional to the energy of the charged products. Spectroscopic information can be derived if all the charge carriers are collected and if the relationship between the incident neutron energy, E_n, and the deposited energy, E_d, is known.

Diamond detectors have been characterized in the past [10–12] and they are currently installed at the ChipIR beamline at ISIS as beam monitors [13,14]. They are also installed at the JET tokamak as neutron spectrometers [15]. In fact, it has been shown that single-crystal diamond detectors can be used as excellent spectrometers for 14 MeV neutrons [16,17] even if they feature several different competing reaction channels, which complicate the spectroscopy. In addition to this, it has been shown that spectroscopy, although with a moderate

* Corresponding author at: Dipartimento di Fisica, "G. Occhialini", Università di Milano-Bicocca, Milano, Italy.
E-mail address: m.kushoro@campus.unimib.it (M.H. Kushoro).

https://doi.org/10.1016/j.nima.2020.164578
Received 3 June 2020; Received in revised form 2 August 2020; Accepted 19 August 2020
Available online 24 August 2020
0168-9002/

energy resolution, can still be performed with 2.5 MeV neutrons [18,19]. However, several studies [20–22] show that diamond detectors suffer from a temporary drop of the count rate after irradiation (~20% less counts after about 10^6 *neutrons*/mm^2) due to partial charge carriers trapping; counteracting this phenomenon requires a periodic inversion of the bias voltage in order to restore the detector properties [1].

A prospected alternative to single-crystal diamonds are Silicon Carbide detectors (SiC) which share with the diamonds a wide bandgap (3.25 eV), compact dimensions [23] and an excellent radiation hardness (was found able to withstand γ-ray exposures of >500 R/h and thermal neutron fluxes of 5000 n/cm^2 s) [24]. It has been observed that SiCs show a good stability under temperature variation even at high temperatures, which is critical for fusion machine environments [8]. On the other hand, the presence of both Silicon and Carbon in the lattice structure further complicates the spectroscopic response of the detector, introducing more reaction channels through which the incident neutron might be detected [2,8], each of which has a different E_n to E_d relationship.

In this work, the response of the SiC used in [2] has been measured at the neutron Time Of Flight (n_TOF) facility at CERN [25] to a larger span of neutron energies (E_n > 1 MeV), with a peculiar focus on the energies between 5 and 15 MeV.

The paper is organized as follows: first, the detector, together with the experimental set-up and the n_TOF facility, will be described (Section 2). Results will be presented and discussed in Sections 3 and 4 respectively. Finally, conclusions and prospects will be drawn in Section 5.

2. Experiment description

2.1. The Silicon Carbide detector and related electronics

The Silicon Carbide detector (SiC) used in these measurements was designed and manufactured at Istituto di Microelettronica e Microsistemi of the Italian National Research Council (IMM-CNR) within the SiCILIA collaboration [26,27]. Although the main goal of SiCILIA was the NUMEN project [28] (which focuses on the detection and identification of heavy ions [29]), the prototypes developed within the collaboration were also successfully tested for other application, like photons [30] and neutrons [2].

The device used in this work is made of a 2 × 2 grid of 5 mm × 5 mm independent active volumes of Silicon Carbide, grown from epitaxial layers on four inch 4H-SiC wafers by means of a CVD (Chemical Vapour Deposition) process. The four volumes were grown on the same substrate (see Fig. 1a). Each pixel is an extrinsic diode made by a 0.3 μm thick p-layer with a doping concentration of Aluminium $N_A = 10^{19}$ cm^{-3} and a 100 μm thick n-layer with a doping concentration of Nitrogen, $N_{N,}$ between 8*10^{13} cm^{-3} and 10^{14} cm^{-3}. The precursors used for the doping were molecular Nitrogen (N_2) for n-type doping and Trimethylaluminium TMA ($Al_2(CH_3)_6$) for p-type doping [26]. The SiC substrate was reduced by a mechanical process from the backside. The ohmic contact has been formed by a titanium/nickel/gold deposition. Several photolithographic steps and etchings by an Inductive Coupled Plasma (ICP) were performed for the definition of the detector area, edge structures and contacts [2]. More details about the detector can be found in [2] and in [26].

The detector is mounted in an aluminium casing for electromagnetic shielding. It is connected to a CIVIDEC CX-L spectroscopic preamplifier [31], which was customized in order to work on a negative polarity. The preamplifier shapes the signal from the detector into a quasi-Gaussian shape, the integral of which is directly proportional to the number of charges collected. This gives a better energy resolution when compared to the C6 preamplifier used in [32] at the expense of a longer shaping time (280 ns full width). The CX-L preamplifier was also chosen in order to match the detector's impedance and it was customized to convey a negative bias to the detector. The bias to the detector (through the preamplifier circuit) was supplied by an ISEG type EBS 8005 HV generator. A negative bias voltage of 200 V was chosen to fully deplete the detector volume without inducing any discharges [2,26]. With such a bias voltage the drift time can be derived as in [33], as:

$$\tau_{drift} = \frac{D}{\mu_0 E_D}\left(1 + \frac{\mu_0 E_D}{v_{sat}}\right) = 1.125 \text{ ns} \quad (1)$$

where the layer depletion depth is D = 100 μm, μ_0 = 800 $\frac{\text{cm}^2}{\text{V s}}$ [26], the drift field $E_D = 2 \cdot 10^6 \frac{\text{V}}{\text{m}}$ [34] and the saturation current $v_{sat} = 2 \cdot 10^7 \frac{\text{cm}}{\text{s}}$ [26]. As such, the upper limit of the count rate is entirely dominated by the 280 ns preamplifier shaping time.

The shaped signal was then sampled by an 8-channel, 14-bit, 500 MHz sampling rate waveform CAEN DT5730 digitizer [35] which stores it on the PC. Two dedicated custom-made C++ and Python codes were then used to process the data off-line.

2.2. n_TOF experiment

The SiC detector was installed at the beam dump position of the first beam line of the neutron Time of Flight (n_TOF) facility at CERN (Geneva, Switzerland), as shown in Fig. 1b–c. n_TOF is a pulsed neutron source where neutrons are generated through spallation processes by the pulsed Proton Synchrotron (PS) beam colliding on a massive lead target. Neutrons are then moderated first by the lead target and then by water in order to produce a wide spectrum of energies: from ultrafast neutrons (~GeV) to thermal neutrons. Thanks to the pulsed operation (about 0.8 Hz with a proton pulse width of about 7 ns r.m.s.) and the long flight path between the target and the first experimental area (l = 197.5 m) it is possible to derive the incident neutron energy (E_n) through the Time of Flight (ToF) technique by applying the simple equation:

$$E_n\,[\text{eV}] = m_n\,[\text{eV}] \cdot \left(\frac{1}{\sqrt{1 - \frac{\frac{l^2}{ToF^2}}{c}}} - 1\right) \quad (2)$$

where m_n is the neutron rest mass and ToF is expressed in nanoseconds.

By selecting the subsets of detected events in a certain range of ToF (*i.e.* in a range of neutron energies) the detector response to quasi-monochromatic neutrons can be obtained. A seven weeks data collection time was chosen in order to get enough statistics for all fast neutron energies.

An example of a waveform acquired at n_TOF is shown in Fig. 2. The detector output is stored by the digitizer in coincidence with the machine trigger, which is related to the timing of the PS protons colliding with the target. At the beginning of every waveform the detector displays a saturated pulse, placed at about 10 500 ns. These pulses are caused by γ-rays and other high-energy particles with ToF indistinguishable from γ-rays (fast electrons, pions and ultra-fast neutrons) which arrive on the detector within the preamplifier shaping time (τ_s = 280 ns) after the γ-rays. These events, referred as "γ-flash", have been used for the ToF calibration, knowing that their ToF equals 658 ns for the 197.5 m flight path at the speed of light c. They were used in order to avoid uncertainties of the machine trigger signal delay.

The γ-flash is followed by many events piled-up to it, as the high-energy instant rate was greater than the inverse of the preamplifier shaping time. Due to this reason, the detector's response saturated for all neutrons with energy >20 MeV, which correspond to a ToF of 2.5 μs. This imposes an upper limit to the range of neutron energy detected. The lower limit of 0.6 MeV is imposed by choice of the length of the acquisition window (18 μs after the $\gamma - flash$).

All the events in the time window between 2.5 and 18 μs after the $\gamma - flash$ have been analysed by a custom-made software in order to extract the arrival time of the event and the pulse height. E_n was then derived from the arrival time through Eq. (2) and E_d was derived from the pulse height. Events are detected through a trapezoidal trigger; that is, the software detects an event when the value of a quasi-derivative

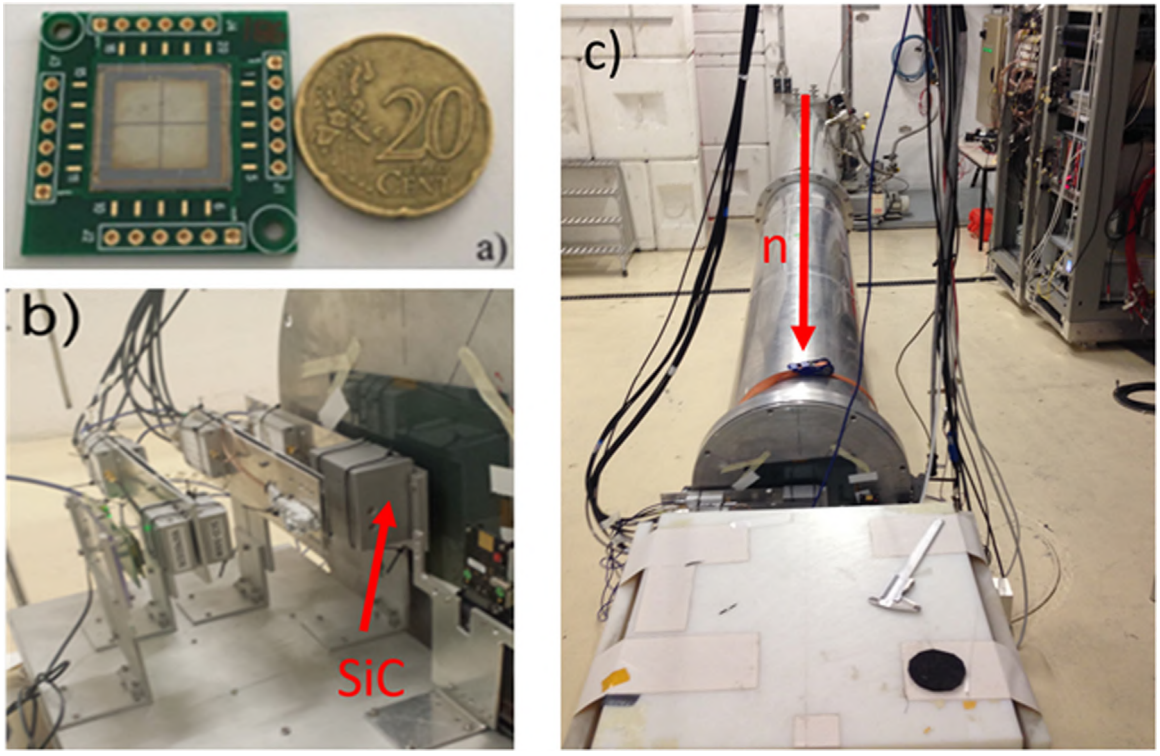

Fig. 1. The 2 × 2 pixels SiC detector (a) housed in an aluminium casing has been installed at the beam dump position (b) at the n_TOF facility (c). (For interpretation of the references to colour in this figure legend, the reader is referred to the web version of this article.)

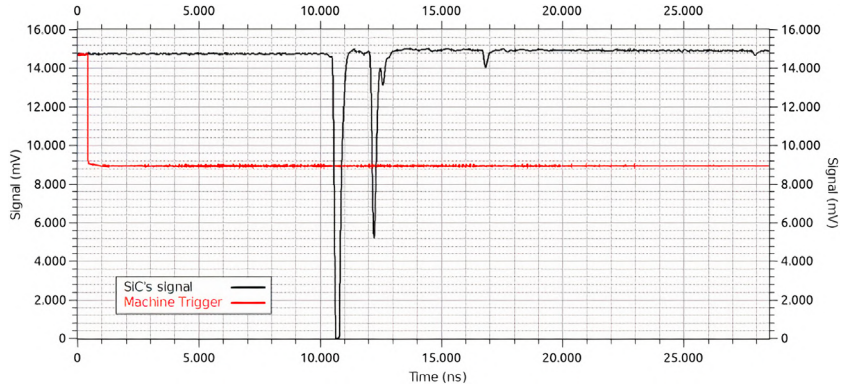

Fig. 2. A waveform example of the SiC output (black) acquired in coincidence with the machine trigger (red). t_0 = 0 ns corresponds to the digitizer pre-trigger on the machine trigger of about 500 ns. (For interpretation of the references to colour in this figure legend, the reader is referred to the web version of this article.)

$f(t)$ of the signal $F(t)$ exceed a certain threshold value. The quasi-derivative is obtained by replacing the signal $F(t)$ with the difference $f(t) = F(t) - F(t - L)$, where L is a time constant close to the typical rise time of the signals. Before operating the quasi-derivation, every $F(t)$ data is also averaged over an interval G, in order to reduce the influence of fast electronic noise. The trapezoidal trigger allows the event identification to be more sensitive to shapes with rise times close to L, thus allowing us to consider events piled-up during the decay time or events affected by undershoot. The information on the number of collected charges is carried on in the form of the height of the transformed shape. The two parameter L and G chosen were 100 ns (∼signal rise time) and 10 ns (≪ signal shaping time) respectively. More details on data treatment can be found in [34,36].

3. Results

Every reconstructed event is plotted as a point on the 2-D density plot (Fig. 3a), where on the X-axis the ToF is in μs (E_n is also reported for reader convenience) and on the Y-axis E_d is in MeV. Here we briefly recall that the ToF is directly related to E_n, while E_d is dependent on the (random) reaction that caused the count into the detector. Peculiar trails, highlighted in red in Fig. 3b, emerge from the density-plot. Each one of those is the effect of a specific nuclear reaction by which a neutron can deposit an amount of energy $E_d = E_n - Q_v$, where Q_v is the reaction's Q-value. Based on the fitted Q_v, the trails were identified as the reactions:

(**A**) $^{29}\mathrm{Si}(n,\alpha)^{26}\mathrm{Mg}$

(**B**) $^{28}\mathrm{Si}(n,\alpha)^{25}\mathrm{Mg}$

(**C**) $^{28}\mathrm{Si}(n,p)^{28}\mathrm{Al}$

(**D**) $^{12}\mathrm{C}(n,\alpha)^{9}\mathrm{Be}$

The two additional trails **(E)** and **(F)**, highlighted in grey in Fig. 3b, represent the loci of the maximum E_d that can be deposited in the detector through an elastic scattering on carbon and silicon respectively. The value of this energy is $E_{d,max} = a \cdot E_n$., where a depends on atomic

mass of the recoiling atom A as $a = \frac{4A}{(1+A)^2}$. Being that the coefficient a is equal to 0.284 for ^{12}C and 0.133 for ^{28}Si, the position of the deposited energy via a head-on scattering on Carbon occurs at higher deposited energies with respect to the ones occurring on Silicon.

Some low-amplitude events appear with a ToF lower than the γ-flash ToF: as the presence of these events was known beforehand as a result of not physics-related events, they have been omitted from the analysis.

The reactions identified by the trails in Fig. 3 are apparent as a peak when considering quasi-monochromatic subsets; that is, considering the projection on the Y-axis of a subset of the density plot within a 1% neighbourhood of a given ToF. In Fig. 4 projections on the deposited energy axis are reported for a set of different neutron energies, as an example. The two-body nuclear reactions, highlighted with red lines in Fig. 3, are fitted with a Gaussian function centred at E_d (*panels I–IV)*. The broadening of these peaks gives the energy resolution while the integral gives the number of events occurred through that specific reaction. Thanks to the fact that in such reactions E_d is directly related to neutron energy ($E_d = E_n - Q_v$), it can be seen in Fig. 4 (*panels I–IV)* that the peaks from ^{12}C(n, α)^{9}Be and ^{28}Si(n, α)^{25}Mg move to higher deposited energies linearly with the increasing of the neutron energy. As an example, for the case of (n, α) reaction on Carbon (for which $Q_v = 5.7$ MeV) the peak position moves from $E_d = 3.3$ MeV for $E_n = 9$ MeV to $E_d = 4.3$ MeV for $E_n = 10$ MeV and to $E_d = 8.3$ MeV for $E_n = 14$ MeV. At lower E_d the two body reactions are under-threshold and the pulse height spectrum is mainly due elastic scattering reactions (*panels V–VI)*.

As stated before, when considering the elastic scattering on ^{12}C or on ^{28}Si, a continuum of energies can be transferred to the crystal, with the maximum deposited energy $E_{d,max}$ proportional to E_n. This means that for a specific neutron energy a continuum of deposited energy up to $E_{d,max}$ can be seen observed in the pulse spectra. This give rise to the edges placed at $E_{d,max} = 0.284 \cdot E_n$, of which two examples are shown in Fig. 4 (*panels V and VI)*. In order to assess the edge position and the broadening due to detector energy resolution the edges are fitted with a step function convoluted with a Gaussian. As an example, in the pulse height spectra obtained with neutrons of 4 MeV and 4.5 MeV, the edge position is $E_{d,max} = 1.14$ MeV and $E_{d,max} = 1.27$ MeV respectively.

4. Data analysis

The neutron detection efficiency (defined as the ratio between number of detected events over the number of neutrons incident onto the detector) is a parameter that is difficult to measure because of the uncertainties on incoming neutron flux at the detector position. Nonetheless, a precise efficiency value is necessary to characterize the detector as a neutron counter, because it is the way to obtain the absolute number of incident neutrons. It is also important to know the detection efficiency in order to understand the range of neutron fluxes in which the detector can operate before being saturated by pile-up events.

4.1. Efficiency (vs.) cross section

The measurement of detector efficiency as a function of E_n is obtained by dividing the number of detected events above a certain E_d threshold by the number of neutrons produced by the PS beam. For this analysis the values of E_n are taken within a bin width of 1%, while the threshold value is set to 1.2 MeV for comparison with data obtained at FNG [2]. The number of impinging neutrons, derived from the PS proton current, is obtained from the n_TOF machine log file. It is reduced by a geometrical factor ε_G (Table 1), which is defined as the ratio between the larger beam cross-section area and the surface area of the detector. This factor accounts for the fraction of beam neutrons which did not intercept the volume of the detector; it does not account for any loss of neutrons along the pipeline (it should be noted that the detector was installed in the beam dump area, which is further down the line from where the neutron flux is determined) nor the radial inhomogeneity of the beam density. As such, the estimated number of impinging neutrons at the test position suffers from large uncertainty, which propagates to the efficiency value. In order to compensate those errors, the efficiency is rescaled by the correction factor $f_{C_{FNG}}$, obtaining the black dots in Fig. 5. The factor $f_{C_{FNG}}$ (Table 1) is obtained by rescaling the efficiency value measured at n_TOF at $E_n = 14$ MeV to the efficiency measured during the FNG experiment [2] (blue dot). Since the absolute neutron yield in FNG is well-known [37], the efficiency measured there is considered as very reliable. The same rescaling factor is then applied to the efficiency of every energy, under the assumption that the factor $f_{C_{FNG}}$ does not depend on E_n.

The rescaled efficiency is then compared to the theoretical efficiency ε_{χ_s} (red dashed line in Fig. 5), obtained as:

$$\varepsilon_{\chi_s} = \frac{N_{Av} \cdot \rho}{A} \cdot z \cdot \varepsilon_G \cdot \sigma(E) \cdot f_{CFNG} \tag{3}$$

where N_{Av} is the Avogadro's Number, ρ the SiC density, A its atomic mass, and z the detector thickness. The total neutron cross section $\sigma(E)$ is calculated averaging the total cross sections of ^{12}C and ^{28}Si obtained from [38], obtaining, as a reference, a value of $\sigma(14\text{ MeV}) = 1.5284$ barn. ε_G is the geometrical factor described earlier, modified by the rescaling factor f_{CFNG} discussed above. The values of the coefficients and the obtained efficiency are displayed in Table 1.

ε_{χ_s} is in good agreement with experimental data only at high energies (i.e. more than about 14 MeV), while it progressively overestimates the data when moving towards lower energies. For example, the ratio between ε_{χ_s} and the rescaled CERN efficiency is 1.17 at $E_n = 16$ MeV, while it increases to 1.538 at $E_n = 10$ MeV, to 2.368 at $E_n = 8$ MeV and to 6.326 at $E_n = 6$ MeV. This is the effect of the threshold: in fact, as E_n increases, the fraction of events whose E_d is lower than 1.2 MeV becomes negligible. For $E_n < 7$ MeV the spectra are increasingly dominated by scattering reactions; therefore, a greater fraction of events falls below the threshold of $E_d = 1.2$ MeV as E_n decreases. As an example, at $E_n = 4$ MeV, the spectrum is entirely dominated by elastic scattering and the maximum energy that can be deposited is $E_d = 0.28 \cdot 4\text{ MeV} = 1.12$ MeV. For this reason, a dedicated GEANT4 simulation has been performed to take into account this effect.

About $5 \cdot 10^8$ neutrons of 11 different energies between 3 and 14 MeV were fired upon the SiC detector. The simulation replicates the trajectories of the interacting particles inside the detector and factorizes in the natural isotopic abundance of the species of C and Si. A low threshold of $E_d = 1.2$ MeV was applied to the result, in order to uniform the simulation data to the beamline data. Simulated results (green in Fig. 5) slightly overestimates the measured values at every energy of about 20% (for example, $\frac{\varepsilon_{sim}}{\varepsilon_{CERN}}(14\text{ MeV}) = \frac{6.52 \cdot 10^{-4}}{5.53 \cdot 10^{-4}} = 1.179$, which corresponds to a 17.9% overestimation). This overestimation was already present at FNG [2]; it could be due to border effects, such as wall effect, or could be due to good events which are either mistaken for noise by the trapezoidal trigger or which are omitted by the threshold. Since both simulation and theoretical prediction reproduce the pattern of the data, the results are deemed satisfactory.

The discrepancy between the data and the prediction suggests that, if a more generic value for the efficiency is needed for the energies lower than 14 MeV, a lower cut should be chosen. The downside of this approach is that reducing the threshold enhances the electronic noise. This is especially true for the set-up used at CERN, which often saturated the output, generating ample electronic oscillations which would result in many false positives. A reduction of the threshold should be accompanied by a choice of a pre-amplifier ensuring a good signal/noise ratio and a gain not so high to saturate the digitizer scale.

A second possible approach for obtaining a reference for the efficiency without lowering the cut is to consider only events occurred through specific nuclear reaction events, thus ignoring all scatterings altogether. The downside of this approach is that is not applicable for the lower neutron energies ($E_n < 6$ MeV), as no relevant nuclear reaction is available for those E_n.

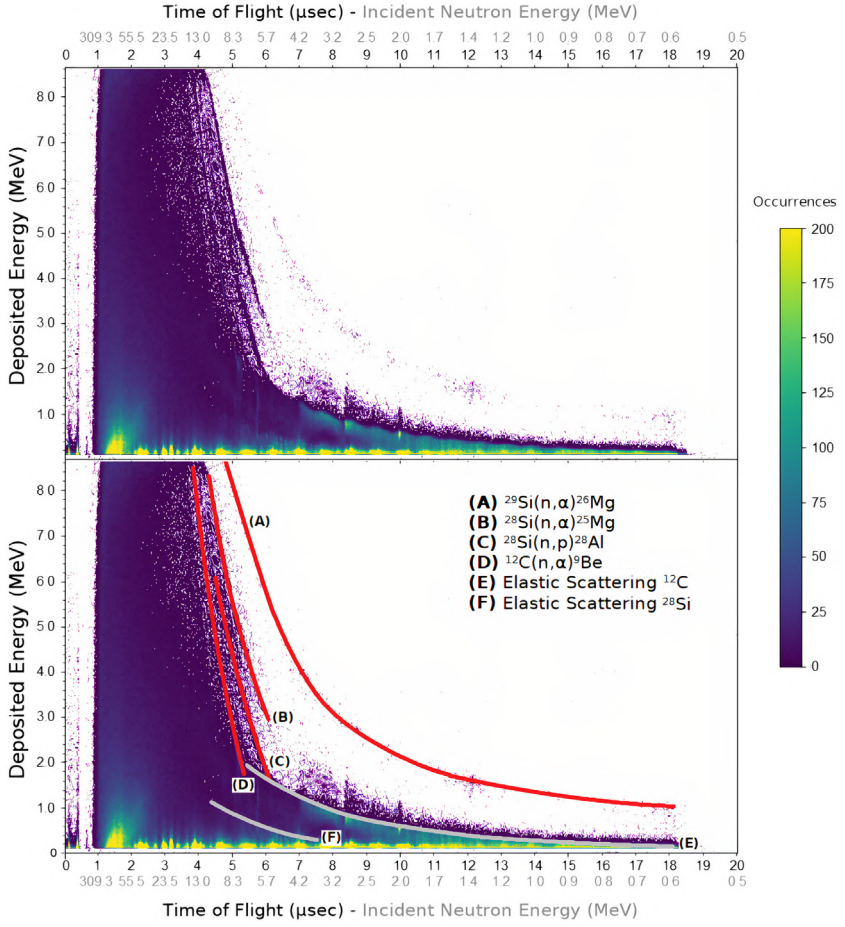

Fig. 3. Event density plot, featuring every detected neutron as a point in ToF (i.e. E_n) vs. E_d plane: red trails identify two-body nuclear reactions, grey lines identifies the maximum energy that can be deposited in the detector via elastic scattering. (For interpretation of the references to colour in this figure legend, the reader is referred to the web version of this article.)

Table 1
Correction factors and coefficients for the efficiency.

Correction factors	
$\epsilon_G = \frac{A_{beam}}{A_{SiC}}$	60.95
$f_{C_{FNG}} = \frac{\epsilon_{CERN}}{\epsilon_{FNG}}$	0.379
$f_{C_{fit}}$	0.24
14 MeV efficiencies	
$\epsilon_{CERN} = \frac{n_{events}}{n_{neut}} \cdot \epsilon_G$	$1.867 \cdot 10^{-3}$
ϵ_{sim}	$6.496 \cdot 10^{-4}$
ϵ_{FNG}	$(5.69 \pm 0.78) \cdot 10^{-4}$
ϵ_{χ_s}	$6.295 \cdot 10^{-4}$

4.2. Single channel efficiency

There are some advantages in considering the efficiency of the single nuclear reactions instead of the overall one. The first advantage is that the measure is independent from the threshold value, as the energy deposited though a nuclear reaction corresponds to a precise value of E_d, which is either higher or lesser than the threshold. This is not the case of scattering, where the range of E_d spans from $E_d = 0$ to $E_d = A \cdot E_n$, so that a fraction of events is under threshold anyway.

Another advantage is that the nuclear reaction peaks in the E_d spectra (Fig. 4) have more isolated and distinct structures than the low energy scattering shoulders for high E_n, allowing for a more precise identification. This is especially important for spectroscopic measurements, as the structure of a handful of non-overlapping peaks is far easier to deconvolute than the convoluted structure of peaks and shoulders in the low amplitude region.

The E_d spectra (Fig. 4) allow to count how many events occurred through any specific reaction channel (if the shape of the peaks is discernible) by integrating the appropriate peak. This allows to compare the efficiency of a single reaction channel to the theoretical estimate, obtained just like for the total one (Eq. (3)):

$$\epsilon_{\chi_{reaction}} = \frac{N_{Av} \cdot \rho}{A} \cdot z \cdot \epsilon_G \cdot \sigma_{channel}(E) \cdot f_{CFNG} \tag{4}$$

The difference being $\sigma_{channel}(E)$, which is the cross section of the specific nuclear reaction, has replaced the total atomic cross-section $\sigma(E)$. The correction factor $f_{C_{FNG}}$ used is the one obtained through FNG data.

The comparison of the two best-fitting peaks, $^{12}C(n,\alpha)^9Be$ and $^{28}Si(n,\alpha)^{25}Mg$, is shown in the top two images of Fig. 6. The data follow the complex pattern of the cross section, displaying a good adherence with the data; although, the prediction again slightly overestimates all the values. A second comparison for the same peaks is displayed in the two bottom images, where $f_{C_{FNG}}$ is replaced by $f_{C_{fit}}$ (see Table 1), which is the value obtained by the simultaneous χ^2 minimization routine operated on both $^{12}C(n,\alpha)^9Be$ and $^{28}Si(n,\alpha)^{25}Mg$ data simultaneously.

The fact that the overestimation of the prediction is rather constant for all energies suggests the source of the discrepancy to be a systematic error. A cause of this can be that the number of counts in Fig. 4 is underestimated, possibly because the subtraction of the baseline excludes correct data along with background ones. A physical cause, on the other hand, could be the loss of energy through wall-effect,

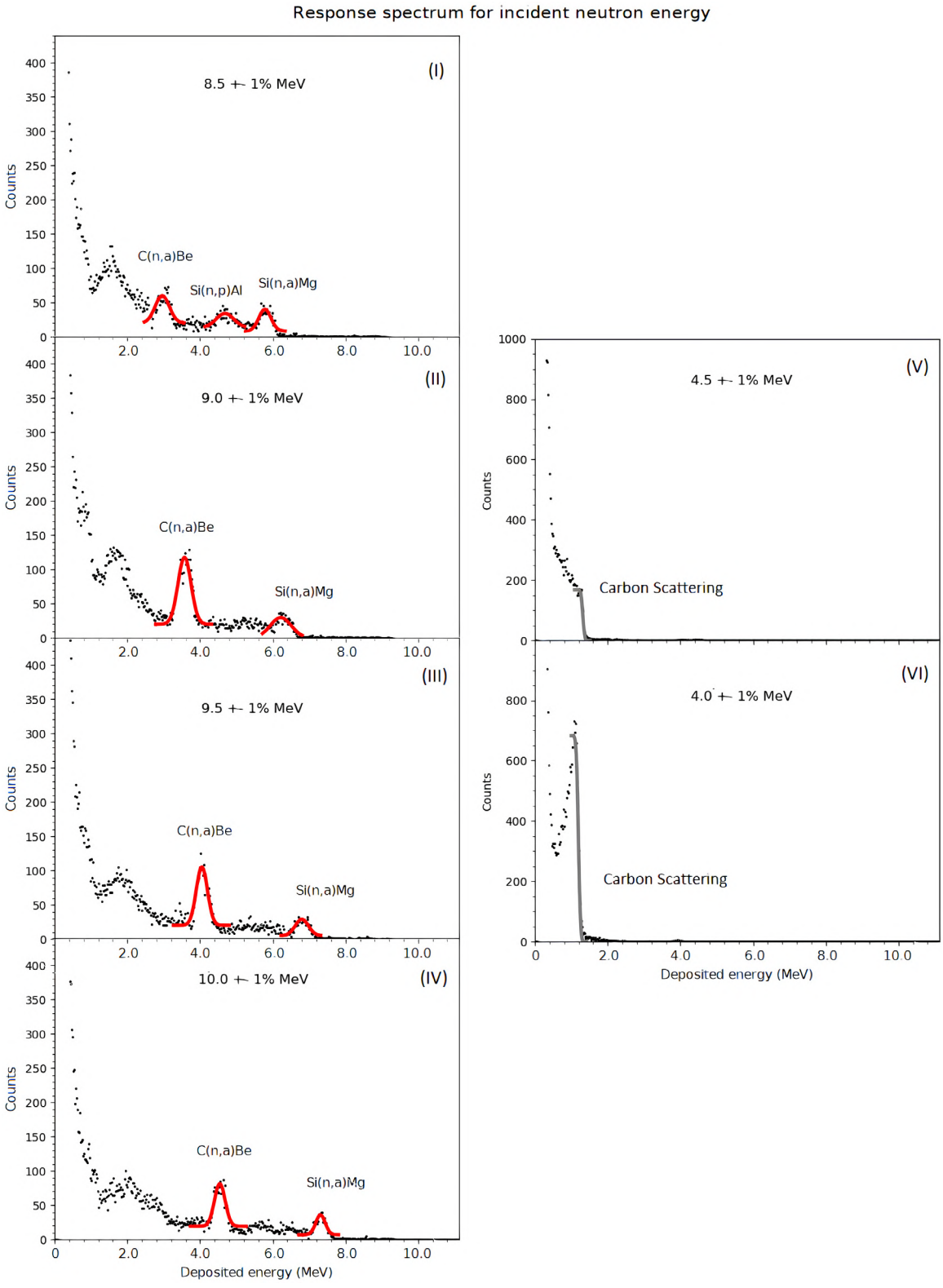

Fig. 4. Deposited energy spectra, obtained from Y-axis projection of the event density plot at the E_n reported in the caption. On the left, panels I–IV show the peaks of three different nuclear reaction channels. On the right, panels V–VI show the carbon scattering shoulders. Red lines are the best fits to a Gaussian of the peaks. Grey lines are the best fits of the shoulders to step function convoluted with a Gaussian. (For interpretation of the references to colour in this figure legend, the reader is referred to the web version of this article.)

by which a fraction of neutrons with energy E_n deposit less than the expected energy because some of the charged products leave the active volume of the detector with a fraction of E_d. This causes the events being detected with the correct E_n but with an underestimated E_d. If that is the case, a thicker detector may solve this issue, reducing the statistical impact of the wall effect.

One other downside of considering only a single channel efficiency is that the efficiency linked to specific nuclear interaction channels is

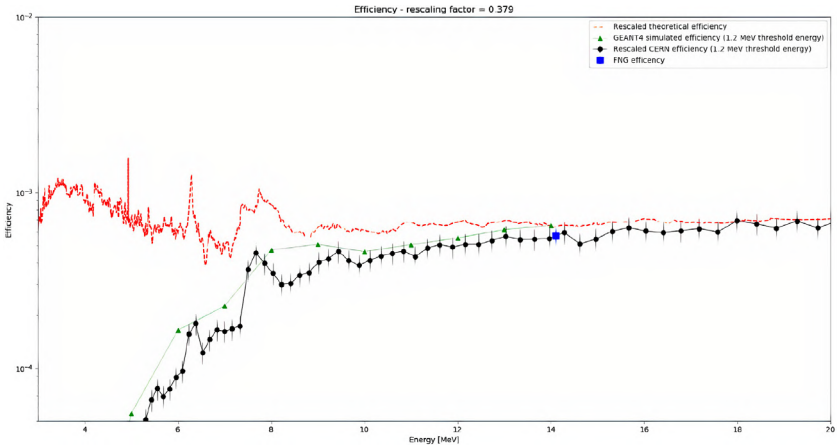

Fig. 5. The SiC detection efficiency for E_n between 3 and 20 MeV measured at n_TOF (black dots) is reported together with the detection efficiency evaluated from the total cross section, as obtained through Eq. (3), (dashed red line) and from a dedicated Geant 4 simulation (green line). The blue dot is the efficiency measured at FNG [2] to which n_TOF and cross-section data are rescaled ($f_{C_{FNG}}$ is used). (For interpretation of the references to colour in this figure legend, the reader is referred to the web version of this article.)

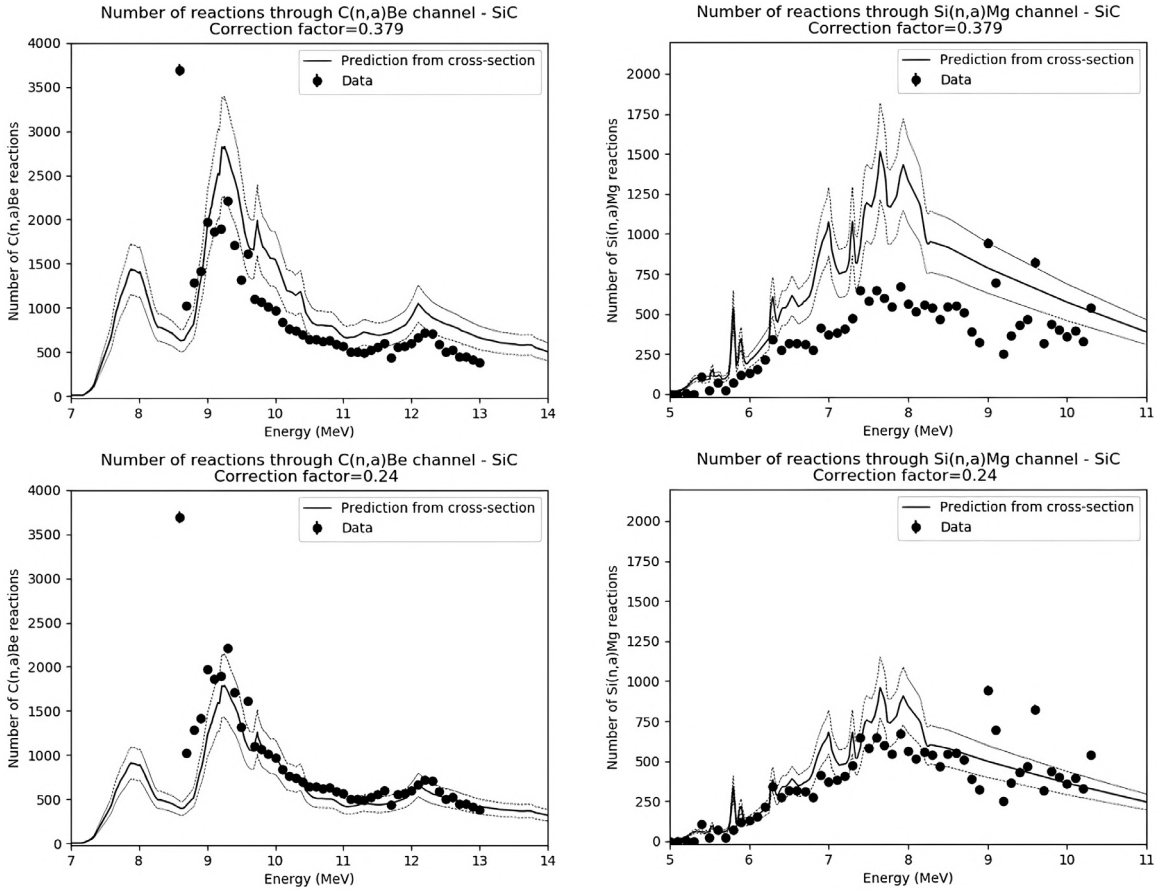

Fig. 6. Comparison between the events which underwent $^{12}C(n,\alpha)^{9}Be$ nuclear reaction (two images on the left) and $^{28}Si(n,\alpha)^{25}Mg$ nuclear reaction (two images on the right). The continuous lines are the theoretical estimate obtained from the nuclear cross sections, as obtained from Eq. (4). The black dots are the number of events, obtained from the quasi-monochromatic cut peaks (Fig. 4). Two correction factors f_C where used: in the top two Figures, the $f_{C_{FNG}}$ (derived from rescaling to FNG data) was used, while in the bottom two Figures the $f_{C_{fit}}$ which best fits the data is used. The values of the two f_C are reported in Table 1. The estimate comes with a 20% error due to $\sigma(E)$ and the neutron flux (dotted line). Counts have a standard error of $\sqrt{}$(counts).

one order of magnitude less than the total efficiency, thus requiring a higher neutron flux in order to obtain the same statistics. Moreover, it is also much more dependent on the neutron energy than the total cross section (for example, $^{12}C(n,\alpha)^{9}Be$ efficiency at 9.5 MeV is 5 times more than the one at 8.5 MeV), which further complicates the spectroscopy.

4.3. Resolution

The energy resolution was obtained considering the broadening of the nuclear reaction peaks of the deposited energy spectra (Fig. 4). The broadening was measured as Full Width at Half Maximum (FWMH),

Table 2
Resolutions for different reaction channel. FNG resolutions are reported as a comparison, where available.

Reaction	n_TOF mean resolution	FNG resolution
$^{12}C(n,\alpha)^{9}Be$	3.62%	2.7%
$^{28}Si\,(n,\alpha)^{25}Mg$	3.66%	3.0%
$^{28}Si(n,p)^{28}Al$	4.71%	–
Weighted mean	3.85%	–

which was obtained from the σ of the Gaussian fit function:

$$FWMH = 2 \cdot \sqrt{2 \cdot \ln(2)} \cdot \sigma \simeq 2.355 \cdot \sigma \quad (5)$$

The energy resolution was then obtained by dividing the FWHM by the E_d value, after subtracting the 1% uncertainty of E_n from it. The values obtained are shown in Table 2.

The energy resolution obtained from the three main reaction channels is slightly higher than the resolution obtained at FNG, possibly due to additional uncertainties linked to the timing calibration (and, therefore, the E_n). The resolution is also higher than the resolution that one may expect from diamond detectors (between 1.67% and 1.84%) [2,32], but it is still inferior to the 5% required to measure the ion temperature in ohmic plasmas [39], thus making the SiC a good candidate as a neutron spectrometer in deuterium–tritium fusion plasmas, especially if its expected grater resilience than diamonds in harsh conditions and at high temperature is confirmed.

5. Conclusions and future prospects

The Silicon Carbide detector has been characterized at n_TOF (CERN). The electronic equipment chain used along with the data analysis followed allowed the study of fast neutron with energies between 3 and 20 MeV.

The detector response to fast neutrons is complex, as multiple reaction channels does not allow for a univocal E_n to E_d relationship. In fact, in addition to the $^{12}C(n,\alpha)^{9}Be$ reaction and the scattering on Carbon (also present in diamond), the Silicon Carbide also features two major new nuclear reactions ($^{28}Si\,(n,\alpha)^{25}Mg$ and $^{28}Si(n,p)^{28}Al$) and the scattering on Silicon. Nonetheless, the nuclear reactions channels can be clearly distinguished if amplitude spectra with fixed E_n are taken. If these are used to conduct spectroscopy, an energy resolution of 3.6% can be achieved for energies $E_n > 6$ MeV.

During the measurement campaign the detector was exposed to a large spectrum of neutron energies, ranging from ultra-fast neutrons (>100 MeV) to thermal neutrons. Although most of the neutrons were not in the energy range of interest, the detector was exposed to all of them anyway, reaching a total neutron fluence of $3.683 \cdot 10^{11}$ n/cm^2 for $E_n > 0.5$ MeV. The absence of instabilities, verified by the good quality of the data, suggests that the Silicon Carbide features a better stability than the diamonds, which, on the other hand, was proven prone to a loss of the count at high neutron fluences. This property of the Silicon Carbide may prove a desirable feature to fusion machine environments. A high-flux irradiation campaign has been scheduled to further explore this property and to quantify the maximum fluency tolerable by the SiC.

The SiC efficiency obtained at every E_n was rescaled to the efficiency previously obtained by the same detector at FNG for 14 MeV neutrons, which is $\varepsilon_{FNG}(14\ \text{MeV}) = 5.69 \cdot 10^{-4}$ [2], in order to account for unmeasured beam inhomogeneities. The resulting efficiency shows good accordance with both GEANT simulated data ($\varepsilon_{sim}(14\ \text{MeV}) = 6.496 \cdot 10^{-4}$) and theoretical estimate from the macroscopic cross-section ($\varepsilon_{\chi_s}(14\ \text{MeV}) = 6.295 \cdot 10^{-4}$). Simulated data also shows good accordance with the efficiency obtained for energies $E_n \neq 14$ MeV, while the theoretical estimate overestimate the data for energies $E_n <$ 14 MeV, due to the E_d threshold.

As the SiC has a very short drift time, the limit on the maximum detection frequency in this experiment is imposed by the electronic chain, most notably by the preamplifier. To improve the detection further an even faster preamplifier is being developed, which is expected to make the SiC work very well as a high flux neutron counter. A new dedicated fast spectroscopy preamplifier is also currently under design to combine good energy resolution with high rate capability. Lastly, an ensemble of geometries (different thicknesses and areas) is being considered for the active volumes, in order to alter the detection efficiency without introducing undesired effects (like the wall effect for thinner volumes, or the charge carrier trapping for thicker volumes).

CRediT authorship contribution statement

M.H. Kushoro: Conceptualization, Methodology, Software, Formal analysis, Investigation, Data curation, Writing - original draft, Visualization. **M. Rebai:** Conceptualization, Methodology, Software, Formal analysis, Investigation, Data curation, Writing - review & editing. **M. Dicorato:** Software, Validation, Formal analysis, Visualization. **D. Rigamonti:** Conceptualization, Methodology, Writing - review & editing. **C. Altana:** Resources. **C. Cazzaniga:** Validation, Investigation, Writing - review & editing. **G. Croci:** Conceptualization. **G. Gorini:** Funding acquisition. **G. Lanzalone:** Resources. **F. La Via:** Conceptualization, Resources. **A. Muoio:** Resources. **A. Muraro:** Conceptualization. **F. Murtas:** Validation, Supervision. **E. Perelli Cippo:** Conceptualization, Writing - review & editing. **M. Tardocchi:** Conceptualization, Supervision, Project administration. **M. Barbagallo:** Resources. **F. Mingrone:** Resources. **S. Tudisco:** Resources.

Declaration of competing interest

The authors declare that they have no known competing financial interests or personal relationships that could have appeared to influence the work reported in this paper.

Acknowledgements

The work leading to this publication was co-funded by the INFN-Group 5 (Technology Research) and by the FuseNet Association. The views and opinions expressed herein do not necessarily reflect those of INFN and Fusenet Association. Authors wish to thank Antonio Trotta, Laura Meda and Eliana de Marchi from ENI s.p.a. for the fruitful and precious discussions.

References

[1] M. Rebai, et al., Time-stability SDD for fast neutron beam diagnostic alpha neutron irradiation, Diam. Relat. Mater. 61 (2016) 1–6.
[2] M. Rebai, et al., New thick silicon carbide detectors: Response to 14 MeV neutrons and comparison with single-crystal diamonds, Nim. A 946 (2019) 162637.
[3] D. Mascali, et al., Rad. Eff. Defec. Solids 165 (6–10) (2010) 730–736.
[4] M. La Cognata, et al., Phys. lett. b, 664 (3) (2008) 157–161.
[5] D. Mascali, et al., Europ, Phys. Lett. 100 (4) (2012) 45003.
[6] L. Giacomelli, et al., Pulsed neutron beam measurements with diamond detectors, Nim. A 720 (2013) 125–127.
[7] J.M. Adams, et al., Nucl. Instrum. Methods Phys. Res. A 329 (1993) 277–290.
[8] F.H. Ruddy, A.R. Dullo, et al., The fast neutron response of 4H silicon carbide semiconductor radiation detectors, IEEE Trans. Nucl. Sci. 53 (3) (2006) 1666–1670.
[9] Glenn F. Knoll, Radiation Detection and Measurements, third edition, John Wiley & Sons, Inc.
[10] M. Pillon, et al., 14 MeV neutron spectra measurements with 4% energy resolution using a type IIa diamond, Nim 101 (4) (1995) 473–483.
[11] M. Rebai, et al., Diamond detectors for fast neutron measurements at pulsed spallation sources, J. Instrum. 7 (2012) C05015.
[12] C. Cazzaniga, et al., Characterization of the high-energy neutron beam of the PRISMA beamline using a diamond detector, J. Instrum. 11 (2016) P07012.
[13] L. Giacomelli, M. Rebai, et al., Pulsed neutron beam measurements with diamond detectors, Nucl. Instrum. Methods Phys. Res. A 720 (2013) 125–127.
[14] M. Rebai, et al., Fission diamond detector tests at the ISIS spallation neutron source, Nuclear Phys. B 215 (2011) 313–315.
[15] https://www.euro-fusion.org/devices/jet/.

[16] D. Rigamonti, et al., Neutron spectroscopy measurements of 14 MeV neutrons at unprecedented energy resolution and implications for deuterium–tritium fusion plasma diagnostics, Meas. Sci. Technol. 29 045502.
[17] L. Giacomelli, et al., Neutron emission spectroscopy of DT plasmas at enhanced energy resolution with diamond detectors, Rev. Sci. Instrum. 87 (2016) 11D822.
[18] M. Rebai, et al., Response function of single crystal synthetic diamond detectors to 1-4 MeV neutrons for spectroscopy of D plasmas, Rev. Sci. Instrum. 87 (2016) 11D823.
[19] A. Muraro, et al., First neutron spectroscopy measurements with a pixelated diamond detector at JET, Rev. Sci. Instrum. 87 (2016) 11D833.
[20] T. Tanaka, et al., Radiation tolerance of type IIa synthetic diamond detector for 14 MeV neutrons, Diam. Relat. Mater. 14 (2005) 2031–2034.
[21] C. Cazzaniga, et al., Charge collection uniformity and irradiation effects of synthetic diamond detectors studied with a proton micro-beam, Nucl. Instrum. Methods Phys. Res. B 405 (2017) 1–10.
[22] A. Lohstroh, et al., The effect of fast neutron irradiation on the performance of synthetic single crystal diamond particle detectors, Diam. Relat. Mater. 19 (2010) 841–845.
[23] R.W. Flammang, John G. Seidel, Frank H. Ruddy, Fast neutron detection with silicon carbide semiconductor radiation detectors, Nucl. Instrum. Methods Phys. Res. A 579 (2007) 177–179.
[24] S. Seshadri, et al., Demonstration of an SiC neutron detector for high-radiation environments, IEEE Trans. Electron Devices 46 (3) (1999).
[25] C. Guerrero, et al., Performance of the neutron time-of-flight facility n_TOF at CERN, Eur. Phys. J. A 49 (2013) 27.
[26] Tudisco, et al., SiCILIA—Silicon carbide detectors for intense luminosity investigations and applications, Sensors 18 (2018) 2289.
[27] S. Tudisco, et al., Nuovo Cimento C 42 (2–3) (2019) 74.
[28] A. Muoio, et al., EPJ Web of Conferences, Vol. 117, 2016, p. 10006.
[29] C. Ciampi, et al., Nim. A 925 (2019) 60–69.
[30] S. Nida, et al., J. Synchrotron Radiat. 26 (2019) 28–35.
[31] https://cividec.at/electronics-Cx.html.
[32] M. Rebai, A. Milocco, et al., Response of a single-crystal diamond detector to fast neutrons, JINST 8 (2013) P10007.
[33] A. Pietropaolo, et al., Single-crystal diamond detector for time-resolved measurements of a pulsed fast-neutron beam, Europhys. Lett. 92 (2010) 68003.
[34] M.H. Kushoro, Characterization of Compact Neutron Detectors for Fusion Application, (master thesis), at Università degli studi di Milano-Bicocca.
[35] https://www.caen.it/products/dt5730/.
[36] Carlo Cazzaniga, Fast Neutron Measurement for Fusion and Spallation Sources Applications, (Ph.D. thesis), at Università degli studi di Milano-Bicocca.
[37] M. Angelone, et al., Absolute experimental and numerical calibration of the 14 MeV neutron source at the frascati neutron generator, Rev. Sci. Instrum. 67 (1996) 2189.
[38] IAEA catalogue ENDF/B-VIII.0, 2018, https://www-nds.iaea.org/exfor/endf.htm (USA, 2018).
[39] W.R. Faust, E.G. Harris, Nucl. Fusion 1 (1960) 62.

5.2 Paper 2

Detector Response to D-D Neutrons and Stability Measurements with 4H Silicon Carbide Detectors

M.H. Kushoro, M. Rebai, M. Tardocchi, C. Altana, C. Cazzaniga, E. De Marchi, F. La Via, L. Meda, A. Meli, M. Parisi, E.Perelli Cippo, M. Pillon, A. Trotta, S. Tudisco and G. Gorini

Materials
2021, 14, 568

Summary:

The paper describes the most important results obtained on the SiC-O and SiC-C under irradiation of spallation neutrons, alpha particles and DD neutrons. In the paper, measurements were performed with neutrons from the ISIS spallation source together with stability measurements performed in a laboratory under alpha-particle irradiation for one week. Some consideration to the impact of the casing of the detector on the detector's counting rate is given. In addition, the detector response to Deuterium-Deuterium (D-D) fusion neutrons is described by comparing neutron measurements at the Frascati Neutron Generator with a GEANT4 simulation. The good stability measurements and the assessment of the detector response function indicate that such a detector can be used as both a neutron counter and spectrometer for 2–4 MeV neutrons. Furthermore, the absence of polarization effects during neutron and alpha irradiation makes silicon carbide an interesting alternative to diamond detectors for fast neutron detection.

materials

MDPI

Article

Detector Response to D-D Neutrons and Stability Measurements with 4H Silicon Carbide Detectors

Matteo Hakeem Kushoro [1,2,*], Marica Rebai [2], Marco Tardocchi [2], Carmen Altana [3], Carlo Cazzaniga [4], Eliana De Marchi [5], Francesco La Via [6], Laura Meda [5], Alessandro Meli [6], Miriam Parisi [5], Enrico Perelli Cippo [2], Mario Pillon [7], Antonio Trotta [5], Salvo Tudisco [3] and Giuseppe Gorini [1,2]

1 Dipartimento di Fisica "G. Occhialini", Università di Milano-Bicocca, 20126 Milano, Italy; giuseppe.gorini@unimib.it
2 Istituto per la Scienza e Tecnologia dei Plasmi, Consiglio Nazionale delle Ricerche, 20126 Milano, Italy; marica.rebai@istp.cnr.it (M.R.); marco.tardocchi@istp.cnr.it (M.T.); enrico.perellicippo@istp.cnr.it (E.P.C.)
3 Istituto Nazionale di Fisica Nucleare (INFN), Laboratori Nazionali del Sud (LNS), Via S. Sofia 62, 95123 Catania, Italy; altana@lns.infn.it (C.A.); tudisco@lns.infn.it (S.T.)
4 ISIS Facility, UKRI-STFC, Rutherford Appleton Laboratory, Didcot OX110 QX, UK; carlo.cazzaniga@stfc.ac.uk
5 ENI S.p.A. CENTR—Renewable Energy & Environmental R&D, 28100 Novara, Italy; Eliana.DeMarchi@eni.com (E.D.M.); laura.meda@eni.com (L.M.); miriam.parisi@eni.com (M.P.); Antonio.Trotta@eni.com (A.T.)
6 Institute for Microelectronics and Microsystems, Consiglio Nazionale delle Ricerche VIII Strada, 5, 95121 Catania, Italy; francesco.lavia@imm.cnr.it (F.L.V.); Alessandro.Meli@imm.cnr.it (A.M.)
7 Associazione EURATOM-ENEA sulla Fusione ENEA C.R. Frascati, Via E. Fermi, 45, 00044 Frascati, Italy; mario.pillon@enea.it
* Correspondence: m.kushoro@campus.unimib.it

Citation: Kushoro, M.H.; Rebai, M.; Tardocchi, M.; Altana, C.; Cazzaniga, C.; De Marchi, E.; La Via, F.; Meda, L.; Meli, A.; Parisi, M.; et al. Detector Response to D-D Neutrons and Stability Measurements with 4H Silicon Carbide Detectors. *Materials* **2021**, *14*, 568. https://doi.org/10.3390/ma14030568

Academic Editor: Sergey Kukushkin

Received: 31 December 2020
Accepted: 20 January 2021
Published: 26 January 2021

Abstract: The use of wide-band-gap solid-state neutron detectors is expanding in environments where a compact size and high radiation hardness are needed, such as spallation neutron sources and next-generation fusion machines. Silicon carbide is a very promising material for use as a neutron detector in these fields because of its high resistance to radiation, fast response time, stability and good energy resolution. In this paper, measurements were performed with neutrons from the ISIS spallation source with two different silicon carbide detectors together with stability measurements performed in a laboratory under alpha-particle irradiation for one week. Some consideration to the impact of the casing of the detector on the detector's counting rate is given. In addition, the detector response to Deuterium-Deuterium (D-D) fusion neutrons is described by comparing neutron measurements at the Frascati Neutron Generator with a GEANT4 simulation. The good stability measurements and the assessment of the detector response function indicate that such a detector can be used as both a neutron counter and spectrometer for 2–4 MeV neutrons. Furthermore, the absence of polarization effects during neutron and alpha irradiation makes silicon carbide an interesting alternative to diamond detectors for fast neutron detection.

Keywords: silicon carbide; fast neutron detection; tokamak

1. Introduction

Solid State Detectors (SSDs) represent a recent option for neutron detection in high-flux applications, since they combine a good pulse height energy resolution and fast response time while having compact dimensions [1,2]. The SSD scene is currently dominated by diamond detectors, which, for instance, are currently installed at the JET tokamak [3] as neutron spectrometers [2,4] and at the ChipIr beamline at ISIS [5] as beam monitors [6,7]. However, the development of large high-power tokamaks (such as ITER [8]) requires neutron detectors to be installed closer to the plasma and, therefore, to be

able to sustain the high temperature and neutron flux of such an environment. This is driving interest in new and more neutron-resilient SSDs, such as silicon carbide detectors.

Silicon carbide detectors (SiC) are a type of SSD whose active volume is made from silicon carbide, a crystalline material known for its resilience and high radiation hardness since the late 1950s [9]. SiC can withstand high temperatures [10], radiation [11] and neutron fluxes [12]; furthermore, in recent years, new manufacturing techniques have allowed the production of SiC detectors with fewer defects and with a wider range of geometries [13]. The detector responses of these new SiC detectors were characterized in the past with 14 MeV Deuterium-Tritium (D-T) neutrons [14] and over a wide range of fast neutron energies [15], showing energy resolutions and efficiencies comparable to those of the diamond detectors.

The objective of this paper was to expand the knowledge on SiC for use in next-generation tokamaks as a neutron counter and spectrometer. To achieve this, the stability of two models of SiC under long-term neutron and α-particle irradiation was experimentally investigated and compared to the stability limits of state-of-art diamond detectors ([16,17]) in order to find the best candidate for measuring prolonged irradiation. Some consideration is given to the effect of the casing on the detector's counting rate. Finally, the characterization conducted in [14] was expanded to D-D neutrons, which are the second most important neutrons emitted from fusion plasma besides D-T neutrons, in order to assert SiC's ability to act as a neutron spectrometer in the 2 to 4 MeV energy range.

2. Detectors and Front-End Electronics

SiC detectors are made of a thin semi-conductive lattice that acts both as a converter and as an active volume. The lattice is built as a p–n junction and behaves like a diode [18]. The interaction of a fast neutron with a silicon (Si) or carbon (C) nucleus induces the generation of charged particles via nuclear reactions or via Si or C recoil ions through scattering collision. These charged particles and ions, in turn, ionize the p–n junction and generate a number of ion–electron pairs proportional to the energy deposited by the charged particles (E_{d}). The pairs abruptly decrease the resistivity of the p–n junction, causing a current signal that is used as a detection mechanism. There is a linear proportionality between E_{d} and the signal amplitude, allowing for the use of SSDs as spectrometers.

SSDs can also be used to detect heavy charged particles (such as alpha particles or protons), which directly generate ion–electron pairs in the lattice via ionization/excitation processes without the need to be converted. The detector is also sensitive to γ-rays, although the sensitivity to them is much lower than the one to neutrons since carbon and silicon have much smaller cross sections for γ-rays than for neutrons and the detector has a small thickness. This is actually a desirable feature for a neutron detector, as γ-rays constitute the most intense source of background in almost all neutron facilities.

Two SiC detectors were used in this paper, both designed and manufactured at the Institute for Microelectronics and Microsystems of the Consiglio Nazionale delle Ricerche (CNR), based in Catania (Italy). The detectors' active volumes were realized by growing 4H-silicon carbide epitaxial layers by means of Chemical Vapor Deposition (CVD). p–n junction doping was achieved by adding N_2 and $Al_2(CH_3)_6$ (trimethylaluminum) to the silicon and carbon gaseous precursors in order to obtain nitrogen and aluminum impurities. The wafers were then treated with several photolithographic steps, among which were Inductive Coupled Plasma (ICP) etching for the definition of the detector area; lithography to construct the edge structures; the deposition of an isolation oxide, with subsequent annealing, in order to produce good electrical contact on the p+ region; and titanium/nickel/gold deposition in order to form ohmic contact. More details of the process can be found in [13] and [19].

The first detector used was made with a single active volume 5 mm × 5 mm wide and 10 μm thick (Figure 1b). The second was made of a 2 × 2 matrix of independent 5 mm × 5 mm-wide and 100 μm-thick active volumes, all grown on the same substrate (Figure 1a). Only one of the four pixels was actively used for the detection.

The active volume of both detectors, which will be referred to as SiC10 and SiC100 from now on, was a 0.3 μm-thick layer with a 10^{19} cm^{-3} doping concentration of Al, matched to a 10 or 100 μm p-layer with a N_2 concentration between 8×10^{13} and 10^{14} cm^{-3}. The inactive substrate of the detectors was 100 μm thick in the case of SiC10 and 350 μm thick in the case of SiC100. Each of the two was encased in an aluminum box between 3 and 7 mm thick, in order to shield the detector from environmental electromagnetic radiation and from dust.

The output signal of the detector was transmitted through 50 Ω coaxial cables and preamplified with a customized charge preamplifier (model CIVIDEC CX-L, manufactured by CIVIDEC Instrumentation GmbH, Wien, Austria), which shaped the signal into a pseudo-Gaussian shape. The CX-L preamplifier features the best energy resolution and signal-to-noise ratio and has a typical shaping time of ≃280 ns. Alternatively, in some measurements, a current amplifier (model CIVIDEC C2) was used. Being a current amplifier, the C2 does not shape the detector signal, which makes it more suited for applications where high fluxes are an issue since it has a much faster response (≃15 ns) [20].

The preamplifiers also convey the bias voltage to the detector. Negative bias voltages of −200 V for the SiC100 and −50 V for the SiC10 were chosen in order to deplete the active volumes of both detectors [14], without incurring any discharges [19]. With such bias voltages, the drift times were of the order of nanoseconds [21]; therefore, with such fast signals, any limitations in the detection rate were imposed by the analyzing chain.

The signal was then read by a 14-bit/500 MHz sampling rate digitizer (model DT5730, manufactured by CAEN, Viareggio, Italy), which allowed storing the data on the PC and recording the timestamp and the pulse integral for each event. The pulse height spectrum was then reconstructed from the stored events.

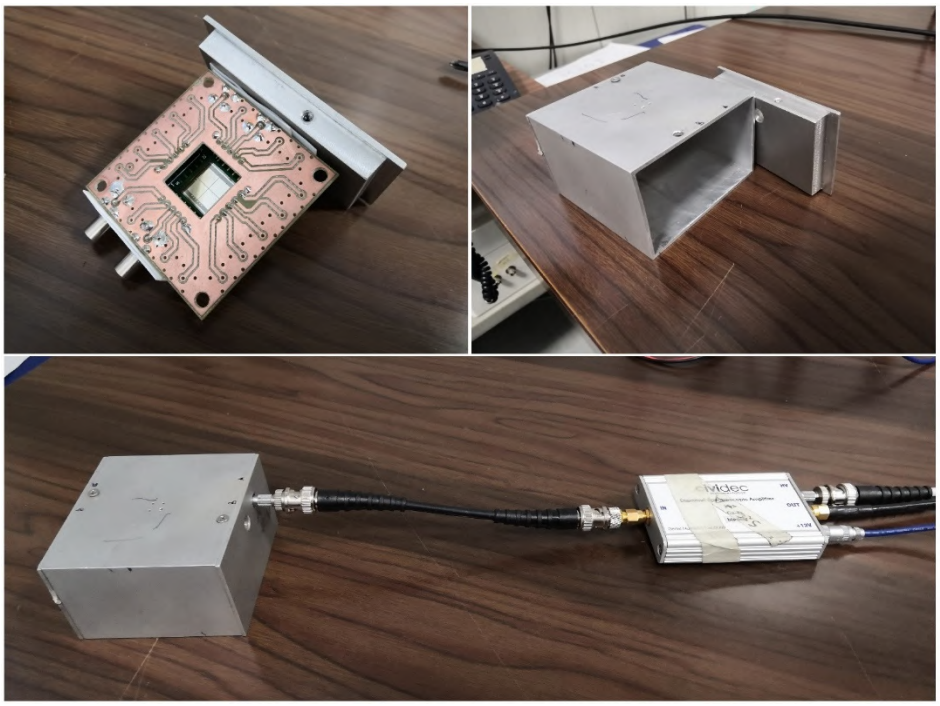

(**a**)

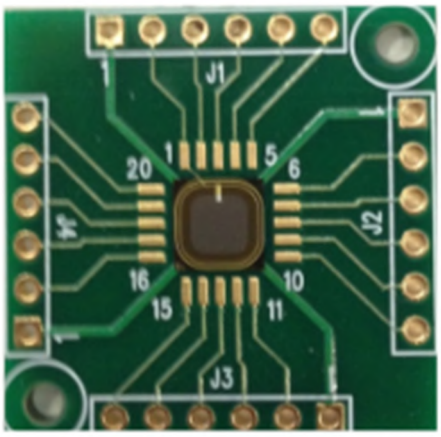

(**b**)

Figure 1. (**a**) The 100 μm silicon carbide detector used in this paper. The four independent pixels and the chip electronics are visible in the center of the top-left figure. The aluminum casing in which it was contained is shown in the top right. The detector assembled and connected to the spectroscopic preamplifier is shown in the bottom figure. (**b**) The chip and the single active volume of the 10 μm silicon carbide detector used in this paper.

3. Irradiation Facilities

3.1. ISIS (ChipIr and ROTAX)

The ISIS Neutron and Muon Source is a spallation source at the UKRI-SFTC Rutherford Appleton Laboratory in Didcot (UK). Neutrons are produced through spallation by a pulsed 800 MeV Proton Synchrotron (PS) beam impinging onto two different tungsten targets (Target Stations 1 and 2). The PS operates in 50 Hz pulsed mode. Every pulse is made by two 70 n- wide proton bunches separated by a time interval of 322 ns. After the spallation process, neutrons, which are emitted in all directions, are firstly reflected by a beryllium assembly, moderated and then collimated in different beam lines, resulting in white neutron spectra ranging from fast (up to 800 MeV) to cold neutrons (<1 meV). Neutrons travel to the various experimental areas, where their energy E_{n} can be measured by means of the time-of-flight technique.

The data for this paper were collected in two different beamlines: ROTAX and ChipIr. The first one is a beamline of the ISIS Target Station 1. It features a 95 K methane moderator, a neutron flight path of 15.5 m, and a thermal neutron flux at the sample position of $\phi_{\mathrm{n_{th}}} \simeq 3 \times 10^6 \frac{n}{\mathrm{cm^2 \cdot s}}$ [22], and it is dedicated to the characterization of single-crystal samples, detectors and equipment. ROTAX features a residual fast neutron flux ($E_{\mathrm{n}} > 10$ MeV) of about $\phi_{\mathrm{n_{fast}}} \simeq 10^4 \frac{n}{\mathrm{cm^2 \cdot s}}$ ChipIr, on the other hand, is a beamline of the ISIS Target Station 2 that has a direct line of sight to the target (not the moderator), and thus, it features a fast neutron spectrum. It is dedicated to the irradiation of microelectronics with a high-energy neutron flux. ChipIr features an atmosphere-like neutron spectrum with a fast neutron flux of $\phi_{\mathrm{n_{fast}}} \simeq 5 \times 10^6 \frac{n}{\mathrm{cm^2 \cdot s}}$ for $E_{\mathrm{n}} > 10$ MeV neutrons. It has a neutron flight path of 10.5 m. A residual thermal flux is also present: ($\phi_{\mathrm{n_{th}}} \simeq 10^5 \frac{n}{\mathrm{cm^2 \cdot s}}$) [23,24].

3.2. FNG

The Frascati Neutron Generator (FNG) is a neutron source based at the ENEA Laboratories in Frascati, Italy. It was specifically built as a research tool for thermonuclear controlled fusion. Neutrons are produced by a 260 keV deuteron beam impinging on a deuterated target via the nuclear reaction $D(D,n)^3He$. The reaction is exothermic: the positive q-value Q_{v} = +3.27 MeV is split between the two reaction products. The neutron energy

depends on the emission angle and ranges from a maximum of E_n = 3.15 MeV, for a neutron emitted with a ϕ = 0° angle (forward direction), to a minimum of E_n = 2.0 MeV, for a neutron emitted with a ϕ = 180° angle. By placing the detector at a known angle ϕ, it is therefore possible to expose it to a quasi-monochromatic neutron beam (if the solid-angle contribution and the beam-energy broadening due to the Doppler effect are neglected).

3.3. Alpha Irradiation

Alpha (α) irradiation was carried out at the Istituto per la Scienza e Tecnologia dei Plasmi (ISTP) laboratories in Milano, Italy. The source used was an Americium-241 electrodeposited radioactive source, which emits monochromatic 5.49 MeV α particles along with 60 keV X-rays. Since the half-life of ^{241}Am is 432 years, the source was assumed to have a constant emission during the period of the measurement.

The source was placed at 16.4 mm from the SiC10 surface and at 25 mm from the SiC100. For this reason, the energy of the α impinging on the detector surface was slowed down to 4.7 and 4.3 MeV, respectively, by air [25]. The holes in the casing that were purposely made for the α particles to reach the detector's surface also granted collimation, limiting the maximum drift from the shortest path to 0.23 mm for the SiC10 and 0.14 mm for the SiC100: this limited the broadening of the energy spectrum of the α particles to 19 and 12 keV, respectively, which corresponded to 0.4% and 0.28% of the relative energies. As the energy resolution of the detector is expected to be one order of magnitude higher [14,15], the α particles can be safely assumed to be monochromatic for the purposes of this paper.

4. Stability Measurements

With "detector stability", we usually refer to the capability of a detector to operate for long irradiation times without altering its response. There are several factors that can alter the response of an SSD, the main one being that the prolonged exposure to ionizing radiation results in free charges trapped inside the lattice that alter the drift electric field. Diamond detectors have shown to be subject to this effect [17]. This is an issue even if the restoration of the initial condition can be achieved by an inversion in the polarity of the detector [16] since it is desirable for a detector in a fusion or spallation environment to be able to operate continuously.

Diamond detectors' stability was measured in the past [16,17], and they were proven to be stable up to $7 \times 10^3 \frac{\alpha}{mm^2}$, after which the count rate dropped significantly. The same was tested with neutrons, showing a 20% decrease in the number of counts after a neutron fluence of $1.2 \times 10^6 \frac{n}{mm^2}$ The measurements described in this paper emulated those tests by using the two SiC detectors and exposing them to α particles and neutrons in the facilities previously described.

4.1. Results for Stability with Alpha Particles

The signal of the α particles produced by the ^{241}Am source was collected by both the SiC10 and the SiC100 detectors. The preamplifier used in these measurements was the CX-L model mentioned earlier. The exposure lasted for 55 and 170 h, respectively, which provided a total detector irradiation of 7.9×10^6 and $9.0 \times 10^6 \frac{\alpha}{mm^2}$.

Both the time and the pulse height of the events were recorded. A threshold of 200 keV was applied, in order to not consider the X-rays produced by the ^{241}Amsource and other background noise. The events were then grouped in 300 s time intervals. For every group, a histogram of the events' pulse heights was made (see Figure 2). The histograms were fitted with a Gaussian function, whose central value x_0 was taken as the mean pulse height for the ensemble. The Full Width at Half Maximum (FWHM) was also obtained through the relation FWHM = $2\sigma \times \sqrt{2 \times \ln(2)}$, where σ is the standard deviation of the Gaussian fit. The energy resolution of the detector was then computed as the ratio between the FWHM and the alpha energy, with the assumption that the incident α-particle spectrum was monochromatic (see Section 3.3).

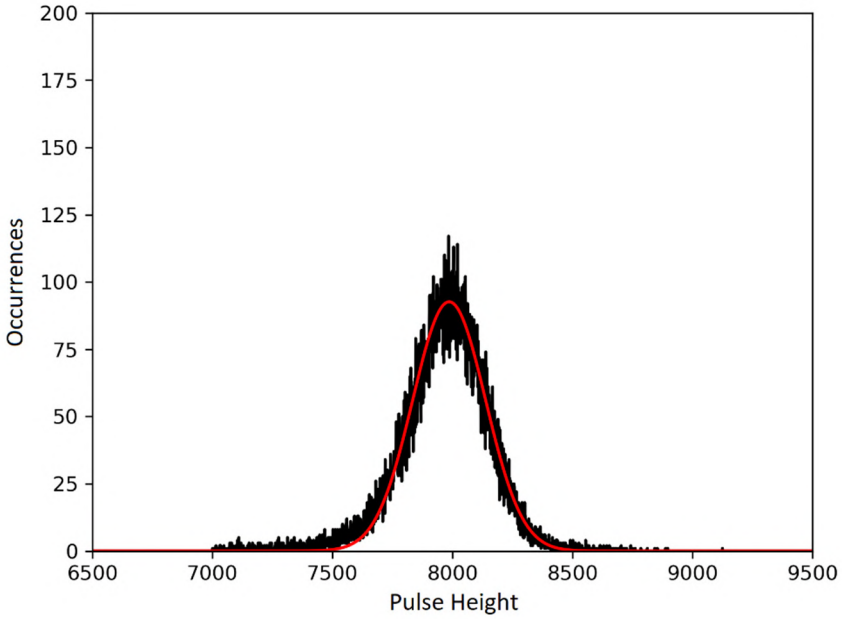

Figure 2. Pulse height distribution for a 300 s exposure of the SiC10 to 4.7 MeV α particles (black line), fitted with a Gaussian function (red line), obtaining a mean pulse height of 7986.34. FWHM is 386.94, which provided an energy resolution of 4.85%.

The number of counts, the mean pulse height and the energy resolution were calculated for every 300 s subset and are plotted in Figure 3 as functions of time. The mean values and dispersions obtained by the fits are then collected in Table 1. Neither the number of counts nor the FWHM had a drift over the multiple-day-long acquisition. The energy resolutions obtained were 4.3% for the SiC10 and 2.9% for the SiC100, the latter confirming the resolution obtained in [15] and in [16]. The overtime trend of the energy resolution did not have any significant drift over the multiple-day exposure and shows only a small Gaussian-shaped dispersion (2–3% of the energy resolution value), which can be interpreted as a statistical error. This proves the stability of the energy resolution over the analysis period. The same considerations may apply to the number of counts, which is linked to the detector's efficiency. For both the SiC10 and the SiC100, the σ of the dispersion around the number of counts perfectly fits the Poisson uncertainty for the number of counts, μ, given by $\sqrt{\mu}$, as shown in the first panel of Table 1.

The same consideration may not be applied to the response function, since the mean value of the pulse height has a slight periodic oscillation and a drift that is dependent on time and, thus, cannot be interpreted as a random error due to statistics. It is worth noting that the change in the response function of the two detectors does not have any correlation with the number of counts or the energy resolution. While the cause of this periodic drift is still unclear, the lack of correlation with the other two parameters suggests that the oscillation could be due to a variability in the energy of the ^{241}Am α particles impinging on the detector rather than a change in the detector response. Since the period of the oscillation is $\simeq$85,000 s (=23.61 h), it has been hypothesized that the cause is the variability of the air-stopping power caused by a change in the pressure of the air, presumably due to the night–day cycle. Indeed, the lab is estimated to have had a thermal excursion between 27 and 30 °C, which would have caused a 1% excursion in the air density (1.176 $\frac{\mathrm{kg}}{\mathrm{m}^3}$ at 27 °C and 1.164 $\frac{\mathrm{kg}}{\mathrm{m}^3}$ at 30 °C, if air humidity is neglected). Since air-stopping power scales linearly with density [25], this reflects a 1% change in the energy of the impinging alpha particle, which is compatible with the 0.87% difference between the maximum and minimum values for the pulse height in the second panel of Table 1.

Table 1. Summary of the mean number of counts, pulse height and energy resolution measured during the alpha particle irradiation.

	Mean No. of Counts, μ	**Dispersion (σ)**	**Poisson Uncertainty (= $\sqrt{\mu}$)**
SiC10	36,460.55	±195.02	190.95
SiC100	94,737.97	±313.11	307.80
	Mean Pulse Height	**Dispersion (σ)**	**Max PH—Min PH**
SiC10	7995.52	± 8.09	-
SiC100	9672.03	± 27.60	9709 − 9625 = 84 (0.87%)
	Mean Energy Resolution	**Dispersion (σ)**	
SiC10	4.356%	± 0.113%	-
SiC100	2.893%	± 0.036%	-

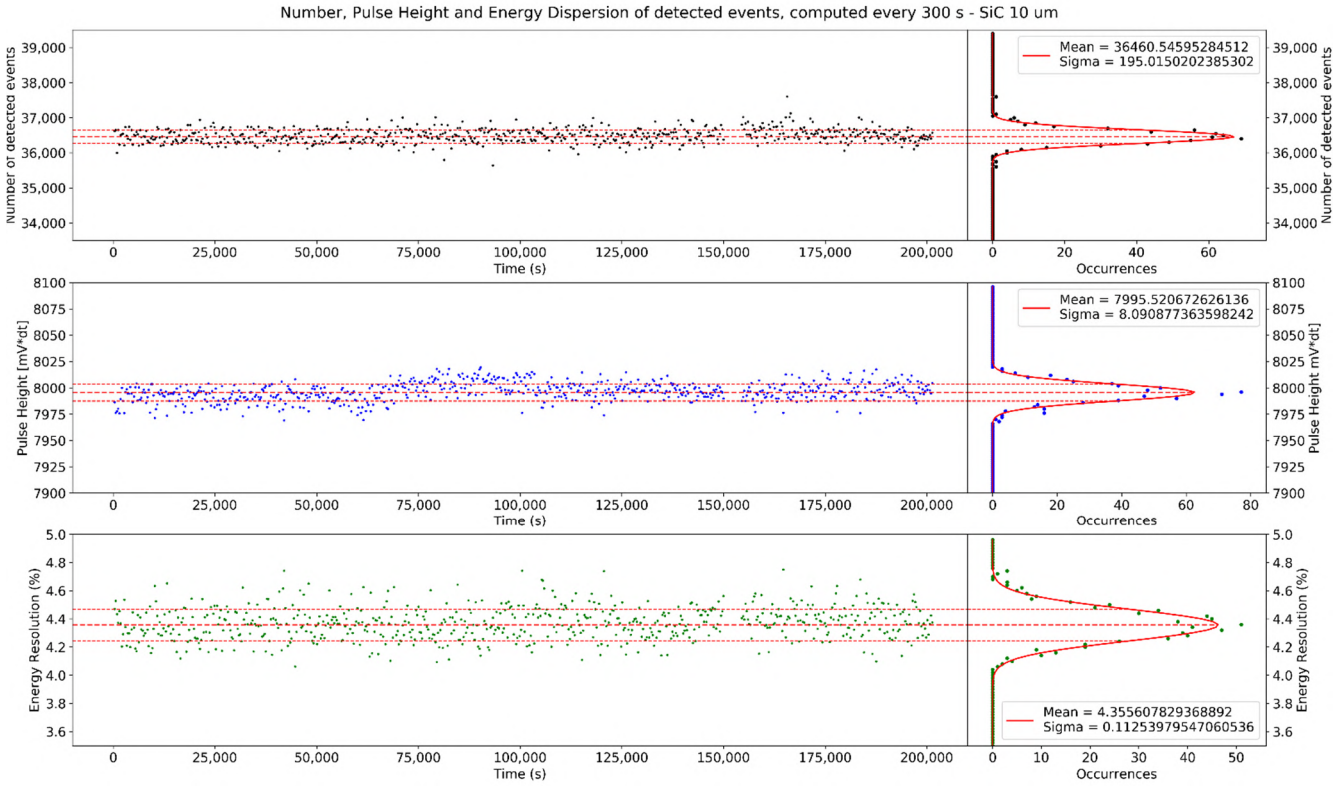

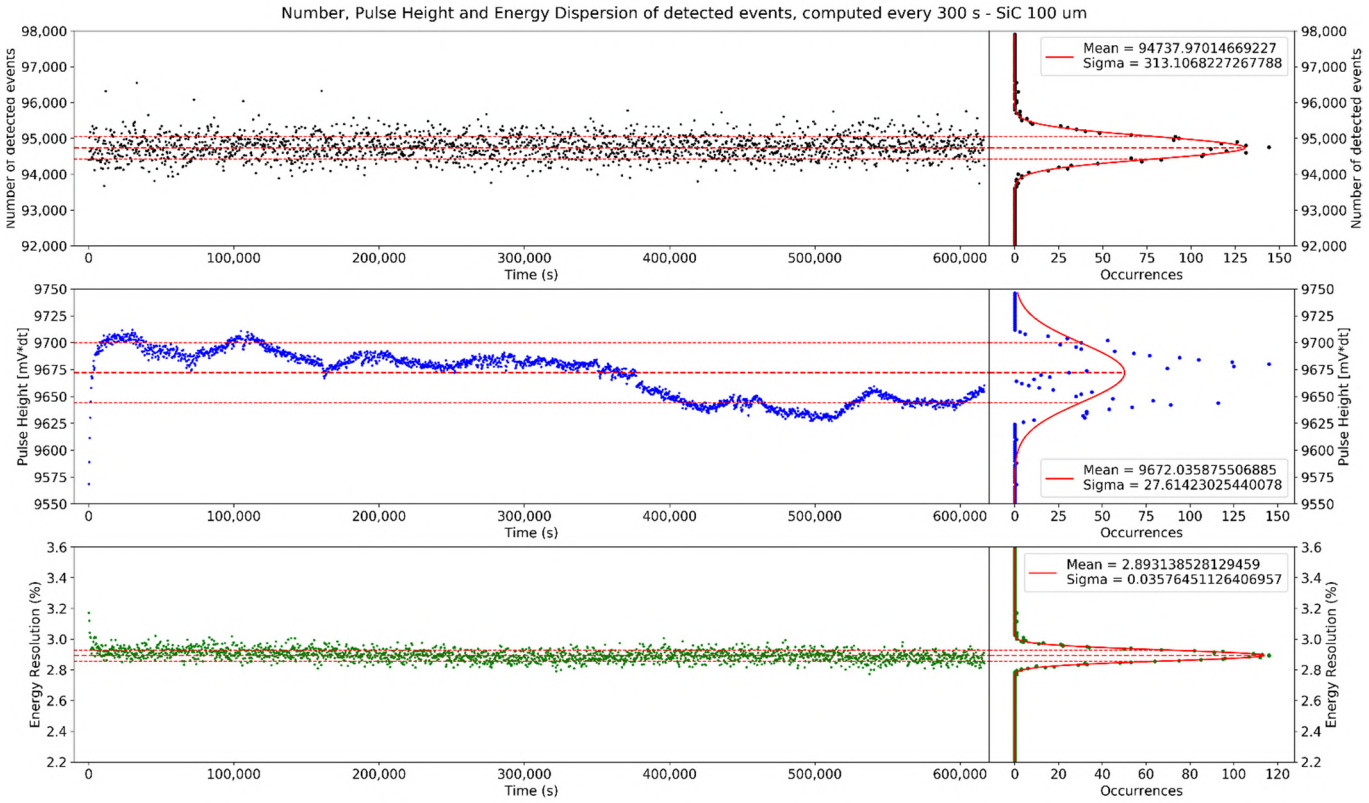

Figure 3. Time evolution of the number of counts (black), the mean pulse height (blue) and the energy resolution (green) for the 10 μm SiC (**top**) and the 100 μm SiC (**bottom**) under irradiation with quasi-monochromatic 4.7 and 4.3 MeV αs, respectively. SiC10 and SiC100 alpha irradiation lasted for 55 and 170 h, respectively. Each of the points corresponds to a 300 s ensemble. On the right, the dispersion of data is projected on the y-axis, and the mean value of the three quantities was computed, along with its standard deviation.

4.2. Results for Stability with Neutrons

The detector stability with neutrons was tested at ChipIr with the SiC10 and at ROTAX with the SiC100. The detectors were exposed to the ISIS pulsed neutron flux, and the pulse height of the events was measured in a 2 μs time window synchronized with the start signal from the PS beam. The window allowed limiting the detection to neutrons with $E_n > 0.5$ MeV, as obtained from the non-relativistic relation:

$$E_n[MeV] = \frac{m_n \times d[m]^2}{2 \times 10^{-18} \times ToF[ns]}$$

where m_n is the neutron mass in Kg, d is the flight path of the neutron (10.5 m at ChipIr; 15.5 m at ROTAX) and ToF is the time of flight, calculated as the time difference between the time of generation of the neutrons and the time of arrival of the event. The former was obtained from the time of the first detected events, under the assumption that those were caused by γ-rays travelling at the speed of light c. The preamplifier used was the CIVIDEC C2 for both the ROTAX and ChipIr experiments. The exposure of the SiC10 at ChipIr lasted for 48 h, with an estimated total neutron flux of $9.06 \times 10^8 \frac{n}{mm^2}$ (above 0.5 MeV), while the exposure of the SiC100 lasted for 96 h, with an estimated total neutron flux of $2.59 \times 10^8 \frac{n}{mm^2}$ (above 0.5 MeV). It must be noted that these fluxes correspond only to the fast neutrons that were detected inside the detection windows: both detectors were also exposed to an undetermined number of slower neutrons, as no shutter was used in order to shield the detection areas from them.

The events recorded both at ROTAX and at ChipIr are shown in Figure 4 in the form of two event density plots, in analogy to the plots of [6,14,15,26]. The data are grouped into two bunches, reflecting the time structure of the proton beam. The red lines represent

the relationship between E_n and ToF and are separated by 322 ns, which mirrors the time difference between the two PS proton bunches. All the events detected fall below those lines, validating the data.

Stability was tested for both the ChipIr and ROTAX data by tracking the evolution over time of the number of events detected in every 300-second ensemble, in analogy to the α-irradiation. Contrary to for the α-irradiation, it was not possible to test the evolution of the response function and of the energy resolution, because the flight paths of both Rotax and ChipIr are too short and the proton beam temporal structure too wide to be able to obtain, for fast neutrons, E_n from the ToF with a sufficient energy resolution. The number of incident neutrons was assumed to be constant, since the number of PS protons fired on the target was proven to be stable with an error of $\pm 1\%$ for the duration of operation. The results are shown in Figure 5.

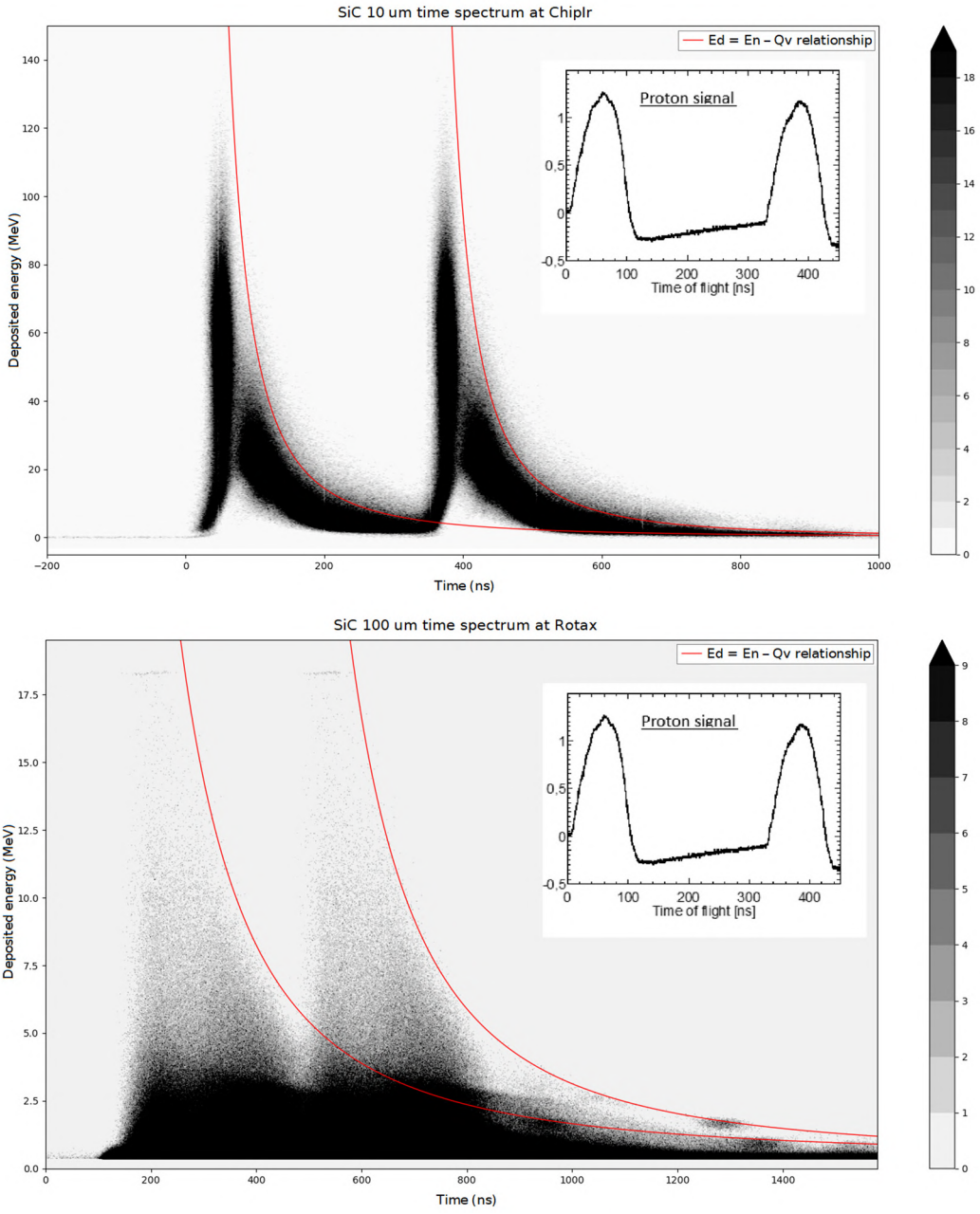

Figure 4. Event density plot (in the time of flight (ToF) vs. E_d space) of 100 µm SiC on ROTAX (top) and of 10 µm SiC on ChipIr (bottom). The two-bunch Proton Synchrotron (PS) spectrum is showcased on the right. The red lines represent the relationship between ToF and E_n and are separated by 322 ns, mirroring the PS spectrum.

The number of counts was fitted with a constant value μ (full red line) corresponding to the mean value of counts per 300 s. Such a value is $\mu_{SiC10} = 5403 \pm 74 \frac{counts}{300\ s}$ for the SiC10 at ChipIr and $\mu_{SiC100} = 1132 \pm 34 \frac{counts}{300\ s}$ for the SiC100 at ROTAX. The error was calculated from the Poisson uncertainty around the number of counts, which is equal to $\pm\sqrt{\mu}$. As the majority of the data fit the value within the error, and no drift over time was observed, the detector was proven stable over the range of fluences tested, which are at least two orders of magnitude higher than the stability fluency ranges for the diamond measured in [17].

A notable exception is given by the subset of the final 8-hour irradiation at ChipIr (highlighted in blue in Figure 5), which features a number of counts of $\mu = 4812 \pm 70 \frac{counts}{300\ s}$. Such a number is 11% lower than the mean value for the rest of the data, while the PS current was the same as for all the other irradiations (within the error). It must be noted that the subset was taken after the front part of the 3 mm aluminum casing was removed and replaced with a thin 50 μm aluminum foil. As such, the difference in the number of counts is supposed to be due to the number of neutrons that were converted to protons in the aluminum casing through the reaction $^{27}Al(n,p)^{27}Mg$; these protons, being charged particles, have an almost 100% chance of being detected by the SiC, thus increasing the number of counts under the same neutron irradiation.

In order to estimate the impact of this phenomenon, we compared the macroscopic cross sections per unit of area of the 3 mm aluminum casing and one of the active volume of the detector. We defined the macroscopic cross section as $\chi = \sigma \times n_{at}/A$, where σ is the atomic cross section of the nuclear reactions (obtained from the ENDF - Evaluated Nuclear Data File - catalogue [27], averaging over neutrons with $5 < E_n < 20$) and n_{at}/A is the number of atoms per unit area, derived from the atomic density ρ (using $n_{at} = \rho \times A \times t$, where t is the thickness of the object). We then compared the macroscopic cross section of the SiC related to all the nuclear reactions induced by the neutron χ_{SiC} (derived from the total nuclear cross section $\sigma \simeq 0.4$ barn), with the macroscopic cross section of the aluminum casing for the specific $^{27}Al(n,p)^{27}Mg$ reaction, χ_{casing} ($\sigma \simeq 0.03$ barn). We obtain:

$$\chi_{SiC} = 9.67 \times 10^{22}\ cm^{-3} \times 10\ \mu m \times 0.4\ barn = 38.7 \times 10^{-6}$$

$$\chi_{casing} = 6.03 \times 10^{22}\ cm^{-3} \times 3\ mm \times 0.03\ barn = 542.7 \times 10^{-6}$$

That is, the number of neutrons that were converted to protons in the thick aluminum shielding were more than thirteen times the neutrons that interacted with the active volume. If we divide the number of protons by the fraction of the solid angle of the detector's area (assuming the proton emission is isotropic), we obtain the SiC's macroscopic cross section relative to the converted protons χ_{SiC-p}:

$$\chi_{SiC-p} = \chi_{casing} \times \frac{A_{SiC}}{4\pi \times (15\ mm)^2} = 4.7 \times 10^{-6}$$

where 15 mm is the distance between the casing and the surface of the detector. By assuming that all the protons, being heavy charged particles, are detected, we determine that the estimated ratio of the proton events over the total events is $\frac{\chi_{SiC-p}}{\chi_{SiC} + \chi_{SiC-p}} = 10.8\%$, which is very close to the decrease in the number of counts experienced by the detector after the casing was replaced with a thinner one.

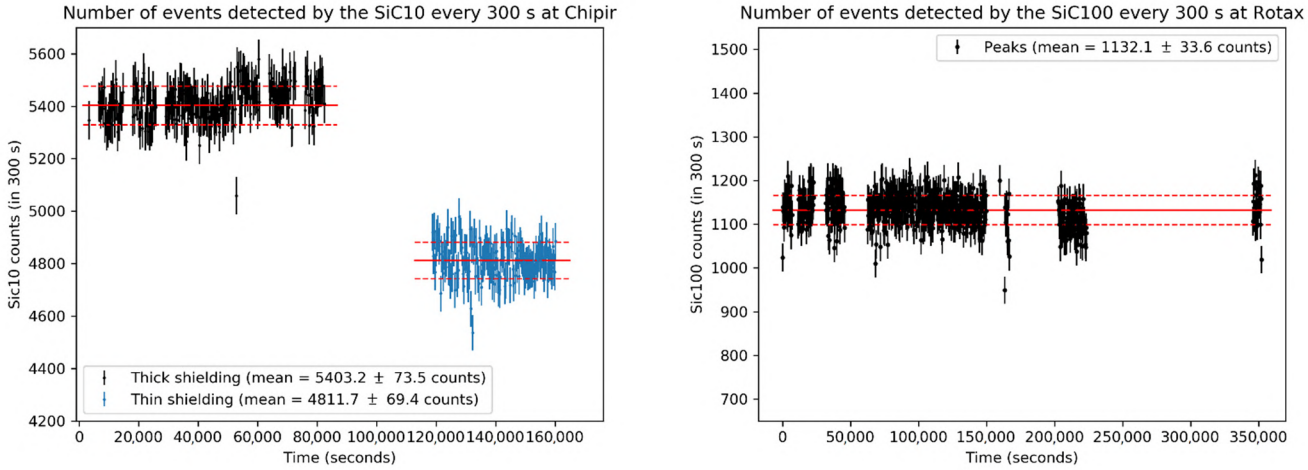

Figure 5. The numbers of events detected every 300 s by the SiC10 on ChipIr (**left**) and by the SiC100 on ROTAX (**right**) are plotted as functions of time for 44 and 98 h-long exposures, respectively. Data from the SiC10 are divided into the data taken with thick aluminum shielding (in black) and those taken with thin shielding (in blue). Red lines represent the count rates, while dashed red lines are the statistical errors for the numbers of counts.

5. Neutron Spectroscopy (3.0 MeV)

The peculiar structure of the FNG (described in Section 3.2) allowed for the exposure of the detector to quasi-monochromatic neutrons. The SiC100 was exposed to D-D neutrons to complement the D-T spectroscopy performed in [14] at the same facility. Three angles were chosen (0°, 30° and 50°) in order to characterize the responses to three different neutron energies (3.15, 3.05 and 2.95 MeV, respectively).

The pulse height spectrum obtained is shown in Figure 6, where the pulse height value was converted to E_{d} by calibrating the detector with the Am_{241} α-source used as described in Section 3.3. Energy thresholds of 300 keV for the measurement at 0° and 600 keV for the 30° and 50° measurements were used in order to ignore noise.

The spectra are dominated by the deposition of energy through elastic scattering reactions, whose cross section is dominant in the lower energy ranges ($E_{\mathrm{n}} < 4\ MeV$). Since in the scattering process, the energy that can be deposited ranges from 0 to a maximum value, the pulse height spectrum features an edge. The shoulder position depends on the neutron energy and on the target nucleus: elastic scattering on carbon $(^{12}C(n,n)^{12}C)$ is clearly visible for $E_{\mathrm{d}} \simeq 0.8 - 0.9$ MeV for all three angles, while the edge due to scattering on silicon $(^{28}Si(n,n)^{28}Si)$ is only visible for the 0° data at lower E_{n}. Table 2 shows that the E_{d} of the four shoulders slightly overestimates the maximum E_{d} based on theory, defined as a fraction of E_{n} ($E_{\mathrm{d_{max}}} = 0.28 \times E_{\mathrm{n}}$ for the carbon, $E_{\mathrm{d_{max}}} = 0.13 \times E_{\mathrm{n}}$ for the silicon).

Table 2. Expected and measured positions of the elastic edges for both ^{12}C and ^{28}Si for the three positions.

	^{12}C(n,n′)^{12}C		^{28}Si(n,n′)^{28}Si	
Angle (deg)	**Meas. (MeV)**	**Theor. (MeV)**	**Meas. (MeV)**	**Theor. (MeV)**
0	0.91	0.882	0.43	0.4095
30	0.9	0.854	-	-
50	0.86	0.826	-	-

The measured spectra were then compared to the results of a Monte Carlo simulation performed with the GEANT4 code, in which the 3D geometry of the SiC active volume, the contacts and the aluminum front panel was reproduced. The interaction of 3×10^8 neutrons from a 1-D monochromatic beam was simulated for each of the three energies.

The simulated spectrum was then broadened with a Gaussian function, in order to simulate the effect of the detector's energy resolution; the broadening chosen as a first approximation was 12% of the E_n value. The simulated spectra obtained are plotted in Figure 6. The number of occurrences of the three angles was normalized to the simulation data.

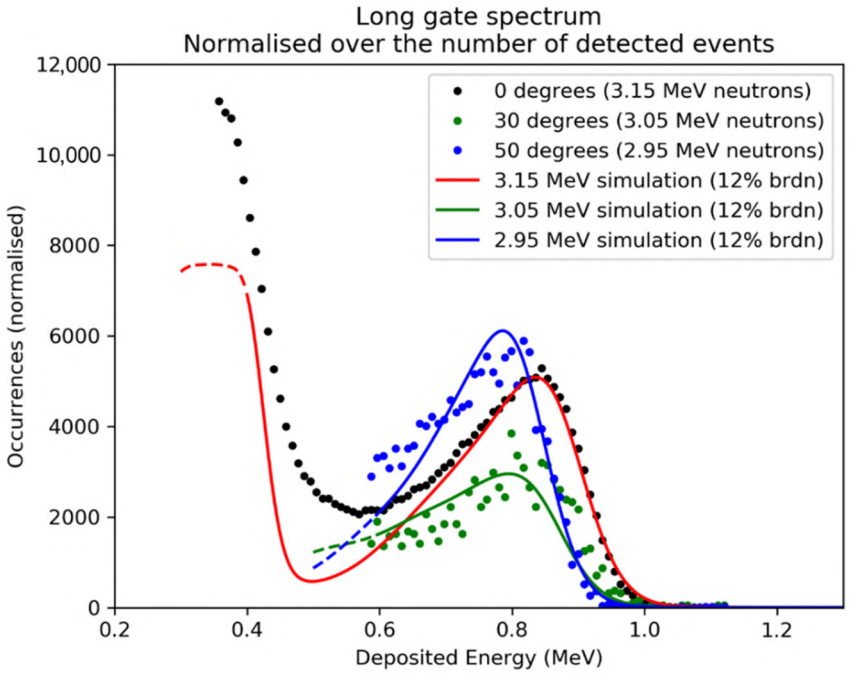

Figure 6. Deposited energy spectra for three different neutron energies at the FNG (3.1, 3.05 and 2.95 MeV). The number of events is normalized. The three sets are compared to three GEANT4 simulations, simulating 3×10^8 monochromatic neutrons. The simulated spectra obtained were broadened through a Gaussian convolution with FWHM = 12% of the energy value, in order to emulate the detector's energy resolution. Simulations are plotted as continuous lines and normalized to fit the data.

6. Conclusions

The stability of two silicon carbide detectors (SiC) was tested under the irradiation of α-particles and neutrons. Both detectors were tested under a $\simeq 10^7 \frac{\alpha}{mm^2}$ irradiation and proven to have stable responses, efficiencies and energy resolutions. Both detectors were also tested with fast spallation neutrons at two different ISIS facilities and proven to have stable response functions after $\simeq 10^9 \frac{n}{mm^2}$ of neutron irradiation. This stability, which is orders of magnitude longer than the stability proven for diamonds in [17], makes the SiC a good candidate as a neutron counter or spectrometer for installation in the harshest environments, such as the breeding blankets of next-generation tokamaks. In order to achieve this, the functionality of the electronic chain, mainly, the preamplifier, will have to be tested in the future under similar levels of irradiation. An alternative could be to couple the SiC to a preamplifier capable of operating far away from the detector, as done for diamond detectors in [28].

Lastly, a SiC detector was tested with D-D quasi-monochromatic neutrons in order to complement the work in [14]. Three energies in the vicinity of E_n = 3 MeV were tested, showing elastic scattering on carbon to be the most robust detection mechanism. The spectra were compared to an ideal simulation with a 12% energy resolution broadening, finding a good agreement. This confirms the possibility of using the SiC as a spectrometer for D-D neutrons.

Author Contributions: Conceptualization, M.R., M.T. and E.P.C.; data curation, M.H.K. and M.R.; formal analysis, M.H.K. and M.R.; funding acquisition, E.D.M. and A.T.; investigation, M.H.K., M.R., M.T. and E.P.C.; methodology, M.R. and E.P.C.; project administration, F.L.V., L.M., M.P. (Miriam Parisi), A.T. and G.G.; resources, C.A., C.C., F.L.V., A.M., M.P. (Mario Pillon) and S.T.; software, M.H.K.; supervision, M.T. and S.T.; validation, C.C., F.L.V., A.M., M.P. (Mario Pillon) and S.T.; visualization, M.H.K. and M.R.; writing—original draft, M.H.K.; writing—review and editing, M.R., M.T. and C.C. All authors have read and agreed to the published version of the manuscript.

Funding: This research received no external funding.

Institutional Review Board Statement: Not applicable.

Informed Consent Statement: Not applicable.

Data Availability Statement: The data presented in this study are available on request from the corresponding author. The data are not publicly available due to restriction imposed by the home institution.

Conflicts of Interest: The authors declare no conflict of interest.

References

1. Ericsson, G. Advanced Neutron Spectroscopy in Fusion Research. *J. Fusion Energy* **2019**, *38*, 330–355, doi:10.1007/s10894-019-00213-9.
2. Rigamonti, D.; Giacomelli, L.; Gorini, G.; Nocente, M.; Rebai, M.; Tardocchi, M.; Angelone, M.; Batistoni, P.; Cufar, A.; Ghani, Z.; et al. Neutron spectroscopy measurements of 14 MeV neutrons at unprecedented energy resolution and implications for deuterium–tritium fusion plasma diagnostics. *Meas. Sci. Technol.* **2018**, *29*, 045502.
3. Available online: https://www.euro-fusion.org/devices/jet/ (accessed on 20 December 2020).
4. Giacomelli, L.; Nocente, M.; Rebai, M.; Rigamonti, D.; Milocco, A.; Tardocchi, M.; Chen, Z.J.; Du, T.F.; Fan, T.S.; Hu, Z.M.; et al. Neutron emission spectroscopy of D-T plasmas at enhanced energy resolution with diamond detectors. *Rev. Sci. Instrum.* **2016**, *87*, 11D822.
5. Thomason, J.W.G. The ISIS spallation neutron and muon source—the first thirty-three years. *Nucl. Instrum. Methods Phys. Res. Sect. A Accel. Spectrometers Detect. Assoc. Equip.* **2019**, *917*, 61–67.
6. Giacomelli, L.; Rebai, M.; Fazzi, A.; Cippo, E.P.; Tardocchi, M.; Frost, C.D.; Pietropaolo, A.; Rhodes, N.; Schooneveld, E.; Gorini, G. Pulsed neutron beam measurements with diamond detectors. *Nucl. Instrum. Methods Phys. Res. Sect. A* **2013**, *720*, 125–127.
7. Rebai, M.; Andreani, C.; Fazzi, A.; Frost, C.D.; Giacomelli, L.; Gorini, G.; Milani, E.; Cippo, E.P.; Pietropaolo, A.; Prestopino, G.; et al. Fission diamond detector tests at the ISIS spallation neutron source. *Nucl. Phys. B* **2011**, *215*, 313–315.
8. Available online: www.iter.org (accessed on 20 December 2020).
9. Franceschini, F.; Ruddy, F.H. Silicon Carbide Neutron Detectors. *Prop. Appl. Silicon Carbide* **2018**, doi:10.5772/15666.
10. Szalkai, D.; Ferone, R.; Issa, F.; Klix, A.; Lazar, M.; Lyoussi, A.; Ottaviani, L.; Tutto, P.; Vervisch, V. Fast Neutron Detection with 4H-SiC Based Diode Detector up to 500 °C Ambient Temperature. *IEEE Trans. Nucl. Sci.* **2016**, *63*, 1491–1498, doi:10.1109/TNS.2016.2522921.
11. Ruddy, F.H.; Siedel, J.G. Effects of gamma irradiation on silicon carbide semiconductor radiation detectors. *IEEE Nucl. Sci. Symp. Conf. Rec.* **2006**, *1*, 583–587. doi:10.1109/NSSMIC.2006.356223.
12. Moscatelli, F.; Scorzoni, A.; Poggi, A.; Bruzzi, M.; Sciortino, S.; Lagomarsino, S.; Wagner, G.; Nipoti, R. Radiation hardness of minimum ionizing particle detectors based on SiC p+n junctions. *IEEE Nucl. Sci. Symp. Conf. Rec.* **2005**, *1*, 490–494, doi:10.1109/NSSMIC.2005.1596300.
13. Tudisco, S.; Altana, C.; Boscardin, M.; Calcagno, L.; Ciampi, C.; Cirrone, G.A.P.; Fazzi, A.; Giove, D.; Gorini, G.; Labate, L.; et al. Silicon carbide for future intense luminosity nuclear physics investigations. *Nuovo Cimento Della Societa Italiana Di Fisica C* **2019**, *42*, 1–4, doi:10.1393/ncc/i2019-19074-1.
14. Rebai, M.; Rigamonti, D.; Cancelli, S.; Croci, G.; Gorini, G.; Cippo, E.P.; Putignano, O.; Tardocchi, M.; Altana, C.; Angelone, M.; et al. New thick silicon carbide detectors: Response to 14 MeV neutrons and comparison with single-crystal diamonds. *Nucl. Instrum. Methods Phys. Res. Sect. A Accel. Spectrometers Detect. Assoc. Equip.* **2019**, *946*, 162637, doi:10.1016/j.nima.2019.162637.
15. Kushoro, M.H.; Rebai, M.; Dicorato, M.; Rigamonti, D.; Altana, C.; Cazzaniga, C.; Croci, G.; Gorini, G.; Lanzalone, G.; La Via, F.; et al. Silicon Carbide characterization at the n_TOF spallation source with quasi-monoenergetic fast neutrons. *Nucl. Instrum. Methods Phys. Res. Sect. A Accel. Spectrometers Detect. Assoc. Equip.* **2020**, *983*, 164578, doi:10.1016/j.nima.2020.164578.
16. Sato, Y.; Shimaoka, T.; Kaneko, J.H.; Murakami, H.; Isobe, M.; Osakabe, M.; Tsubota, M.; Ochiai, K.; Chayahara, A.; Umezawa, H.; et al. Radiation hardness of a single crystal CVD diamond detector for MeV energy protons. *Nucl. Instrum. Methods Phys. Res., Sect. A* **2015**, *784*, 147–150.
17. Rebai, M.; Fazzi, A.; Cazzaniga, C.; Croci, G.; Tardocchi, M.; Cippo, E.P.; Frost, C.D.; Zaccagnino, D.; Varoli, V.; Gorini, G. Time-stability of a Single-crystal Diamond Detector for fast neutron beam diagnostic under alpha and neutron irradiation. *Diam. Relat. Mater.* **2016**, *61*, 1–6, doi:10.1016/j.diamond.2015.11.002.
18. Ruddy, F.H.; Dulloo, A.R.; Seidel, J.G.; Das, M.K.; Ryu, S.H.; Agarwal, A.K. The fast neutron response of silicon carbide semiconductor radiation detectors. *IEEE Nucl. Sci. Symp. Conf. Rec.* **2004**, *7*, 4575–4579. doi:10.1109/nssmic.2004.1466901.

19. Tudisco, S.; La Via, F.; Agodi, C.; Altana, C.; Borghi, G.; Boscardin, M.; Bussolino, G.; Calcagno, L.; Camarda, M.; Cappuzzello, F.; et al. Sicilia—silicon carbide detectors for intense luminosity investigations and applications. *Sensors* **2018**, *18*, 2289, doi:10.3390/s18072289.
20. Available online: https://civideC.At/ (20 December 2020).
21. Pietropaolo, A.; Andreani, C.; Rebai, M.; Giacomelli, L.; Gorini, G.; Cippo, E.P.; Tardocchi, M.; Fazzi, A.; Rinati, G.V.; Verona, C.; et al. Single-crystal diamond detector for time-resolved measurements of a pulsed fast-neutron beam. *Europhys* **2010**, *92*, 68003.
22. Schäfer, W.; Jansen, E.; Skowronek, R.; Will, G.; Kockelmann, W.; Schmidt, W.; Tietze-Jaensch, H. Setup and use of the ROTAX instrument at ISIS as angle-dispersive neutron powder and texture diffractometer. *Nucl. Instrum. Methods Phys. Res. Sect. A Accel. Spectrometers Detect. Assoc. Equip.* **1995**, *364*, 179–185.
23. Cazzaniga, C.; Frost, C.D. Progress of the Scientific Commissioning of a fast neutron beamline for Chip Irradiation. *J. Phys. Conf. Ser.* **2018**, *1021*, 012037.
24. Chiesa, D.; Nastasi, M.; Cazzaniga, C.; Rebai, M.; Arcidiacono, L.; Previtali, E.; Gorini, G.; Frost, C.D. Measurement of the neutron flux at spallation sources using multi-foil activation. *Nucl. Instrum. Methods Phys. Res. Sect. A Accel. Spectrometers Detect. Assoc. Equip.* **2018**, *902*, 14–24.
25. ASTAR-NIST Catalogue. Available online: https://physics.nist.gov/PhysRefData/Star/Text/ASTAR.html (accessed on 1 November 2020).
26. Rebai, M.; Milocco, A.; Giacomelli, L.; Cippo, E.P.; Tardocchi, M.; Fazzi, A.; Pietropaolo, A.; Gorini, G. Response of a single-crystal diamond detector to fast neutrons. *J. Instrum.* **2013**, *8*, doi:10.1088/1748-0221/8/10/P10007.
27. Available online: https://www-nds.iaea.org/exfor/endf.htm (accessed on 1 November 2020).
28. Angelone, M.; Cardarelli, R.; Paolozzi, L.;Pillon, M. Development of a low-noise amplifier for neutron detection in harsh environment. *Eur. Phys. J. Plus* **2014**, *129*, 1–5, doi:10.1140/epjp/i2014-14205-1.

5.3 Paper 3

Performance of a thick 250 µm silicon carbide detector: stability and energy resolution

M.H. Kushoro, M. Rebai, F. La Via, A. Meli, L. Meda, M. Parisi, E. Perelli Cippo, O. Putignano, A. Trotta and M. Tardocchi

Journal of Instrumentation
(2023) 18 C03007

Summary:

This paper describes the first characterizations performed on two SiC250, SiC-D and SiC-E. Prototypes are tested with alpha particles following the same process conducted in the past for thinner prototypes. The new custom-developed preamplifier is tested as well. A stable detection is demonstrated, along an energy resolution that, if projected to DT neutrons, could become the lowest achieved so far with a SiC detector (1.3%). Some difficulties in reaching a full depletion are highlighted, as long as perspectives of a partial depleted operation of the detectors.

Journal of Instrumentation

PAPER • **OPEN ACCESS**

Performance of a thick 250 μm silicon carbide detector: stability and energy resolution

Published by IOP Publishing for Sissa Medialab

Received: *January 12, 2023*
Accepted: *February 9, 2023*
Published: *March 15, 2023*

5th International Conference Frontiers In Diagnostics Technologies
Enea Frascati Research Centre, Frascati, Italy
19–21 October 2022

Performance of a thick 250 µm silicon carbide detector: stability and energy resolution

M.H. Kushoro,[a,b,*] M. Rebai,[b] F. La Via,[c] A. Meli,[c,e] L. Meda,[d] M. Parisi,[d] E.P. Cippo,[b] O. Putignano,[a,b] A. Trotta[d] and M. Tardocchi[b]

[a] *Dipartimento di Fisica "G. Occhialini", Università di Milano-Bicocca, 20126 Milano, Italy*
[b] *Istituto per la Scienza e Tecnologia dei Plasmi, Consiglio Nazionale delle Ricerche, 20126 Milano, Italy*
[c] *Institute for Microelectronics and Microsystems, Consiglio Nazionale delle Ricerche, VIII Strada, 5, 95121 Catania, Italy*
[d] *ENI S.p.A. CENTER—Renewable Energy & Environmental R & D, 28100 Novara, Italy*
[e] *Università di Catania, 95123 Catania, Italy*

E-mail: m.kushoro@campus.unimib.it

Abstract: Silicon carbide detectors represent an alternative to diamond detectors for fast neutron detection in harsh environments, especially fusion plasmas. Previous studies on thin prototypes (either 10 µm or 100 µm thick) suggested that thicker active volumes might be better suited for spectroscopy measurements, due to the higher chance of retaining the neutron interaction products inside the active volume. Therefore, in this work two 250 µm SiC prototypes are tested with alpha particles following the same process conducted in the past for thinner prototypes. A stable detection is demonstrated, along an energy resolution that, if projected to DT neutrons, could become the lowest achieved so far with a SiC detector (1.3%). Some difficulties in reaching a full depletion are highlighted, as long as perspectives of a partial polarization operation of the detectors.

Keywords: Solid state detectors; Neutron detectors (cold, thermal, fast neutrons); Nuclear instruments and methods for hot plasma diagnostics

*Corresponding author.

https://doi.org/10.1088/1748-0221/18/03/C03007

Contents

1 Introduction

Solid State Detectors (SSD) are object of interest in the field of fast neutron detection and spectroscopy in tokamaks [1]. Their solid structure, ability to discriminate neutrons from gamma radiation [2] and insensitivity to magnetic field makes them prime candidates for neutron detection close to the plasma [3]. Furthermore, the fact that their detection mechanism doesn't rely on a conversion stage outside the active volume allows for very low energy resolutions. In perspective, their small dimensions also allow for their installation in arrays enabling the survey of the tokamak volume along multiple lines of sight [4]. There are also solid prospects for the functionality of SiC in harsh environments (such as high temperature [5, 6] or high radiation [7–10]) such as the one encountered inside the breeding blanket (or, in general, close to the plasma).

There is abundant research on both silicon and diamond SSDs, enshrining the latter as the state of art for SSDs fast neutron detection [4, 11–17]. The silicon carbide detector (SiC), on the other hand, has received less coverage: while it combines the reaction channel of both silicon and carbon (leading to a more complicated response of the detector [18, 19]) there is a larger experience on manufacturing SiC wafers up to 200 mm in diameter with a low degree of defects, allowing for purer and cheaper detectors when compared to diamond (the maximum dimension of which is about $5 \times 5\,\mathrm{mm}^2$). SiC has also been proven more stable than diamond [20], since the latter has been proven to experience a loss of counts over prolonged irradiation due to a polarization effect [21, 22]. There are also more solid perspectives for high temperature operation for the SiC [6, 23] than the diamonds [5, 24, 25]: this drives the interest on furthering the research on the SiC as a fast neutron detector for fusion plasma harsh environments [7, 26].

2 Detectors and scope

Silicon carbide active volume is made by a hexagonal lattice of 50% silicon and 50% carbon, grown by the means of CVD technique [27] on a substrate. Contrarily to diamond detectors (which are intrinsic semiconductors), the SiC is structured as an inversely polarized p–n junction in which a depletion region is formed by applying a reverse bias. The interaction of a neutron on

2023 JINST 18 C03007

an atom of the lattice inside the depletion region creates ions and/or charged particles (depending on the type of reaction triggered) which are slowed down inside the lattice, generating a number of electron-hole pairs proportional to the energy deposited by the neutron (E_d). Those pairs are separated by the electric field in the diode generating a current pulse proportional to E_d, which can be read at the two electrodes of the active volume.

Some prototypes of silicon carbide were tested in the past under neutron and alpha particle irradiation (while the interest in the detection of the latter is marginal, alphas are used as a more manageable, easy-to-handle calibration source). The prototypes were manufactured through a collaboration between INFN and IMM-CNR [26, 27]. The detectors are grown by the means of CVD technique, having active volumes of either 10 µm or 100 µm thickness and area of the single detector between 12.5 mm^2 and 25 mm^2. They feature a 0.3 µm p-layer with a doping concentration between 10^{18} and 10^{19} cm^{-3}, and a n-layer with a doping concentration of 8×10^{13} cm^{-3} [26]. Their functionality was demonstrated [18] with a 2.7% energy resolution to 14 MeV neutrons [19] and 2.9% to 4.3 MeV alpha particles [20] with a detection stability exceeding by at least two orders of magnitude the limited stability of diamond [21]. The efficiency to neutrons was proven proportional to the active volume size (6×10^{-4} for a 5 mm × 5 mm × 100 µm SiC to 14 MeV neutrons) [18]: the very low efficiency is, perhaps counterintuitively, a feature, since future tokamak DT experiments will be characterized by very high neutron fluences which would saturate a detector with a higher efficiency.

On the other hand, low thicknesses experience more often the loss of the charged products of the neutron interaction before they deposit their entire energy E_d, severely hampering spectroscopic capability [28, 29]. This is true for both SiC10 and SiC100: in fact, one of the most interesting reaction channels for 14 MeV neutrons is $^{12}C(n, \alpha)^9Be$, producing a 5.75 MeV alpha particle [30] which has a range in SiC of about 18.86 µm (path which is comparable with the SiC thicknesses). This range was obtained by averaging the projected range for carbon (16.20 µm) and silicon (21.52 µm) through the continuous slowing down approximation, as obtained from the ASTAR NIST catalogue [31] assuming a SiC density of 3.22 g/cm^2 [27]. Considering this, a relevant percentage of high-E_d products in the SiC100 (and a vast majority of high-E_d products in the SiC10) will escape the lattice before depositing their energy, hampering the energy resolution and the detection quality. This is part of the reason by which the absolute value of the energy resolution to 14 MeV neutrons (14 MeV × 2.7% = 378.0 keV [19]) is higher than the absolute value to 4.3 MeV alphas (4.3 MeV × 2.9% = 124.7 keV [20]).

This consideration drove the interest toward thicker SiC detectors. A new series of prototypes of thickness 250 µm ("SiC250") were developed in the same collaboration above though the same CVD technique and with similar doping [32]. The new thickness brought forward some unprecedented requirements for the polarization required to fully deplete the active volume. In fact, the depletion region extends parallelly to the surface of the active volume to a depth d as a function of the bias potential V. From [33]:

$$d \simeq \sqrt{\frac{2\varepsilon_{SiC}}{eN_A} \cdot V}$$

By substituting the dielectric constant of the silicon carbide $\varepsilon_{SiC} = 8.633 \times 10^{-11} \frac{C^2}{N\,m^2}$, the electron charge $e = 1.602 \times 10^{-19}$ C, the n-layer doping concentration $N_A = 8 \times 10^{13}$ cm^{-3} and

2023 JINST 18 C03007

reversing the equation, we obtain that the potential needed to fully deplete the 250 µm active volume is 4600 V. Such high voltage is unachievable at present date, due to the limits imposed by the preamplifier; as such, it was chosen to conduct a preliminary alpha particle irradiation on a partially polarized SiC in order to test its functionality, obtain the energy resolution of the new detector and evaluate its stability, similarly to what was performed in [20]. Since the alpha particle source chosen was an americium-241 source (emitting alphas with energy $E_\alpha = 5.49$ MeV, which are then slowed down in air) a 100 V bias was chosen in order to deplete 36.7 µm of the detector, which is deep enough to fully stop the alpha particles.

3 Experimental setup

The detectors and the electronic chain are depicted in figure 1. Two different SiC250 prototypes, named SiCD and SiCE, are installed in aluminum casings connected with the ground, acting as a Faraday cage. Each of the detectors is connected to a Cividec SiC Amplifier [34], which was developed on the specific characteristics of the SiC. The preamplifier conveys the supplied HV to the detector and amplifies the signal obtained, forming it into a 100 ns long semi-Gaussian shape. The signal is then read by a CAEN 5730 analog to digital converter [35] which identifies events through a threshold-over-baseline method.

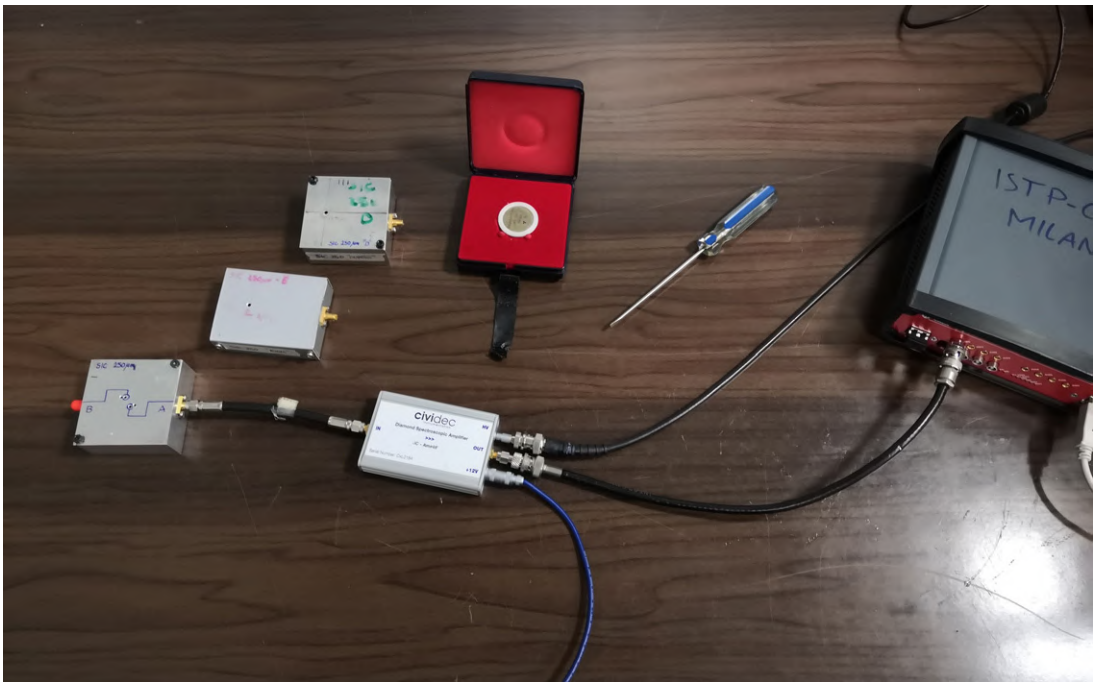

Figure 1. Experimental setup. On the right the three SiC detectors are shown inside their aluminum casing (from top to bottom: SiCD, SiCE and a third SiC, not used in this work). The bottom SiC is connected to the Cividec Preamplifier, powered by a 12 V power source (blue cable at the bottom) and supplying the detector the bias tension (top cable). The middle cable feeds the signal, shaped by the preamplifier, to the CAEN 5730 ADC (on the right). The electrodeposited ^{241}Am source (on top, inside the red box) is put on the top of the aluminum casings, the holes in which allows alphas to reach the active volumes beneath.

2023 JINST 18 C03007

The irradiation source is an electrodeposited ^{241}Am source moderated in air. The Americium decay produces a constant flux of 5.49 MeV alpha particles, which are slowed down in the air between the source and the surface of the detector. By measuring the distance and the stopping power of air [31] the energy of the alpha interacting with the SiC was calculated for each of the detectors: 4.17 MeV for the SiCD and 4.69 MeV for the SiCE. The path in air of all alpha particles was assumed constant, due to:

- The alpha particle flux was conveyed through a hole in the aluminum casing, allowing for a collimation of the particles.
- The ratio between the mean total path within the CSDA approximation and the projection along the direction of emission of the alpha particles is 0.9925 [31]: since the two values are equal within a 1% uncertainty, the straggling can be neglected, and all alpha particles can be assumed to walk a straight path.

Following the same process performed in [20] the signals detected were grouped up in five-minute spectra, on which a gaussian fit favouring the higher energies of the gaussian (the right side) was performed. From the fit three information are extracted:

- Number of counts every five minutes, which is proportional to the detector efficiency to alphas.
- Center value of the gaussian, which gives information about the response function.
- Full width at half maximum of the gaussian (FWHM), obtained from the σ of the gaussian fit via FWHM $= 2\sqrt{2 \cdot \ln 2} \cdot \sigma$.

Such information is computed every five minutes along all the irradiations for each of the two detectors and plotted as a function of time. The two irradiations lasted for 72 h and 86 h, consisting in alpha fluences up to $\phi \simeq 9.2 \times 10^7$ cm^{-2}. The goal is to demonstrate the stability of the detection by proving that the three quantities above do not change as a function of time and irradiation. By dividing the FWHM by the center value of the Gaussian, a first estimate of the energy resolution of the setup (SiC250 + new preamplifier) can be obtained.

4 Results

The value of the number of counts, center value of the Gaussian and energy resolution obtained in every five-minute interval is plotted in figure 2. The absence of drifts in all three quantities for both detectors proves the detection stability. The only visible drift is the SiCE pulse height, which slightly declines by about 1.5% in the region between 200000 seconds to 250000 second ($\simeq$14 hours); the fact that the drift is comparatively small and has no analogue in the other quantities suggests it could be due to changes in the air stopping power due to humidity or temperature shifts rather than actual variation in the response function of the detectors.

By taking the mean value of the energy resolution we can obtain the energy resolution of the two detectors, which is reported in the table below. In the same table is also reported the FWHM and the projected value of energy resolution to 14 MeV neutrons if the same FWHM (and, thus, the absolute value of the energy resolution) is kept the same. The same values for SiC100 from [20] are also reported, paired with the energy resolution to 14 MeV neutrons obtained through experiment [19].

2023 JINST 18 C03007

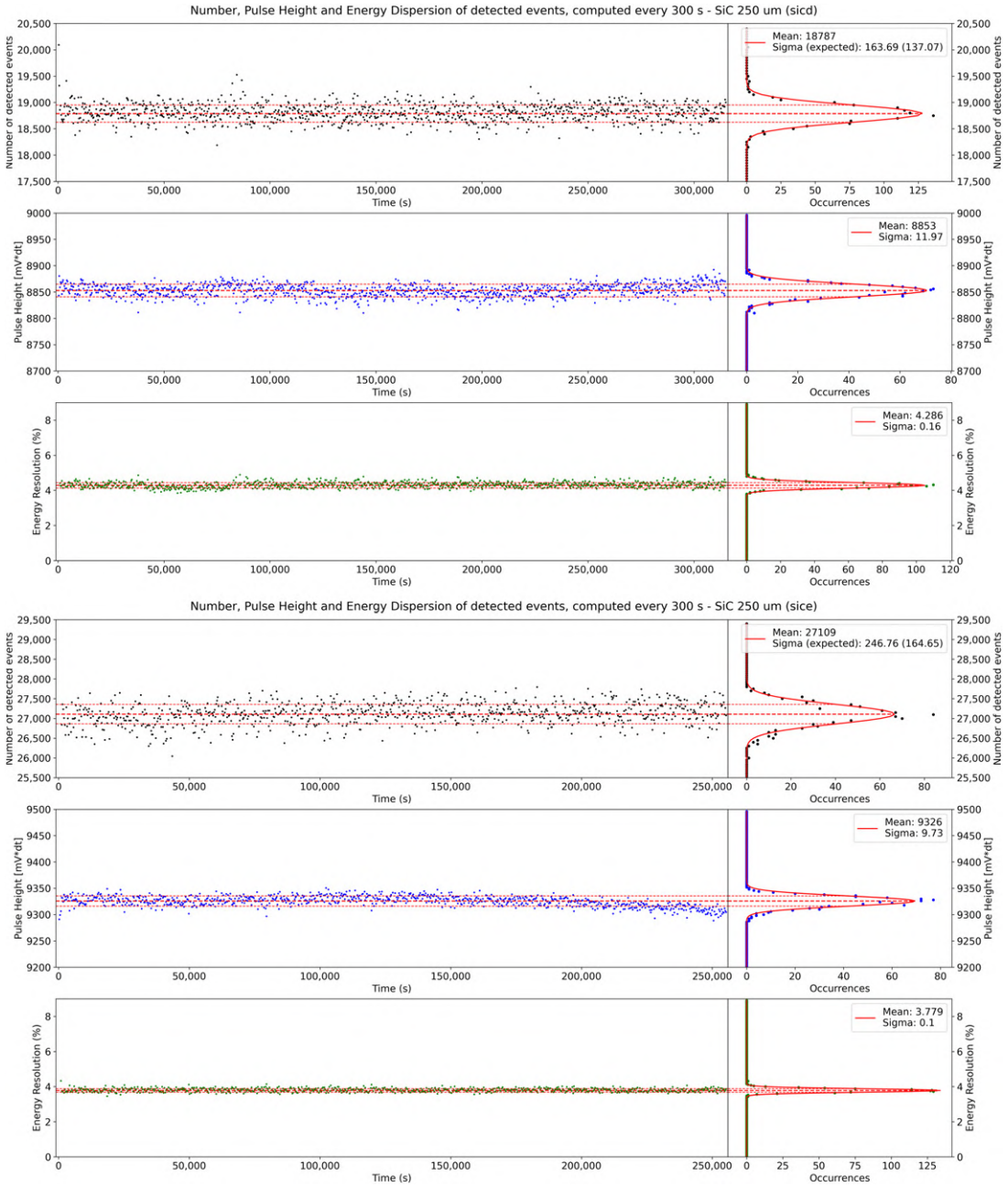

Figure 2. Time evolution of the number of counts (black), the mean pulse height (blue) and the energy resolution (green) for the two SiC250, SiCD (top) and SiCE (bottom), under irradiation of monochromatic alpha particles (4.17 MeV and 4.69 MeV respectively). Each of the points correspond to a 300 s ensemble. On the right, the dispersion of the data is projected on the *y*-axis, computing the mean value of the three quantities along with its standard deviation. For the number of counts the standard deviation is compared to the expected dispersion due to statistical error (equal to the square root of the number of counts). The figure is the direct analogue of figure 3 from [20] for the SiC250.

2023 JINST 18 C03007

Detector name	Energy resolution (alpha energy)	Full width at half maximum	Projected value of energy resolution to 14 MeV neutrons
SiCD	4.30% (4.17 MeV)	179.31 keV	1.28%
SiCE	3.80% (4.69 MeV)	178.22 keV	1.27%
			En. Res. to 14 MeV Neut. (experiment)
SiC100	2.89% (4.3 MeV) [20]	124.7 keV [20]	2.7% [19]

The energy resolution to alphas obtained for both detectors is higher (and, thus, worse) than the 2.89% value obtained on the SiC100 (corresponding to a FWHM = 124.7 keV). In order to exclude the possibility of the higher energy resolution being due to the new preamplifier 30 minutes irradiations were performed with the same setup and the preamplifier used in [19], yielding an energy resolution of 4.57% (for the SiCD). The worst performance, therefore, could be due to dark currents flowing inside the active volume adding to the integral of the signal and therefore broadening its spectrum. Such currents are presumably due to trapped charges into crystal defects [36], which are expected to be more common in thicker SiCs [32, 37].

5 Conclusions

Two prototypes of silicon carbide detector with unprecedented thicknesses (250 µm) were tested with monoenergetic alpha particles. Their stability to fluences up to $\phi \simeq 9.2 \times 10^7$ cm^{-2} were proven by verifying the invariability of counting efficiency, response function and energy resolution along a two to three days irradiation to monoenergetic alpha particles: this confirms that SiC250 prototypes share the same good stability of the 10 µm and 100 µm counterparts assessed in [20]. The energy resolution to alphas obtained was nearly equal for two prototypes (around 179 keV FWHM, resulting in a 3.8% energy resolution to 4.69 MeV alphas and 4.3% resolution to 4.17 MeV alphas). Both resolutions are higher than the one demonstrated with a 100 µm SiC in [20]: this could be due to dark currents flowing inside the 250 µm detectors, possibly due to a higher density of defects and charge-trapping sites.

Nevertheless, if the FWHM of the detectors can be maintained to 14 MeV neutrons, the two thick SiCs coupled with the new electronics could reach a 1.27% energy resolution, which would be unprecedented for the SiC, putting them almost on par with the best energy resolutions achieved with diamonds (1% [14]). This would require very high bias voltages (4600 V) to fully deplete the thick crystals, which is unreachable with the current electronics. The functionality proven in this paper, though, suggests that it is possible to use the detectors even with a partial depletion region, which would allow for an online tuning of the size of the active volume, and therefore the efficiency of the detector. This might prove also a feature for high temperature operation, where lower biases have been demonstrated to be more suitable for the detection [6, 23]. All these perspectives will be analyzed in an upcoming work.

2023 JINST 18 C03007

References

[1] G. Ericsson, *Advanced neutron spectroscopy in fusion research*, *J. Fusion Energy* (2019) **38** 330.

[2] F.H. Ruddy et al., *Development of a silicon carbide radiation detector*, *IEEE Trans. Nucl. Sci.* **45** (1998) 536.

[3] J.M. Gómez-Ros, *Solid state detectors for neutron radiation monitoring in fusion facilities*, *Radiat. Meas.* **71** (2014) 421.

[4] M. Tardocchi et al., *High rate neutron and gamma ray spectroscopy of magnetic confinement fusion plasmas*, 2020 *JINST* **15** C01010.

[5] C. Weiss et al., *High-temperature performance of solid-state sensors up to 500 °C*, *Nucl. Instrum. Methods Phys. Res., Sect. A* **1040** (2022) 167182.

[6] D. Szalkai et al., *Fast neutron detection with 4H-SiC based diode detector up to 500 °C ambient temperature*, *IEEE Trans. Nucl. Sci.* **63** (2016) 1491.

[7] F. La Via, *Silicon carbide devices for radiation detection and measurements*, *J. Phys.: Conf. Ser.* **1561** (2020) 012013.

[8] A. Owens, & A. Peacock, *Compound semiconductor radiation detectors*, *Nucl. Instrum. Methods Phys. Res., Sect. A* **531** (2004) 18.

[9] E.V. Kalinina et al., *Performance of p–n 4H-SiC film nuclear radiation detectors for operation at elevated temperatures (375 °C)*, *Tech. Phys. Lett.* **34** (2008) 210.

[10] G. Bertuccio et al., *Study of silicon carbide for x-ray detection and spectroscopy*, *IEEE Trans. Nucl. Sci.* **50** (2003) 175.

[11] C. Cazzaniga et al., *A diamond based neutron spectrometer for diagnostics of deuterium–tritium fusion plasmas*, *Rev. Sci. Instrum.* **85** (2014) 11E101.

[12] A. Muraro et al., *First neutron spectroscopy measurements with a pixelated diamond detector at JET*, *Rev. Sci. Instrum.* **87** (2016) 11D833.

[13] M. Rebai et al., *Response function of single crystal synthetic diamond detectors to 1–4 MeV neutrons for spectroscopy of D plasmas*, *Rev. Sci. Instrum.* **87** (2016) 11D823.

[14] D. Rigamonti et al., *Neutron spectroscopy measurements of 14 MeV neutrons at unprecedented energy resolution and implications for deuterium-tritium fusion plasma diagnostics*, *Meas. Sci. Technol.* **29** (2018) 045502.

[15] M. Rebai et al., *Fission diamond detector tests at the ISIS spallation neutron source*, *Nucl. Phys. B Proc. Suppl.* **215** (2011) 313.

[16] L. Giacomelli et al., *Pulsed neutron beam measurements with diamond detectors*, *Nucl. Instrum. Methods Phys. Res., Sect. A* **720** (2013) 125.

[17] L. Giacomelli et al., *Neutron emission spectroscopy of DT plasmas at enhanced energy resolution with diamond detectors*, *Rev. Sci. Instrum.* **87** (2016) 11D822.

[18] M. Rebai et al., *New thick silicon carbide detectors: response to 14 MeV neutrons and comparison with single-crystal diamonds*, *Nucl. Instrum. Methods Phys. Res., Sect. A* **946** (2019) 162637.

[19] M.H. Kushoro et al., *Silicon carbide characterization at the n_TOF spallation source with quasi-monoenergetic fast neutrons*, *Nucl. Instrum. Methods Phys. Res., Sect. A* **983** (2020) 164578.

[20] M.H. Kushoro et al., *Detector response to D–D neutrons and stability measurements with 4H silicon carbide detectors*, *Materials* **14** (2021) 568.

[21] M. Rebai et al., *Time-stability of a single-crystal diamond detector for fast neutron beam diagnostic under alpha and neutron irradiation*, *Diamond Relat. Mater.* **61** (2016) 1.

[22] M. Hodgson et al., *Neutron detection performance of silicon carbide and diamond detectors with incomplete charge collection properties*, *Nucl. Instrum. Methods Phys. Res., Sect. A* **847** (2017) 1.

[23] J.H. Ha et al., *4H-SiC PIN-type semiconductor detector for fast neutron detection*, *Prog. Nucl. Sci. Technol.* **1** (2011) 237.

[24] R. Pilotti et al., *Development and high temperature testing by 14 MeV neutron irradiation of single crystal diamond detectors*, 2016 *JINST* **11** C06008.

[25] M. Angelone et al., *High temperature response of a single crystal CVD diamond detector operated in current mode*, *Nucl. Instrum. Methods Phys. Res., Sect. A* **943** (2019) 162493.

[26] S. Tudisco et al., *Silicon carbide for future intense luminosity nuclear physics investigations*, *Il Nuovo Cimento C* **42** (2019) 74.

[27] S. Tudisco et al., *SiCILIA-silicon carbide detectors for intense luminosity investigations and applications*, *Sensors* **18** (2018) 2289.

[28] F.H. Ruddy et al., *The fast neutron response of 4H silicon carbide semiconductor radiation detectors*, *IEEE Trans. Nucl. Sci.* **53** (2006) 1666.

[29] K. Sedlackova et al., *Properties of SiC semiconductor detector of fast neutrons investigated using MCNPX code, 19th International Conference on Applied Physics of Condensed Matter* available on ResearchGate: https://www.researchgate.net/publication/284191754_Properties_of_SiC_semiconductor_detector_of_fast_neutrons_investigated_using_MCNPX_code.

[30] https://www.nndc.bnl.gov/qcalc/.

[31] https://physics.nist.gov/PhysRefData/Star/Text/ASTAR.html.

[32] A. Meli et al., *Epitaxial growth and characterization of 4H-SiC for neutron detection applications*, *Materials* **14** (2021) 976.

[33] G.F. Knoll, *Radiation Detection and Measurement*, John Wiley & Sons, New York (2010).

[34] https://cividec.at/index.php?module=public.category&cat=5.

[35] https://www.caen.it/products/dt5730/.

[36] M. De Napoli, *SiC detectors: a review on the use of silicon carbide as radiation detection material*, *Front. Phys.* **10** (2022) 898833.

[37] F. La Via et al., *Mechanisms of growth and defect properties of epitaxial SiC*, *Appl. Phys. Rev.* **1** (2014) 031301.

2023 JINST 18 C03007

5.4 Paper 4

Partially Depleted Operation of 250µm-thick Silicon Carbide Neutron Detectors

M.H. Kushoro, M. Angelone, D. Bozzi, G. Gorini, F. La Via, E. Perelli Cippo, M. Pillon, M. Tardocchi, and M. Rebai

Nuclear Instruments and Methods in Physics Research: A
Submitted 7 August 2023 – Under Review

Summary:

Following the observation on partial depleted operation of the SiC250 in the previous paper, this paper acknowledges the perspectives of such operation for high flux environments. The paper also describes the characterization of a series of SiC250 detectors (SiC-A, SiC-B, SiC-D and SiC-E) operated with a fraction of the polarization needed to achieve full depletion. Two SiC10 (SiC-C and SiC-L) are also tested as a comparison. The characterization is performed through I/V measurements, alpha irradiation in vacuum and neutron irradiation. A functionality with excellent detection characteristics is demonstrated, reaching an energy resolution of 1.05% for 5.5 MeV alphas and 2.05% for 14 MeV neutrons. Some limitations on the maximum bias will be also discussed, pointing out some challenges for the manufacturing of thick SiCs in the future.

Nuclear Instruments and Methods in Physics Research A 1058 (2024) 168918

Contents lists available at ScienceDirect

Nuclear Inst. and Methods in Physics Research, A

journal homepage: www.elsevier.com/locate/nima

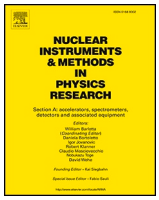

Partially depleted operation of 250 μm-thick silicon carbide neutron detectors

M.H. Kushoro [a,b,*], M. Angelone [c], D. Bozzi [a], G. Gorini [a], F. La Via [d], E. Perelli Cippo [b], M. Pillon [c], M. Tardocchi [b], M. Rebai [b]

[a] Dipartimento di Fisica "G. Occhialini", Università di Milano-Bicocca, 20126, Milano, Italy
[b] Istituto per la Scienza e Tecnologia dei Plasmi, Consiglio Nazionale delle Ricerche, 20126, Milano, Italy
[c] Associazione EURATOM-ENEA Sulla Fusione ENEA C.R. Frascati, 00044, Frascati, Italy
[d] Institute for Microelectronics and Microsystems, Consiglio Nazionale delle Ricerche, 95121, Catania, Italy

ARTICLE INFO

Keywords:
SiC detectors
Solid state detectors
Neutronics
Fusion plasma
Fusion diagnostics

ABSTRACT

Fusion experiments put many challenges on the neutron detection methods, since they require fast neutron counters and spectrometers with good energy resolution capable of operating in harsh environments under a large range of neutron flux intensities. Recently, SiC detectors were proposed for these roles due to their outstanding properties. Among those, the operation of SiC with partial polarization is of interest since it might allow for a fast neutron detector with efficiency tunable online, which would allow a good functionality under a large range of flux intensities.

This paper describes the characterization of a series of SiC detectors operated with a fraction of the polarization needed to achieve full depletion. The characterization is performed through I/V measurements, alpha irradiation in vacuum and neutron irradiation. A functionality with excellent detection characteristics is demonstrated, reaching an energy resolution of 1.05 % for 5.5 MeV alphas and 2.05 % for 14 MeV neutrons. Some limitations on the maximum bias will be also discussed, pointing out some challenges for the manufacturing of thick SiCs in the future.

1. Introduction

The use of Solid-State Detectors (SSDs) for fast neutron detection and spectroscopy is expanding, since fusion plasma advancements require fast, compact neutron detectors with good energy resolution inspecting the plasma [1]. Among SSDs, Silicon Carbide (SiC) has received attention [2,3,4,5] as an alternative manufacturing material to diamond, which constitute the state-of-art of SSDs [6,7,8,9,10,11]: in fact, while featuring detection characteristics similar to diamonds (in terms of efficiency, energy resolution and more [12]), SiC detectors have a more mature technological background thanks to the experience matured in power devices for electric vehicles. SiC detectors are also produced in wafers with large dimensions (150 mm, to be expanded to 200 mm in the near future), as opposed to diamonds featuring only small substrates (5 mm) and a higher density of defects [4]. For all these reasons, SiC detectors can be produced in a more scalable, industrialized way that allows for lower costs of production without compromising the detection performance. A collaboration between CNR-ISTP and CNR-IMM is ongoing, manufacturing and characterizing a series of SiC-based detectors. The goal is to assess their potential as fusion plasma monitors and to find their optimal characteristics (in terms of geometry, quality of the active volume, etc.) for them to operate as neutron detectors and/or spectrometers for the harsh environments in upcoming fusion plasma experiments (like SPARC or ITER).

After the experience gained in the past on sensors with 10 μm and 100 μm thicknesses [12,13,14], a series of SiC detectors with active region with a 250 μm thickness (which will be referred to as SiC250 from now on) was manufactured [15]. The interest toward higher thicknesses was justified by the need of reducing partial charge deposition effect: lower thicknesses, in fact, increase the statistical relevance of energetic neutron reaction products leaving the active volume without depositing the entirety of their energy, leading to an incorrect relation between the deposited energy and the detected signal (thus worsening the spectra quality and the energy resolution). Higher thicknesses have also a benefic effect on the carrier lifetime [15], which also lead to an improvement of the signal. On the other hand, since voltage bias needed

* Corresponding author. Dipartimento di Fisica "G. Occhialini", Università di Milano-Bicocca, 20126, Milano, Italy.
E-mail address: m.kushoro@campus.unimib.it (M.H. Kushoro).

https://doi.org/10.1016/j.nima.2023.168918
Received 8 August 2023; Received in revised form 26 October 2023; Accepted 9 November 2023
Available online 13 November 2023

to achieve full depletion of the active volume of SiC scales quadratically with the thickness (see Section 2), it is impossible to achieve full depletion of the thickest prototypes with current electronics. Nevertheless, an experience on two SiC250 prototypes (detailed in Ref. [16]) revealed that SiC detectors can detect alpha particles with a good stability and energy resolution ($\simeq$ 4 % @4.2 MeV) even while using a fraction of such bias voltage. Since there is a dependence between the efficiency of the detector to neutrons and the depth of the depletion region (which, in turn, depends on the bias applied) the use of a partially polarized SiC presents itself as a way to tune online the efficiency of the detector. This might be a very desirable feature for detectors expected to work under very different neutron fluxes: this is particularly true for neutron detectors in Tokamaks capable of tritium operation, where the neutron flux is predicted to span five order of magnitude and more [17].

The perspectives for a neutron detector with tunable efficiency based on SiC calls for the characterization of the operation of SiC250 while partially polarized. In this article four different SiC detectors, described in Section 2 and 3, are characterized through a I/V scan (Section 4), an alpha irradiation in vacuum (Section 5) and a 14 MeV neutron irradiation (Section 6), finding the detection characteristics as a function of polarizations up to 150 V. Results and conclusion will be drawn in the last section (Section 7).

2. Detector principles

SiC SSDs active volume is made by a doped silicon carbide lattice arranged either in a p-n configuration or as a Schottky diode. The application of an inverse bias potential on the two active volume ends causes the growth of a depletion region whose extension d in the crystal as a function of the bias potential V_{bias} [18]:

$$d \simeq \sqrt{\frac{2\epsilon \cdot V_{bias}}{e \cdot n_A}}$$

Where n_A is the n-side doping level (measured in m^{-3}), e the electron charge and ϵ the dielectric constant of SiC [19].

The depletion region, being emptied from free charge carriers, has a very high resistivity. When an energetic particle interacts with the atoms of the lattice, it causes them to ionize, generating a number of electron-hole (e-h) pairs proportional to the energy deposited by the particle in the crystal (E_d). Such electron and holes act as charge carriers, decreasing abruptly the resistivity of the active volume and allowing for a fast current signal. In the case of fast neutrons, the interaction is with a nucleus of a lattice atom: this can occur through different reaction channels (either scatterings or nuclear reactions, each of which has a unique relation between the neutron energy E_n and E_d) and it's "point-like" (i.e., the neutron likely undergoes a single disruptive interaction inside the active volume of the detector). Since the probability of a neutron interacting with a medium is equal to the path traveled inside the detector times the macroscopic cross section (which is constant for neutrons with the same energy in the SiC), there is a direct proportionality between the probability of an interaction occurring inside the depleted region and the depth of the depleted region. If the detector can only measure neutrons interacting with the depleted volume, the probability of a neutron being detected (i.e., the detector's efficiency) is directly linked to the depleted region depth, which is, in turn, linked to V_{bias}.

If full depletion is achieved, in a 250 µm active volume the electrons and holes drift in the lattice for a $\tau_{drift} = 2.82ns$ (calculated from formula 1 in page 2 of reference [13] and from formula 1 in page 2 of reference [20]). From this, the typical currents involved in the detection I can be estimated from the energy needed to produce a e-h pair in the SiC ($E_{eh} = 8.0eV$):

$$I = \frac{E_d}{E_{eh}} \cdot \frac{2e}{\tau_{drift}}$$

Assuming a particle depositing $E_d = 7MeV$ as a reference, we obtain a typical current of $99.5\mu A$. This puts an upper limit of about $\simeq 100\mu A$ on the current flowing through the depleted region in the steady state, called leakage current: higher leakage currents would have random fluctuations that would submerge the signal from the particles, making that indistinguishable from the noise [18].

3. Detector prototypes and setup

The SiC detector prototypes were developed by CNR-IMM, in a collaboration with INFN and CNR-ISTP. Four 250 μm-thick SiC detectors (named SiCA, SiCB, SiCD and SiCE) were assembled and tested. The detectors active volume is made by a n-layer doped with a $8{\cdot}10^{13} cm^{-3}$ concentration of nitrogen, grown by the means of the Chemical Vapor Deposition (CVD) technique [21]. All four devices were realized with a Ni_2Si Schottky contact that gives a Schottky barrier height of 1.6 eV at RT [22]. The top metallization is completed by a thin Ti layer (80 nm) that acts as a metallurgical barrier and a thicker Al layer (1 µm) that is needed for the bonding. The backside metallization is realized also by a Ni_2Si layer but annealed at higher temperature (1000 °C) with respect to the front side metallization (650 °C). The detail mechanism of the Schottky-Ohmic transition is explained in Ref. [23].

SiCA and SiCB differs from the other two by being a couple of early prototypes made as a test of the manufacturing process, while SiCD and SiCE are two fully developed prototypes with a complete characterization, the results of which are detailed in Ref. [15]. SiCA and SiCB also share the same substrate, as it can be seen in Fig. 1. A thin SiC with 10 µm of epitaxial layer thickness (named SiCL) was also tested along the thicker models. This detector was manufactured using a p^+ epitaxial layer on the surface through a more complex process described in Ref. [24]. All the detectors are installed on printed circuit boards and encased in an aluminum casing acting as a faraday cage to shield them from environmental EM-radiation. Data on the detectors are collected in Table 1.

The signal extracted from all the SiCs is fed to a preamplifier developed ad-hoc by Cividec, based on the Cx-L preamplifier [25]. The preamplifier shapes the signal into a semi-gaussian shape with 100 ns FWHM, 50 ns rise time, and a 120 ns fall time. The gain of the

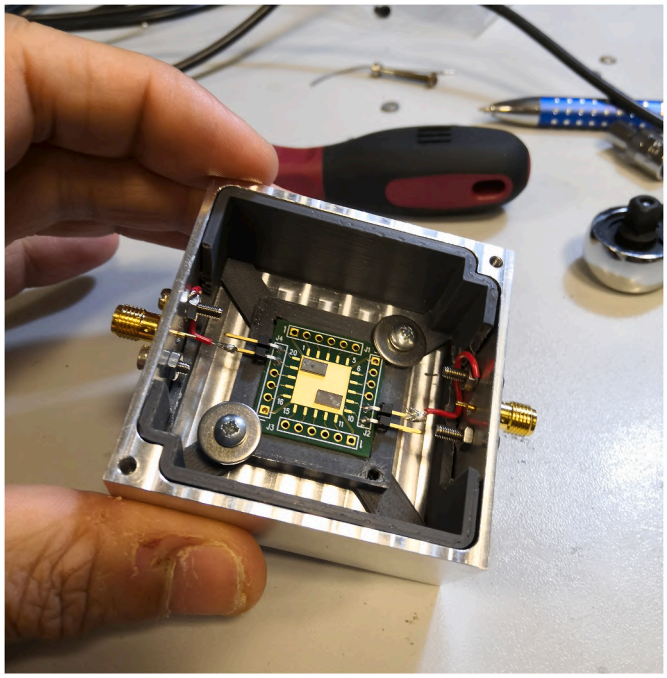

Fig. 1. Picture of the SiCA and SiCB installed inside the aluminum casing.

Table 1
List of the names of the five SiC detectors used in this paper along with their sizes, contact types and thicknesses.

Detector Name	Thickness	Area	Contact Type	Other …
SiCA	250 μm	2.5 mm × 5 mm	Schottky	Early prototype
SiCB	250 μm	2.5 mm × 5 mm	Schottky	Early prototype
SiCD	250 μm	5 mm × 5 mm	Schottky	
SiCE	250 μm	5 mm × 5 mm	Schottky	
SiCL	10 μm	5 mm × 5 mm	p/n junction	

preamplifier is 4.1 mV/fC, meaning that a particle depositing 5.5 MeV of energy will result in a signal with a 188 mV amplitude after amplification. The signal is then transmitted to a 500 MHz CAEN 5730 ADC [26] that samples the waveform and saves the data on a hard drive. The bias potential is produced by a 710 Quad 1 kV Ortec Bias Supply module [27] having a precision of ± 1 V and is transmitted to the detector through the preamplifier.

A preliminary I/V characterization was conducted, studying the evolution of the leakage current of the detectors as a function of the bias HV in the range between 0 and 500 V. The study was performed using a Keithley 6487 Picoamperometer [28], which was used both as a current readout and voltage source. The detectors were directly connected to the Picoamperometer without any preamplification stage. The current reading was performed through an automatic procedure developed ad-hoc, through which the current value is the mean current calculated between $t_{start} = 30s$ and $t_{stop} = 37s$, with $t_0 = 0s$ being the moment in which the new voltage value was set. The 30s wait between the set of the voltage value and the start of the readout was put in place for the dark current to reach a stable state regardless of the HV inputted.

The detectors then underwent an alpha particle irradiation in vacuum using the electronics detailed above. The vacuum was produced in a stainless-steel vacuum chamber (shown in Fig. 2) emptied by a rotative pump, allowing for a pressure between $2{\cdot}10^{-2}$ mbar and $7{\cdot}\ 10^{-2}$ mbar. The alpha source is an Americium-241 electrodeposited source manufactured by Campoverde, producing 5.486 MeV alpha particles with a small broadening of less than 20 keV [29]. It must be pointed out that all the 250 μm-thick SiCs were not designed for alpha detection (for example, they feature dead depths on the aluminum contacts that the alpha particles interact with without contributing to the signal formation). In this sense, the alpha characterization was used as a readily available test of functionality for the detectors and as a relative comparison between them more than an absolute estimate of their characteristics.

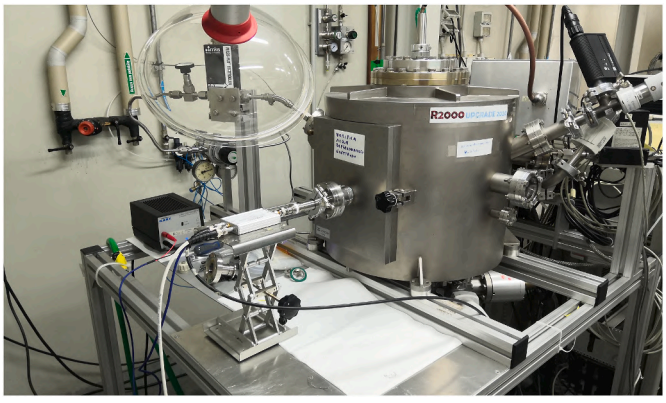

Fig. 2. Picture of the vacuum chamber used for the alpha particle irradiation. The preamplifier (little white box in the center left) is kept outside of the vacuum and is connected to the SiC inside the vacuum chamber through a vacuum-proved feedthrough connector.

Finally, two of the detectors (the 250 μm-thick SiCD and the 10 μm-thick SiCL) were irradiated with 14.1 MeV neutrons at the Frascati Neutron Generator facility (FNG) in Frascati, Italy [30]. The neutrons are produced by a DT fusion reaction obtained with a deuterium beam impinging on a tritium target. The detectors were installed perpendicularly to the beam, as shown in Fig. 3, in order ignore the kinetic contribution of the impinging deuterium to the neutrons and thus irradiating the detectors only with 14.1 MeV neutrons. Each irradiation consisted in mean neutron fluxes between $1.70{\cdot}10^{10} n/s$ and $3.45{\cdot}10^{10} n/s$ over the entire solid angle, corresponding to an approximate neutron flux between $5.4{\cdot}10^{5} n/s$ and $1.1{\cdot}10^{6} n/s$ through each of the detector's surfaces. Both the signals measured with the alpha particles in vacuum (having a known energy) and the spectral structures obtained in the pulse height spectrum in the neutron irradiation were used to calibrate the detector, that is linking the pulse height to E_d (the energy deposited in the detector).

4. I/V characterization

The I/V characterization was performed with the specifics detailed in Section 3 inputting biases between 2 V and 500 V. The results of the four SiC250 are plotted in Fig. 4, along with the SiC10 (SiCL). The SiC250 feature two distinct behaviors:

- SiCD and SiCE, along with the 10 μm thick SiCL, feature a negligible ($< 100pA$) dark current up to a threshold bias, after which a leakage current increases very rapidly with the growing bias, exceeding the 100 μA limit discussed in Section 2. The threshold is between 100 V and 150 V for the two SiC250 (SiCD and SiCE), while it is higher (200 V) for the SiC10. The same behavior happens for the p-n junction 10 μm-thick SiCL though at slightly higher biases (400 V).
- SiCA and SiCB (which share the same substrate) both feature a linear increase of the current with the increasing bias. This resistive behavior is not by design and is reasonably due to either defects in the devices or damage due to previous irradiations. It's worth to stress again that SiCA and SiCB were the earliest iterations of SiC250, made as test prototypes which didn't underwent the same extensive characterization that the other detectors did. By fitting the data with a linear correlation, it can be found the impedance of the two being 2.25 $M\Omega$ for the SiCA and 328.38 $M\Omega$ for the SiCB. The impedance of SiCA is comparable to the one of the preamplifier (5 $M\Omega$) and, therefore, cannot guarantee that the potential difference between the

Fig. 3. Picture of the SiCE and SiCL installed on the FNG facility. The deuterium beam (coming from the right) incide on the tritium target (center of the picture) producing neutrons. The two SiCs are installed beneath the target, perpendicularly to the beam, in order to be irradiated by 14 MeV neutrons.

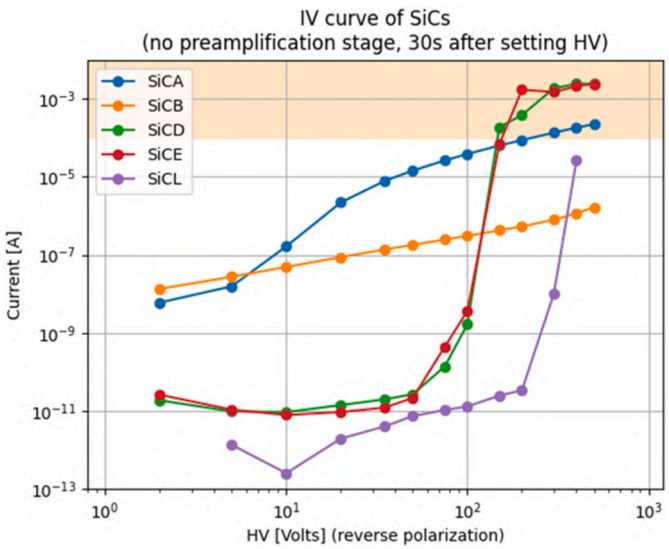

Fig. 4. Behavior of the leakage current (obtained while not under irradiation) as a function of the bias voltage for all the SiCs under investigation. SiCA and SiCB exhibit ohmic behaviour (linear rise of current with potential), while the other incur in a sudden rise of the leakage current after a threshold potential. Currents higher than 100 μA that prevents the functionality of the detector are highlighted in orange.

two ends of the active volume being the same as the one inputted. On the other hand, the resistive behavior of SiCB makes it so that the limit of 100 μA in the leakage current is never reached in the 0–500 V range.

The data shows that the SiCD and SiCE experience a breakdown for lower biases than the SiC10, presumably due to the low efficient edge structure (field plate) of the simple Schottky diode, as opposed to the more sophisticate edge structure of the p/n junction having a junction termination extension (JTE). This puts some limitations in the availability of biases for the SiC250 since high leakage currents prevents the detection process.

5. Alpha particle irradiation in vacuum

The SiCs pulse height spectra while under irradiation of the Am-241 alpha particles were analyzed (an example is reported in Fig. 5). By assuming the alpha particles to be monoenergetic, three detector values

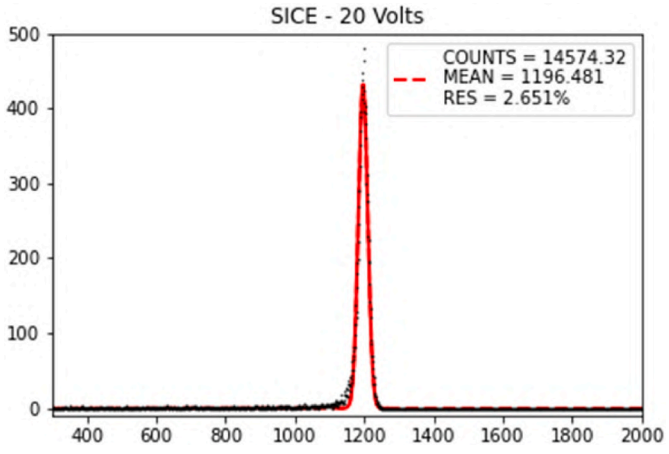

Fig. 5. Exemplificative pulse height spectrum of the SiCE with alphas in vacuum. The gaussian fit in red is used to determine the number of particles detected, the mean value and the energy resolution.

are extracted from the spectra:

- Number of alpha particles detected per unit time by the SiC (which is linked to the detector's charge collection efficiency).
- SiC detectors response function (derived from the mean value of the signals integrals spectra).
- SiC detectors energy resolution (derived from the broadening of the gaussian fit of the spectra $EnRes = \frac{FWHM}{\mu_0} = \frac{2\sqrt{2\ ln(2)}\cdot\sigma}{\mu_0}$, where μ_0 is the mean value of the gaussian fit).

The dependency of the three values to the bias voltage for all the SiCs is depicted in Fig. 6. The bias voltage was limited to 150 V (which is the voltage at which detectors experienced the breakdown - see Section 4).

From the figure some observations can be derived:

- All detectors experience a shift in the response function at lower biases (<50 V) by which reducing the bias the integrals of the pulses (i.e. the charge collected) are also reduced. This is believed to be due to the depletion region for biases lower than 50 V being smaller than the distance traveled by the alpha particles in the SiCs, causing the detector to capture only a fraction of the energy deposited by the slowing down of the particle. To prove this, the path traveled by the 5.486 MeV alpha particles in a 3.21 g/cm^3 SiC material was calculated using the stopping power data from ASTAR NIST [31], averaging between the stopping power values of carbon and silicon. This led to a 26.1 μm path in order to stop the 5.486 MeV alphas in the SiC. This measure was compared with the expected thickness of the depletion region for a 50 V bias, using the first equation of Section 2, obtaining a depletion depth of $d(50V) = 25.95\mu m$. The similarity between the two values is a proof to the thesis above. Another prove comes from the fact that the same plateau in the response function is reached at 7.5 V for the SiCL, which is exactly the value needed to achieve a depletion region of 10 μm (and, thus, achieving its full depletion).

It must also be noted that, at low biases, SiCs still operates very solidly as particle detectors: the number of counts per unit time is unchanged and the rise in the energy resolution follows the shift to lower mean values of the integral (while the FWHM of the signal remains constant).

- The breakdown observed in the previous section for the SiCD and SiCE for biases higher than 100 V has, as expected, a damaging effect on the detection ability of the detector. The detector experiences a sharp rise in the energy resolution due to the high ($\simeq mA$) levels of leakage current. In addition, the detectors also experience a sharp drop (more than −90 %) in the number of counts per second, presumably due to the charges produced by alpha interaction being submerged by the leakage current.
- Even if SiCA and SiCB demonstrated an ohmic behavior (which is not by design) the detection capabilities of the two detectors are not impaired. SiCB demonstrates a very good energy resolution (1.3 % @5.486 MeV). Charge collection efficiency and response functions remain stable, regardless of the leakage current demonstrated in Section 4.

Considering the above considerations, the good functionality of the SiC250 with partial polarization is confirmed for all the biases that do not trigger a breakdown. The best figures for the energy resolution, reported in the legend of Fig. 6, go down to 1.06 % @5.486 MeV for the SiCD. The energy resolution includes the broadening due to the alpha source, but since the latter is at least three times smaller than the former it was neglected. These are one of the smallest energy resolutions achieved by SiC detectors to high energy particles, even if the SiC250s were not manufactured to optimize alpha particle spectroscopy. While the

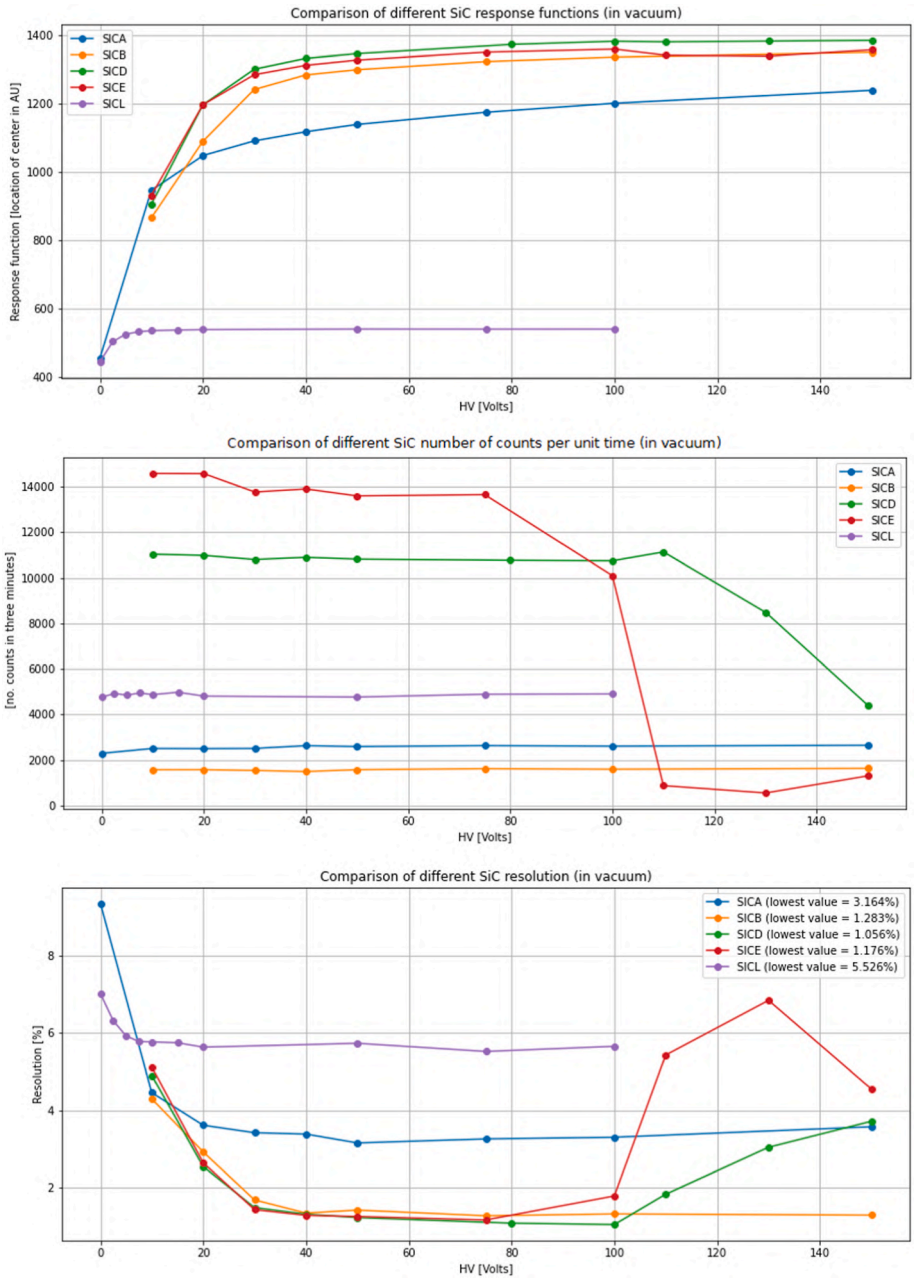

Fig. 6. Evolution of the response function (top), number of counts per unit time (middle) and energy resolution (bottom) of all the SiCs under investigation as a function of the bias voltage. The 150 V threshold for the SiCD and SiCE observed in Fig. 4 is confirmed in the evolution of the three parameters above. The shift in the response function of all detectors at lower biases is due to the bias depleting a detector thickness smaller than the path traveled by the alphas in SiC, causing a partial charge deposition.

energy resolutions obtained are still worse than the best resolutions obtained by other detectors (0.4 % for 5.486 MeV alphas [19,32] and 1 % for 14.1 MeV neutrons [9]) the fact that it was obtained through partially polarized SiCs whose manufacturing did non optimize alpha particle spectroscopy is an extremely encouraging result.

6. DT neutron irradiation

The DT irradiation campaign was conducted performing a scan of the bias voltage. Four biases were used on the SiCD, which are detailed in Table 2 along with the respective depletion region thicknesses. It must be noted that during the experiment the detector was able to operate up to 150 V before incurring in the breakdown preventing the detection, which is a slightly higher threshold than the one incurred in the I/V and alpha characterizations.[1] The 10 μm-thick SiCL was also used to draw a comparison.

Data were gathered in spectra as a function of E_d. To calibrate the pulse height of the signal to E_d, the peaks in the pulse height spectra due to nuclear reactions (like the ones in Figs. 7 and 8) were identified using the spectra in Ref. [12] as a reference and related to their Q-value. By fitting the pulse height with the theoretical E_d with a linear function a

[1] It must be reported that the neutron irradiation was performed chronologically before the alpha and I/V characterization: this opens the hypothesis of this difference being due to some wearing down process and/or neutron damage suffered by the detector reducing the maximum voltage before incurring in the sharp rise of the leakage current.

Table 2
Depletion region depth in the SiCD during neutron irradiation as a function of HV bias applied, as obtained from the relation defined in the first equation of Section 2. Counts and broadening of the C (n,α)Be peak (the only one identified in all four conditions with good statistics) are also reported, obtained as the area underlying the gaussian fit. Counts with the lowest bias are incompatible with the others due to poor functionality of the detector with 7.5 V and were therefore excluded from Fig. 9.

Bias (V)	Depletion region depth (μm)	C (n,α)Be counts	C (n,α)Be peak broadening	Si(n,α)Mg ground state peak broadening
7.5	10	78.75	8.53 %	6.49 %
50	26	178.38	4.09 %	3.30 %
100	37	326.27	3.54 %	2.75 %
150	46	775.38	4.02 %	3.21 %

calibration function was obtained for each irradiation, through which the pulse height was replaced with E_d. Data were also normalized to the same number of neutrons produced at the source; since the position of the detector was unchanged between irradiations, to normalize to the neutrons at the source corresponds to normalize to the neutron fluence through the detector surface. Results are depicted in Figs. 7 and 8.

As before, a number of observations were made on the data:

- Regardless of depletion, 250 μm feature the same E_d spectral shape to neutrons than the ones obtained in the past with fully depleted detectors (see Refs. [12,13]). A notable exception is the 7.5 V spectra, whose features are too broadened out to extract meaningful information.
- 7.5 V spectra differ from the spectra of the 10μm SiC SiCL (Fig. 7). As expected, SiCL feature a spectrum losing many counts in the high E_d region (due to the partial deposition effect) but manages to keep a broadening of the peaks close to the broadening of the SiCE with high biases. On the other hand, the 7.5 MeV spectrum is deteriorated to the point in which features can barely be distinguished, suggesting that the bias is too small to achieve good detector operation.
- A new estimate on the energy resolution to neutrons was computed by taking the gaussian fit of the three identified reactions and by dividing the FWHM (in units of energy) by the energy of the neutrons (i.e., 14.1 MeV). The best results are obtained from the $^{28}Si(n,\alpha)^{25}Mg$ ground state, which is the reaction at the highest E_d. Energy resolution is fairly constant at varying biases, ranging between 2.75 %

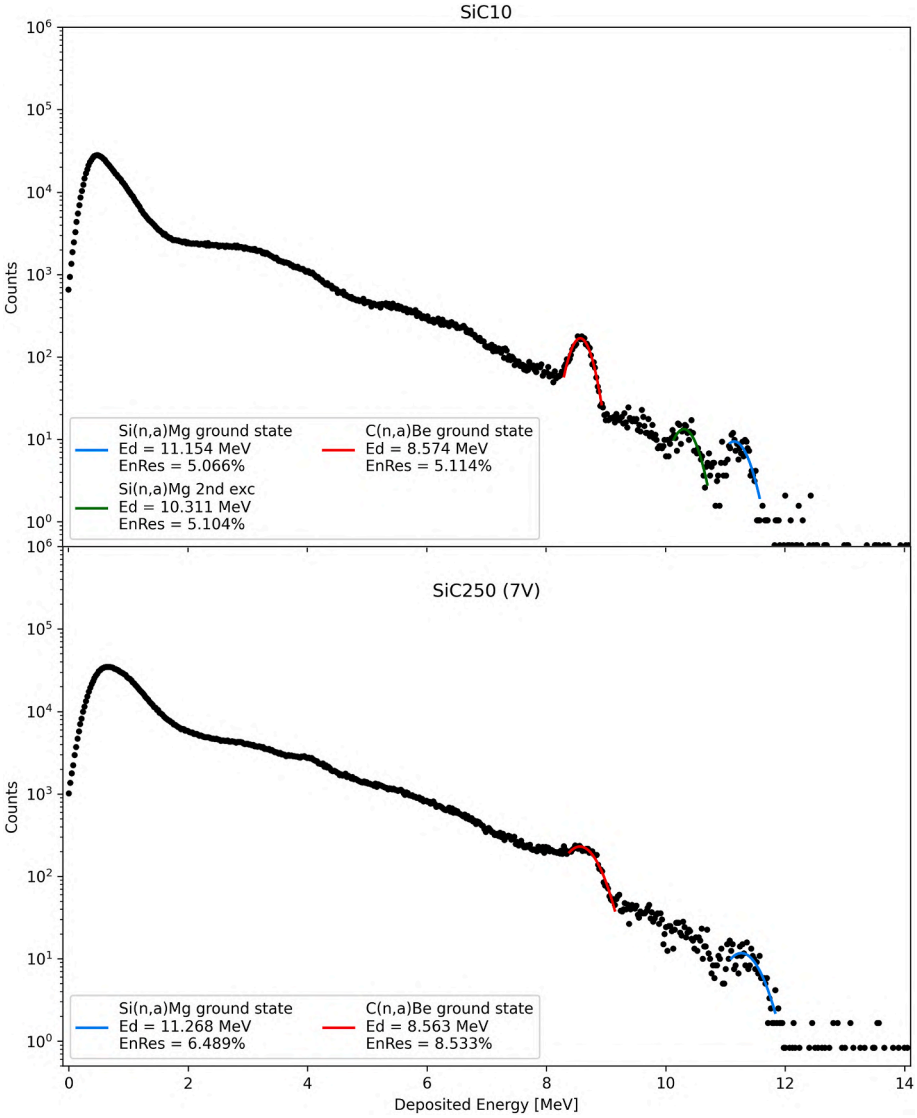

Fig. 7. Deposited energy spectra for the 10 μm-thick SiCL (top) versus the 250 μm-thick SiCE polarized with 7.5 V, which is enough to achieve a 10 μm deep depletion region. The deposited energy is on the x-axis, having a linear scale expressed in MeV, while the counts are on a logarithmic scale. The coloured lines are gaussians fits performed on the ^{12}C (n,α)^{9}Be peak and two of the ^{28}Si(n,α)^{25}Mg peaks.

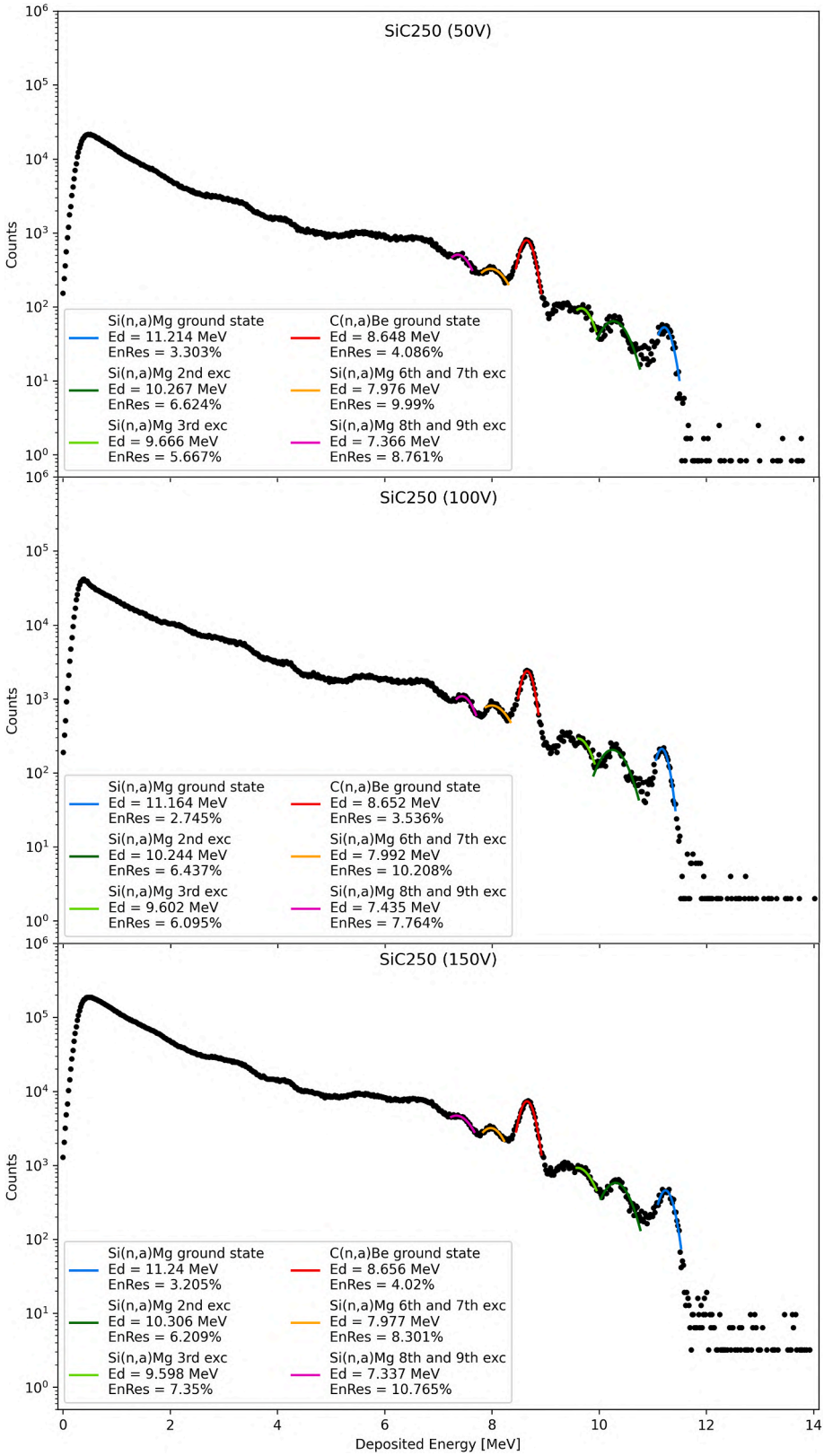

Fig. 8. Deposited energy spectra for the 250 μm thick SiCE polarized with 50 V (top), 100 V (middle) and 150 V (bottom) enough to achieve a depletion region of 26 μm, 37 μm and 46 μm respectively. The deposited energy is on the x-axis, having a linear scale expressed in MeV, while the counts are on the y-axis on a logarithmic scale. The coloured lines are gaussians fits performed on the ^{12}C (n,α)^{9}Be peak and several of the ^{28}Si(n,α)^{25}Mg peaks.

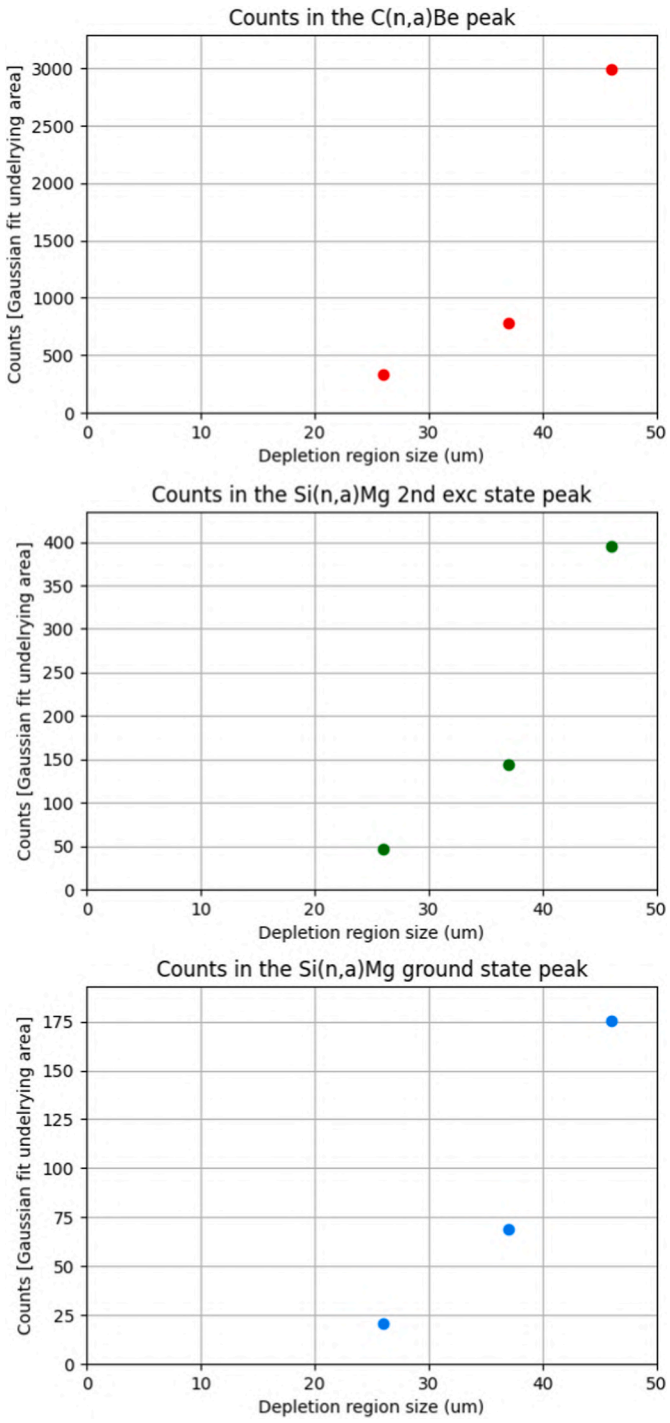

Fig. 9. Number of counts in each of the three peaks from Fig. 8 as a function of the depletion region size, obtained by calculating the area underlying the gaussian fit function (the same values are also reported also in Table 2). The counts were expected to display a linear correlation, but lower HVs feature lower counts than expected.

and 3.3 % @14.1 MeV, with the best resolution falling on the 100 V irradiation. One factor increasing the energy resolution is the ADC settings, which calculated the baseline by performing an integration over a shorter time (128 ns instead of the 2048 ns used for the alphas), increasing the uncertainty of the baseline evaluation and, therefore, the uncertainty of E_d. To assess the magnitude of this factor, a comparison between the pulse height spectra to 4.7 MeV alphas moderated in air with the two different settings was performed, finding it accounting for a increase of 0.7 % in the energy resolution. This corrects the estimate of the energy resolution 2.05 % and 2.6 % @14.1 MeV.

- The number of counts for each reaction for each HV setting was calculated by taking the area underlying the gaussian fit of three of the identified peaks ($^{12}C(n,\alpha)^{9}Be$, $^{28}Si(n,\alpha)^{25}Mg$ ground state and 2° excited state). The higher HVs feature a higher number of counts, as expected from the deepening of the depletion region. On the other hand, a linear relationship between the depth of the region (calculated with the first equation in Section 2) and the number of counts was expected but did not result in the data. Fig. 9 shows that lower HVs feature less counts than expected. The same trend is observed for all the three peaks, ruling out the hypothesis of it being due to a distortion of one of the spectra. The reason behind this could be due instead to the increasing electric field in the active volume of the detector increasing the lifetime of the charge carriers, allowing for a more higher charge collection efficiency. This unpredicted behavior warrants further investigation on the matter in the future.

7. Conclusions

Following the activity detailed in Ref. [16], four 250 μm-thick SiC detectors were tested with the aim of exploring the functionality of the SiC detectors while partially depleted, which could open the perspective for a neutron detector and spectrometer with an efficiency tunable online. An I/V characterization, in combination with an alpha particle irradiation in vacuum, revealed that the detectors experience a junction breakdown, resulting in sudden rise in the leakage current for biases around 150 V, preventing the good detection for higher biases. This behavior can be solved in the future using a more sophisticated edge termination structure to reduce the high electric field at the edge of the device.

Detector were tested for biases <150 V, producing a very low energy resolution to alpha particles (1.05 % @5.5 MeV). One of the detectors was used to detect DT neutrons at the FNG facility, producing recognizable deposited energy spectra with an energy resolution between 2.05 % and 2.6 % @14.1 MeV; this result, despite the partial polarization (having a bias between 50 and 150 V, in front of a 5 kV needed for a full depletion), is already an improvement if compared to the energy resolution achieved with 100 μm-thick SiC detector achieved in the past (2.7 % @14.1 MeV [13]).

Results indicate that the operation with a partially polarized SiC is indeed viable without compromises on the detection characteristics. In the present experiment, a very simple Schottky structure with a field plate edge termination has been used just for the first experiments on very thick epitaxial layers, observing very interesting resolutions both in the case of alpha particles (1.05 % @5.5 MeV) and in the case of neutrons (2.05 % @14.1 MeV). One main limit of this technology is the quality of the edge structure, which should be used to increase considerably the breakdown voltage and then reduce the leakage current in higher biases range (150 V to 5 kV). Another improvement path is achieving a lower doping concentration of the epitaxial layer (about $2 \times 10^{13}/cm^3$) which would allow to obtain a complete depletion with a bias lower than 1 kV. This second aspect is essentially connected to the technology of the electronic chain that cannot work at bias higher than 1 kV.

Declaration of competing interest

The authors declare that they have no known competing financial interests or personal relationships that could have appeared to influence the work reported in this paper.

Data availability

Data will be made available on request.

Acknowledgements

A special acknowledgement goes to the R&D division group of Eni s.p.a., and especially to the Linea 5 line of research, whose contribution was instrumental in making progress with the research activity. The authors thank in particular the contributions from Antonio Trotta, Miriam Parisi and Laura Meda.

References

[1] M. Tardocchi, et al., A high-resolution neutron spectroscopic camera for the SPARC tokamak based on the Jet European Torus Deuterium-Tritium experience, Rev. Sci. Instrum. 93 (11) (2022), 113512, https://doi.org/10.1063/5.0101779.
[2] J.M. Gómez-Ros, Solid state detectors for neutron radiation monitoring in fusion facilities, Radiat. Meas. 71 (2014) 421–424, https://doi.org/10.1016/j.radmeas.2014.05.003.
[3] M. Hodgson, et al., Characterization of silicon carbide and diamond detectors for neutron applications, Meas. Sci. Technol. 28 (13pp) (2017), 105501, https://doi.org/10.1088/1361-6501/aa7f8b.
[4] F. La Via, et al., Silicon Carbide devices for radiation detection and measurements, in: Journal of Physics: Conference Series, vol. 1561, IOP Publishing, 2020, 012013, https://doi.org/10.1088/1742-6596/1561/1/012013.
[5] F.H. Ruddy, et al., Performance and applications of silicon carbide neutron detectors in harsh nuclear environments, in: EPJ Web Conf, vol. 253, ANIMMA 2021 – Advancements in Nuclear Instrumentation Measurement Methods and their Applications, 2021, https://doi.org/10.1051/epjconf/202125311003.
[6] M. Angelone, C. Verona, Properties of diamond-based neutron detectors operated in harsh environments, J. Nucl. Eng. 2 (2021) 422–470, https://doi.org/10.3390/jne2040032.
[7] L. Giacomelli, et al., Neutron emission spectroscopy of DT plasmas at enhanced energy resolution with diamond detectors, Rev. Sci. Instrum. 87 (2016), 11D822, https://doi.org/10.1063/1.4960307.
[8] M. Rebai, et al., Response function of single crystal synthetic diamond detectors to 1-4 MeV neutrons for spectroscopy of D plasmas, Rev. Sci. Instrum. 87 (2016), 11D823, https://doi.org/10.1063/1.4960490.
[9] D. Rigamonti, et al., Neutron spectroscopy measurements of 14 MeV neutrons at unprecedented energy resolution and implications for deuterium–tritium fusion plasma diagnostics, Meas. Sci. Technol. 29 (2018), 045502, https://doi.org/10.1088/1361-6501/aaa675, 9.
[10] M. Tardocchi et al, "High rate neutron and gamma ray spectroscopy of magnetic confinement fusion plasmas", J. Inst. Met. 15 C01010, doi: 10.1088/1748-0221/15/01/C01010.
[11] A. Muraro, et al., First neutron spectroscopy measurements with a pixelated diamond detector at JET, Rev. Sci. Instrum. 87 (2016), 11D833, https://doi.org/10.1063/1.4961557, 10.1063/1.4961557.
[12] M. Rebai, et al., New thick silicon carbide detectors: response to 14 MeV neutrons and comparison with single-crystal diamonds, Nucl. Instrum. Methods Phys. Res. A 946 (2019), 162637, https://doi.org/10.1016/j.nima.2019.162637.
[13] M.H. Kushoro, et al., Silicon Carbide characterization at the n_TOF spallation source with quasi-monoenergetic fast neutrons, Nucl. Instrum. Methods Phys. Res. A 983 (2020), 164578, https://doi.org/10.1016/j.nima.2020.164578.
[14] M.H. Kushoro, et al., Detector response to D-D neutrons and stability measurements with 4H silicon carbide detectors, Materials 14 (2021) 568, https://doi.org/10.3390/ma14030568.
[15] A. Meli, et al., Epitaxial growth and characterization of 4H-SiC for neutron detection applications, Materials 14 (2021) 976, https://doi.org/10.3390/ma14040976.
[16] M.H. Kushoro et al., "Performance of a thick 250 μm silicon carbide detector: stability and energy resolution" J. Inst. Met. 18 C03007, doi: 10.1088/1748-0221/18/03/C03007.
[17] Jinwei Yang, et al., Fusion neutron flux monitor for ITER, Plasma Sci. Technol. 10 (2008) 141.
[18] G.F. Knoll, "Radiation Detection and Measurement", fourth ed., Wiley, Hoboken, 2010.
[19] S. Tudisco, et al., SiCILIA—silicon carbide detectors for intense luminosity investigations and applications, Sensors 18 (2018) 2289, https://doi.org/10.3390/s18072289.
[20] A. Pietropaolo, et al., Single-crystal diamond detector for time-resolved measurements of a pulsed fast-neutron beam, EPL 92 (2010), 68003, https://doi.org/10.1209/0295-5075/92/68003.
[21] F. La Via, et al., Mechanisms of growth and defect properties of epitaxial SiC, Appl. Phys. Rev. 1 (2014), 031301, https://doi.org/10.1063/1.4890974.
[22] F. Roccaforte, et al., Richardson's constant in inhomogeneous silicon carbide Schottky contacts, J. Appl. Phys. 93 (11) (2003) 9137, https://doi.org/10.1063/1.1573750.
[23] F. La Via, et al., Schottky–ohmic transition in nickel silicide/SiC-4H system: is it really a solved problem? Microelectron. Eng. 70 (2003) 519–523, https://doi.org/10.1016/S0167-9317(03)00464-7.
[24] S. Tudisco, et al., Silicon carbide for future intense luminosity nuclear physics investigations, Il Nuovo Cimento 42 C (2019) 74, https://doi.org/10.1393/ncc/i2019-19074-1.
[25] Technical specs, available online: https://cividec.at/electronics-Cx-L.html.
[26] Technical specs, available online: https://www.caen.it/products/dt5730/.
[27] Technical specs, available online: https://www.ortec-online.com/products/electronics/power-supplies-and-nuclear-instrument-module-nim-bins/710.
[28] Technical specs, available online: https://download.tek.com/manual/6487-901-01(B-Mar2011)(Ref).pdf.
[29] Technical specs, available online: https://campoverde.it/wp-content/uploads/2021/10/Catalogo-Campoverde-Sorgenti-di-taratura.pdf. section "Sorgenti per spettrometria alfa").
[30] M. Martone, et al., The 14 MeV Frascati neutron generator, J. Nucl. Mater. 212–215 (1994) 1661.
[31] M. Berger, et al., "ESTAR, PSTAR, and ASTAR: computer programs for calculating stopping-power and range tables for electrons, protons, and helium ions, version 1.21, http://physics.nist.gov/Star, 1999. (Accessed 3 August 2023), http://physics.nist.gov/Star [online].
[32] C. Altana, et al., Radiation damage by heavy ions in silicon and silicon carbide detectors, Sensors 23 (14) (2023) 6522, https://doi.org/10.3390/s23146522.

5.5 Paper 5

Functionality of 250µm-thick SiC Detector to DT Neutrons at High Temperatures

M.H. Kushoro, M. Angelone, D. Bozzi, S. Cancelli, G. Gorini, F. La Via, E. Perelli Cippo, O. Putignano, M. Tardocchi and M. Rebai

Fusion Engineering and Design
Submitted 10 October 2023 – Under Review

Summary:

This paper expands on the previous works by proving the detection of fast neutrons with good detection parameters of a 250µm-thick 4H-SiC detector prototype (SiC-m) at temperatures up to 250°C. The experiment is conducted with similar instrumentation that the one used in the past with diamond detectors, using as source of irradiation the DT generator of ENEA, the Frascati Neutron Generator. SiC-m electronic schematics mimicked the one used in the past to demonstrate the limits in the high temperature operation of the diamond detectors, serving as a comparison between the two SSDs. The SiC's excellent resilience to temperature is presented, highlighting its suitability for operation in high temperature environments like the breeding blanket. Perspectives are drawn to increase the temperature even further in the future.

1. Introduction

The construction of high-power fusion plasma machines, like ITER, is driving the interest toward the development and refining of tokamak technologies. Among those, one critical aspect is the supply of tritium, the production of which is planned to be done in the Breeding Blanket (BB) – a physical region close to the plasma where the fast neutrons interact with ^{6}Li (after being slowed and multiplied) producing tritium through the ^{6}Li(n,α)T and ^{7}Li(n,n+α)T reactions. To date, no volumetric neutron sources with fluences comparable to the ones in a tokamak exist on which to test the BB designs [5-1]. The first of this type of sources will probably be ITER, which will feature a series of Test Blanket Modules (TBM) to experiment four possible designs of tritium production and fuel cycling [5-2]. ITER's data will then be used as a basis for the DEMO design [5-1]. On the other hand, ARC (the successor of SPARC) is prospected to feature a tritium cycle based on liquid metal [5-3] which is still in the conceptual design phase. In any case, to date the knowledge about the practical application of tritium production is very limited, and mostly obtained from numerical simulations. For this reason, the ground is fertile for the development of diagnostics to be installed in future BB experiments to produce data validating the simulations.

The detection of fast neutrons can be useful to both validate the neutron multiplication rate and measure the statistical relevance of the ^{7}Li(n,n+α)T (which has a lower energy threshold of about 2.8 MeV). To do either, though, fast neutron detectors are required to feature small dimensions, intense flux measurement capabilities and an high radiation hardness. It is also required for them to be able to withstand high temperatures, since the temperature range expected inside ITER's TBM is between 300°C and 600°C [5-4]. Both Single Crystal Diamond detectors (SCDs) [5-5][5-6][5-7] and Silicon Carbide detectors (SiCs) [5-8][5-9][5-10] were characterized in the past, prospecting them as good candidates for neutron detection in tokamak's harsh environments. In fact, diamond detectors are already used at JET [5-11] and are part of the design of future tokamaks neutron cameras [5-12]. The functionality of diamond under high temperature (HT) was also studied [5-5][5-13][5-14], finding a strong dependence on the type of contacting and the size of the active volume. Various diamond featured a response declining in quality after 200°C, making them not ideal candidates for BB neutron detection. On the other hand, functionality of SiC under HT was proven on a few occasions (ex: [5-15][5-16]), achieving very promising results. A work detailing the response function of a 4H solid state SiC fast neutron detector without conversion stage as a function of the temperature is still lacking. The scope of this article is then to make the first step towards the characterization of the HT behaviour of the SiC detectors already tested in the past.

2. Instrumentation and Setup

2.1 Detectors

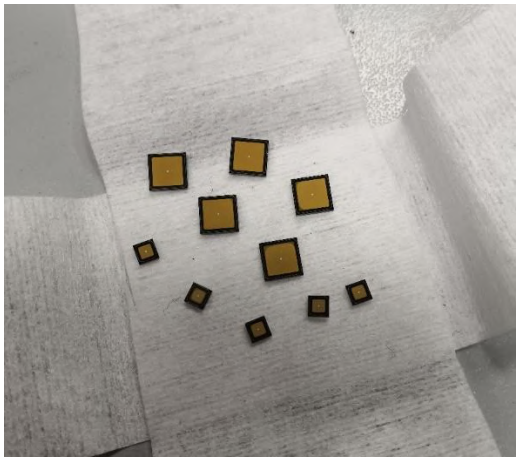

Fig. 1. SiC250 p-n active volumes. The one on top-right is the 5x5 mm^2 used in this article.

The detector under test is made from a 4H-SiC active volume developed by CNR-IMM in Catania, similarly to the detector tested in the past ([5-9][5-17][5-18][5-19]). The volume is a 250 μm thick, 5 mm x 5 mm wide SiC lattice. The active volume differs from the one of the detectors tested in [5-19] since it is arranged in a p-n junction structure as opposed as a Schottky contact. The edge structure was also manufactured with a higher quality, in order to achieve a higher voltage breakdown than the one experimented in [5-19]. For the structure and manufacturing of

the active volume refer to [5-20][5-21], while for the specifics of the active volume used in this work refer to [5-22].

The contacting used for the detector is much different than the ones used in the past. Instead of being welded on a conducting surface of a PCB, the active volume was contacted through pressure, being closed between a solid cable (acting as the line transmitting the HV and the signal) and a stainless-steel scaffold, whose purpose was to keep the detector in place as well as connecting is p-side to the ground of the cable. The reason for choosing a pressure contact was to avoid components incapable to withstand high temperatures without melting or altering electric properties. A picture of the active volumes can be seen in Figure 1, while the scaffold and the contacting can be seen in Figure 2. All the device was then enveloped in conducting tape (connected to the same ground reference of the cable) in order to reduce EM noise.

2.2 Cables and Electronics

Fig. 2. SiC250 active volume with the pressure contacts. The T-shaped steel scaffold is on the left and can move parallel to the mineral cable (on the right) in order to push the signal pin (in the centre) against the active volume, keeping it in position.

The signals collected by the detector were processed by a Cividec SiC preamplifier, which was custom developed on the Cividec CX-L amplifier [5-23]. The signal was then fed to an analog-to-digital convertor CAEN 5730 [5-24], sampling the voltage signal at a 500 MHz rate. Both elements are the same used in the past for 250 µm thick detectors ([5-19]). The transmission of the signal (and the supply of the HV to the active volume) was performed through a custom-made mineral cable manufactured by Thermocoax which features low noises due to temperature and is certified to temperatures up to 1200°C. The cable used was the same used for the diamond detectors by Angelone in [5-13]: the choice was done in order to trace a comparison between the diamond and the SiC with as few differing elements in the setup as possible.

2.3 Heating Mechanism

The high temperatures were achieved through an oven constituted by a resistive spiral winded around a metallic cylinder. The inside of the cylinder is hollow, allowing for the detector and the cable to be inserted from one of the two ends. The cylinder is covered in an insulating foam in order to increase its thermal capacity and allow to soften the temperature gradients, both temporally and spatially. The temperature control was achieved by controlling the amperage of the current flowing through the resistance. The temperature was read through a small (mm-thin) thermistor, with a nominal precision of 0.1 °C. The feedback cycle was performed by hand, altering the current to increase, decrease or keep stable the temperature.

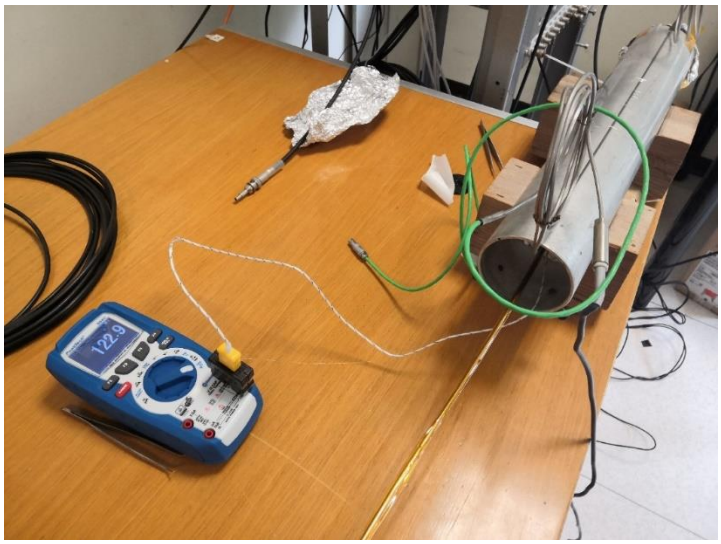

Fig. 3. Cylindrical oven (on the top right) in which the SiC is inserted. The mineral cable, enveloped in a Kapton foil, can be seen emerging from the oven. On the left a multimeter is measuring the temperature inside the oven. The thermistor is inside the oven, in the vicinity of the SiC active volume.

2.4 Neutron Irradiation

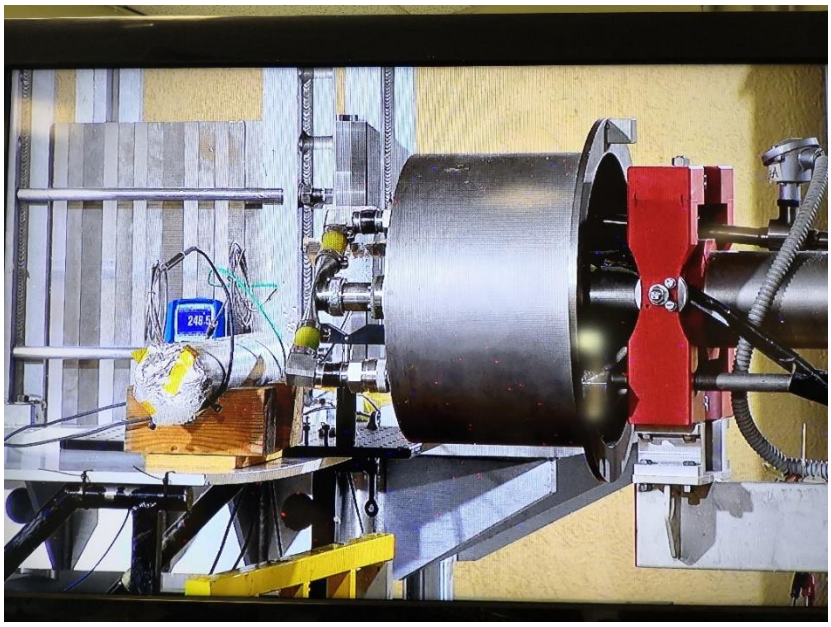

Fig. 4. The entire apparatus (the oven containing the SiC and the cable, the thermistor, the multimeter temperature readout) is on the left, placed in front of the FNG tritium target in the centre. The deuterium beam (on the right) impinges on the target (small T-shaped pipe in the centre), producing DT neutrons along the entire solid angle.

The entire setup was irradiated with DT neutrons at the Frascati Neutron Generator facility [5-25]. Neutrons were generated from a beam of deuterium impinging on a tritium target, as illustrated in Figure 4. Due to cinematic reasons, neutrons are emitted with an energy dependent on the scattering angle, with neutrons emitted perpendicularly to the deuterium beam being 14.06 MeV neutrons. It was not possible to insert the detector setup (and relative mineral cable and oven) on a perpendicular line of sight, so the detector was placed on a 45° angle with respect of the beam, allowing for a flux of neutron with a spectrum centred on 14.6 MeV [5-25].

Irradiations were performed by targeting a temperature and regulating the current in order to reach it within a certain interval of stability. Temperatures chosen were 100°C, 200°C, 250°C and 300°C. At each temperature an irradiation was performed firing between $1.5 \cdot 10^{13}$ and $6.0 \cdot 10^{13}$ neutrons on the whole solid angle. Each

irradiation lasted between 15 and 45 minutes, during which the temperature was kept within ±5°C from the target. A run at room temperature (around 25°C) was also performed before the HT irradiations as a comparison.

3. Results

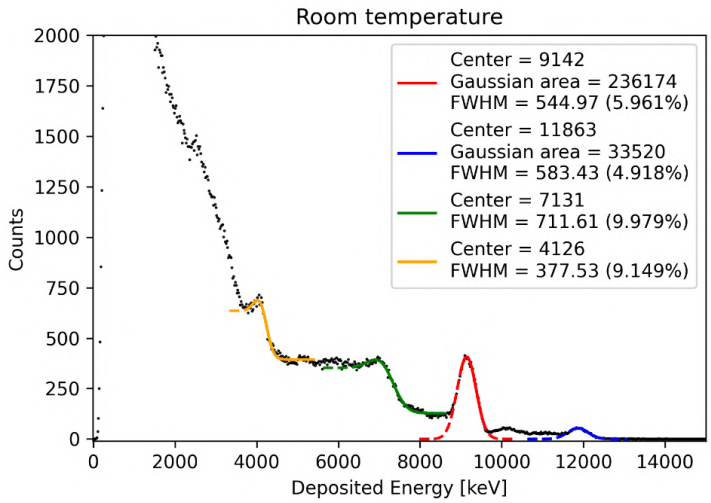

Fig. 5. Deposited energy spectrum obtained with the SiC at room temperature. The typical SiC spectral features are highlighted in different colours: from the highest-energy ones they are ^{28}Si(n,α) ^{25}Mg (in blue), ^{12}C(n,α) ^{9}Be (in red), ^{12}C(n,n)3α (in green) and the elastic scattering on carbon (in yellow). All the features are fitted with either a gaussian function or a step-function convoluted and added to a gaussian: from the parameters of the fits the centre, area and broadening of the spectral feature are extracted, to be compared in Figure 7.

Signals detected during all irradiations were stored and plotted in histograms as a function of their pulse height (PH) integral. Histograms were then calibrated using the most prominent SiC spectral features (see [5-17] for details), obtaining the deposited energy spectra. An exemplificative spectrum is plotted in Figure 5, highlighting the spectral feature on which the spectrum itself is calibrated, as well as the fit parameters of the peaks serving as a basis for the inspection of the detection parameters.

All the calibrated spectra are plotted in one figure in Figure 6 for comparison, after being normalized for the number of neutrons produced in the target during every irradiation. 100°C, 200°C and 250°C spectra present outstanding similarities with the room temperature spectrum, being almost undistinguishable. The only apparent difference between the spectra is the number of low-energy counts in the 250°C irradiation, due to the fact that a rising level of noise submerged the signals with the lowest PH. This, although, do not affect the functionality of the SiC as a neutron detector, since the spectral features of interest are the ones with higher deposited energies. The latter conforms perfectly with the room temperature spectrum even for the 250°C spectrum. This certifies the detection capability of the SiC being unchanged up to 250°C.

The dependence of three detection characteristics, response function, efficiency, and the peak's broadening (measured in terms of FWHM – Full Width at Half Maximum – as a percentage of the mean value of the peak) is plotted as a function of the temperature in Figure 7. The relative flat evolution of the three parameters confirms the excellent solidity to temperature of the SiC, the only exception being in the number of counts for the 250°C irradiation, due to the reduced number of low PH events detailed in the previous paragraph.

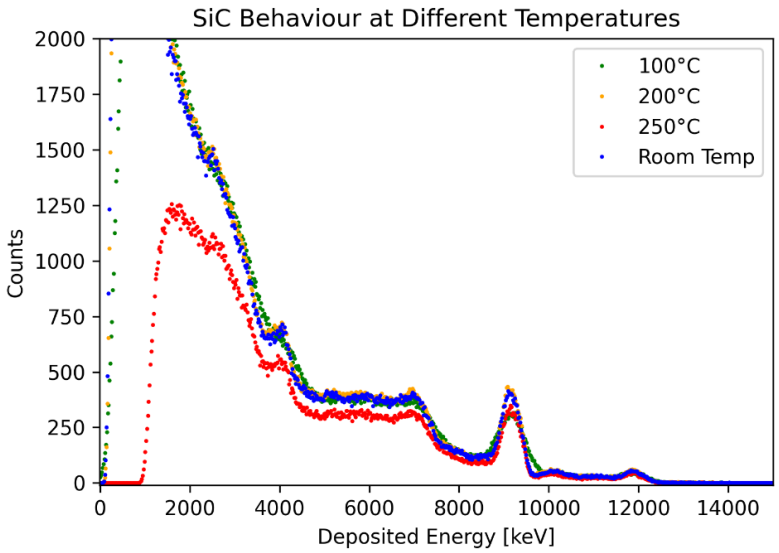

Fig. 6. Comparison between the deposited energy spectrum (after normalization on the number of neutrons) obtained at different temperatures. The remarkable similarities between the spectra at HT and the spectra at RT demonstrate the very stable performance of the SiC at high temperatures.

It was not possible to perform a 300°C spectrum since, while increasing the temperature between 250°C and 260°C, the neutron detection abruptly stopped, as well as the background noise. By reducing the temperature under 250°C again the detection was able to restart. The reason for such an abrupt cutoff in the detection was not confirmed, but, since it is paired with a stop of the noise, it's not deemed probable to be due to a propriety of the SiC active volume. Instead, the most probable cause is a difference in the thermal expansion of the electrical components (the cable and the scaffold) causing a detachment between the hot pin and the active volume. It must be noted, in fact, that the scaffold used did not feature a spring to push the scaffold against the pin, which was instead used by Angelone in [5-13]. In order to prove this an I/V dependence test will be performed with the same setup at the critical temperatures found: if a sudden drop of the leakage current through the detector will be found at temperature between 250°C and 260°C, the detachment will be confirmed as a cause for the SiC's temperature cutoff.

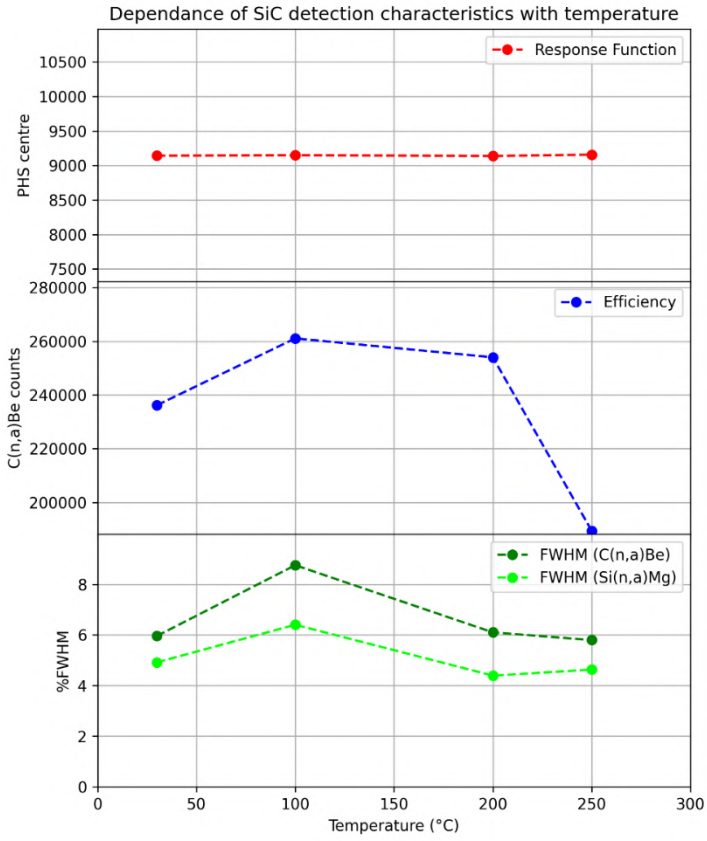

Fig. 7. Evolution of the detection characteristics of the SiC as a function of the temperature (on the x-axis). The three graphs monitor the evolution of the response function (in red, on top) the number of counts per 10^{13} neutrons produced at the neutron source, which is connected to the efficiency (in blue, centre) and the broadening of two different peaks (in green, bottom).

4. Summary

In this paper the functionality and detection characteristics of a SiC fast neutron detector prototype were tested at high temperatures under irradiation of DT neutrons (with 14.6 MeV energy). The experimental setup was chosen similar than the oone used by Angelone in [5-13] in order to compare the results with diamond's. While the diamond tested in the past appear to experience a degradation in the response function as early as 160°C, the SiC demonstrated an outstanding solidity in the detection parameters up to 250°C, to the point in which the most important features of the deposited energy spectra look undistinghishable between room temperature and at 250°C. Temperatures higher than 250°C were not reached, possibly due to a design fault of the pressure contacts. Activities in the near future will try to solve the issue (for example, by adopting a spring-based contacting system) in order to characterize the detector for temperatures as high as 600°C, which are the highest temperatures expected inside ITER's breeding blanket [5-4].

Acknowledgments

A special thanks goes to the Joint Research Agreement Eni-CNR (Linea 5), whose contribution was instrumental in making progress with the research activity.

References

[5-1] G. Federici et al., An overview of the EU breeding blanket design strategy as an integral part of the DEMO design effort, Fusion Engineering and Design, Volume 141, April 2019, Pages 30-42.

[5-2] L.M. Giancarli et al., Overview of the ITER TBM Program, Fusion Engineering and Design, Volume 87, Issues 5–6, August 2012, Pages 395-402.

[5-3] S. Segantin et al., Neutronic Comparison of Liquid Breeders for ARC-like Reactor Blankets, Fusion Engineering and Design, Volume 160, November 2020, 112013.

[5-4] L.M. Giancarli et al., Tritium and heat management in ITER Test Blanket Systems port cell for maintenance operations, Fusion Engineering and Design 89 (2014) 2088–2092.

[5-5] M. Angelone and C. Verona, Properties of Diamond-Based Neutron Detectors Operated in Harsh Environments, J. Nucl. Eng. 2021, 2(4), 422-470.

[5-6] L. Giacomelli, Neutron emission spectroscopy of DT plasmas at enhanced energy resolution with diamond detectors, Review of Scientific Instruments 87, 11D822 (2016).

[5-7] M. Rebai et al., Response of a single-crystal diamond detector to fast neutrons, JINST 8 P10007.

[5-8] M. Hodgson et al., Characterization of silicon carbide and diamond detectors for neutron applications, Meas. Sci. Technol. 28 (2017) 105501 (13pp)

[5-9] M. Rebai et al., New thick silicon carbide detectors: Response to 14 MeV neutrons and comparison with single-crystal diamonds, Nuclear Inst. and Methods in Physics Research, A 946 (2019) 162637.

[5-10] M. De Napoli, SiC detectors: A review on the use of silicon carbide as radiation detection material, Front. Phys. 10:898833.

[5-11] D. Rigamonti et al., Neutron spectroscopy measurements of 14 MeV neutrons at unprecedented energy resolution and implications for deuterium–tritium fusion plasma diagnostics, Measurement Science and Technology, 29 (2018) 045502 (9pp).

[5-12] M. Tardocchi et al., A high-resolution neutron spectroscopic camera for the SPARC tokamak based on the Jet European Torus Deuterium-Tritium experience, Rev Sci Instrum. 2022 Nov 1;93(11):113512.

[5-13] M. Angelone et al., Systematic study of the response of single crystal diamond neutron detectors at high temperature, Journal of Instrumentation, Volume 15, March 2020.

[5-14] C. Weiss et al., High-temperature performance of solid-state sensors up to 500 °C, Nuclear Inst. and Methods in Physics Research, A 1040 (2022) 167182

[5-15] D. Szalkai et al., Fast Neutron Detection With 4H-SiC Based Diode Detector up to 500 ◦C Ambient Temperature, IEEE Transaction on Nuclear Science, vol. 63, no. 3, June 2016.

[5-16] F.H. Ruddy, Performance and Applications of Silicon Carbide Neutron Detectors in Harsh Nuclear Environments, EPJ Web of Conferences 253, 11003 (2021).

[5-17] M.H. Kushoro et al., Silicon Carbide characterization at the n_TOF spallation source with quasi-monoenergetic fast neutrons, Nuclear Inst. and Methods in Physics Research, A 983 (2020) 164578.

[5-18] M.H. Kushoro et al., Detector Response to D-D Neutrons and Stability Measurements with 4H Silicon Carbide Detectors, Materials 2021, 14, 568.

[5-19] M.H. Kushoro et al., Performance of a thick 250 μm silicon carbide detector: stability and energy resolution, 2023 JINST 18 C03007.

[5-20] S. Tudisco et al., SiCILIA—Silicon Carbide Detectors for Intense Luminosity Investigations and Applications, Sensors 2018, 18, 2289.

[5-21] F. La Via et al., Silicon Carbide devices for radiation detection and measurements, J. Phys.: Conf. Ser. 1561 012013.

[5-22] A. Meli et al., Epitaxial Growth and Characterization of 4H-SiC for Neutron Detection Applications, Materials 2021, 14, 976.

[5-23] Available online: https://cividec.at/electronics-Cx-L.html

[5-24] Available online: https://www.caen.it/products/dt5730/

[5-25] A. Pietropaolo et al., The Frascati Neutron Generator: A multipurpose facility for physics and engineering, IOP Conf. Series: Journal of Physics: Conf. Series 1021 (2018) 012004.

Chapter 6
Summary and Conclusions

Solid state detectors represent a good solution for the many requirements for neutron detection in Tokamaks. They feature very small, solid active volumes which are mostly insensitive to magnetic fields and gamma radiation; they also have good energy resolutions and, when coupled with proper electronics, are also very fast in their signal processing, allowing for the detection and energy measurement of neutrons in pulse mode with detection rates up to about 2 Mcps. This, along with their low efficiencies, makes them ideal for the very high flux regimes typical of high-power fusion plasma.

Diamond detectors were experimented extensively both on tokamaks and accelerator-based neutron sources, finding excellent performances and detection capabilities, as well as some limits in their time stability and high temperature performance. Silicon Carbide detector is a promising design, potentially being an easier-to-manufacture alternative to diamond detectors. Beyond developing and characterizing those detectors, the thesis also draws a comparison between the two solid state detectors, highlighting advantages and disadvantages of each as well as pointing out prospects for improvement. The experience matured in the research activity also allowed for the improvement of the prototypes and the electronics. For example, different active volume sizes were tested, experimenting on the trade-off between more complex operation and manufacturing of thick SiCs, and a higher charge deposition effect with thin SiCs.

The first characteristic of the SiC to take into consideration when comparing it with diamond is the fact that the presence of Silicon atoms along Carbon atoms increases the number of reaction channels available for neutron interaction, causing a more complex **response function**. The nuclear reaction $^{12}C(n,\alpha)^{9}Be$ was proven to be the best candidate for the DT spectroscopy for both the diamond and the SiC, but in the latter case other nuclear reactions with Silicon ions give rise to spectral structures whose low-energy tails overlap with the $^{12}C(n,\alpha)^{9}Be$ peak, making it more difficult to extract information and reducing the precision of it. The higher number of reactions makes also more complicated to match simulated results with experimental ones, making it more difficult to verify the simulations and operate a deconvolution of results.

On the topic of energy resolution (which is an essential characteristic for DT fusion plasma spectroscopy), the SiC demonstrated **energy resolutions** to 14 MeV neutrons between 2% and 3% and energy resolutions to 5.5 MeV alpha particles between 1% and 5%. The large range of results means that the prototype, electronics, and environmental conditions influence more the energy resolution than the active volume material itself. Nevertheless, the resolutions are worse than the best ones obtained with diamond (1% to 14 MeV neutrons and 0.4% [48] with alphas) but are good enough to be used for Tokamak's spectroscopic applications (which requires energy resolutions better than 5% [24]).

For **spectroscopic applications** the role of the SiC can be object of debate. On one hand the SiC demonstrates a lower energy resolution and a more complicated response function, which might further complicate the response analysis; the latter factor, in particular, might cause problems for applications were matching pulse height spectra to simulation is key, like the measurement of fuel ion ratio (see section 2.2.2). On the other hand, SiC demonstrated (contrarily to the diamond) an outstanding stability, which will prove very important in upcoming fusion machines featuring longer plasma discharges with higher neutron fluency. It must be noted that good progress is made in the CVD diamond field to manufacture them with higher purities, trying to solve or alleviate the causes for the lack of stability. This comes in

parallel to the progressive increase to the energy resolution of the SiC achieved during this thesis by improving materials and measurement techniques. It might therefore be expected a convergence, with the SiC improving its energy resolution to match diamond's and the diamond improving its stability to match SiC's.

One characteristic of the SiC which cannot be replicated with diamond, though, is the **partially depleted operation**. It was demonstrated in the thesis that the partial depleted operation, obtained by operating a thick detector with a lower bias that the one necessary for full depletion, does not worsen its detection capabilities. Such operation mode would allow for the online tuning of efficiency without replacing the detector, which might be a feature for tuning the efficiency to match the expected neutron flux, allowing the detector to reach the optimal count rate of few hundreds of kcps both when exposed to lower fluxes (for example, the ones due to a DD plasma) or higher fluxes (for example, the ones due to a DT plasma). To match such flux would allow the SiC to collect the amount of data needed to build a pulse height spectrum faster when exposed to lower fluxes, therefore granting it a better time resolution. In order to obtain the same effect, most advanced diamond designs feature multiple diamonds with different active volume sizes, which comes at the cost of the added complexity and cost of employing an higher number of detectors in parallel. It must be noted, though, that for a SiC to operate with very different depleted region sizes would require thick SiCs operating a very high (>kV) bias over a crystal with thicknesses below 1mm; this operation, although well inside the properties of the SiC found in literature, has not been proven in the course of the thesis and will require for a high voltage electronics.

One area where the SiC produces better results than diamond are the "stress tests": SiC demonstrates better stability, better longevity and better **operativity in temperature** than the diamond, regardless of the size of the active volume, and there are clues about it having at least the same radiation hardness of the diamond. This means that the SiC is more suitable than the diamond for any application with very harsh environments, like the breeding blanket of a DT plasma device. In such environments the SiC can also be an alternative to passive detectors (most and foremost activation foils): the advantage of the SiC compared to them is its ability to measure the flux (thus, to have a temporal resolution) and to perform spectroscopy, which might be useful as a validation of the Montecarlo codes simulating the very intense neutron fluxes inside the breeding blanket.

As a final summary, the Silicon Carbide detector prospects itself being a good candidate for neutron detection in fusion plasmas. SiC doesn't constitute an overall improvement on the diamond detector, since some of the properties that make the diamond the state of art of solid state detectors for fast neutrons – first and foremost its energy resolution – are still unparalleled. It, although, represents an interesting alternative for the harsh environment close to the plasma, an alternative detector featuring a fine-tuning of the efficiency and also a compromise candidate for neutron spectrometer that sacrifice some detection quality for easier manufacturing. The research on SiC, nonetheless, has still plenty of room for improvement, and the result found out in this thesis suggests that further research is very promising. One future important step will be to install a SiC prototype on a volumetric neutron source (nominally, a tokamak) in order to test it in a fusion-relevant environment.

References

[1] Available online: https://ourworldindata.org/energy-mix

[2] Energy Institute Statistical Review of World Energy (2023); Vaclav Smil (2017)

[3] B. Lehner et al., "High-resolution mapping of the world's reservoirs and dams for sustainable river-flow management", Front Ecol Environ. 2011; 9(9): 494–502, doi:10.1890/100125

[4] Available online: https://world-nuclear.org/information-library/nuclear-fuel-cycle/mining-of-uranium/uranium-mining-overview.aspx#:~:text=Uranium%20is%20a%20naturally%20occurring,than%20cobalt%2C%20lead%20or%20molybdenum.

[5] Available online: chrome-extension://efaidnbmnnnibpcajpcglclefindmkaj/https://www.oecd-nea.org/upload/docs/application/pdf/2020-12/7555_uranium_-_resources_production_and_demand_2020__web.pdf

[6] S. Meschini et al., "Review of commercial nuclear fusion projects", Front. Energy Res., 07 June 2023 Sec. Nuclear Energy Volume 11 - 2023 | https://doi.org/10.3389/fenrg.2023.1157394

[7] S. Entler, "Engineering Breakeven", Journal of Fusion Energy volume 34, pages513–518 (2015), doi: https://doi.org/10.1007/s10894-014-9830-2

[8] G. McCraken, P. Stott "Fusion: The Energy of the Universe", doi: https://doi.org/10.1016/B978-0-12-481851-4.X5000-8

[9] M. Greenwald, "Density limits in toroidal plasmas", Plasma Phys. Control. Fusion 44 (2002) R27-R53

[10] D.A. Gates and L. Delgado-Aparicio, "Origin of Tokamak Density Limit Scalings", Phys. Rev. Lett. 108 (2012) 165004

[11] "Summary of the ITER Final Design Report," July 2001, p.9.

[12] V.A.Chuyanov, ITER Test Blanket Working Group, "ITER Test Blanket Working Group activities: a summary, recommendations and conclusions", Fusion Eng. Design 61–62(2002) 273–281.

[13] Federici, G.; Boccaccini, L.; Cismondi, F.; Gasparotto, M.; Poitevin, Y.; Ricapito, I. (2019-04-01). "An Overview of the EU breeding blanket design strategy as an integral part of the DEMO design effort". Fusion Engineering and Design. Amsterdam, Netherlands: Elsevier. 141: 30–42. doi:10.1016/j.fusengdes.2019.01.141.

[14] E.A. Azizov, "Tokamaks: from A D Sakharov to the present", 2012 Phys.-Usp. 55 190, doi: 10.3367/UFNe.0182.201202j.0202

[15] JET Team, "Fusion energy production from a deuterium-tritium plasma in the JET tokamak", 1992 Nucl. Fusion 32 187 doi:10.1088/0029-5515/32/2/I01

[16] M. Keilhacker et al., "The scientific success of JET", Nucl. Fusion 41 1925 doi: 10.1088/0029-5515/41/12/217

[17] Available online: https://euro-fusion.org/programme/demo/

[18] A. Creely et al., "Overview of the SPARC tokamak". Journal of Plasma Physics. (2020) 86 (5): 865860502. Bibcode:2020JPlPh..86e8602C. doi:10.1017/S0022377820001257. ISSN 0022-3778.

[19] G. Ericsson, "Advanced Neutron Spectroscopy in Fusion Research", Journal of Fusion Energy (2019) 38:330–355, doi: 10.1007/s10894-019-00213-9(0123456789().,-volV)(0123456789,-().volV)

[20] "ITER Neutron Activation System DDD", ITER_D_3UYPYF v 3.0

[21] C.W. Barnes et al., "Measurements of DT and DD neutron yields by neutron activation on the Tokamak Fusion Test Reactor", Rev. Sci. Instrum. 66, 888–890 (1995), https://doi.org/10.1063/1.1146195

[22] G.Q. Zhong et al, "Development of a wide-range neutron flux monitoring system in EAST", 2020 JINST 15 P05011, doi: https://doi.org/10.1088/1748-0221/15/05/P05011

[23] L. Yang et al, "Development of a wide-range and fast-response digitizing pulse signal acquisition and processing system for neutron flux monitoring on EAST", NUCL SCI TECH 33, 35 (2022). https://doi.org/10.1007/s41365-022-01016-y

[24] M. Angelone, A. Klix, "TASK-3.1: TBM nuclear instrumentation and research plan SECOND INTERIM REPORT"

[25] F. Pompili et al., "Radiation and thermal stress test on diamond detectors for the Radial Neutron Camera of ITER", Nuclear Inst. And Methods in Physics Research, A936 (2019) 62–64, doi: https://doi.org/10.1016/j.nima.2018.10.110

[26] T. Vasilopoulou at al., "Activation foil measurements at JET in preparation for D-T plasma operation", Fusion Engineering and Design, Volume 146, Part A, 2019, Pages 250-255, ISSN 0920-3796, https://doi.org/10.1016/j.fusengdes.2018.12.038. (https://www.sciencedirect.com/science/article/pii/S0920379618308032)

[27] J. Bielecki, A. Kurowski, "Neutron Diagnostics for Tokamak Plasma: From a Plasma Diagnostician Perspective", Journal of Fusion Energy (2019) 38:386–393 doi: 10.1007/s10894-018-0195-9

[28] R. Rodionov et al., "Fusion neutron emissivity tomography for ITER Vertical Neutron Camera", Nuclear Inst. And Methods in Physics Research, A1040 (2022) 167127, https://doi.org/10.1016/j.nima.2022.167127

[29] O.N. Jarvis, "Neutron measurement techniques for tokamak plasmas", 1994 Plasma Phys. Control. Fusion 36 209, doi: 10.1088/0741-3335/36/2/002

[30] M. Angelone et al., "Calibration of the neutron yield measurement system on FTU tokamak", 1990 Rev. Sci. Instrum. 61 3536

[31] L. Giacomelli et al., "Advanced neutron diagnostics for JET and ITER fusion experiments", Nucl. Fusion 45 (2005) 1191–1201 doi:10.1088/0029-5515/45/9/019

[32] Available online: https://uu.diva-portal.org/smash/get/diva2:1190103/FULLTEXT01.pdf

[33] M. Gatu Johnson et al. "The 2.5-MeV neutron time-of-flight spectrometer TOFOR for experiments at JET". Nuclear Instruments and Methods in Physics Research A, 591:417, 2008.

[34] L. Giacomelli, "Development of Neutron Emission Spectroscopy Instrumentation for Deuterium and Deuterium-Tritium Fusion Plasmas at JET", Digital Comprehensive Summaries of Uppsala Dissertations from the Faculty of Science and Technology 339, http://uu.diva-portal.org/smash/get/diva2:170674/FULLTEXT01.pdf

[35] G. Ericsson et al., "Neutron emission spectroscopy at JET—Results from the magnetic proton recoil spectrometer". Review of Scientific Instruments, 72:759, 2001.

[36] E. Andersson Sundén et al., "The thin-foil magnetic proton recoil neutron spectrometer MPRu at JET", Nuclear Instruments and Methods in Physics Research Section A: Accelerators, Spectrometers, Detectors and Associated Equipment Volume 610, Issue 3, 11 November 2009, Pages 682-699, doi: 10.1016/j.nima.2009.09.025

[37] F. Binda, "Liquid scintillators as neutron diagnostic tools for fusion plasmas - System characterization and data analysis", Digital Comprehensive Summaries of Uppsala Dissertations from the Faculty of Science and Technology, 1646, https://uu.diva-portal.org/smash/get/diva2:1190103/FULLTEXT01.pdf

[38] J. Bielecki et al., "Phillips-Tikhonov regularization with a priori information for neutron emission tomographic reconstruction on joint european torus", Rev. Sci. Instrum. 86 (2015) 093505.

[39] M. Tardocchi et al., "A high-resolution neutron spectroscopic camera for the SPARC tokamak based on the Jet European Torus Deuterium-Tritium experience", Rev Sci Instrum. 2022 Nov 1;93(11):113512. doi: 10.1063/5.0101779.

[40] D.B. Syme et al., "Fusion yield measurements on JET and their calibration", Fusion Engineering and Design Volume 89, Issue 11, November 2014, Pages 2766-2775 doi: 10.1016/j.fusengdes.2014.07.019

[41] Knoll, G.F. "Radiation Detection and Measurement. 4th Edition", (2010) Wiley, Hoboken, 217

[42] V.V. Gaganov et al., "Experimental characterisation of diamond-based neutron spectrometer", JINST 17 T09001 doi: 10.1088/1748-0221/17/09/T09001

[43] D. Rigamonti et al., "Neutron spectroscopy measurements of 14 MeV neutrons at unprecedented energy resolution and implications for deuterium–tritium fusion plasma diagnostics", Meas. Sci. Technol. 29 (2018) 045502 (9pp) doi: 10.1088/1361-6501/aaa675

[44] L. Giacomelli et al., "Neutron emission spectroscopy of DT plasmas at enhanced energy resolution with diamond detectors", Rev. Sci. Instrum. 87, 11D822 (2016) doi: 10.1063/1.4960307

[45] Available online: http://riegler.web.cern.ch/lectures/lecture5.pdf

[46] E. Steinbauer et al., "Energy resolution of silicon detectors: approaching the physical limit", Nuclear Instruments and Methods in Physics Research Section B: Beam Interactions with

Materials and Atoms, Volume 85, Issues 1–4, 2 March 1994, Pages 642-649, doi: 10.1016/0168-583X(94)95898-X

[47] L. Lehtilä, "Implementation and characterization of Silicon detectors for studies on neutron-induced nuclear reactions", 2019, Uppsala University

[48] S. Tudisco et al., "Silicon carbide for future intense luminosity nuclear physics investigations", IL NUOVO CIMENTO 42 C (2019) 74, DOI 10.1393/ncc/i2019-19074-1

[49] R. Cheung, "Silicon carbide microelectromechanical systems for harsh environments". (2006) Imperial College Press. p. 3. ISBN 1-86094-624-0.

[50] A. Bauer et al., "Structure refinement of the silicon carbide polytypes 4H and 6H: unambiguous determination of the refinement parameters", Acta Cryst. (2001). A57, 60-67, doi: 10.1107/s0108767300012915

[51] G L Zhao and D Bagayoko, "Electronic structure and charge transfer in 3C- and 4H-SiC" 2000 New J. Phys. 2 16, doi: 10.1088/1367-2630/2/1/316

[52] S. Tudisco et al., "SiCILIA—Silicon Carbide Detectors for Intense Luminosity Investigations and Applications", Sensors 2018, 18, 2289; doi:10.3390/s18072289

[53] M. Mittal et al., "Chapter 7 - Nanofabrication techniques for semiconductor chemical sensors", Handbook of Nanomaterials for Sensing Applications Micro and Nano Technologies, 2021, Pages 119-137, doi: 10.1016/B978-0-12-820783-3.00023-3

[54] F. La Via et al., "Silicon Carbide devices for radiation detection and measurements" 2020 J. Phys.: Conf. Ser. 1561 012013, doi:10.1088/1742-6596/1561/1/012013

[55] M. Angelone et al., "Systematic study of the response of single crystal diamond neutron detectors at high temperature", 2020 JINST 15 P03031, doi: 10.1088/1748-0221/15/03/P03031

[56] Available online: https://physics.nist.gov/PhysRefData/Star/Text/ASTAR.html

[57] Available online: https://physics.nist.gov/PhysRefData/Star/Text/PSTAR.html

[58] Available online: https://www.thermocoax.com/signals-transmission/

[59] M. Rebai et al., "New thick silicon carbide detectors: Response to 14 MeV neutrons and comparison with single-crystal diamonds", Nuclear Inst. and Methods in Physics Research, A 946 (2019) 162637, doi: 10.1016/j.nima.2019.162637

[60] D.A. Brown et al., "ENDF/B-VIII.0: The 8th major release of the nuclear reaction data library with CIELO-project cross sections, new standards and thermal scattering data", Nucl. Data Sheets 148(2018)1.

[61] Technical specifications available online: https://cividec.at/index.php?module=public.category&cat=5

[62] Technical specifications available online: chrome-extension://efaidnbmnnnibpcajpcglclefindmkaj/https://www.ortec-online.com/-/media/ametekortec/manuals/7/710-mnl.pdf?la=en&revision=d4d10328-c254-4e0d-ab9d-aa5b89d2207c

[63] Technical specifications available online: chrome-extension://efaidnbmnnnibpcajpcglclefindmkaj/https://galileo.phys.virginia.edu/research/groups/g-2/Wiener_MPOD_3-0/Manuals%20and%20Doc%20files/WIENER_Catalog_2013.pdf

[64] Technical specifications available online: https://www.caen.it/products/n1471/

[65] Technical specifications available online: https://www.testequipmenthq.com/datasheets/KEITHLEY-6487-Datasheet.pdf

[66] Technical specifications available online: https://www.caen.it/products/dt5730/

[67] Carlo Cazzaniga, Fast Neutron Measurement for Fusion and Spallation Sources Applications, (Ph.D. thesis), Università degli studi di Milano-Bicocca

[68] [Technical specs available online: https://campoverde.it/wp-content/uploads/2021/10/Catalogo-Campoverde-Sorgenti-di-taratura.pdf, section "Sorgenti per spettrometria alfa"

[69] C. Guerrero, "Performance of the neutron time-of-flight facility n_TOF at CERN", Eur. Phys. J. A 49, 27 (2013). https://doi.org/10.1140/epja/i2013-13027-6

[70] C. Cazzaniga and C.D. Frost, "Progress of the Scientific Commissioning of a fast neutron beamline for Chip Irradiation", 2018 J. Phys.: Conf. Ser. 1021 012037 DOI: 10.1088/1742-6596/1021/1/012037

[71] Available online: https://www.eai.enea.it/archivio/ricerca-e-innovazione-per-la-sfida-spaziale/il-frascati-neutron-generator-e-i-test-di-resistenza-a-radiazione.html

[72] Python library documentation available online: https://docs.scipy.org/doc/scipy/reference/generated/scipy.optimize.curve_fit.html